TUM School of Computation, Information and Technology
Technical University of Munich

3D Microwave Cavity-Controlled Nanoelectromechanical Systems

for Cavity Electromechanics and Quantum Sensing

Anh Tuan Le

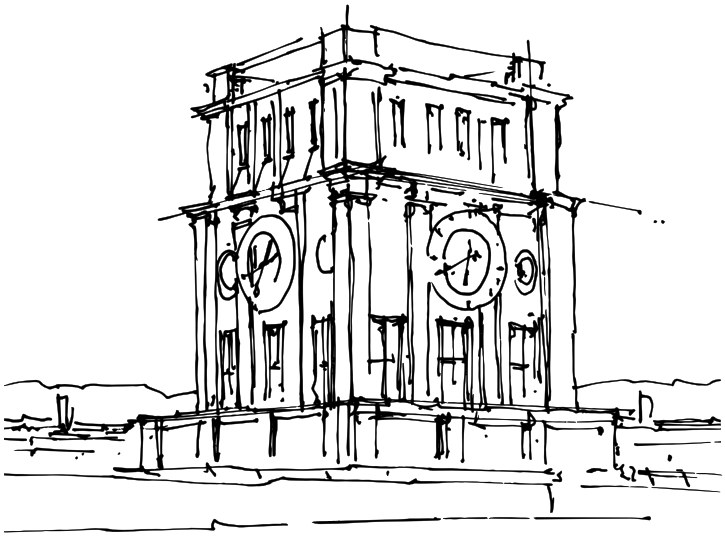

3D Microwave Cavity-Controlled Nanoelectromechanical Systems

for Cavity Electromechanics and Quantum Sensing

Anh Tuan Le

TUM School of Computation, Information and Technology
Technische Universität München

3D Microwave Cavity-Controlled Nanoelectromechanical Systems

for Cavity Electromechanics and Quantum Sensing

Anh Tuan Le

Vollständiger Abdruck der von der TUM School of Computation, Information and Technology der Technischen Universität München zur Erlangung des akademischen Grades eines

Doktors der Ingenieurwissenschaften (Dr.-Ing.)

genehmigten Dissertation.

Vorsitz:
Prof. Dr. Bernhard Wolfrum

Prüfer*innen der Dissertation:
1. Prof. Dr. Eva M. Weig
2. Prof. Dr. Gary A. Steele

Die Dissertation wurde am **16.11.2022** bei der Technischen Universität München eingereicht und durch die TUM School of Computation, Information and Technology am **10.03.2023** angenommen.

"Enthusiasm is everything.
It must be taut and vibrating like a guitar string."

*— **Pelé** (Edson Arantes do Nascimento)*

Abstract

This thesis explores the rich dynamics of nanomechanical resonators using cavity-assisted detection scheme at room temperature. The PhD project initially focuses on the development of a novel detection scheme to replace the on-chip coplanar waveguide architecture to enhance the detection efficiency of the nanomechanical displacement. We follow the recent development in the field of circuit quantum electrodynamics and employ the key element that is used to protect superconducting qubits from decoherence and to conduct nondemolition measurements. This element is the three dimensional microwave cavity that has large volume modes, strong electric and magnetic field confinement and it offers a high quality factor even at room temperature.

In the first part of this work, we focus on the cavity electromechanical system that operates in the sideband resolved regime at room temperature. To this end, a non-metallized silicon nitride string resonator is dielectrically coupled to transverse magnetic (TM_{110}) mode of a cylindrical 3D microwave cavity, which offers almost perfect sideband resolution. We characterize the electromechanical coupling by two measurements, the cavity-induced eigenfrequency shift of the mechanical resonator and the optomechanical induced reflection (OMIR). While the former is dominated by dielectric effects, the latter reveals a clear signature of the dynamical backaction of the cavity field on the mechanical resonator. Our first attempt to implement a room temperature cavity electromechanical system reveals a relative small single photon coupling rate in the sub-mHz regime. Due to the large number of photons circulating inside the 3D cavity, it is possible to verify the coupling. The required strong red-detuned drive in the OMIR experiment results in nonlinear response of the mechanical resonator.

In the second part, we provide a comprehensive description in the development (both theoretical and experimental) of the iterative adaptive frequency sensing protocol based on the ubiquitous Ramsey interferometry of a two-level system. In particular, the protocol enables the estimation of unknown frequencies with high precision from short and finite signals. The implementation of Magnus-based corrections to the coherent control pulses of the two-level system allows to overcome experimental constrains such as bandwidth limitation in pulse generation. At the same time, it mitigates leakages in sensing and readout state preparations of the Ramsey protocol. From the signal processing point of view, the protocol suppresses loss mechanisms that hinder correct frequency estimation from Fourier transforms. By applying zero-padding and window techniques to the signals in the time domain, the protocol substantially suppresses spectral leakage and scalloping losses. In the experimental realization of the iterative adaptive sensing protocol, we apply again the cavity-assisted detection scheme using a coaxial $\lambda/4$ microwave 3D cavity for mechanical motion detection. Additionally, we employ the coherent nature of the nanomechanical two-mode system which consists of two strongly coupled flexural in-plane and out-of-plane modes. The application of coherent control pulses to the classical two-level system is possible due to the dielectric frequency tuning capability and the high mechanical quality factor. The two mechanical flexural modes can exchange energy coherently in the resonant condition, orders of magnitude faster than the decay time. Thus, it enables to investigate the system dynamics in time-resolved measurements.

The experimental results confirm the validity of our iterative adaptive sensing scheme and demonstrate for the first time the correct implementation of the theoretically proposed Magnus-based corrections. Thus, a better coherent control in state preparation of the two-level system can be obtained. As a proof

of principle, we perform the sensing capability of the two-level system by modifying the electric field environment inside the 3D microwave cavity, in which the nanomechanical resonator is embedded. To this end, we observe a clear shift in the level splitting of the two flexural modes caused by the change in the before mentioned electric field.

Zusammenfassung

In dieser Arbeit wird die Dynamik von nanomechanischen Resonatoren mit Hilfe eines kavitäten gestützten Detektionsmechanismus bei Raumtemperatur untersucht. Die Dissertation konzentriert sich zunächst auf die Entwicklung eines neuartigen Detektionssystems, das die koplanare Wellenleiterarchitektur auf dem Chip ersetzen soll, um die Detektionseffizienz der nanomechanischen Verschiebung zu verbessern. Wir folgen den jüngsten Entwicklungen auf dem Gebiet der Quantenelektrodynamik und setzen das Schlüsselelement ein, das verwendet wird, um supraleitende Qubits vor Dekohärenz zu schützen und um zerstörungsfreie Messungen durchzuführen. Bei diesem Element handelt es sich um einen dreidimensionalen Mikrowellenhohlraum mit großen Volumenmoden, starker elektrischen und magnetischen Feldeinschränkung und einer hohen Güte selbst bei Raumtemperatur.

Im ersten Teil dieser Arbeit konzentrieren wir uns auf die Untersuchung des elektromechanischen Hohlraumsystems, das bei Raumtemperatur im seitenbandaufgelösten Bereich fungiert. Zu diesem Zweck wird ein nicht-metallisierter Siliziumnitrid-Stringresonator dielektrisch an die transversale magnetische (TM_{110})-Mode eines zylindrischen 3D-Mikrowellenresonators gekoppelt, der eine nahezu perfekte Seitenbandauflösung bietet. Wir charakterisieren die elektromechanische Kopplung durch zwei Messungen: die kavitätsinduzierte Eigenfrequenzverschiebung des mechanischen Resonators und die optomechanisch induzierte Reflexion (OMIR). Während erstere von dielektrischen Effekten dominiert wird, zeigt letztere eine deutliche Signatur der dynamischen Rückwirkung des Hohlraumfeldes auf den mechanischen Resonator. Unser erster Versuch, ein elektromechanisches System mit Hohlraum bei Raumtemperatur zu realisieren, zeigt eine relativ geringe Kopplungsrate für einzelne Photonen im Sub-mHz-Bereich. Aufgrund der großen Anzahl von Photonen, die innerhalb des 3D-Hohlraums zirkulieren, ist es jedoch möglich, die Kopplungsstärke zu verifizieren. Die erforderliche starke Rotverstimmung im OMIR-Experiment führt zu einem nichtlinearen Verhalten des mechanischen Resonators.

Im zweiten Teil berichten wir ausführlich über die Entwicklung (sowohl theoretisch als auch experimentell) des iterativen adaptiven Frequenzbestimmungsprotokolls, das auf der Ramsey-Interferometrie eines Zwei-Niveau-Systems basiert. Das Protokoll ermöglicht eine hochpräzise Schätzung unbekannter Frequenzen aus kurzen und endlichen Signalen. Die Implementierung von Magnus-basierten Korrekturen an den kohärenten Kontrollpulsen ermöglicht es, experimentelle Einschränkungen wie Bandbreitenlimitierung bei der Pulserzeugung zu überwinden. Gleichzeitig werden Leck-Effekte bei der Vorbereitung des Ramsey-Protokolls für den Abtast- und Auslesezustand reduziert. Aus Sicht der Signalverarbeitung unterdrückt das Protokoll Verlustmechanismen, die eine korrekte Frequenzschätzung aus Fourier-Transformationen verhindern. Die Anwendung der Zero-Padding-Technik und der Fensterfunktion auf die Signale unterdrückt spektrale Leck-Effekte und Scalloping-Verluste erheblich. Bei der experimentellen Umsetzung des iterativen adaptiven Sensing-Protokolls verwenden wir wiederum den kavitäten gestützten Detektionsmechanismus. In diesem Fall wird die zylindrische 3D Kavität durch eine $\lambda/4$ Mikrowellenkavität ersetzt. Außerdem nutzen wir die Eigenschaft des nanomechanischen Zweimodensystems aus, das aus zwei stark gekoppelten *in-plane* und *out-of-plane* Biegemoden besteht, um die kohärente Kontrolle zu untersuchen. Die Anwendung von kohärenten Steuerimpulsen auf das klassische Zwei-Niveau-System ist aufgrund der dielektrischen Frequenzabstimmung und des hohen mechanischen Qualitätsfaktors möglich. Die mechanischen Biegemoden

können im Resonanzzustand, um Größenordnungen schneller als die Abklingzeit, kohärent Energie austauschen. Dadurch kann die Systemdynamik in zeitaufgelösten Messungen untersucht werden.
Die experimentellen Ergebnisse bestätigen die Gültigkeit unseres iterativen, adaptiven Sensing-Schemas. Sie zeigen erstmalig die korrekte Implementierung der theoretisch entwickelten Magnus-basierten Korrekturen. Mit dieser kann eine bessere Kohärenzkontrolle bei der Vorbereitung der Zustände des Zwei-Niveau-Systems gewährleistet werden. Zum Beweis demonstrieren wir die Sensing-Fähigkeit des Zwei-Niveau-Systems. Dafür verändern wir die elektrische Feldumgebung innerhalb des 3D-Mikrowellenhohlraums, in welchem sich der nanomechanische Resonator befindet. Wir beobachten dabei eine deutliche Verschiebung in der Niveauspaltung der stark gekoppelten Biegemoden. Diese wird durch eine Veränderung des zuvor erwähnten elektrischen Feldes verursacht.

Contents

List of Figures

List of Tables

1 Introduction

In their *news & reviews* article [1], C. H. Mielke and A. V. Balatsky portray a spectacular destruction of a suspension bridge built over the Tacoma Narrows in Washington state in the US (see Fig. 1.1). Before the total collapse in November 1940, the bridge underwent severe mechanical deformations owing to gale-force wind at 64 km/h. These strong side-winds were the cause for the aerodynamics self-excitation effect of the bridge [2]. The induced fundamental antisymmetric torsion mode forced the bridge to oscillate with larger and larger amplitudes and hence, ripping vital suspender cables apart. This catastrophic but spectacular event sets a good example of a self-sustained mechanical oscillator.

Figure 1.1 | Suspended Tacoma Narrows Bridge in November 1940.
The total collapse of the Tacoma Narrows bridge sets a macroscopic example for the dynamics of self-sustained oscillators. Nowadays, a variety of micrometer and nanometer size suspended structures are used in modern laboratories to study numerous physical phenomena in different fields of research.
Reprinted from Ref. [1], with the permission of Springer Nature.

Many decades later, researchers from all over the world have successfully employed the vibrational motions of such suspended structures (but much smaller) to study a multitude of physical phenomena

including the before mentioned self-sustained oscillation [3], synchronization [4], frequency stabilization [5] and advanced sensing applications [6–11].

F. Beil et al. [12] fabricate such a freely suspended structure that is about two billion times smaller than the Tacoma Narrows bridge and can oscillate in a more extreme manner without collapsing. This nanosized bridge is also known as a nanomechanical resonator that is made by suspending a beam of gallium arsenide between two acoustic transducers. In their experiment, Beil and co-workers use the acoustic transducers at both ends of the nanobridge to generate sound waves that, in turn, set up surface acoustic waves in the GaAs. The researchers also introduce confined two-dimensional electron gas (2DEG) into the beam to study the interaction between the confined electrons and the vibration of the crystal lattice known as phonons. The remarkable feature in this experiment is that the system can be driven beyond the harmonic motion to explore extreme conditions in a controllable fashion. In order to reach the so-called shock waves regime, the two transducers are simultaneously driven with phase locked radio frequency (rf) signals. By adjusting the relative phase shift ϕ of the two signals, standing wave patterns can be formed causing deformations in the nanomechanical device. The existence of the shock waves can then be proven by probing the response of the confined two-dimensional electrons gas.

The experiments discussed above, however, are examples for systems that operate solely in the classical regime. As technological advances in patterning mechanical structures with nanometer-scale have made massive strides, researchers hope to conduct experiments with nanomechanical devices at the quantum limit that further illuminate the boundary between microscopic realm, governed by quantum mechanics, and the macroscopic world, governed by classical mechanics [13, 14]. The impressive progress in the study of nano- and micromechanical resonators and the common goal of exploring the quantum regime of mechanical systems can be observed at the biennial Gordon Research Conference [15]. From the first meeting in 2008 [16] to the current date in 2022 [17], the conference has brought together scientists and engineers from diverse background, ranging from astrophysical gravity waves detection [18–21], mesoscopic condensed matter physics [22–27] to quantum optics [28–31], to increase the level of communication and collaboration between researchers. It all has started with experimental results and possible theoretical ideas *towards* the quantum regime in the past. To date in 2022, researchers are formulating experiments that harness quantum behaviour of novel mechanical devices in an increasing range of precision measurements [32–35], quantum devices [36–38], and tests of fundamental physics [39–41]. Among many researchers, O'Connell and his colleagues are the first to bring the mechanical device reliably to its quantum ground state of motion that can, at the same time, strongly coupled to a different quantum system [42]. Here, they use a quantum bit (qubit) device to attain quantum control over individual mechanical quanta (phonons). This result has paved the long road for many subsequent experiments to verify the principle of quantum mechanics and applications in quantum information processing.

Particularly, coherent control and state manipulation of a two-level system are fundamental requirements for the implementation of quantum bits [43–45]. They enable high-fidelity gate operations, which are essential for building fault-tolerant quantum computers [46]. In this thesis, we study the coherent control of a two-level system using a classical approach. We employ the linear and coherent dynamics of two strongly coupled harmonic oscillators as the toy model system to test the dynamics of a quantum mechanical two-level system. The concept of "classical two-level system", in contrast to its quantum mechanical counterpart, can be found in a nanomechanical system with two strongly coupled flexural modes with high mechanical quality factor. Here, the strong coupling mediates coherent exchange in excitation energy of the two respective modes in orders of magnitude faster than the decoherence time of the system. In the remainder of this thesis, we refer to the classical two-level system as the two-mode system.

In their experiment using the nanomechanical string resonator, Faust et al. [47] report the possibility to coherently control and manipulate the two-mode system with pulse schemes that are well-established for nuclear magnetic resonance (NMR) in spins manipulation [48, 49], such as Rabi oscillation [50], Ramsey fringe [51], and Hahn echo [52]. Hence, the system's coherent dynamics can be fully described in the generic picture of the Bloch sphere representation. Similar to a quantum two-level system, the different pulse sequences allow the determination of energy relaxation time T_1 and dephasing times T_2 and T_2^* of the system. It has been found that these characteristic times are almost equal indicating that the phase relaxation mechanism is negligible compared to the energy decay rate [47]. So the system coherence time can be improved with increased quality factor.

A further quantum-classical analogy can be found in experiments demonstrating Landau-Zener transitions [53, 54] and Stückelberg interferometry [55] of two strongly coupled nanomechanical resonator modes. In the framework of the Landau-Zener dynamics, the two flexural modes coherently exchange energy during the single passage through the avoided crossing. Depending on the coupling strength and the detuning speed of the two modes, we can distinguish between two scenarios. In the case of slow detuning, the excitation energy will remain in the same branch in which it was initialized and thus, gradually transforming the initial oscillation to the other orthogonal mode. In the high tuning speed scenario, the diabatic behaviour dominates and there is no mixing between the two modes and hence, causing a transition at the avoided crossing [56]. This non-adiabatic process represents the classical analog to the quantum mechanical Landau-Zener tunnelling of a quantum mechanical two-level system [53, 54]. As a direct consequence of the wave nature of particle in quantum mechanics, the particle can penetrate through classically forbidden region, such as energy gap in band structures of solids. This tunneling barrier can be represented in the classical case by the virtual coupling spring between two mechanical oscillators that is attributed to the energy level splitting of the avoided crossing [57]. In the Stückelberg interferometry experiment [55], the two-level system undergoes a double passage through an avoided crossing within the coherence time. During the transition, the system experiences phase accumulation, which leads to self-interference, which in turn causes oscillations in the return probability. This effect has been experimentally observed exclusively in quantum systems [58–61]. However, Seitner et al. [62, 63] are able to perform Stückelberg oscillations within the framework of a classical approach, demonstrating the possibility to create superposition states of two mechanical modes for sensing applications.

To follow the progress in coherent control of the two strongly coupled nanomechanical flexural modes, we demonstrate in this thesis the theoretical and experimental development of an iterative adaptive sensing (IAS) protocol based on Ramsey interferometry [51, 64, 65] of a nanomechanical two-mode system. Our proposed scheme allows one to estimate unknown frequencies from short and finite signal with high precision, which can be used for sensing application. The experimental results demonstrated in this thesis are purely classical in nature. However, we would like to emphasize that our developed IAS protocol is valid for both the classical and quantum regimes.

This thesis is structured as follow:

- In chapter 2, we start with the relevant description of the nanomechanical string resonator using the Euler-Bernoulli beam theory and approximate the dynamics of the coupled flexural in-plane and out-of-plane modes by solving equation of motions of linear harmonic oscillators. In the second part of the chapter, we introduce different types of three dimensional non-superconducting microwave cavities for the implementation of cavity-assisted mechanical motion detection scheme at room temperature. We then describe the fabrication process for generating free-suspended silicon nitride string resonators.

- Chapter 3 describes dynamics the cavity electromechanical system that operates in the sideband-resolved regime at room temperature. In this chapter, the operating principle of cavity-assisted detection and dielectric actuation is explained in detail.

- In Chapter 4, we introduce the theoretical development of our coherent sensing protocol. We demonstrate how to enhance the ubiquitous Ramsey interferometry of a two-mode system and how to overcome short comings associated with discrete Fourier transform. To the end of this chapter, we show that the iterative adaptive spectroscopy indeed mitigates systematic errors such as spectral leakage and scalloping loss in order to improve frequency estimation.

- In chapter 5, we employ the coherent nature of the strong coupling of the two flexural modes of the string resonator to implement the theoretically proposed IAS protocol to develop a coherent sensor.

- Finally, in the last chapter 6, we sum up the key results of the thesis and provide a perspective in the development of the coherent sensing protocol in the quantum regime using non-classical squeezed states.

2 Experimental and Theoretical Basics

In this chapter, we begin with the theoretical foundations of our nanomechanical string resonator. Subsequently, the various geometries for designing three-dimensional microwave cavities and the mechanisms for coupling to these types of cavities are discussed. In the last part of this chapter, we provide step-by-step descriptions on the nano fabrication procedure in order to obtain freely-suspended, doubly clamped, pre-stressed silicon nitride string resonators.

2.1 The Nanomechanical String Resonator

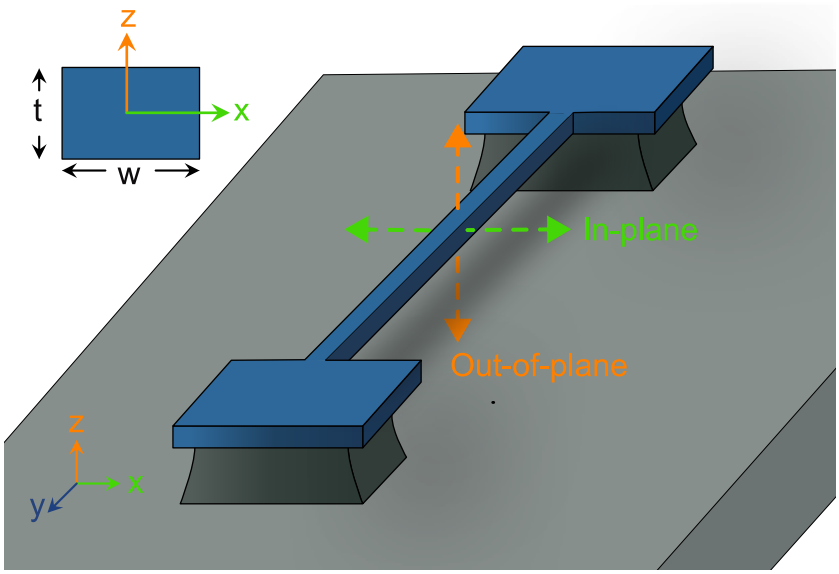

Figure 2.1 | Schematic Visualization of a Freely Suspended Doubly-Clamped Nanomechanical Resonator. The polarization directions of the two fundamental flexural modes in-plane (green arrows) and out-of-plane (orange arrows) are indicated. In addition, we demonstrate the rectangular cross-section of the nano resonator with the thickness t along the z-axis and the width w oriented along the x-axis.

The dynamical behavior of the nanomechanical string resonator can be derived from the elastic beam theory that treats the static deformation problem of homogeneous, linear and isotropic solids [66, 67]. Especially the Euler-Bernoulli beam theory can accurately predict the behaviour of systems with small total displacements and large aspect ratios (i.e. length $\gg$ thickness, width). Therefore, the rotational inertia and shear deformations are neglected to reduce the calculation of flexural vibrations to a one-dimensional problem. Additionally, thin films used in microfabrication tend to have a process related tensile stress and string resonators made of such thin films are therefore usually pre-stressed. By combining the Euler-Bernouilli beam theory and Newton's third law we can derive the equation of motion for the pre-stressed, doubly clamped silicon nitride (Si_3N_4) nanomechanical string resonator as [67]

$$\rho A \frac{\partial^2 u(x,t)}{\partial t^2} + E I_\mathrm{i} \frac{\partial^4 u(x,t)}{\partial x^4} = \sigma A \frac{\partial^2 u(x,t)}{\partial x^2}. \tag{2.1}$$

Here, $u(x,t)$ is the spatial and time-dependent displacement, ρ is the mass density, $A = w \times t$ is the rectangular cross-section with the width w and the thickness t, E is the Young's modulus, I_i is the geometric moment of inertia and σ is the tensile stress. To solve the differential equation in (2.1), we can use the ansatz of separating the spatial and temporal variables

$$u(x,t) = \sum_{n=1}^{\infty} U_n(x) \cos(\omega t). \tag{2.2}$$

Assuming the string has a sinusoidal mode shape with the wavenumber β_n, then we can write the spatial dependent amplitude as:

$$U_n(x) = U_{0,n} \sin(\beta_n). \tag{2.3}$$

For the case of a simply supported doubly clamped beam with the length L, the boundary conditions are defined as [68]

$$U_n(0) = U_n(L) = \frac{\partial^2 U_n(0)}{\partial x^2} = \frac{\partial^2 U_n(L)}{\partial x^2} = 0. \tag{2.4}$$

These boundary conditions form a system of linear equations of fourth order. By substituting Eq. (2.3) in the Ansatz (2.2) and choosing $\beta_n = n\pi/L$ to satisfy the boundary conditions, the set of linear equations can be solved and we find the eigenfrequencies (in the angular units) of the n^{th} modes

$$\omega_{0,n,i} = \left(\frac{n\pi}{L}\right)^2 \cdot \sqrt{\frac{EI_i}{\rho A}} \cdot \sqrt{1 + \frac{\sigma A L^2}{EI_i \pi^2 n^2}}. \tag{2.5}$$

Note that, due to the rectangular cross-section (perpendicular to the neutral y-axis) of nanomechanical string, we define the local polar moment of inertia for each transverse axis i with $i \in \{x, z\}$ as [66]

$$I_i = \int_A i^2 \, \mathrm{d}A. \tag{2.6}$$

Here, we choose the string's width w along the x-axis and the thickness t along z-axis. The flexural vibration mode along the sample substrate can be defined as the *in-plane* (IP) mode with $I_x = I_\mathrm{IP} = tw^3/12$ (see green arrows in Fig. 2.1) and the perpendicular polarized vibration mode along the z-axis is the *out-of-plane* (OOP) mode with the corresponding moment of inertia $I_z = I_\mathrm{OOP} = wt^3/12$ (orange arrows). Due to the difference in the flexural rigidity, we expect the eigenfrequency of the IP-mode to be higher than the OOP-mode for $w > t$.

2.2 Linear Harmonic Oscillators

The vibration of any mechanical resonator is the manifestation of a periodic exchange between the kinetic and potential energy. On the one hand, the deformation of an elastic body due to external forces allows the system to store potential energy that leads the resonator out of its position of rest. On the other hand, the restoring forces accelerate the masses of the system back to the position of equilibrium and hence generate kinetic energy. In turn, this kinetic energy leads the system to traverse the position of rest and generates new deflection energy which, again, represents the potential energy. In a real mechanical resonator, the energy exchange can not last forever since the resonator is coupled to the environment where energy can be dissipated. There are many sources that cause the resonator into damping e.g. the surrounding medium (liquid or gas), the clamping to the substrate and intrinsic losses that result from the resonator's material. Unwanted interactions with the medium can be simply reduced by enclosing the system in vacuum. Clamping losses are caused by radiation of vibrational energy through the anchor of a mechanical resonator [67] and can have a substantial contribution to the total loss mechanism. However, Rieger et al. [69] demonstrate that the effect of clamping losses is negligible in our doubly clamped string resonator geometry. This is due to the large acoustic impedance mismatch between the string and the clamping region. Here, we assume that intrinsic losses such as defects in the material and, even more likely, defects on the resonator's surface are the limiting damping mechanism of our operating nanomechanical device.

Note that highly stressed resonators are known to "dilute" the dissipation intrinsic to the material [70–72], and hence, high mechanical quality factor can be achieved even at room temperature [73]. Additionally, one can combine the dilution dissipation with the so-called "soft clamping" technique, where the mechanical mode penetrates evanescently into the phononic bandgap around the mode frequency [74, 75]. This approach strongly suppresses the radiation to the substrate and further improves the coherence of the mechanical system dramatically. Recent work has shown that by choosing crystalline materials over amorphous or glassy materials and combining them with dilution dissipation and soft-clamping techniques [76] have further boosted the coherence of the mechanical resonator and make it a promising candidate for force, mass sensing and enabling quantum operations at room temperature.

In the following, we discuss the fundamental dynamics of a driven mechanical resonator. We assume the resonator is driven in the linear regime, which can be assured by keeping the total displacement amplitude small. Hence, the dynamics of the driven mechanical resonator can be simplified as the ones of a linear harmonic oscillator with an effective mass m_{eff} which approximates the structure to a point mass located at the maximum deflection. For the fundamental flexural modes of a doubly clamped string resonator the effective mass is found to be $m_{\mathrm{eff}} = \frac{1}{2}m_0$, with the total string mass $m_0 = \rho L w t$ [67]. The equation of motion for a driven and damped harmonic oscillator is the second order differential equation [67]:

$$\frac{\mathrm{d}^2}{\mathrm{d}t^2}u(t) + \Gamma\frac{\mathrm{d}}{\mathrm{d}t}u(t) + \omega_0^2\, u(t) = f(t). \tag{2.7}$$

Here, ω_0 is the eigenfrequency of the resonator from Eq. (2.5), where we have omitted the indices n, i for simplicity. Γ is the linear damping coefficient and $f(t) = F(t)/m_{\mathrm{eff}}$ is the external driving force divided by the effective mass of the string resonator.

2.2.1 Undriven Harmonic Oscillator

Let us first consider the case of an undriven system, where the external drive is set to zero. Hence, the equation of motion (2.7) becomes

$$\frac{\mathrm{d}^2}{\mathrm{d}t^2}u(t) + \Gamma\frac{\mathrm{d}}{\mathrm{d}t}u(t) + \omega_0^2\, u(t) = 0. \tag{2.8}$$

Using the harmonic Ansatz $u(t) = u_0 \exp(\lambda t)$ we can find the solutions

$$\lambda_{1,2} = -\frac{\Gamma}{2} \pm \sqrt{(\Gamma/2)^2 - \omega_0^2}. \tag{2.9}$$

From these solutions we can distinguish the dynamics of the oscillator for two different cases. For $\Gamma \geq \omega_0$, where the damping is larger than the system's eigenfrequency, the solution in Eq. (2.8) is simply an exponential decay (over-damped case). When the damping is relatively small, that is $\Gamma \leq \omega_0$ (under-damped) case, Eq. (2.9) become imaginary. The solution in this case is the linear combination of the paramters λ_1, λ_2 inserting into the harmonic Ansatz. By applying the Euler's formula we obtain the solution for Eq. (2.8)

$$u(t) = u_0\, \mathrm{e}^{-\frac{\Gamma}{2}t} \cos\left(\sqrt{\omega_0^2 - (\Gamma/2)^2}\, t\right). \tag{2.10}$$

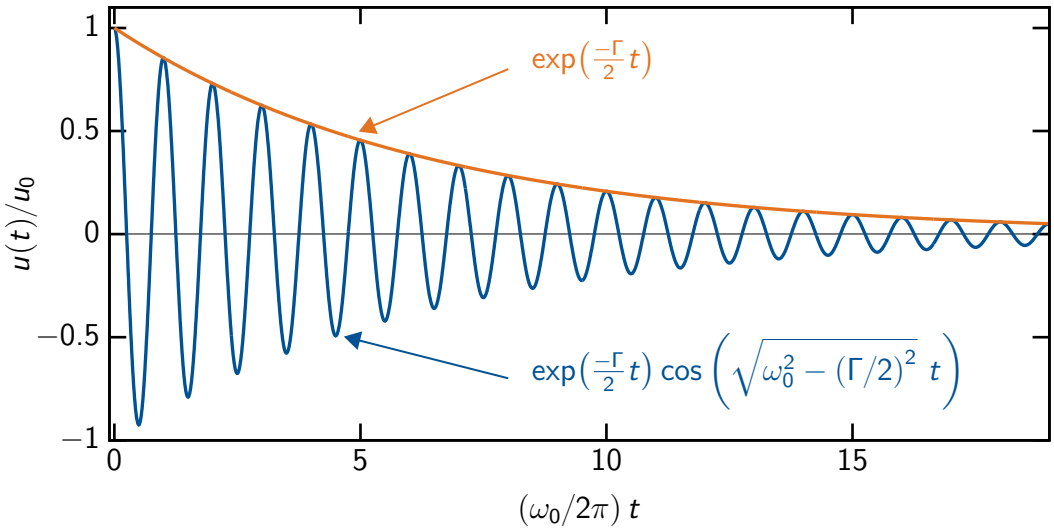

Figure 2.2 | The Time Evolution of an Under-Damped Harmonic Oscillator.
In the absence of the drive the amplitude follows an exponential decay by the rate $\Gamma/2$ (orange curve). We choose the ratio $\omega_0/\Gamma = 20$. The system exhibits an exponential decay [see Eq. (2.10)] together with an oscillation at frequency $\omega_\mathrm{r} = \sqrt{\omega_0^2 - (\Gamma/2)^2}$, also referred as the *natural frequency*. In the weakly damped case, where $\omega_0 \gg \Gamma$, the natural frequency is almost identical to the eigenfrequency of the mode that is $\omega_\mathrm{r} \approx \omega_0$.

The solution for the under-damped case is illustrated in Fig. 2.2 with the ratio that $\omega_0/\Gamma = 20$. The amplitude of the resonator follows an exponential decay by the rate $\Gamma/2$. In the real experiment it is often desirable to measure the decay in energy $E(t) \propto |u(t)|^2$ of the system that is referred as the ring-down measurement. By extracting the characteristic decay time of $E(t)$ that is $1/\Gamma$ we can obtain the information about the coherence of the system under investigation. Note that all measurements conducted in this work, are deeply in the under-damped regime.

2.2.2 Driven Harmonic Oscillator

Now, we consider the case where the point mass is periodically driven by an external force $F(t) = F_0 \exp(\mathrm{i}\omega t)$. The oscillator will follow the driven force $F(t)$ after a certain transient time, hence we only consider a specific steady solution. Using the Ansatz $u(t) = u_0\, \mathrm{e}^{\mathrm{i}\omega t}$ to solve Eq. (2.7), we obtain

$$u_0 = \frac{F_0/m_{\mathrm{eff}}}{\left(\omega_0^2 - \omega^2\right) + \mathrm{i}\Gamma\omega}. \tag{2.11}$$

This complex amplitude can be converted to the polar form $u_0 = |u_0|\mathrm{e}^{\mathrm{i}\varphi}$ with the norm

$$|u_0| = \frac{F_0/m_{\mathrm{eff}}}{\sqrt{\left(\omega_0^2 - \omega^2\right)^2 + \Gamma^2\omega^2}}, \tag{2.12}$$

which is defined as the amplitude response of the driven resonator. The corresponding phase response is

$$\tan(\varphi) = \frac{\mathfrak{Im}\{u_0\}}{\mathfrak{Re}\{u_0\}} = \frac{\Gamma\omega}{\omega^2 - \omega_0^2}. \tag{2.13}$$

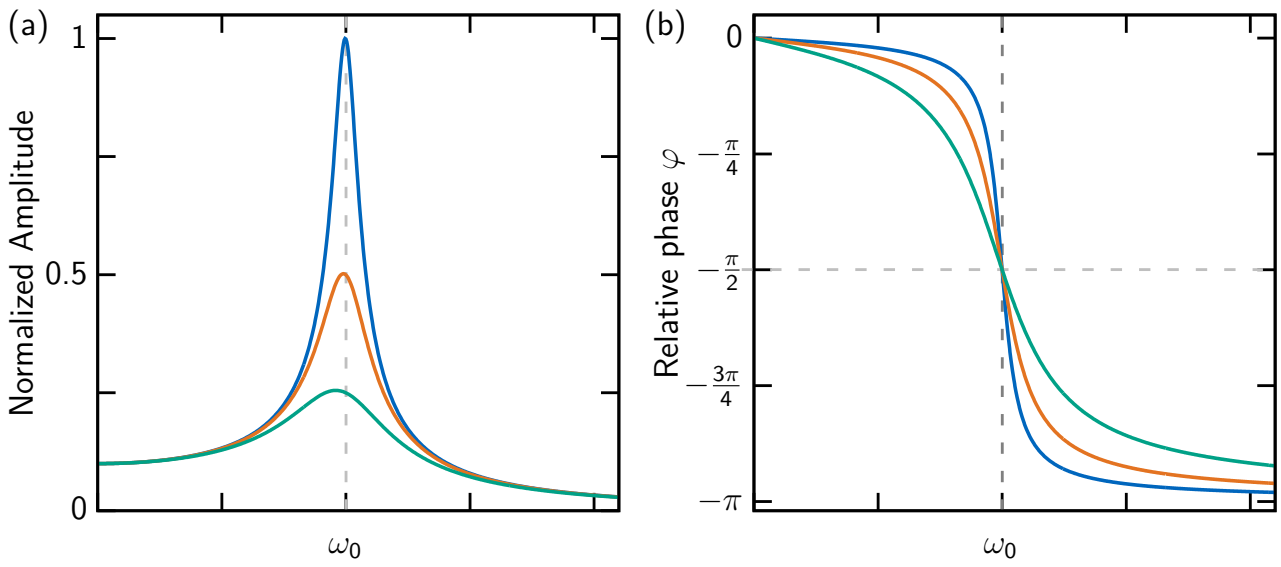

Figure 2.3 | Periodically Driven, Damped Harmonic Oscillator.
Normalized amplitude response (a) and the relative phase response (b) of a harmonic oscillator driven by an external force $F(t) = F_0 \exp(\mathrm{i}\omega t)$. Here, we choose the ratios $\omega_0/\Gamma = \{10, 5, 2.5\}$ (blue, orange, green) respectively.

In Fig. 2.3, we plot the normalized amplitude response and the relative phase from Eqs. (2.12) and (2.13) as a function of the drive frequency ω for different damping rates (see figure description). It is apparent in Fig. 2.3 (a), that a larger damping rate will lead to a broadening of the linewidth in the amplitude response. The frequency at the highest amplitude $\omega_{\mathrm{r}} = \sqrt{\omega_0^2 - \Gamma^2}$ is defined as the resonance frequency. In the case of low damping the resonance frequency is similar to the systems's eigenfrequency $\omega_{\mathrm{r}} \approx \omega_0$. On resonance, the relative phase lag is $\varphi = -\pi/2$, for $\omega \ll \omega_0$ the phase lag becomes negligible and if the drive frequency is much higher than the resonance frequency we find $\varphi \approx -\pi$ [see Fig. 2.3 (b)]. Additionally, we want to introduce a very important figure of merit to

characterize the mechanical oscillator, that is the so-called *'Quality factor'* (Q). The definition of the quality factor is the ratio between the total energy that is stored in the system and the energy lost per cycle [66]

$$Q = 2\pi \frac{\text{total energy}}{\text{energy lost per cycle}} = 2\pi \frac{\mathrm{W}}{\Delta \mathrm{W}} = \frac{\omega_\mathrm{r}}{\Gamma} = \frac{\omega_0}{\Gamma} \cdot \sqrt{1 - \frac{2\Gamma^2}{\omega_0^2}}. \tag{2.14}$$

For resonators with high quality factor we have $2\Gamma^2/\omega_0^2 \ll 1$ and Eq. (2.14) becomes

$$Q \approx \frac{\omega_0}{\Gamma} = \frac{\omega_0}{\Delta\omega}. \tag{2.15}$$

Here $\Delta\omega$ is the full width at half maximum (FWHM) that we can extract from the resonator's amplitude response by using the square root of a Lorentzian fit.

2.2.3 Coupled Linear Harmonic Oscillators

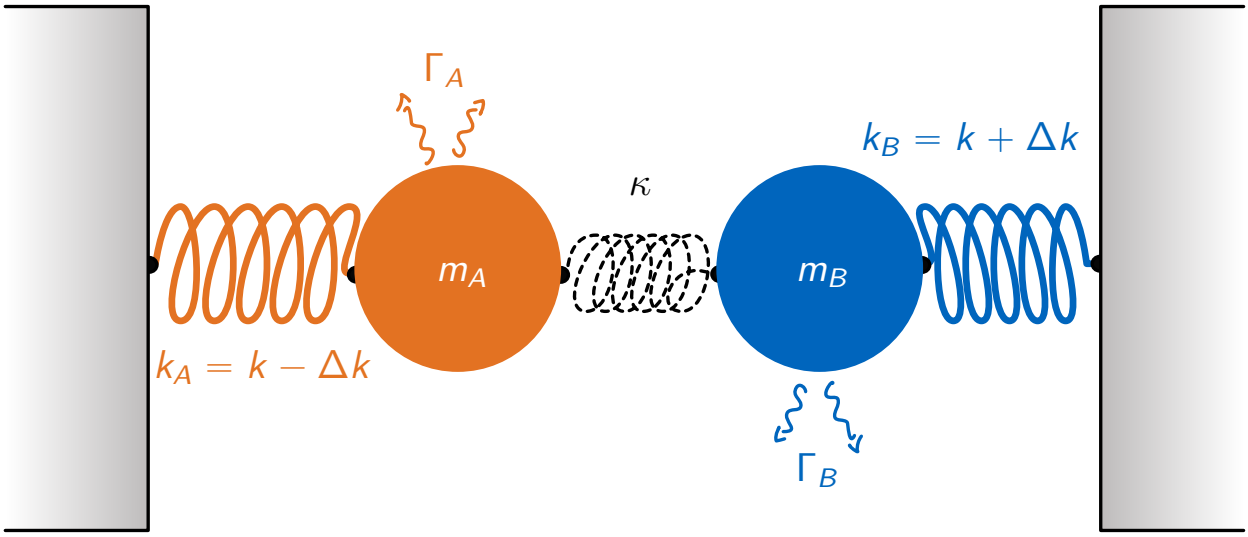

Figure 2.4 | Coupled Harmonic Oscillators.
Schematic drawing of two coupled linear damped resonators with the masses m_A and m_B. Both masses are coupled via the mutual spring with spring constant κ, the damping rates for both resonators are Γ_A and Γ_B, respectively.

Two coupled harmonic oscillators are considered as a generic model system that can be used to describe a wide range of systems in various fields of physics, depending on the specific type of coupling employed. For example, in the field of quantum electrodynamics, oscillator A can be the two level atom and oscillator B describes a cavity field. In cavity optomechanics oscillator, A would represent the mechanical oscillator, while the oscillator B is an optical resonator.

In our specific case, the two coupled oscillators would describe the coupling of the flexural in-plane and out-of-plane modes. In the following, we consider two strongly coupled harmonic oscillators with masses m_A and m_B. The corresponding spring constants $k_\mathrm{A} = k - \Delta k(t)$ and $k_\mathrm{B} = k + \Delta k(t)$ with small detuning $\Delta k(t)$ are tunable and can be time dependent. The corresponding eigenfrequencies can be definded as $\omega_{0,\mathrm{A}} = \sqrt{k_\mathrm{A}/m_\mathrm{A}}$ and $\omega_{0,\mathrm{B}} = \sqrt{k_\mathrm{B}/m_\mathrm{B}}$, respectively. Both oscillators are weakly damped by the rate $\Gamma_A = \Gamma_B = \Gamma$. The two oscillators are coupled by a spring with the spring constant

κ where the condition for strong coupling ($\kappa > \Gamma$) is fulfilled. The graphical illustration of such simple coupled system is shown in Fig. 2.4.

Following the work from Frimmer and Novotny [77], we derive the equations of motion for the displacements of the two modes u_j for $j \in \{A, B\}$. We consider the case of constant detuning Δk = constant and assume the masses of the oscillators are equal ($m_\mathrm{A} = m_\mathrm{B} = m$)

$$\begin{aligned} \frac{\mathrm{d}^2}{\mathrm{d}t^2}u_A(t) + \Gamma\frac{\mathrm{d}}{\mathrm{d}t}u_A(t) + \left[\frac{k+\kappa}{m} - \frac{\Delta k}{m}\right]u_A(t) - \frac{\kappa}{m}u_B(t) = 0, \\ \frac{\mathrm{d}^2}{\mathrm{d}t^2}u_B(t) + \Gamma\frac{\mathrm{d}}{\mathrm{d}t}u_B(t) + \left[\frac{k+\kappa}{m} + \frac{\Delta k}{m}\right]u_B(t) - \frac{\kappa}{m}u_A(t) = 0. \end{aligned} \tag{2.16}$$

For the sake of simplicity, we define the carrier frequency Ω_x, the detuning frequency Ω_d and the coupling frequency Ω_c as

$$\begin{aligned} \Omega_x^2 &= \frac{k+\kappa}{m}, \\ \Omega_d^2 &= \frac{\Delta k}{m}, \\ \Omega_c^2 &= \frac{\kappa}{m}. \end{aligned} \tag{2.17}$$

We can rewrite Eq. (2.16) in the matrix form

$$\left[\frac{\mathrm{d}^2}{\mathrm{d}t^2} + \Gamma\frac{\mathrm{d}}{\mathrm{d}t} + \Omega_x^2\right]\begin{bmatrix} u_A(t) \\ \\ u_B(t) \end{bmatrix} + \begin{bmatrix} -\Omega_d^2 & -\Omega_c^2 \\ \\ -\Omega_c^2 & \Omega_d^2 \end{bmatrix}\begin{bmatrix} u_A(t) \\ \\ u_B(t) \end{bmatrix} = \begin{bmatrix} 0 \\ \\ 0 \end{bmatrix}. \tag{2.18}$$

The solutions for these coupled differential equations can be found by using $u_j(t) = u_{0,j}\exp(\mathrm{i}\omega t)$. Inserting this harmonic Ansatz into Eq. (2.18) we obtain a new set of coupled linear equations for $u_{0,A}$ and $u_{0,B}$ that can be, again, expressed in the matrix form $\boldsymbol{M}\left[u_{0,A},\, u_{0,B}\right]^\mathrm{T} = 0$. The nontrivial solutions for this homogeneous system of equations exist only if $\det[\boldsymbol{M}] = 0$. Finally we obtain the eigenvalues

$$\omega_\pm = \left(\Omega_x^2 \mp \sqrt{\Omega_d^4 + \Omega_c^4}\right)^{1/2}. \tag{2.19}$$

Here, ω_+ is the frequency of the symmetric eigenmode, which is lower than the frequency of the antisymmetric mode ω_-.

In Fig. 2.5, we illustrate the eigenfrequencies from Eq. (2.19) as a function of detuning Δk. In case of no coupling ($\kappa = 0$), the two modes follow the straight dashed lines and intersect at $\Delta k = 0$. However, in the present of finite coupling, the two modes are no longer degenerated at $\Delta k = 0$ and we observe the characteristic behaviour that is called the *avoided-crossing* of the eigenfrequencies. We can calculate the frequency splitting Ω_0 of the two modes at resonance $\Delta k = 0$

$$\Omega_0 = \omega_- - \omega_+ \approx \frac{\Omega_c^2}{\Omega_x} = \frac{\kappa}{m\Omega_x}. \tag{2.20}$$

Here, we use the first order of the Taylor series expansion, that is $f(x) = \sqrt{1+x} \approx 1 + \frac{1}{2}x$. Additionally, we assume that the coupling is much smaller than the spring constant of the system $\Omega_c \ll \Omega_x$. The avoided-crossing is a characteristic fingerprint of strong coupling. It is apparent in Eq. (2.20) that the splitting increases with the coupling strength ($\Omega_0 \propto \kappa$). Note that we have neglect the damping term Γ in our calculation.

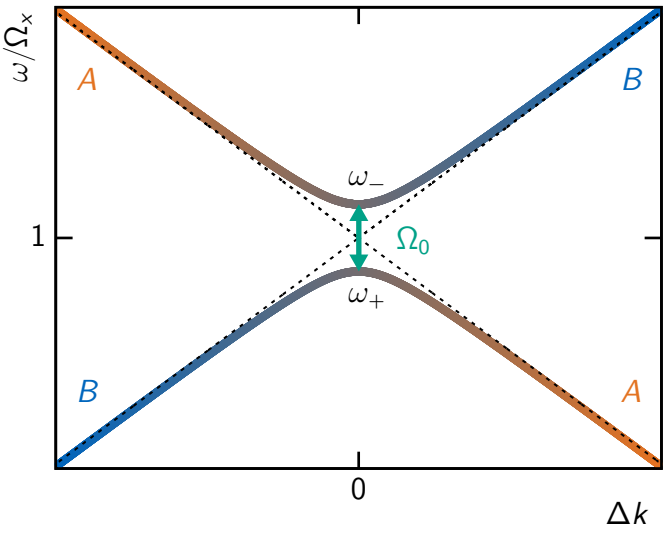

Figure 2.5 | Two Strongly Coupled Modes and Avoided Crossing.
Eigenfrequencies $\omega_\pm$ are plotted versus the static detuning Δk. The dashed lines indicate the tuning behaviour in the absence of mutual coupling $\kappa = 0$. For finite coupling κ the characteristic avoided crossing is observed and the frequency splitting at resonance ($\Delta k = 0$) is Ω_0. For large detuning, where $\Delta k \gg 0$, the oscillators A and B exhibit pure eigenmodes (see color codes orange and blue). However, on resonance, the eigenmodes are symmetric (ω_+) and anti-symmetric (ω_-) superpositions of the two individual oscillators, where the two eigenmodes hybridize.

By solving the eigenwert problem with the damping term, we obtain (rather complicated) complex eigensolutions, where the imaginary part describes the linewidth, and the real part represents the amplitude of the coupled system. The friction terms in Eq. (2.16) and (2.18) are responsible for the 'smear-out' of the curves that corresponds to the finite linewidth in the response of the respective oscillator. In order to observe strong coupling, the frequency splitting should be larger than the sum of the mechanical linewidths

$$\frac{\Omega_0}{2\Gamma} > 1. \tag{2.21}$$

If the dissipation in each system is smaller than the coupling strength, the modes can coherently exchange energy. In the strong coupling regime we can observe interesting time-dependent phenomena that were originally encountered only in quantum mechanics and initially thought of purely quantum mechanical nature. For example, the quantum phenomenon of electromagnetically induced transparency was observed in a classical system using two linearly coupled RLC circuits [78].

Additionally, adiabatic and nonadiabtic dynamics of two strongly coupled resonator modes described by the Landau-Zener transitions were observed in Ref. [56]. Remarkably, T. Faust et al. demonstrated the coherent control of a nanomechanical two-mode system [47] that can be fully described by the Bloch sphere manipulation, that is the Rabi oscillation [50], Ramsey fringes [51] and Hahn Echo [52].

Furthermore, previous work of our group showed the classical analog of the Stückelberg interferometry demonstrating the coherent transfer of energy in a nanomechanical two-mode system [63]. Following the work of Notvotny et al. [77], we describe the analogy between the coupled pair of classical harmonic oscillators and a quantum mechanical two-level system.

2.2.4 A Classical Two-Level-System

In order to understand the dynamics of the harmonic oscillator's eigenmodes, we consider the case where $\kappa \ll k$ and define a new Ansatz

$$\begin{aligned} u_A(t) &= a(t)\exp(\mathrm{i}\Omega_x t), \\ u_B(t) &= b(t)\exp(\mathrm{i}\Omega_x t). \end{aligned} \tag{2.22}$$

Here, each mode oscillates rapidly at the carrier frequency Ω_x and is modulated by the slowly varying complex amplitudes $a(t)$ and $b(t)$ that full-fill the normalization condition $|a(t)|^2 + |b(t)|^2 = 1$. We substitute the expressions from Eq. (2.22) into the equation of motion (2.18).

Consider the case where $\kappa \ll k$, we assume that the amplitudes $a(t)$ and $b(t)$ do not change significantly during an oscillation period $2\pi/\Omega_x$ [77]. This allows us to neglect the second derivative, where $\ddot{a}(t) \ll \mathrm{i}\Omega_x\dot{a}(t)$ and $\ddot{b}(t) \ll \mathrm{i}\Omega_x\dot{b}(t)$. This method is called the '*Slow Varying Envelope Approximation*' (SVEA). Furthermore, we only consider the weak damping case where $\Gamma \ll \kappa$. Hence, we can use $2\mathrm{i}\Omega_x + \Gamma \approx 2\mathrm{i}\Omega_x$. By applying these approximations we can derive the equation of motion for the eigenmode amplitudes

$$\mathrm{i}\begin{bmatrix} \dot{a} \\ \dot{b} \end{bmatrix} = \frac{1}{2}\begin{bmatrix} \omega_d - \mathrm{i}\Gamma & \Omega_0 \\ \Omega_0 & -\omega_d - \mathrm{i}\Gamma \end{bmatrix}\begin{bmatrix} a \\ b \end{bmatrix}. \tag{2.23}$$

In order to simplify the notation, we introduce the rescaled detuning frequency $\omega_d = \Omega_d^2/\Omega_x$ and from Eq. (2.20) we have the relation $\Omega_0 \approx \Omega_c^2/\Omega_x$.

For vanishing damping ($\Gamma = 0$) we obtain the dynamical matrix

$$D = \frac{1}{2}\begin{bmatrix} \omega_d & \Omega_0 \\ \Omega_0 & -\omega_d \end{bmatrix} = \frac{1}{2}(\omega_d\sigma_z + \Omega_0\sigma_x). \tag{2.24}$$

Equation (2.24) resembles the time dependent Schrödinger equation $\mathrm{i}\hbar\,\partial_t|\Psi\rangle = \hat{H}|\Psi\rangle$ for the state vector $|\Psi\rangle = a(t)|g\rangle + b(t)|e\rangle$, that is the superposition of the ground state $|g\rangle$ and the excited state $|e\rangle$. This two-level system is coupled by $\langle e|\hat{H}|g\rangle = \hbar\Omega_0/2$.

Note that our nanomechanical two-mode system differs from its quantum mechanical counterpart, where the detuning Ω_d and coupling Ω_0 are interchanged. When treating the system close to resonance ($\Delta k = 0$), the eigenmodes are symmetric and antisymmetric superpositions [see Eq. (2.19)] of the two individual oscillators (two-level system). Hence, the system's equations of motion can be transformed into a different basis [77].

In our case, we will study the dynamics of the system in a larger range $\Delta k \gg 0$ where the two oscillator modes are far detuned from the avoided crossing region showing independent mode behavior. Therefore, we use Eq. (2.24) to describe the tuning dynamics of our coupled two-mode system.

2.3 Three Dimensional Microwave Cavity Resonators

Research in microwave engineering has been pushed forward with an incredible speed in the past decades and has brought substantial developments in RF and microwave technology such as wireless communications, microwave integrated circuits, network and sensing applications. Microwave resonators are important components for the application of microwave systems. They can be used as filters, oscillators and tuned amplifiers to enhance certain physical interactions. To this end, superconducting microwave resonators in the bulk form play the central role as highly sensitive detectors in experiments searching for dark-matter axions [40, 79, 80]. The static high magnetic field inside the tunable, superconducting high-Q microwave cavity stimulates the axions that enter the cavity to convert into a single, detectable microwave photon.

Furthermore, these bulk cavities, commmonly referred as *three dimensional (3D) cavities*, are attracting considerable attention due to the integration of the Josephson junction based quantum bit (qubit) into the cavity. Significantly enhanced relaxation and decoherence time on the order of hundreds of microseconds have been demonstrated [81]. With the increased coherence time and the long single photon lifetimes, microwave 3D cavities have enabled a series of key experiments for fundamental study of quantum mechanics in the field of circuit quantum electrodynamics (cQED) [82] such as single photon Kerr effect [83], tracking the photon jumps [84], entangled qubits [85].

Other experiments further demonstrate the coupling of the 3D cavities to different physical quantities e.g. spin ensembles in nitrogen vacancy centers [86] and YIG sphere [87]. The implementation of such bulk cavity has a distinct advantage compared to the conventional and well established on-chip coplanar waveguide resonators [88] that is the confined high electric field strength $E_{\max} \sim 10\,\mathrm{MV/m}$ combined with the large mode volume while maintaining remarkably high quality factors. The build-up and localization of electromagnetic energy within the cavity make it possible to enhance radiation interactions with matter. The radiation pressure acting on the mechanical element inside the cavity gives rise to optomechanical and electromechanical phenomena such as parametric amplification, sideband cooling and squeezing [24, 89–94].

However, the field of cavity electromechanics mentioned above is limited to millikelvin temperatures, since it relies on superconducting circuits. Room temperature cavity electromechanics is impeded by the non-zero resistance of the normal conducting circuits, which gives rise to dissipation. Hence, it is quite challenging to conduct experiments using cavity electromechanics effects at room temperature [95].

In this thesis, we demonstrate a scheme, where we employ a method for cavity-assisted displacement sensing and optomechanically induced reflection (OMIR) of a nanomechanical resonator at room temperature. Since the operation of microwave resonators is very similar to that of lumped-element resonators of circuit theory [96], we start this section by reviewing the basic characteristics of a parallel RLC resonant circuit. We will then discuss the different types of microwave 3D cavities and the various techniques to couple to these resonators and how to determine their quality factors.

2.3.1 RLC Lumped-Element Resonator

Near resonance, an ideal cavity resonator can be represented by either an RLC parallel circuit or an RLC series circuit, depending on the position of the reference plane in the coupling line [97]. Following the work from Pozar [96], we derive the dynamics of a parallel RLC lumped-element circuit (see Fig. 2.6) with the corresponding resistance (R), the capacitance (C) and the inductance (L).

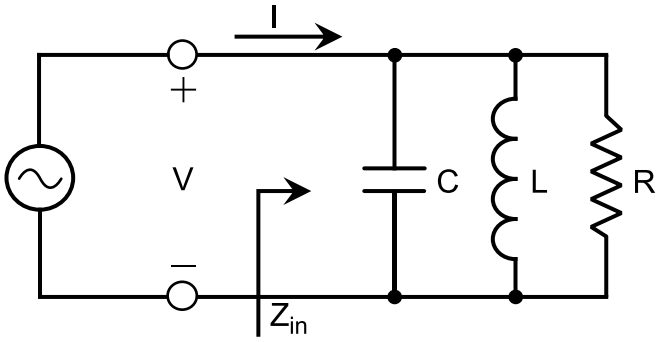

Figure 2.6 | Parallel RLC Lumped-Element Circuit.
The dynamics of a microwave cavity resonator can be described by the lumped-element circuit representation with the capacitance (C), the inducatance (L) and the resistance (R). The RLC-circuit can be driven by an external AC source.

The frequency dependent input impedance for the parallel circuit is

$$Z_{\text{in}}(\omega) = \left(\frac{1}{R} + \frac{1}{\mathrm{j}\omega L} + \mathrm{j}\omega C\right)^{-1}. \tag{2.25}$$

The complex power delivered to the resonator is defined as

$$P_{\text{in}}(\omega) = \frac{1}{2}|V|^2\left(\frac{1}{R} + \frac{\mathrm{j}}{\omega L} - \mathrm{j}\omega C\right). \tag{2.26}$$

Furthermore, we can find the energy quantities that are related to each lumped-element in the resonator

$$P_{\text{loss}} = \frac{1}{2}\frac{|V|^2}{R}, \tag{2.27a}$$

$$W_{\text{e}} = \frac{1}{4}|V|^2 C, \tag{2.27b}$$

$$W_{\text{m}} = |I_L|^2 L = \frac{1}{4}|V|^2\frac{1}{\omega^2 L}, \tag{2.27c}$$

where P_{loss} is the dissipated power by the inverse resistor R^{-1}, W_{e} is the average electric energy stored in the capacitor C and W_{m} is the average magnetic energy stored in the inductor L with the current I_L that flows through the inductor. Then the complex power in Eq. (2.26) can be rewritten as

$$P_{\text{in}} = P_{\text{loss}} + 2\mathrm{j}\omega(W_{\text{m}} - W_{\text{e}}). \tag{2.28}$$

The input impedance from Eq. (2.25) can be expressed in similar way

$$Z_{\text{in}} = \frac{2P_{\text{in}}}{|I|^2} = \frac{P_{\text{loss}} + 2\mathrm{j}\omega(W_{\text{m}} - W_{\text{e}})}{\frac{1}{2}|I|^2}. \tag{2.29}$$

In case of resonance, the average stored magnetic and electric energy are equal that is $W_\mathrm{m} = W_\mathrm{e}$. Hence, the input impedance on resonance is

$$Z_\mathrm{in} = \frac{P_\mathrm{loss}}{\frac{1}{2}|I|^2} = R, \tag{2.30}$$

which is a purely real value. From Eqs. (2.27b), (2.27c) and with the resonance condition $W_\mathrm{m} = W_\mathrm{e}$, we can define the resonant frequency as

$$\omega_0 = \frac{1}{\sqrt{LC}}. \tag{2.31}$$

We can define the quality factor Q of the harmonic oscillator (see also discussion in Sec. 2.2) as

$$Q = \omega \frac{\text{average energy stored}}{\text{energy loss rate}} = \omega \frac{W_\mathrm{m} + W_\mathrm{e}}{P_\mathrm{loss}}. \tag{2.32}$$

Hence, Q is an important figure of merit that defines the loss of a resonance circuit - lower loss implies higher Q. In this parallel lumped-element circuit the loss is represented by the inverse resistance R^{-1} [see Eq. (2.27a)]. For real microwave resonators, losses can be due to many types of dissipation channels such as conductor loss at room temperature, dielectric loss, radiation loss and contact resistance (seam loss). An additional source of loss is the coupling to an external network to perform measurements. All of these loss mechanisms will have contributions in lowering the quality factor. In the absence of external coupling, we can denote Q as *unloaded* quality factor Q_0. For our parallel resonant circuit we can evaluate the unloaded quality factor Q_0 from the resonant condition $W_\mathrm{m} = W_\mathrm{e}$

$$Q_0 = \omega_0 \frac{2W_\mathrm{m}}{P_\mathrm{loss}} = \frac{R}{\omega_0 L} = \omega_0 RC. \tag{2.33}$$

Note that the energy loss in the parallel lumped-element circuit is proportional to the inverse resistance R^{-1} [see again Eq. (2.27a)]. Thus, the unloaded quality factor of the parallel resonant circuit increases as R increases.

Additionally, we can rewrite the input impedance from Eq. (2.25) for the near resonance case as

$$Z_\mathrm{in}(\omega) \simeq \frac{R}{1 + \mathrm{j}2Q_0 \Delta\omega/\omega_0}, \tag{2.34}$$

where we have the relation $\omega = \omega_0 + \Delta\omega$ and $\Delta\omega$ is small. Hence, we can use the series expansion that is

$$\frac{1}{1+x} \simeq 1 - x + \cdots .$$

At the end, we want to consider the *half-power fractional bandwidth* of the resonator (BW). As the name suggests the fractional bandwidth is defined when the average power delivered to the circuit is decreased by one-half at resonance. The half-power bandwidth is defined as the difference in half-power frequencies ω_1 and ω_2 with

$$|Z_\mathrm{in}(\omega)| = \frac{1}{\sqrt{2}} |Z_\mathrm{in}(\omega_0)|. \tag{2.35}$$

From Eqs. (2.34) and (2.35) we find

$$\frac{R}{\sqrt{1 + 4Q_0^2 (\Delta\omega/\omega_0)^2}} = \frac{R}{\sqrt{2}}. \tag{2.36}$$

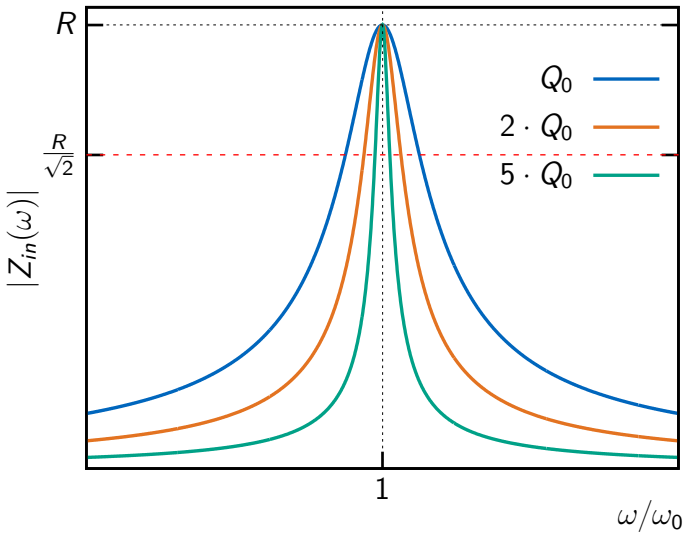

Figure 2.7 | Parallel RLC Lumped-Element Resonator's Response.
Resonator's response versus frequency for three different unloaded quality factors $\{Q_0, 2Q_0, 5Q_0\}$. The response curve broadens when decreasing the quality factor. The red dashed line indicates the position of the half-power bandwidth of the resonator, where the frequency is such that $|Z_{\text{in}}| = 2R^2$. Here, the average power delivered to the circuit is one-half that delivered at resonance (see black dash lines). Note that we keep the resistance R and resonant frequency ω_0 constant while varying the capacitance C [see Eq. (2.33)] to demonstrate the effects on the resonator's response at different quality factors.

The Eq. (2.36) is only valid when $4Q_0^2(\Delta\omega/\omega_0)^2 = 1$ and hence

$$\Delta\omega = \pm\frac{\omega_0}{2Q_0}. \tag{2.37}$$

The half-power frequencies are symmetric to the resonant frequency for pure modal structure

$$\begin{aligned} \omega_1 &= \omega_0 + \frac{\omega_0}{2Q_0}, \\ \omega_2 &= \omega_0 - \frac{\omega_0}{2Q_0}. \end{aligned} \tag{2.38}$$

The bandwidth is by definition

$$\text{BW} = |\omega_1 - \omega_2| = \frac{\omega_0}{Q_0}. \tag{2.39}$$

The quality factor is then given by

$$Q_0 = \frac{\omega_0}{\text{BW}}. \tag{2.40}$$

Therefore, the determination of the half-power bandwidth from the resonator's response curve will give direct access to the quality factor. In Fig. 2.7, we show the magnitude of the input impedance versus the frequency that exhibits a square root of the Lorentzian resonance whose form is Q-dependent. As the quality factor decreases, the resonator's response becomes more broadened and the half-power bandwidth increases accordingly. The position of the half-power bandwidth is indicated in Fig. 2.7 (see red dashed-line).

2.3.2 Rectangular Cavity Resonator

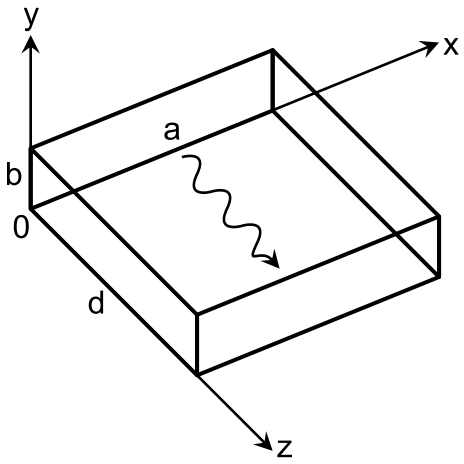

Figure 2.8 | The Rectangular Cavity Resonator's Geometry.
The waveguide is short circuited at both ends ($z = 0, d$) with rectangular cross-sections and dimensions (a, b). The microwave resonator supports both transverse electric (TE) and transverse magnetic (TM) modes.

Three dimensional (3D) microwave resonators are usually formed from waveguide resonators that are short circuited at both ends and thus, forming a closed box (cavity). The electric and magnetic energy is strongly confined and stored inside the cavity enclosure and hence, the radiation loss can be reduced substantially. Nevertheless, these geometries are not completely free of losses. The stored power can dissipate into the metallic walls of the cavity as well as in the dielectric material that may fill the cavity. Also the metal-oxide layer and the roughness on the cavity's surface, the imprecision in manufacturing and spurious contact resistance at seams (cavities can be made of different parts) can open up additional loss channels. An elaborated investigation of the loss mechanism of 3D microwave cavities can be found in Ref. [98].

A widely used type of 3D cavity in various experiments is the rectangular cavity. It has been shown, that the rectangular microwave 3D cavity suppresses decoherence of Josephson junction qubits [99] by providing a well defined and low loss environment. It can also be used to mediate coherent coupling between magnon and qubit [100], and since the electric field is confined in small volume it can enhance the light-matter interaction via radiation pressure and allows ground state cooling of the mechanical system [101–103]. The theoretical treatment of a cavity resonator consists of solving the Maxwell's equations with the corresponding boundary conditions. In Fig. 2.8, a typical geometry of the rectangular cavity is illustrated.

The 3D cavity consists of a single conductor with air-filled rectangular cross-section of dimensions (a, b). Along the propagation direction z, the rectangular waveguide is shorted at $(z = 0, d)$. These boundary conditions force the propagating electromagnetic fields, that is injected inside the cavity, to form standing waves and establish resonant conditions. From Ref. [96], we know that the rectangular waveguide support transverse electric (TE) and transverse magnetic (TM) modes. In the following we only consider the fundamental propagating TE_{101} mode with the condition $E_z = 0$. The fields components in this case are

$$E_y = E_0 \sin \frac{\pi x}{a} \mathrm{e}^{-\mathrm{j}\beta z}, \tag{2.41a}$$

$$H_x = \frac{\mathrm{j}\beta a}{\pi} H_0 \sin \frac{\pi x}{a} \mathrm{e}^{-\mathrm{j}\beta z}, \tag{2.41b}$$

$$H_z = H_0 \cos \frac{\pi x}{a} \mathrm{e}^{-\mathrm{j}\beta z}, \tag{2.41c}$$

$$E_x = E_z = H_y = 0. \tag{2.41d}$$

The wave impedance $Z_{\mathrm{TE}} = -\frac{E_y}{H_x} = \frac{\omega\mu}{\beta}$ relates the transverse electric and magnetic fields with the scaling

$$|E_0| = \frac{\omega\mu a}{\pi}|H_0|. \tag{2.42}$$

Here, μ is the permeability of the material filling the cavity and β is the propagation constant. The boundary conditions establish resonances in the rectangular waveguide. In case of short circuited waveguide at $(z = 0, d)$, the resonant frequency of the mode $\mathrm{TE}_{mn\ell}$ is given by

$$f_{mnl} = \frac{c}{2\pi\sqrt{\mu_r\epsilon_r}}\sqrt{\left(\frac{m\pi}{a}\right)^2 + \left(\frac{n\pi}{b}\right)^2 + \left(\frac{\ell\pi}{d}\right)^2}, \tag{2.43}$$

where c is the speed of light, ϵ_r is the relative permittivity (dielectric constant), μ_r is the relative permeability and the indices m, n, ℓ indicate the number of variations in the standing wave pattern in the x, y, z directions, respectively. The mode with the lowest resonant frequency for the condition $b < a < d$ is the TE_{101} mode, which is often referred to as the dominant TE mode. In the following, we define the TE_{101} mode as the fundamental mode of the rectangular cavity and the corresponding frequency is found to be [96]

$$f_0 = \frac{c}{2\pi\sqrt{\mu_r\epsilon_r}}\sqrt{\left(\frac{\pi}{a}\right)^2 + \left(\frac{\pi}{d}\right)^2}. \tag{2.44}$$

In Fig. 2.9, we show the CAD generated drawing of the rectangular cavity investigated in the context of this work and the corresponding dimensions. The cavity is physically realized by milling out from two separated blocks of metal (usually copper for room temperature applications) with high purity. The two halves are then enclosed by screws to form a cavity. The input and output coupling to the cavity occurs via antenna SMA pins that penetrate into the cavity volume through circular holes with radii of $r \approx 1$ mm. These pin ends will introduce electromagnetic excitations into the cavity volume via an external microwave signal generator. The variation of the pin's insertion depth allows us to control the coupling of the cavity to the environment. We will discuss the coupling mechanism later below in Sec. 2.3.5.

A very convenient way to analyse and pre-define the properties of the cavities before the manufacturing is to use finite element method (FEM) simulations. The FEM is a numerical technique for solving versatile problems which are described by partial differential equations. It can be used in many disciplines, e.g. solid and structural mechanics, fluid dynamics, acoustic, thermal conduction and electromagnetics. In FEM the domain of interest is subdivided into small cells of simple shape. For example a 2D domain can be subdivided into triangles or quadrilaterals and a 3D domain can be split into tetrahedron or cubes. This structured grids are commonly referred to as *mesh*. The solution can be found by introducing a set of finite basis functions that are typically non-zero in a few adjacent elements. The solution to the differential equation problems is then projected into the function space in such a way that the residual norm is minimized on average [104]. The main reason why the FEM simulation is a favorite method in many branches of engineering, is the ability to deal with complex geometry.

Our FEM simulation software of choice is *COMSOL Multiphysics* with the electromagnetics (RF) module. In the COMSOL interface, three dimensional structures are discretized into tedrahedral mesh. On the designed geometry, Maxwell's equations can be solved for each individual nodes and the resonant condition for the corresponding electric and magnetic field distribution can be determined. The boundary conditions are found from the electronic properties of the metals and the dielectric materials, both are available in the COMSOL materials library. In Fig. 2.10, the electric field

distribution of the rectangular 3D microwave cavity is illustrated. The field distribution corresponds to the fundamental TE_{101} mode with the cavity dimensions $(a \times b \times d) : (38.5\text{mm} \times 7.4\text{mm} \times 37.3\text{mm})$. The resonant frequency for the fundamental mode is $f_{101} \approx 5.6\,\text{GHz}$. Here the boundary conditions are set as perfect electric conductors for the metallic walls and the dielectric material that fills the cavity is air. Beside the determination of the resonant condition and the illustration of the field distributions of the modes, it is possible to calculate the scattering parameters in the frequency domain by introducing ports into the cavity.

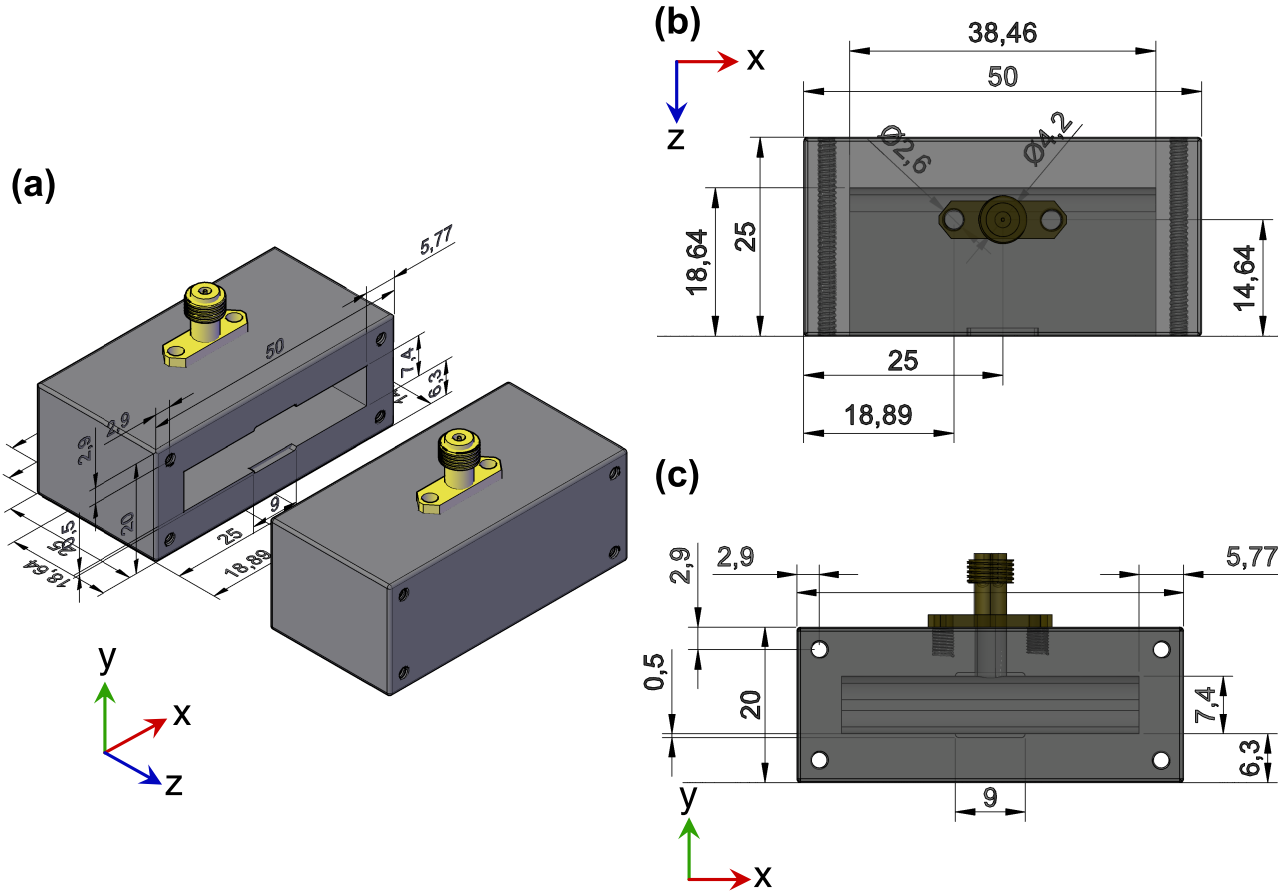

Figure 2.9 | CAD Drawing of the 3D Microwave Cavity.
(a) The cavity is made from two parts that are connected via screws. The SMA connectors (yellow) are used for the input and output coupling. **(b)** Top view and **(c)** front view with the corresponding dimensions (mm) of the cavity part.

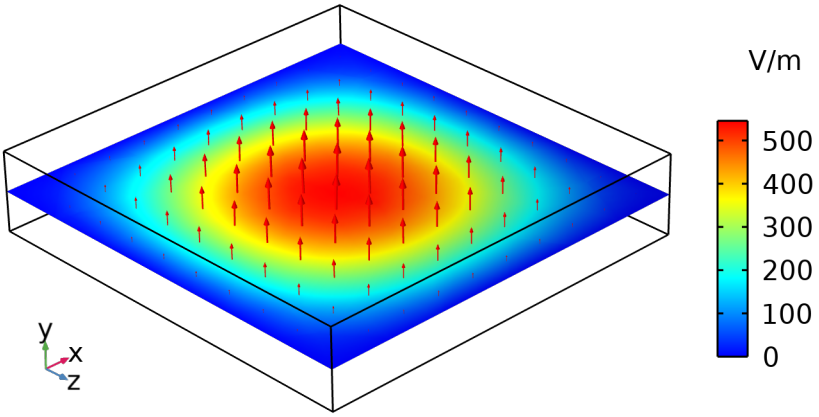

Figure 2.10 | Rectangular Cavity Field Distribution using COMSOL Multiphysics.
Electric field distribution of the fundamental TE_{101} mode of the rectangular cavity. The metallic walls are set as perfect electric conductors and the dielectric material filled inside the cavity is air from the materials library. The electric field is concentrated in the center of the cavity and the field strength is almost zero at the cavity's side wall. The colorbar denotes the electric field amplitude inside the cavity and the red arrows indicate the field direction.

2.3.3 Cylindrical Cavity Resonator

Similar to rectangular cavities discussed above, the cylindrical 3D microwave cavity can be constructed from a section of circular waveguide that is shorted at both ends. This type of cavity can be found in ultra-low-noise experiment, that serves as a sensitive detector in the search for dark-matters [79]. It can also be used as narrow band-pass filter, where the cavity is designed with a movable top lid to allow mechanical tuning of the resonant frequency [62, 63, 105]. The resonant frequencies for the $TE_{nm\ell}$ and $TM_{nm\ell}$ cylindrical cavity modes can be derived by solving Maxwell's equations and finding solutions that satisfy the boundary conditions on the walls of the circular waveguide and short circuited at both ends along the propagation direction [96]. The resonant frequency of the $TM_{nm\ell}$ mode is found to be

$$f_{nm\ell} = \frac{c}{2\pi\sqrt{\mu_r \epsilon_r}} \sqrt{\left(\frac{p_{nm}}{a}\right)^2 + \left(\frac{\ell\pi}{d}\right)^2}. \tag{2.45}$$

The corresponding $TE_{nm\ell}$ mode is

$$f_{nm\ell} = \frac{c}{2\pi\sqrt{\mu_r \epsilon_r}} \sqrt{\left(\frac{p'_{nm}}{a}\right)^2 + \left(\frac{\ell\pi}{d}\right)^2}. \tag{2.46}$$

With a, d are the radius and height of the cylindrical cavity and p_{nm} is the m^{th} zero of the Bessel functions of the first kind $J_n(x)$. p'_{nm} is the m^{th} root of $J'_n(x)$, so that $J'_n(p'_{nm}) = 0$ and $J'_n(x)$ is the derivative of $J_n(x)$ with respect to the argument x.

Figure. 2.11 illustrates the mode chart for a few lower order resonant modes of the cylindrical cavity. Such mode chart is particularly helpful to pre-define the desired resonant frequency and to determine the cavity dimensions with less effort. It is visible in the chart that the dominant (the mode with the lowest frequency) TE mode is the TE_{111} mode, whereas the dominant TM mode is the TM_{010} mode.

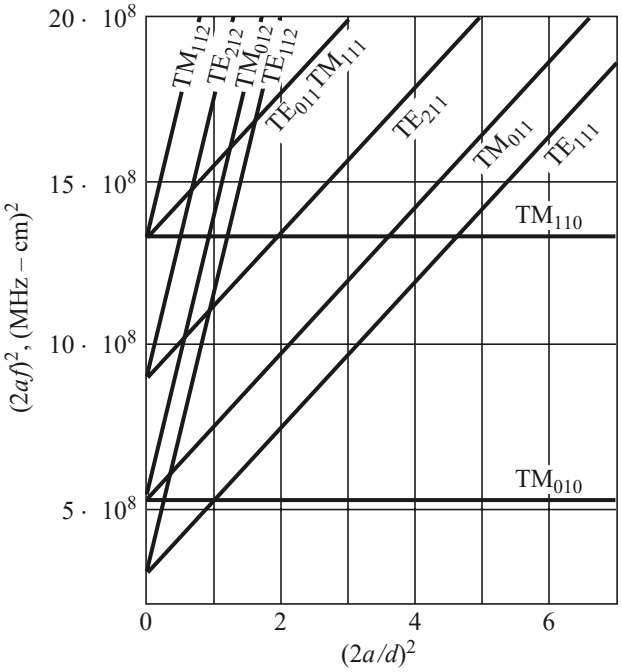

Figure 2.11 | Cylindrical Cavity's Resonant Mode Chart.
The fundamental TM mode is the TM_{010} mode and the dominant TE mode is the TE_{111} mode. The two modes TE_{011} and TM_{111} are degenerated. Used with permission of John Wiley & Sons - Books, from *Microwave Engineering*, Pozar David M., 4th Edition, 2012.

Particularly, the TE_{011} mode of the cylindrical cavity exhibits exceptionally high quality factor due to the electric field distribution of the mode itself. It has no dielectric participation and zero currents flowing across the corners of the geometry [98]. The non-zero fields of the TE_{011} mode are [96]

$$H_z = H_0 J_0\left(\frac{p_{11}\rho}{a}\right)\sin\frac{\pi z}{d}, \tag{2.47a}$$

$$H_\rho = -\frac{\beta a H_0}{p_{11}} J_1\left(\frac{p_{11}\rho}{a}\right)\cos\frac{\pi z}{d}, \tag{2.47b}$$

$$E_\phi = -\frac{\mathrm{j}k\eta a H_0}{p_{11}} J_1\left(\frac{p_{11}\rho}{a}\right)\sin\frac{\pi z}{d}. \tag{2.47c}$$

Here $\eta = \sqrt{\mu/\epsilon}$ and we use the relation $p'_{01} = p_{11} \approx 3.83$, $J'_{-n}(x) = (-1)^n J_n(x)$ and hence $J'_0(x) = -J_1(x)$. It is immediately apparent from Eq. (2.47c) that at the sidewalls ($\rho = a$) we have $J_1(p_{11}) = 0$ so the electric fields are zero. Additionally, the same conditions apply on the lid ($z = 0, d$) where $\sin(0) = \sin(\pi) = 0$. Therefore, the electric field vanishes at all cavity surfaces for the TE_{011} mode and there is no dielectric loss and the surface resistance is negligible for the specific mode. Following Eqs. (2.47a) and (2.47a), we further find that at the corners of the geometry ($z = 0, d$) and ($\rho = a$)

$$H_z\Big|_{\text{corner}} = H_\rho\Big|_{\text{corner}} = 0. \tag{2.48}$$

Hence, we have zero currents flowing across the corners and the seam loss of the cavity is strongly suppressed. With these two arguments mentioned above, the TE_{011} mode of the cavity is expected to be only limited by the conductor loss and this can be further reduced by exploiting the superconducting property of the metal, such as aluminum or niobium at low temperature.

In the field of cQED it has been shown that these types of cavity can exhibit quality factors up to 10^9 [106]. At room temperature, conductor loss from the metal is the main loss channel but by careful

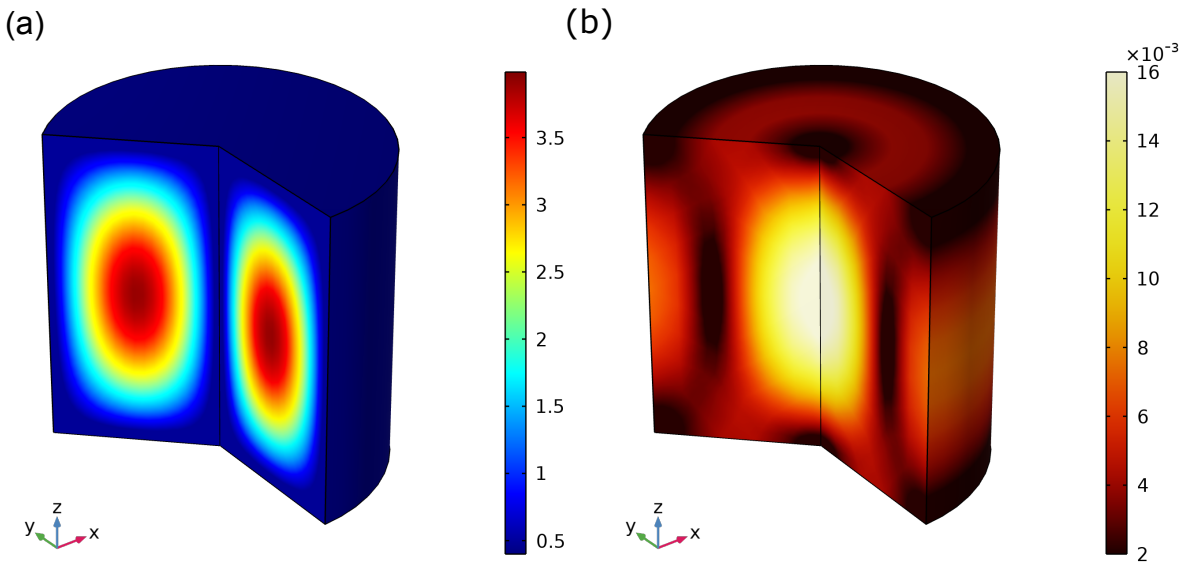

Figure 2.12 | COMSOL Multiphyisics Simulation of the Cylindrical Cavity TE_{011} Mode .
(a) The electrical field distribution of the TE_{011} mode. The E-field exhibits a donut-shape around the cylindrical z-axis. The field becomes zero at the cavity wall (see color code). **(b)** The corresponding magnetic field distribution with the maximum at the center of the cavity and is almost zero at the corners. The cylindrical geometry has the dimensions $(a \times d)$: $(35\text{mm} \times 70\text{mm})$.

treatment of the surface and using metal with high purity, it is still possible to reach reasonably high quality factors up to 10^4 [96]. Finally, we can find the resonant frequency of the cylindrical TE_{011} mode from Eq. (2.46) as

$$f_{011} = \frac{c}{2\pi}\sqrt{\left(\frac{p_{11}{}^2}{a}\right) + \left(\frac{\pi z}{d}\right)^2}. \tag{2.49}$$

From the relation $J_0'(x) = -J_1(x)$ and the Eqs. (2.45), (2.46) we can see that the TE_{011} and the TM_{111} are degenerated for all aspect ratios a/d of the cylindrical cavity. This relation is also apparent in the mode chart illustrated in Fig. 2.11. In order to lift off the degeneracy, we need to introduce a shape perturbation. For example, a ring-shape extrusion of at the upper corner lid will effectively reduce the mode volume of the TM_{111} mode, while the TE_{011} remains relatively unaffected [106, 107]. In Fig. 2.12 (a) we use COMSOL simulation to plot the electrical field distribution of the TE_{011} mode, that exhibits a donut-shape about the cylindrical z-axis. It is apparent from the color code that the electric field goes to zero at the cavity wall. The magnetic field distribution is shown in Fig. 2.12 (b). At the corners the surface magnetic field nearly vanishes and the field's maximum is at the center of the cavity. The COMSOL simulations here confirm the calculations discussed above and give a reasonable explanation for the high quality factor of the TE_{011} mode.

2.3.4 Coaxial $\lambda/4$ Cavity Resonator

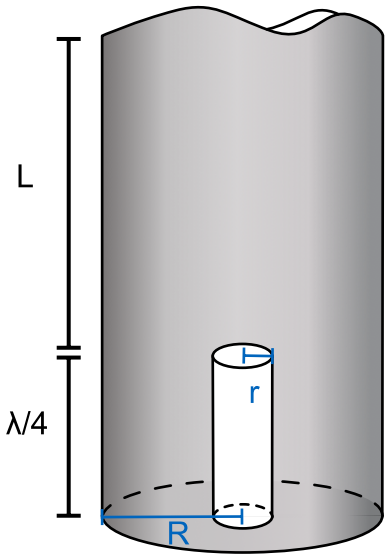

Figure 2.13 | The Coaxial $\lambda/4$ Resonator.
The quarter-wave coaxial resonator is constructed out of the coaxial transmission line with an inner conductor of radius r that is shorted on one end (bottom) and open at the distance $\lambda/4$. At the distance L the cavity is basically a cylindrical waveguide that is the outer conductor with the radius R. The cavity has no lid on the top part and is open into free space.

In this section, we discuss the novel third type of 3D microwave cavity that was developed in the R. Schoelkopf lab [81]. The so-called coaxial $\lambda/4$ cavity exhibits high quality factor up to $Q \approx 10^8$ at cryogenic temperature and enhances superconducting transmon qubit's coherence up to millisecond. The high Q makes them ideal memory elements and this type of cavities form the backbone of many quantum control experiments [108–114]. The geometry of the $\lambda/4$ microwave 3D cavity is illustrated in Fig. 2.13. The cavity is formed out of the geometry of a coaxial transmission line (TL) where r and R are the radii of the inner and outer conductor, respectively. The inner conductor of the transmission line with the length of $\lambda/4$ is shorted on one end and open circuited into the other end that is a circular waveguide. Note that, instead using dielectric material, the coaxial cavity is simply filled with air. Since the system is made of two conductors, the coaxial transmission line is known to support a transverse electromagnetic (TEM) mode with fields [96, 98]

$$\bar{E} = \frac{V_0 \mathrm{e}^{-\gamma z}}{\rho \ln R/r} \hat{\rho}, \tag{2.50a}$$

$$\bar{H} = \frac{V_0 \mathrm{e}^{-\gamma z}}{2\pi\eta\rho} \hat{\phi}. \tag{2.50b}$$

The mathematical treatment is similar to the calculation of the cylindrical geometry but the boundary conditions of the coaxial cavity are much more complex and hence, the exact determination of the field distributions and the resonant conditions are quite challenging in this case. Nevertheless, the resonance frequency can be simply estimated from the length of the transmission line that is $\ell \approx \lambda/4$ and hence, we find the resonance frequency for the fundamental mode of the coaxial cavity

$$f_0 \approx \frac{c}{\lambda} = \frac{c}{4\ell}. \tag{2.51}$$

Since the cavity is a $\lambda/4$ resonator, we expect the next TEM harmonic should appear near $3\lambda/4$ that is three times higher than the fundamental mode implying a very clean spectrum. The electrical field distributions and the resonance conditions can be determined using FEM simulation software COMSOL Multiphysics.

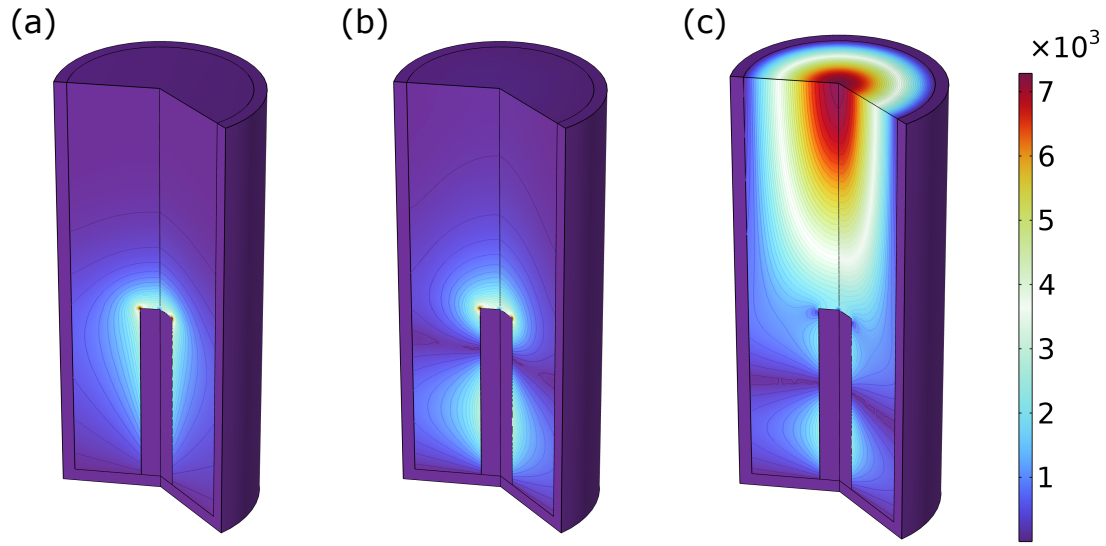

Figure 2.14 | COMSOL Simulation of the Coaxial Cavity TEM Modes.
(a) The electric field distribution of the fundamental TEM mode. The field is distributed mainly around the inner conductor and the mode's energy density decreases exponentially into the waveguide section. The resonant frequency of the fundamental mode is $f_0 = 3.66\,\text{GHz}$. The geometry of the coaxial cavity allows confinement of the fundamental mode and no light is leaked outside the cavity. **(b)** The electric field distribution of the second harmonic TEM mode of the cavity. The eigenfrequency of this mode is $f_{2\text{nd}} = 10.80\,\text{GHz}$, that is three times higher than the fundamental mode, as expected. Therefore, the coaxial provide a remarkably clean frequency spectrum. **(c)** The dominant cylindrical waveguide mode TE_{11} start to play a role at much higher frequency that is $f_{\text{TE11}} = 14.65\,\text{GHz}$.

We illustrate the simulated results for the coaxial cavity in Fig. 2.14. Here, the cavity dimensions are $r = 1.8\,\text{mm}$, $R = 8\,\text{mm}$, $\ell = \lambda/4 = 18\,\text{mm}$ and $L = 22\,\text{mm}$. Due to the design where, the fundamental TEM mode of the coaxial cavity is well below the circular waveguide mode, the fundamental mode's energy density decreases exponentially into the waveguide section and no light is leaked outside the cavity. This behavior is confirmed by the COMSOL simulation in Fig. 2.14 (a), where the electric field distribution is mainly around the top part of the inner conductor and decays exponentially towards the cylindrical waveguide. The resonance frequency of the fundamental TEM mode of the cavity is $f_0 = 3.66\,\text{GHz}$. The resonance frequency of the second harmonic TEM mode [see Fig. 2.14 (b)] is sufficient far away from the first that is $\sim 3f_0$ and hence, the coaxial cavity provides a clean frequency spectrum that allows us to avoid multimode coupling issues. As illustrated in the cylindrical mode chart of Fig. 2.11 the dominant waveguide TE_{11} can be closer to the cavity's fundamental mode. However, we define the dimensions of the cavity in a way, that the waveguide mode [see Fig. 2.14 (c)] starts to kick in at $\omega_{\text{TE11}} = 14.65\,\text{GHz}$ and this is sufficient separated from any frequency modes we want to exploit in our measurements.

2.3.5 Cavity Coupling Mechanisms

As mentioned at the beginning of this section, all types of microwave cavities suffer from losses that cause the signals inside the cavity to decay over time. In general, we distinguish between internal and coupling losses. Internal losses, described by the *unloaded* quality factor Q_0 from Eq. (2.33), are related to intrinsic loss mechanisms such as conductor losses, dielectric loss or seam loss etc (see discussion in Sec. 2.3.1). External loss, however, is the direct consequence of coupling the signals into and out of cavity using external circuitry and can be related to the coupling or external quality factor Q_e. And hence, the total or *loaded* quality factor Q_l can be obtained by adding up the reciprocal values of these two contributing quality factors [96]

$$\frac{1}{Q_l} = \frac{1}{Q_0} + \frac{1}{Q_e}. \tag{2.52}$$

In order to perform measurements with the microwave cavity, input and output ports need to be introduced at the cavity's wall. If we want to measure the device in reflection, only a single port is needed. Transmission measurements, however, require a two port device. The coupling to the cavity can be realized using a coaxial transmission line (TL) that carries microwave signals into the cavity via a narrow section of circular aperture with radius $r_0 \approx 1$ cm.

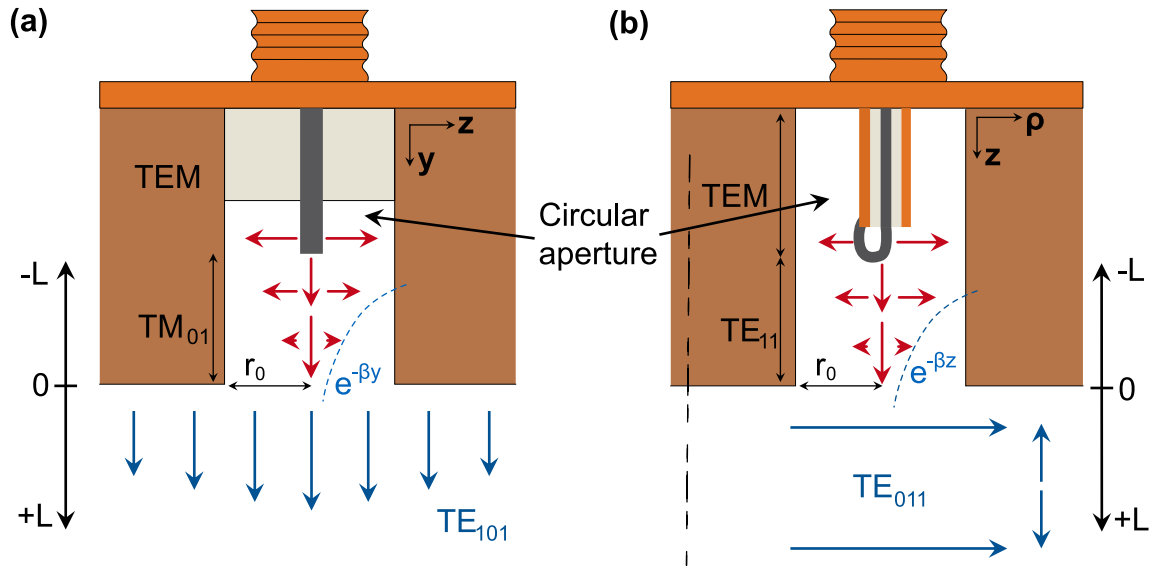

Figure 2.15 | Excitation of 3D Microwave Cavities .
(a) Capacitive coupling to the 3D cavity by turning signals from the coaxial line that support TEM mode into propagating circular waveguide mode (TM_{01}). This type of configuration is suited for the rectangular geometry. Below cutoff frequency, the signal decays exponentially along the waveguide length L. **(b)** Inductive loop coupling to the 3D cavity. The center conductor is bent and soldered to the metallic shield of the pin coupler. The coupling mechanism from a circular aperture to the hollow cavity can be described by the dipole excitation problem when the radius of the aperture is smaller than the wavelength $r \ll \lambda$. This configuration is suitable for the cylindrical cavity geometry.

As visible in Fig. 2.15 (a), there is an abrupt transition between the TL and the circular aperture, where many waveguide modes can be excited by this transition. Since the radius r_0 of the circular aperture is much smaller than the wavelength of the cavity's resonant mode $r_0 \ll \lambda$, the coupling via aperture can be mathematically treated as a dipole radiation problem [115]. Hence, the electric or magnetic field can radiate energy into the cavity like a small dipole antenna. As an example, the coupling to the

rectangular cavity is achieved by transforming signals from the TEM mode of the transmission line to a propagating circular waveguide mode (TM_{0m}) [98] with the propagation constant

$$\beta_{\mathrm{TM}0m} = \sqrt{k^2 - \left(\frac{p_{0m}}{r_0}\right)^2}. \tag{2.53}$$

Here, p_{0m} is again the m^{th} zero of the zeroth Bessel function $J_0(x)$ of the first kind. The propagation constant of Eq. (2.53) becomes imaginary when $\omega < \frac{p_{0m}c}{r_0}$. So below this cutoff frequency the signal is attenuated exponentially in the length of the waveguide section L [see Fig. 2.15 (a)]. We expect the external quality factor to scale exponentially with the length of the waveguide section [98]

$$Q_e \propto \mathrm{e}^{-2\beta_{\mathrm{TM}01}L}. \tag{2.54}$$

The coupling to the cylindrical cavity is accomplished in a similar way. Here, the center pin of a coaxial cable is bent and soldered to the outer shield, where a loop is formed. The size of the loop is smaller than the wavelength, therefore the voltage is nearly zero and the current is large. The current generates a magnetic field that radiates like a magnetic dipole [see Fig. 2.15 (b)]. The magnetic moment of the loop is constant along its surface area $\hat{n}$. The coupling is strongest, when the magnetic field of the resonance mode is perpendicular to the plane $\hat{n}$. Therefore, we align the coupling loop to the $\hat{\rho}$ vector of the cavity [98]. This method allows both TE and TM types of circular waveguide to contribute to the evanescent coupling to the cavity. Similarly, we expect for the coupling to the cavity resonant mode of interest TE_{011} that the external quality factor should scale exponentially in the length of the waveguide section L

$$Q_e \propto \mathrm{e}^{-2\beta_{\mathrm{TE}11}L}. \tag{2.55}$$

A comprehensive analysis of the coupling mechanisms to the 3D cavities can be found in the bachelor thesis of Daniel Anic [116] and the dissertation of M. Reagor [98].

2.3.6 Quality Factor Determination

Traditionally, the determination of the unloadede quality factor Q_0 provides direct information about intrinsic loss mechanisms inside the cavity and hence microwave cavity can be used to study dielectric loss in materials [117, 118]. In the field of cavity optomechanics [90, 119], it is important to have a good knowledge about the cavity's external coupling, since most of the experiments are operated in the cavity "overcoupled" regime. With this condition most of the photons emerged from the cavity are not absorbed inside the cavity and can, more likely, interact with the mechanics. In the "undercoupling" regime, however, the cavity damping is dominated by different sources of intrinsic losses. For most experiments, this coupling condition is often not desirable due to the loss of information. In the following, we provide two different possibilities to determine the different quality factors.

Q Determination from Two-Ports Measurement Generally, a direct measurement of the unloaded quality factor Q_0 is not possible because the coupling to the external circuitry will always have a finite contribution to the total loss of the cavity. However, from Ref. [96], we know that it is possible to determine Q_0 from the frequency response of a loaded resonator that is connected to a transmission line.

In Fig. 2.16 we show the circuit representation of the coupling scheme. The microwave input signals drive the parallel RLC resonator from a transmission line with impedance $R_0 = 50\,\Omega$. The cavity response is measured by an amplifier that is connected to a second transmission line with the same impedance R_0 and that forms a two-port network. The input-output coupling from the

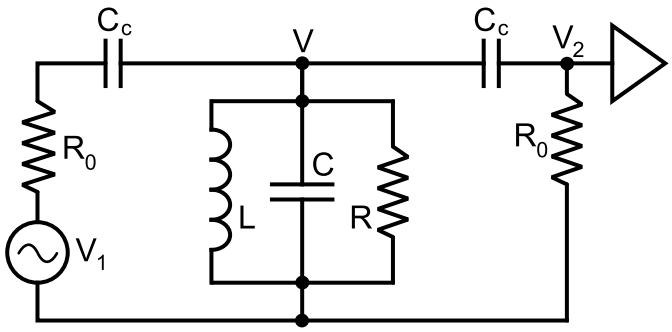

Figure 2.16 | Circuit Diagram of Resonator Coupled to Transmission Lines.
Schematic diagram of the 3D microwave cavity (RLC resonator) capacitively coupled to transmission lines via coupling capacitance C_c forming a two port device. The transmission lines have input impedance $R_0 = 50$. The cavity's response is measured using an amplifier that is connected to the second transmission line.

transmission lines with the resonator arises via coupling capacitors C_c with the impedance $Z_c = 1/i\omega C_c$. Our coupling scheme shown in Fig. 2.15 (a) from the previous section fits perfectly to this circuit representation. The inductive (loop) coupling can be treated in a similar manner. From the calculation of the impedance of a RLC lumped-element resonator [see Eq. (2.34)], we know that the cavity exhibits a Lorentzian response curve. However, by measuring the cavity with a microwave network analyzer, it is more convenient to express the cavity response in terms of scattering matrix $S-$parameter S_{21} as a ratio of the output to the input voltage [120]

$$S_{21}(\omega) = \frac{2V_2}{V_1} = \frac{S_{21}(\omega_0)}{1 + i2Q_l(\omega - \omega_0)/\omega_0}. \tag{2.56}$$

Here, $S_{21}(\omega_0)$ is the maximum transmission coefficient that occurs at the peak of the resonance. The square modulus $|S_{21}(\omega)|^2$ of the cavity response then yields a lorentzian curve

$$|S_{21}(\omega)|^2 = \frac{|S_{21}(\omega_0)|^2}{1 + 4Q_l^2\left(\frac{\omega}{\omega_0} - 1\right)^2}. \tag{2.57}$$

The loaded quality factor Q_l can simply be calculated by the relation $Q_l = \omega_0/\mathrm{BW}$. By introducing the coupling coefficient $g = Q_0/Q_e$, we can express the unloaded Q_0 from Eq. (2.52) as

$$Q_0 = (1 + g)Q_l. \tag{2.58}$$

Similar to cavity optomechanical systems, we can distinguish between three cases:

- $g < 1$: The cavity is *undercoupled* to the feedline.
- $g = 1$: The cavity is *critically coupled* to the feedline.
- $g > 1$: The cavity is *overcoupled* to the feedline.

Furthermore, we find the coupling coefficient can be defined as follows

$$g = \frac{|S_{12}(\omega_0)|^2}{1 - |S_{12}(\omega_0)|^2}. \tag{2.59}$$

How to determine Q_0 and Q_e:
All together, in order to find both the unloaded and the external quality factors $\{Q_0,\ Q_e\}$ we need to determine the loaded quality factor Q_l first. This can be done by fitting the cavity response $|S_{21}(\omega)|^2$ from Eq. (2.57) using the Lorentzian fit. In the next step, the coupling coefficient g from Eq. (2.59) should be extracted. To obtain Q_0 we use Eq. (2.58) and the relation (2.52) gives Q_e.

As an example, we illustrate in Fig. 2.17 (a) the tuning behaviour of the rectangular cavity's coupling efficiency g versus the penetration depth L of the coaxial inner conductor.

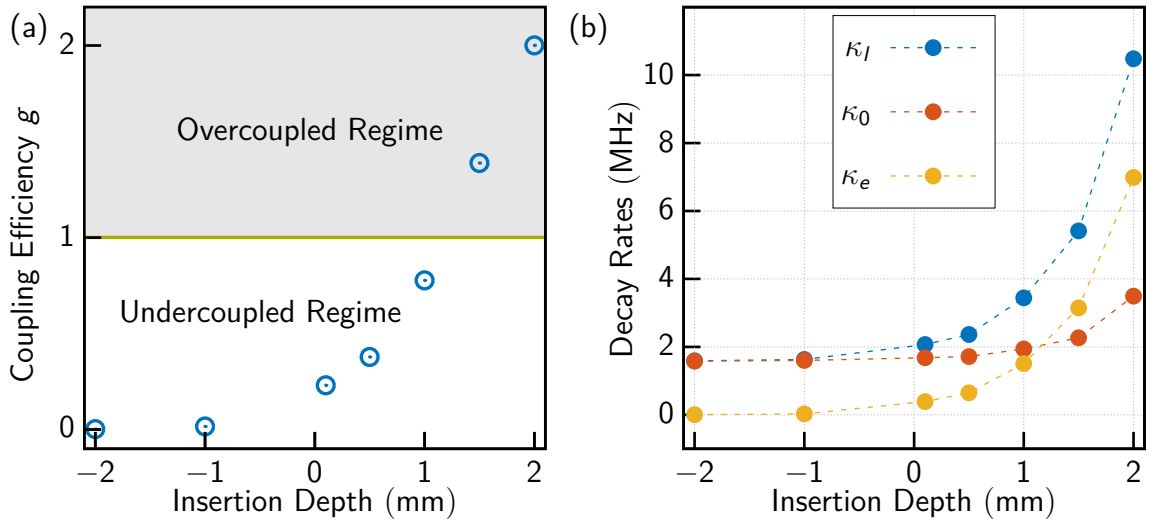

Figure 2.17 | Coupling Efficiency of the Rectangular Microwave Cavity.
(a) Coupling efficiency $g = Q_e/Q_0$ versus penetration depth L. Negative values indicate that the coaxial inner pin is still inside the circular aperture [see Figs. 2.15 (a) and (b)]. The over and undercoupled regimes are separated by the critically coupled line (green) where $g = 1$. **(b)** Cavity's decay rates versus penetration depths L. In the weak coupling regime, the external coupling rate is zero. By increasing the penetration depth, the external coupling rate can exceed the cavity internal losses $\kappa_e > \kappa_0$. The dashed line is a guideline to the eye.

Note that, for negative values of L, the coaxial pin tip is still inside the cylindrical coupling aperture [see Figs. 2.15 (a) and (b)]. Positive values of L, on the other hand, indicate that the coaxial pin is located inside the rectangular cavity box. The case for critical coupling occurs when $L \sim 1.1\,\text{mm}$. Instead of the quality factor Q_x, we plot the rectangular cavity decay rates $\kappa_x = \omega_0/Q_x$ versus the pin insertion depths in Fig. 2.17 (b), where $x \in \{l, 0, e\}$ indicates the parameters for the loaded, unloaded and external coupling cases. In the undercoupling regime $\kappa_e \ll \kappa_0$, the cavity losses are dominated by the intrinsic loss mechanisms. When the external coupling exceeds the internal loss mechanisms ($\kappa_e \gg \kappa_0$), the cavity is in the overcoupled case and the injected microwave signals can reach the measurement port without being absorbed inside the cavity. Ideally, the cavity intrinsic loss would remain the same during the measurement. But since the coaxial pin is inserted inside the cavity, it would open up a new decay channel, where the signal can be reflected back into the input line and hence the internal decay rate κ_0 increases slightly when we operate the cavity in the overcoupled regime. The loaded or total decay rate is the sum of the unloaded and external coupling rates $\kappa_l = \kappa_0 + \kappa_e$. Note that, we use this insertion depth variation technique discussed above to extract the quality factors for the rectangular and coaxial cavities since they are two port devices. Therefore, the measured transmission gives direct access to the scattering parameter S_{21} (or cavity response). It appears as a peak whose square modulus exhibits a Lorentzian distribution.

Circle Fit Technique The second technique to determine the microwave cavity's parameters is to use the so-called circle fit algorithm. The mathematical description of this algorithm was first derived by Chernow and Lesort [121]. Probst et al. [122] utilize this circle fit technique as the implementation for robust fitting and calibration of complex resonator scattering data. Instead of using only power or amplitude response of the cavity, we can utilize a full complex transmission of the scattering parameter data S_{21} provided by the network analyzer. For instance, this method is more appealing for reflection measurements because the results provide a reference baseline, that allows us to extract the distortions coming from the environment such as cable delay, attenuation and gain in the measurement, ect. The coupled system can be described in the "notch type" resonator [122] geometry, where the resonator is coupled to one transmission line [see Fig. 2.18 (a)]. The transmitted amplitude of the notch type geometry in Fig. 2.18 (b) appears with a dip, that is the resonance of the LRC resonator.

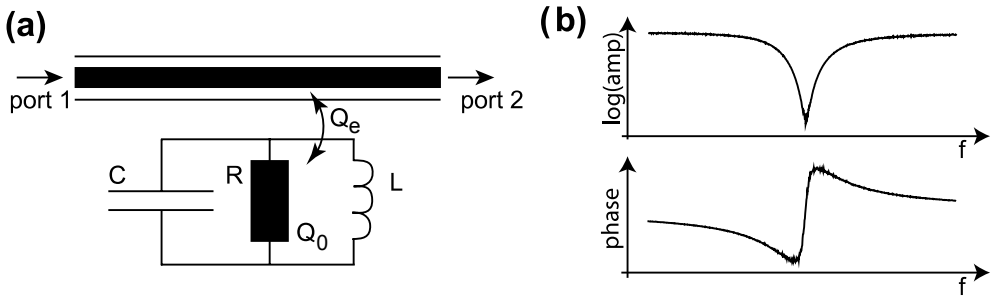

Figure 2.18 | Notch Type Geometry.
(a)A RLC resonator coupled to the transmission line forming the notch type geometry for measurements in reflection.**(b)** Transmitted amplitude and phase as a function of frequency with added noise. The transmission shows a dip in the amplitude. **Reprinted from Ref. [122], with the permission of AIP Publishing.**

Before describing the fit procedure, we want to discuss the notch type geometry, that is the resonator coupled to a transmission line, as the most generic two-port device. In this case, the scattering parameter S_{21} appears with a dip in the transmission [123]

$$S_{21} = 1 - \frac{\kappa}{\kappa + \mathrm{i}(\omega - \omega_0)}. \tag{2.60}$$

Here, κ is the total decay rate of the resonator and is, in general, a complex number. For an ideal dissipationless resonator, κ is real and describes the external coupling strength $\kappa = \kappa_e$. By introducing the dissipation to the resonator, the complex κ can be split into real and imaginary components $\kappa = \kappa_R + \mathrm{i}\kappa_I$. Additionally, the dissipation can add an imaginary component to the resonance frequency, thus, $\omega_0 \rightarrow \omega_0 + \mathrm{i}\xi$. Equation (2.60) can be expressed as

$$S_{21} = 1 - \frac{\kappa_R + \mathrm{i}\kappa_I}{(\kappa_R + \xi) + \mathrm{i}(\omega - (\omega_0 - \kappa_I))}. \tag{2.61}$$

Similar to the harmonic oscillator, the damping effectively shifts the resonance frequency of the resonator and hence, we define a new resonance frequency for the dissipation case as $\widetilde{\omega}_0 = \omega_0 - \kappa_I$. We re-define $\kappa_I = -\delta\omega$ as an induced shift in the cavity resonance frequency due to dissipation and the Eq. (2.61) is simplified to

$$S_{21} = 1 - \frac{\kappa_R - \mathrm{i}\delta\omega}{(\kappa_R + \xi) + \mathrm{i}(\omega - \widetilde{\omega}_0)}. \tag{2.62}$$

We can further modify Eq. (2.62) by replacing the real part of the denominator as the total (or loaded) quality factor Q_0 that is by definition $Q_l = \frac{\widetilde{\omega}_0}{2(\kappa_R + \xi)}$. Remember that we can decompose the total quality factor into unloaded and external components

$$\frac{1}{Q_l} = \frac{1}{Q_0} + \frac{1}{Q_e} = \frac{2\xi}{\widetilde{\omega}_0} + \frac{2\kappa_R}{\widetilde{\omega}_0}. \tag{2.63}$$

So we can express Eq. (2.62) in terms of quality factors as

$$S_{21} = 1 - \frac{\frac{\widetilde{\omega}_0}{2Q_e} - \mathrm{i}\delta\omega}{\left(\frac{\widetilde{\omega}_0}{2Q_e} + \frac{\widetilde{\omega}_0}{2Q_0}\right) + \mathrm{i}(\omega - \widetilde{\omega}_0)}. \tag{2.64}$$

By rearrange Eq. (2.64) we get

$$S_{21} = 1 - \frac{\frac{Q_l}{Q_e}\left(1 - \mathrm{i}Q_e\frac{2\delta\omega}{\widetilde{\omega}_0}\right)}{1 + 2\mathrm{i}Q_l\left(\frac{\omega}{\widetilde{\omega}_0} - 1\right)}. \tag{2.65}$$

Note that for $\delta\omega = 0$, the cavity resonance has the so-called *symmetric* response and Q_e is a real number. For $\delta\omega \neq 0$ the external quality factor becomes complex and the shape of the resonance dip can become asymmetric. This might arise from the impedance mismatch of the system or from the reflections between the input and output ports [122, 124]. In their work, Khalil et al.[125] take the impedance mismatch into account that is quantified by ϕ and therefore, we have $Q_e = |Q_e| \exp(-i\phi)$. All together, we obtain the final expression for a generic notch type resonator coupled to a transmission line that is[122, 125]

$$S_{21} = 1 - \frac{(Q_l/|Q_e|)\mathrm{e}^{\mathrm{i}\phi}}{1 + 2\mathrm{i}Q_l\left(\frac{\omega}{\widetilde{\omega}_0} - 1\right)}. \tag{2.66}$$

Now, we discuss the fitting of the cavity's resonance parameters using the circle fit technique provided by Probst et al. [122]. In addition to the general model for the complex S_{21} scattering coefficient of the notch type resonator, we need to take the effect of the coupling environment into account. Hence, Eq. (2.66) becomes

$$S_{21}(\omega) = a\mathrm{e}^{\mathrm{i}\alpha}\mathrm{e}^{-\mathrm{i}2\pi\omega\tau}\left[1 - \frac{(Q_l/|Q_e|)\mathrm{e}^{\mathrm{i}\phi}}{1 + 2\mathrm{i}Q_l\left(\frac{\omega}{\widetilde{\omega}_0} - 1\right)}\right]. \tag{2.67}$$

The first term in Eq. (2.67) denotes the added *environment* that refers to all contributions coming from the outside of the system. Here, a denotes the additional amplitude gain. The phase shift α and the delay time τ are caused by the cable length and the finite speed of the signal propagating inside the microwave cables. In general, it is possible to use Eq. (2.67) to simultaneously fit all the 7 unknown parameters. However, this non-linear and multiple-parameter fit routine can be extremely sensitive to initial start parameters and hence the results become unreliable. For that reason, Probst et al. [122] suggested to break down the fitting problem into several independent fitting steps, where each only contains a few parameters. We illustrate the fitting procedure in Fig. 2.19. The cable delay causes a circular distortion of the ideal resonance circle [see Fig. 2.19 (a)] with the radius a, that represents attenuation or amplification in the setup. The cable delay tilts the phase signal by a slope $2\pi\tau$. In order to estimate the delay time a simple linear fit function should be carried out. When obtaining a good estimate for the delay time τ, we can perform a non-linear least square fit on the twisted loop like curve. Here, the fit parameter is the cable delay and the error function to be minimized is the deviation from the ideal circular shape $\epsilon^2 = \sum_{i=1}^{n} r_0^2 - \left[(x_i - x_c)^2 + (y_i - y_c)^2\right]$. From the algebraic circle fit we get r_0, x_c and y_c that are the radius and the corresponding center coordinates of the circle [see Fig. 2.19 (b) red circle]. The impedance mismatch can be directly calculated by $\phi_0 = -\arcsin(y_c/r_0)$. Note from the diameter of the circle, we obtain the ratio $d = Q_l/|Q_c|$. Even though, the data already exhibits a circular shape, they are still not equivalent to the ideal case due to the attenuation/amplification and phase shift $a\mathrm{e}^{\mathrm{i}\alpha}$. In order to determine a and α, the circle is translated back to the origin [margenta

circle in Fig. 2.19 (b)]. Subsequently, a phase vs. frequency fit is performed, which yields the resonance frequency ω_0 and the total quality factor [see Fig. 2.19 (c)]

$$\theta(\omega) = \theta_0 + 2\arctan\left(2Q_l\left[1 - \frac{\omega}{\omega_0}\right]\right). \tag{2.68}$$

From θ_0 and the center position, is it possible to translate the circle to its canonical position, where the off-resonant point $P = 1$ [Fig. 2.19 (d)]. Since the circle is in its canonical form, we can calculate the external (or coupling) quality factor $Q_e = Q_l/(2r_0 \exp(-i\phi_0))$. The internal (unloaded) quality factor can be again calculated by the relation $Q_0^{-1} = Q_l^{-1} - Q_e^{-1}$.

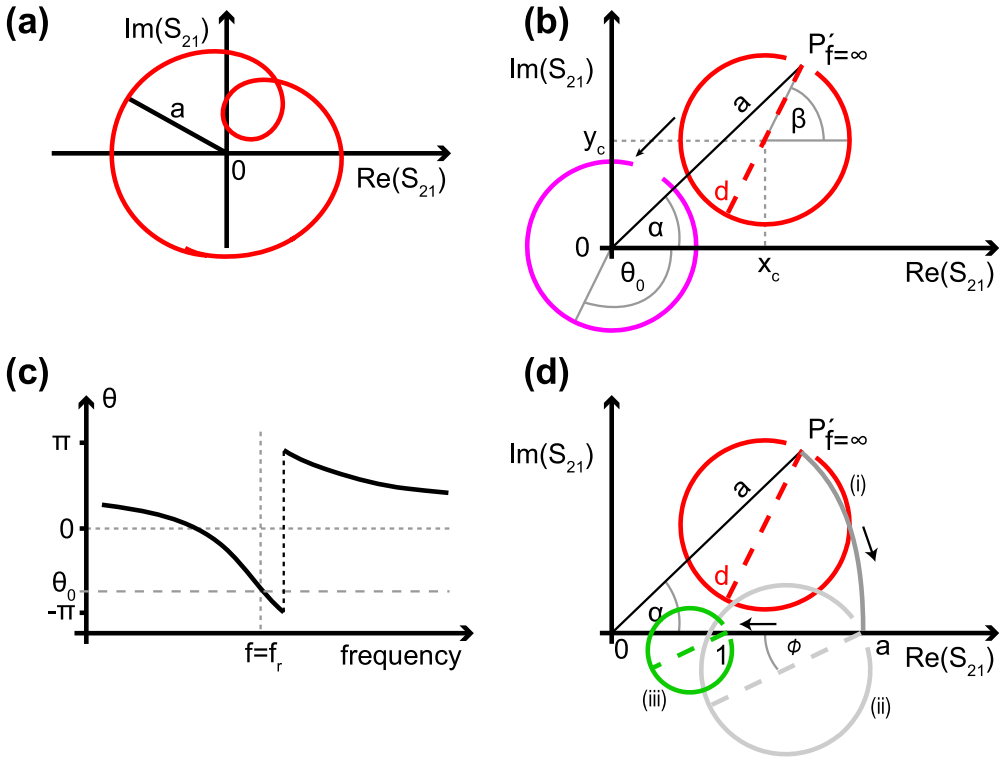

Figure 2.19 | Circle Fit Algorithm on Cavity's Complex Scattering Data.
(a) Uncalibrated complex scattering data of a resonator. The cable delay causes a distortion of the ideal circular shape of the resonance circle. **(b)** Algebraic circle fit to determine the circle diameter d and its center position $(x_c,\ y_c)$. By the translation to the origin, the prefactors a and α can be determined. **(b)** The phase versus frequency fit to obtain the resonance frequency ω_0, the unloaded (total) quality factor Q_0 and the offset phase θ_0. **(d)** Last step to transform the cirle to its canonical position where $P = 1$. **Reprinted from [122], with the permission of AIP Publishing.**

In Figs. 2.20 and 2.21, we demonstrate the circle fit algorithm applied to the complex scattering data of the cylindrical cavity mode TM_{110} in reflection. Note that in reflection, we obtain the cavity amplitude response with a Lorentzian distribution that is equivalent to the scattering parameter S_{21} of the notch type resonator in Eq. (2.67) [also see Fig. 2.18 (a) and (b)] . As expected, the cavity raw complex scattering data in Fig. 2.20 (a) exhibit a distorted loop rather than a circular shape of the cavity's resonance caused by cable delay. In Fig. 2.20 (b) the cavity amplitude response $|S_{21}|$ shows a Lorentzian distribution with an uncalibrated dip. Additionally, the cable delay tilts the cavity phase response by a slope $2\pi\tau$ [see Fig. 2.20 (c)].

By applying the circular fit routine the raw data can be re-calibrated. Figure 2.21 (a) shows that the distorted loop becomes a perfect circular shape by using the nonlinear least square fit. Additionally, the amplitude response is properly re-normalized and the phase response shows a phase jump on resonance without a slope [see Fig. 2.21 (b)-(c)]. The circle fit algorithm offers a fast and accurate analysis of noisy complex scattering data of our microwave 3D cavities without any need of calibration. The python based implementation of the algorithm can be found on Ref. [126].

Note that the circle fit technique discussed here assumes that the occurrence of the asymmetric lineshapes (Fano effects) in the cavity response is due to impedance mismatches at the input and output port. Hence, we can use the model described by Eq. (2.66). In a more generic picture, the Fano feature in the cavity response can occur from the "cross talk" between the resonant signal and the background. For example, the direct leakage due to the finite isolation in the input and output ports of the circulator in a reflection measurement can lead to interference with the cavity output. Generally, the resulting amplitude and phase of the Fano interference are unknown. In principle, the asymmetric lineshape itself is harmless and does not affect the analysis of the S-parameter. The problem occurs, however, when the leakage does not cause any asymmetric lineshape, but still add an unknown systematic error in the calculated internal quality factor that cannot be calibrated out. Rieger et al. suggest a procedure to extract Q_0 with a range of uncertainty based on an upper bound for the interference amplitude [127]. This range of uncertainty increases strongly with the cavity's coupling strength. Since our system operates in the undercoupled regime, we assume that the error in the internal quality Q_0 determination is relatively small.

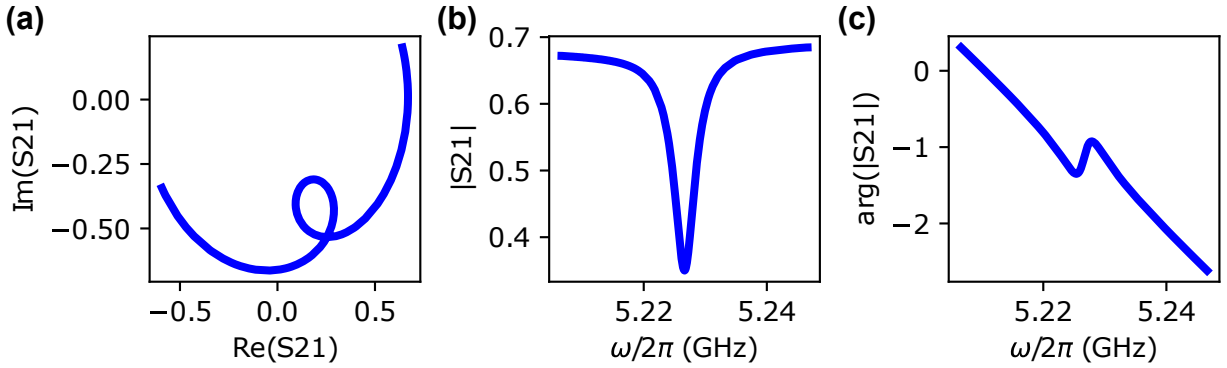

Figure 2.20 | Cylindrical Cavity Complex Scattering Data.
(a) Uncalibrated complex scattering data of the cylindrical cavity mode TM_{110} with distorted loop shape of the cavity resonance. **(b)** Cavity amplitude response exhibits a dip with Lorentzian distribution at the resonance frequency. Almost no asymmetry in the cavity's response indicating small impedance mismatch between input and output coupling. **(c)** Phase versus frequency response of the cavity. The slope in the phase response is a direct consequence of the cable delay.

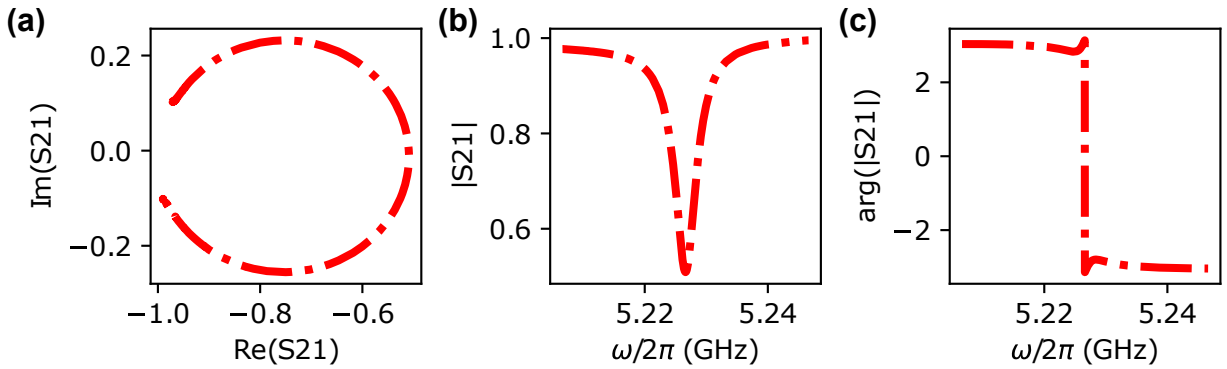

Figure 2.21 | Cylindrical Cavity Data with Circle Fit Algorithm.
(a) The cavity's complex scattering data after the implementation of the circular fit procedure showing a perfect circle on resonance. **(b)** The cavity's amplitude response is renormalized. **(c)** The cavity phase response after proper calibrations showing a phase jump on resonance.

2.4 Nano Fabrication Procedures

In this section, we provide an overview of the methods for fabricating the double-clamped no string resonators that we described theoretically in Sec. 2.1. Note that all manufacturing steps described below are performed in the clean room facility "Nanolab" of the University of Konstanz. Since the group has recently moved to the Technical University of Munich (TUM), new fabrication processes have been developed by F. David and B. Yalaman for both silicon nitride (SiN) [128] and silicon carbide (SiC) [129] string resonators. In this work, we employ the so-called "top down" fabrication technique only for SiN string resonators, which relies heavily on electron beam lithography (EBL).

Electron Beam Lithography

There is a variety of nano-lithography techniques, e.g. deep ultraviolet (DUV) lithography, extreme ultraviolet lithography (EUV) and also electron beam lithography. DUV and EUV are mainly used for mass production in the semiconductor industry, as these processes are fast and highly reproducible. EBL, however, is primarily used in research and development (R&D). The maskless nature of this technique offers flexibility in design and remarkably high resolution (5 nm and below). Therefore, EBL is more suitable for test purposes and allows the design of small geometries.

The EBL system uses a focused electron beam (e-beam) to directly irradiate the top surface of a resist-coated material to create the desired pattern. Electron beam resists are mainly chemical compounds that are highly sensitive to electrons. Their chemical structures are modified after the e-beam exposure to either form new bonds between the molecules in the resist (negative) or breaking existing bonds (positive). The exposed area of a negative resist becomes insoluble after development in a suitable developer, while the positive resist becomes soluble after exposure to the electron beam. In our case, we use a positive resist [1] to define the structure of electrodes flanking the nanomechanical string resonator on both sides for dielectrical transduction [70, 130].

A second step of e-beam lithography is employed to align the structure of the doubly clamped string resonator between the narrow gap of the electrodes. Typically, the electrodes are designed to have 400 nm – 500 nm wide gap. Since the width of the strings are 250 nm – 300 nm, it is essential to add markers in the first lithography step to obtain an alignment process with high precision. Using the alignment marks, the deflection of the electron beam is calibrated in such a way that the beam motion correctly matches the lengths defined by the coordinates of the previously designed pattern in the writing field. In the following, we provide a step by step description of our nano fabrication procedure that is developed and now well established by the group over many years.

Figure 2.22 shows the first fabrication steps to realize the desired geometry in the nanometer range. Our sample consists of a stoichiometric silicon nitride (Si_3N_4) layer with a thickness of 100 nm, industrially grown on 500 µm fused silica (SiO_2) substrate using low pressure chemical vapor deposition (LPCVD) technique [Fig. 2.22 (a)]. For reasons of reproducibility and to support orientation during the fabrication process, the wafer is diced into chips measuring $5 \times 5\,mm^2$, which form the basis of all successive steps.

At first, the samples are rinsed in ultrasonic bath using acetone and isopropanol (IPA) solutions, each for 5 minutes. The electron sensitive resist is then spin-coated on the surface of the chip with a rotation speed of 5000 rpm in 30 s to obtain a film thickness of 450 nm. Subsequently, the sample is softbaked on a hotplate by 180 °C for 90 s. Due to the non-conductive nature of the quartz substrate, an additional layer of conductive polymer [2] is required to avoid charging effects during the e-beam

[1] MicroChem PMMA 950k A6
[2] Allresist Electra 92 (AR-PC 5090)

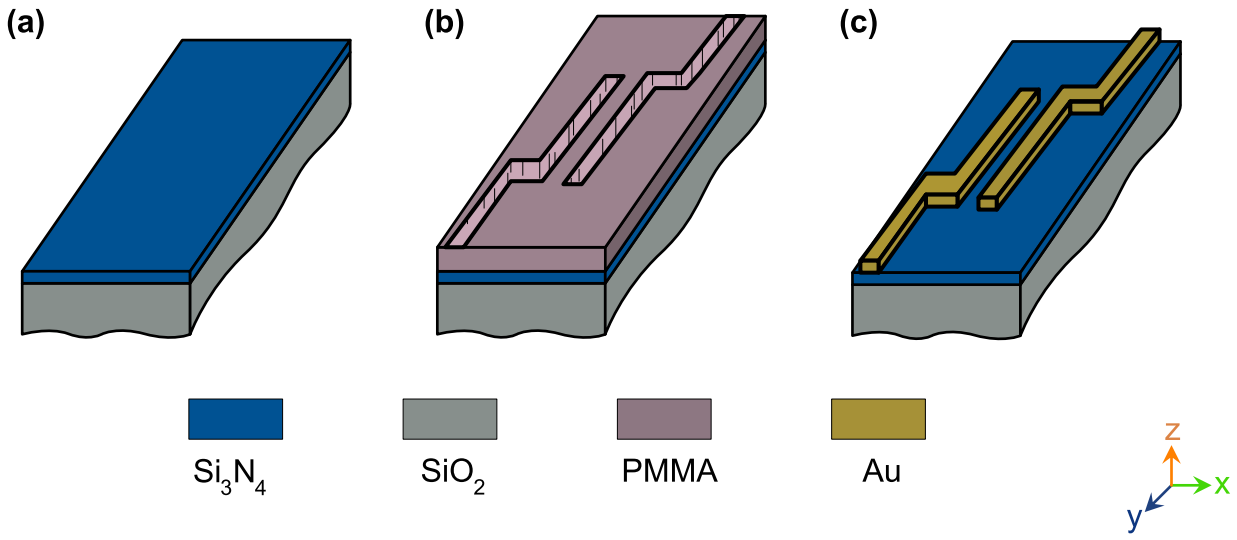

Figure 2.22 | Electrodes Patterning with Electron Beam Lithography.
(a) 100 nm silicon nitride (dark blue) is grown on quartz substrate (gray) served as basis for fabrication of doubly clamped nano string resonators. **(b)** Sample after the e-beam exposure and development. By using positive resist, the patterned structures are dissolved in the developer. **(c)** The remaining gold electrodes after e-beam evaporation and lift-off process on top of the SiN layer.

exposure. Here, we spin-coat Electra 92 on top of the previously coated PMMA with 2000 rpm in 60 s and the conductive polymer is subsequently baked for 2 minutes with 90 °C. The sample is now ready for the e-beam exposure.

In the clean room facility "Nanolab" of the university of Konstanz we use the scanning electron microscope [3] from Zeiss with a beam controlled software [4] to pattern the structures of the electrodes [see Fig. 2.22 (b)], alignment markers and bondpads (not shown). Note that the alignment markers are essential for the second exposure, as we use them for orientation to align the string structures between the small gaps of the electrodes (see for instance Ref. [128]). The e-beam exposure is performed at a working distance of 8.6 mm and an acceleration voltage of 10 kV. In this case, two different apertures are used since we have structures that differ greatly in sizes. As a result, the 20 µm aperture with the dose of 90 $\mu C/cm^2$ is primarily employed to pattern the electrodes structures and the 120 µm aperture and 196 $\mu C/cm^2$ is used for the millimeter-sized bond pads that electrically connect the electrodes to the drive sources. Note that we change apertures during the exposure to pattern both bond pads and electrode structures in a single step. The exposure time calculation and the offset compensation due to the change in aperture is carried out by the beam control software.

After the e-beam patterning, the conductive layer is removed simply by submerging the sample in deionized water for 60 s. The positive resist is then developed by using the mixture of MIBK [5] and IPA with a ratio of 1:3 with a duration of 50 s and the rinse in only IPA will stop the development process. We gently blow dry the sample with a nitrogen gun to complete the first exposure step. Since we use a positive resist, the exposed areas should be dissolved after the development leaving empty structures behind [see Fig. 2.22 (b)].

[3] Zeiss Crossbeam 1540XB
[4] Neomicra
[5] Methylisobutylketone

E-Beam Evaporation

The metallization of the sample to obtain gold structures is done by the physical vapor deposition (PVD) technique. In this work, we utilize the so-called e-beam evaporation. Here, an intense beam of electrons is generated from a filament and directed towards the crucible that contains the source target (i.e. gold, chromium ect.) using electric and magnetic fields to vaporize it within a vacuum environment. This process allows the atoms to leave the metallic surface and traverse through the vacuum. With sufficient thermal energy, the atoms from the metallic source can reach the sample target that is located above the crucible. This mechanism can be used to coat the substrate that is attached on the target. In our lab, we employ the e-beam evaporation technique [6] to deposit 5 nm of chromium that serves as adhesion layer [7], and 100 nm of gold on the sample. For chromium, we use an evaporation rate of 0.3 Å/s and for gold we increase the evaporation rate to 1 Å/s, respectively. Note that we decide to evaporate 120 nm gold, since the thickness of the gold electrodes will be reduced to $\approx$ 50 nm after the anisotropic etching process. However, this proceeding demands relatively high consumption of gold and therefore we suggest to add an additional etch mask (i.e. 30 nm of chromium) to protect the gold electrodes from degradation during the etch process. With the protective etch mask, we can reduce the thickness of the gold layer to 50 nm. In the successive lift-off process, we dissolve the remaining resist PMMA by submerging the evaporated sample in acetone solution where the overlying metallic coating can be removed. Only the structures that are previously written by the e-beam lithography, (and now filled with a gold layer) are preserved [see Fig. 2.22 (c)].

Protective Anisotropic Etch Masks for String Resonators

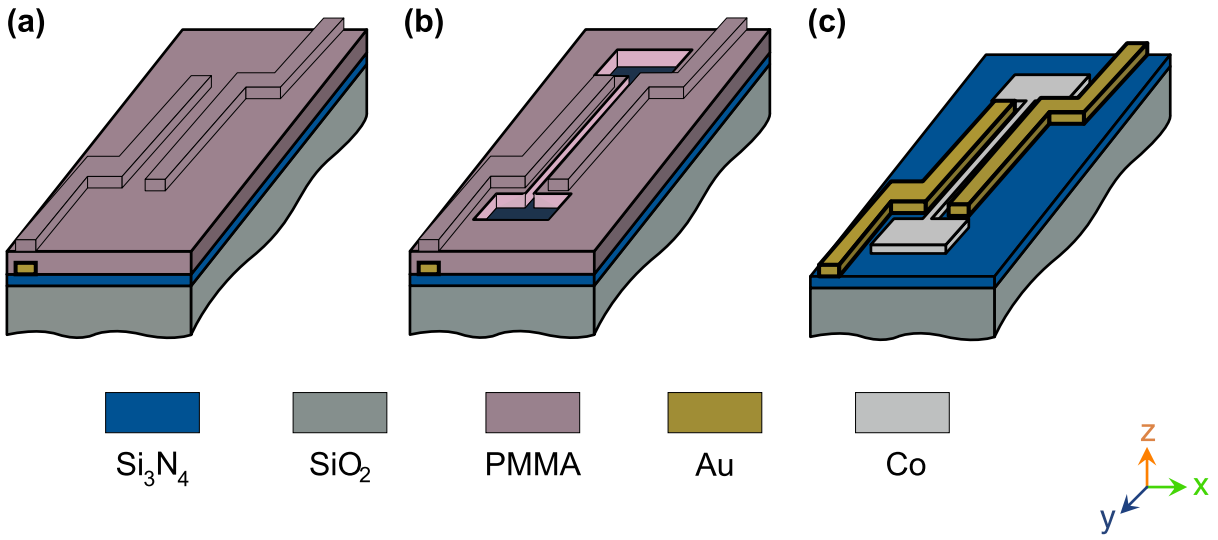

Figure 2.23 | E-Beam Patterning of String Resonators.
(a) PMMA coated sample with electrodes before e-beam lithography. **(b)** Sample after e-beam exposure and development. **(c)** Sample after vapor deposition and lift-off process. A cobalt mask with the geometry of a doubly-clamped string resonator will protect the underlying SiN layer from anisotropic etch process.

After the lift-off process, we are now ready to begin the second e-beam lithography step to define the geometry of the doubly clamped strings which is located between the two electrodes defined in

[6] AJA Internaltional ATC Orion 8-T
[7] Note that titanium, which is used as a standard material for adhesion, is not applicable in our case due to the application of buffered hydroflueric acid (bHF).

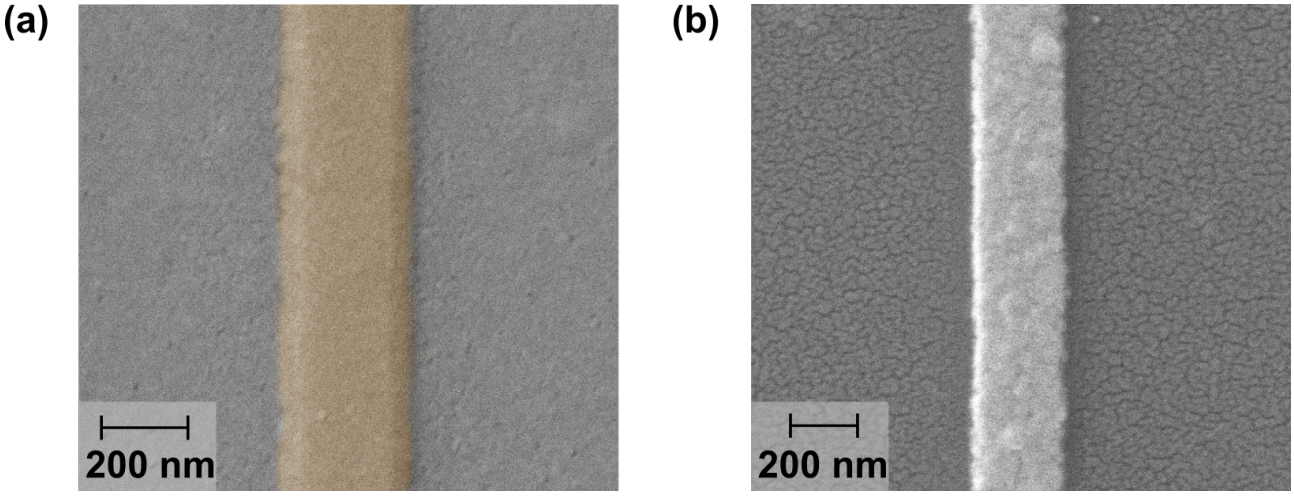

Figure 2.24 | Metallic Etch Masks.
(a) Scanning electron microscope (SEM) image of the evaporated cobalt string etch mask (deposition rate 0.5 Å/s) shows relatively smooth edges. **(b)** Aluminum etch mask with large grain size by deposition rate 0.5 Å/s will lead to string resonators with rough edges and hence lower the quality factor.

the previous steps (see Fig. 2.23). We repeat the procedure of spin-coating the resist and conductive polymer Electra described above to obtain the same starting conditions before e-beam patterning [see Fig. 2.23 (a)]. As mentioned earlier, the second exposure requires careful alignment to correct the mismatch between the stage coordinates (xyz) and the sample coordinates (uvw) in the Neomicra software. The predefined markers from the first step provide the beam control software *Neomicra* with good orientation for alignment procedures such as angle corrections, zoom factor, lateral and horizontal offsets ect. We execute the e-beam exposure with the configurations similar to the first step. Due to small dimensions of the strings, we use the 20 µm aperture with a dose of 117 $\mu C/cm^2$ to pattern the geometry. Subsequently, the exposed sample can be developed [Fig. 2.23 (b)] and we can deposit the metallic mask to protect the below lying SiN layer from the anisotropic etch process.

We would like to emphasize that the choice of material for the etch mask is crucial for the smoothness of the string edges, which in turn have a direct influence on the quality factor. An etch mask with high roughness will directly imprint its shape to the underlying protected layer after the isotropic etching process. Consequently, string resonators with rough edges exhibit considerable low quality factors in contrast to the ones with smooth edges. In this thesis, we want to compare the smoothness of the aluminum to cobalt etch mask. Aluminum provides a relatively inexpensive and straightforward solution in vapor deposition of thin films. It is also known as one of the most important material in microelectronics. However, it is well known that the coated aluminum film builds up clusters during evaporation and hence, showing grain structures on the thin film. It has been shown, that the grain size strongly depends on the evaporation rates of aluminum and also on the material of the substrate [131]. The best results can be achieved with glass substrate and an evaporation rate of 0.1 Å/s, where the thin aluminum films show grains with diameters ranging from 20 nm – 40 nm. In our case, we use e-beam deposition to evaporate 35 nm of aluminum with a rate of 1 Å/s that serves as the etch mask. As apparent in Fig. 2.24 (b), the aluminum mask with the high deposition rate shows relatively large grain size and hence, the strings will suffer from the roughness and the quality factor is accordingly low. The second material of choice in our experiment is cobalt. The mask from cobalt evaporation [see Fig. 2.24 (a)] offers much smoother surface and edges, thus, the quality factors of the string resonators are expect to be higher than the ones from an aluminum mask. However, Cobalt is generally not the first choice material, because it is relatively expensive due to the high demands in lithium- ion battery technology, and also due the characteristic ferromagnetic nature of the material. Cobalt is nowadays

rarely found in most evaporation chambers. Many groups performing experiments in low temperature environments are likely to avoid to evaporate this type of metal in the same chamber, where they fabricate their device, i.e. superconducting qubits or coplanar microwave resonator. The residue of cobalt and its the ferromagnetic nature can destroy the superconducting properties of such devices. Fortunately, in the laboratory of Prof. Elke Scheer at the University of Konstanz, we can find an e-beam evaporation champer to deposit cobalt. Here, we use an evaporation rate of 0.5 Å/s to deposit 35 nm cobalt etch mask on our SiN samples. Note that all the samples used in this thesis are deposited with cobalt since they give the highest quality factors.

The third material of choice that can be used as a protective etch mask is chromium. It combines both advantages (smoothness and inexpensiveness) of the two other materials and has proven to be a good material for ICP-RIE etching. However, using chromium mask will lead to some fabrication challenges, which we will not discuss here in this thesis. A comprehensive comparison between chromium and aluminum etch masks can be found in the PhD thesis of Y. Klass [132].

Anisotropic Etching (ICP-RIE)

After the second lithography step and the etch mask deposition with cobalt, the sample is now ready for the etching process to faithfully reproduce the pattern defined by the e-beam lithography. In our case, we use the anisotropic dry etch process, the so-called inductively coupled plasma - reactive ion etching (ICP-RIE) technique. The etch mechanism occurs by using reactive gases that interact either physically (by bombardments of ion) or chemically (by radicals) with the surface atoms of the sample. The reactive plasma state of the gas is generated by an external radio frequency (RF) source. The RF-field causes the electrons to oscillate rapidly. With large RF-power, the electrons gain enough power to impact nearby atoms or molecules generating more electrons and leaving behind positive ions or highly reactive radicals. In order to enhance the plasma density, a second RF-source (a coil) is added to the vacuum chamber. The added magnetic field causes the electrons to spiral inside the vacuum chamber. In other words, the spiral movement extends the electron's mean free path where they can cause more collisions before hitting the chamber wall. The control over the two independent RF-source gives full control over the etch behaviour of the highly reactive plasma cloud. The ICP can generate both ions and radicals. On the one hand, ions get accelerated towards the sample surface and cause physical etch process. The physical etching is directive and we call this process "anisotropic etching". Radicals, on the other hand, diffuse into the sample and cause chemical etching. This type of etch process occurs in all directions and hence, we call this mechanism "isotropic etching". For a more comprehensive description about the working principle of the ICP-RIE (see Ref. [133]).

The obtain the pattern predefined by the e-beam lithography, we solely utilize the directive anisotropic etch process that is conducted in the "Nanolab" using the ICP-RIE [8] technique. The reactive gases used here are sulfur hexaflouride (SF_6) and argon (Ar). The etch procedure is executed at 10 °C wafer temperature and we use the gas flow of 4 sccm and 2 sccm for Ar and SF_6, respectively. We adjust the ICP power to 350 W and the RIE power is set to 65 W. The chamber pressure reaches 2 mTorr during the etch process. The etch time is 3:04 min, that results in an etching depth of 340 nm, which is more than sufficient to etch through the SiN layer deposited on the fused silica substrate. After this anisotropic dry etch process we continue the fabrication procedure with isotropic chemical etching to finally release the SiN structures to obtain free suspended string resonators.

[8] ICP-RIE Oxford Plamalab 100

Isotropic Chemical Etching

In order to fabricate string resonators with high quality factors, we need to keep the sample free from impurities that are the metallic residues from the etch mask. It has been reported, that the inverse quality factor scales linearly with the thickness of the metallic layer deposited on the string [134]. For this reason, we remove the remaining cobalt etch mask by immersing the sample in a piranha solution for 2 minutes. The piranha solution is the mixture of sulfuric acid (H_2SO_2) and 30 % hydrogen peroxide with a ratio of (3:1). Another positive effect of piranha solution is the strong chemical reaction to organic materials. Hence, the piranha treatment will further remove organic residues from our sample. Note that the aluminum mask can be removed by sodium hydroxide (NaOH) with the concentration of 1 mol/l in 1 minute. After the removal of the metallic etch mask, the sample is now ready for the final isotropic chemical etching step. Here, we use buffered hydrofluoric acid (BHF) [9] to release the silicon nitride string resonators. BHF offers high selectivity in the etch process, where only the sacrificial material (SiO_2) is removed while the device layer (SiN) still remains intact. By doing so, we submerge the sample into BHF solution for 3 min 30 s to under-etch the below lying quartz substrate and the SiN string resonators are freely suspended after this step. Note that the sacrificial material (SiO_2) below the electrodes structures are also partly remove. Due to the larger thickness (1 µm) the electrodes are not released from the substrate. Subsequently, the sample is rinsed in de-ionized (DI) water to stop the etch process. Note that the sample is constantly submerged in liquid environment during the chemical etch procedure. If we simply remove the sample from the liquid, the thin and long string resonators will be most likely damaged or attached to the substrate due to the strong surface tension. The first step to minimize the damage is to replace the rinse DI water with IPA because the solution exhibits appreciably small surface tension. Additionally, we can further reduce the tension by heating the IPA up to 50 °C before drying the sample. At last, the sample should be gently blow dried with a nitrogen gun along the direction of the strings.

Critical Point Drying

An even more gentle method to transfer the sample from liquid to gaseous phase is to use the *critical point drying* (CPD) technique. Here, the transition between the liquid and gaseous phase is bypassed over the critical point to reach the so-called *supercritical* fluid state. In this high pressure and high temperature regime it is not possible to distinguish between the gaseous and liquid phase since they both have the same density. For this process the most common medium of choice is CO_2 that has a critical point at 73.8 bar and 31 °C. In the CPD chamber [10], we slowly replace the IPA solution with the sample immersed inside with liquid CO_2. The chamber is then heated up to overcome the critical point and we then slowly reduce the pressure to end up in the gas phase. A detailed description of the working principle of the CPD can be found in the PhD dissertation of M. Bückle [133]. In Fig. 2.25, we illustrate a schematic drawing of the final result of our nano fabrication procedure, where the nanomechanical string resonator is clamped by the pads and flanked by the electrodes on both sides for dielectrical transduction. All the important fabrication parameters are listed on table 2.1. We portrait a real SEM image of the doubly clamped silicon nitride string resonators taken after the successful nano fabrication procedure in Fig. 2.26.

[9] TECHNIC Hydroflouric Acid BOE 7-1
[10] Baltec CPD 030

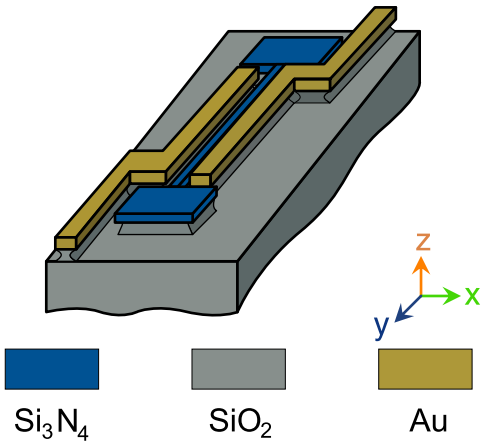

Figure 2.25 | Doubly-Clamped String Resonator with Electrodes.
Schematic representation of a doubly-clamped string resonator with electrodes flanking on both sides after a successful implementation of the nano fabrication procedures.

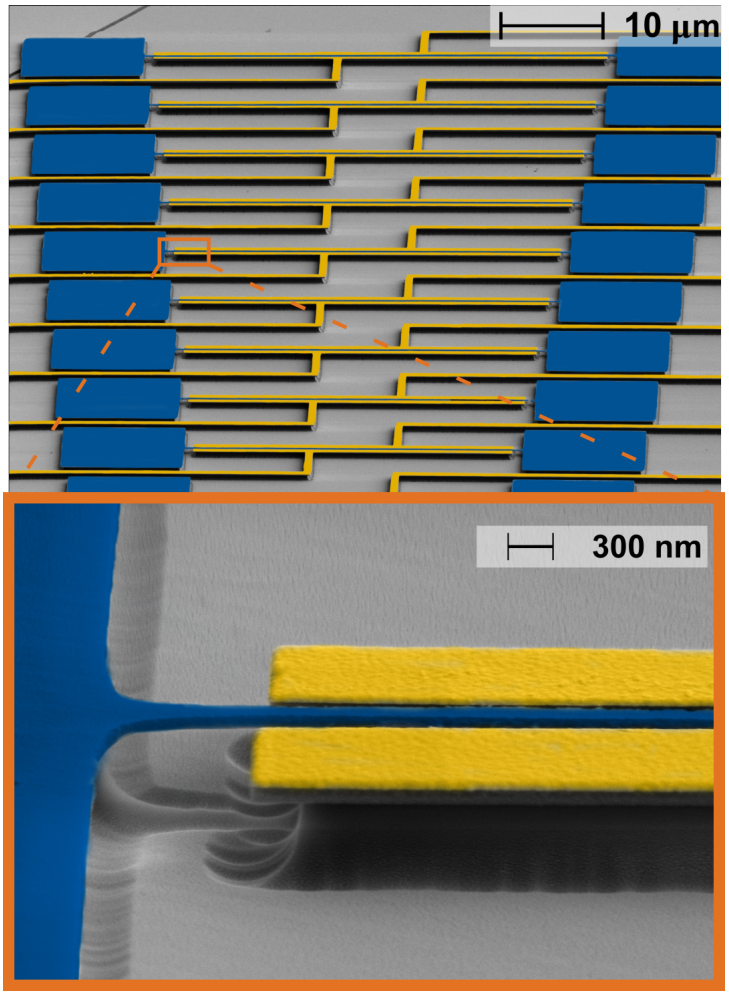

Figure 2.26 | SEM Micrographs of Multiple String Resonators with Electrodes.
A series of nanomechanical string resonators are designed to improve the yield of the fabrication process. Here, we increase the length of the strings by 5 µm steps. The corresponding eigenfrequencies range from 5 MHz – 10 MHz. The inset (orange) shows an enlarged view of a freely suspended string resonator that is fixed on both sides by clamping pads.

Table 2.1 | Fabrication Parameters.
Overview of the most important parameters and devices for the fabrication of nano-string resonators and electrodes.

Spin coating / Bake		
Resist	Process	Details
PMMA	Spin coater	5000 rpm & 30 s
	Softbake	180 °C & 90 s
Electra 92 (conductive layer)	Spin coater	2000 rpm & 60 s
	Softbake	90 °C & 120 s
Electron Beam Lithography (Zeiss Crossbeam 1540XB)		
Step	Aperture	Dose
Electrodes	20 µm	90 µC/cm^2
Bondpads	120 µm	196 µC/cm^2
String	20 µm	117 µC/cm^2
E-Beam Evaporation (AJA Orion-8)		
Step	Material	Thickness & Rate
Bondpads/Electrodes	Cr	5 nm & 0.3 Å/s
Bondpads/Electrodes	Au	120 nm & 1 Å/s
String protective Etch mask	Co	35 nm & 0.5 Å/s
String protective Etch mask (alternative)	Al	35 nm & 1 Å/s
ICP-RIE (Oxford Plasmalab 100)		
Reactive gas		Process
SF_6 / Ar		2 sccm (SF_6)
		4 sccm (Ar)
		ICP Power 350 W
		Rie Power 65 W
		Pressure 2 mTorr
		Wafer Temperature 10 °C
		Etch Time 3:04 min
Isotropic Underetch		
Solution		Etch Time
Buffered Hydrofluoric Acid (BHF)		3:15 min

3 Room Temperature Cavity Electromechanics

The following chapter is based on our manuscript:

A. T. Le, A. Brieussel and E. M. Weig, "Room temperature cavity electromehanics in the sideband-resolved regime", *Journal of Applied Physics*, **130**, 014301 (2021). Reference [107]

The published work has explicitly been written by the author. Therefore, the following chapter will partly contain passages of the original publication. All the figures are reprinted under permission of AIP Publishing and indicated as such.

In this chapter, we combine the two main ingredients that are the doubly clamped nanomechanical resonator and the microwave 3D cavity geometry discussed in the previous sections 2.1 and 2.3. We want to establish a cavity electromechanical system that operates under the same principles as their cavity optomechanical analogues [90]. But rather relying on a light field circulating inside an optical cavity, an electromagnetic circuit is employed to realize a cavity mode in the microwave regime which parametrically couples to a mechanical resonator. Motivated from recent developments in the field of circuit quantum electrodynamics (cQED), where 3D microwave cavities have replaced coplanar waveguide architectures due to their large mode volumes and remarkably high quality factors, three dimensional *superconducting* microwave cavities have been adapted for cavity electromechanics by capacitive coupling to a mechanical resonator [102, 103, 135]. However, the field of cavity electromechanics is limited to millikelvin temperatures, since it relies on superconducting circuits. Room temperature cavity electromechanics is impeded by the non-zero resistance of a normal conducting circuit, which gives rise to strong dissipation. In the past, our group has successfully employed non-superconducting microwave cavities such as copper microstrip resonators for cavity-assisted displacement sensing of nanomechanical resonators at room temperature [56, 130]. Their use for cavity electromechanics, however, is limited by a cavity quality factor of about 100 due to dielectric and conductor losses, which not only constrains the displacement sensitivity but also keeps the system to reside deeply in the unresolved sideband. This is the so-called bad cavity regime, where the linewidth $\kappa/2\pi$ of the cavity exceeds the eigenfrequency of the mechanical mode $\Omega_m/2\pi$. In the following, we will demonstrate a room temperature cavity electromechanical system that is capable of sideband-resolved ($\kappa < \Omega_m$) operations. The rest of this chapter is structured as follows: First, we start to discuss the fundamental mechanism, that is the sidebands generation in cavity electromechanics and how to employ the microwave cavity to probe the displacement of a strongly pre-stressed silicon nitride nanostring resonator. The heterodyne in-phase quadrature (IQ) mixing technique for frequency down-conversion is explained subsequently. Second, we continue with the actuation technique, where the dielectric property of the mechanical resonator is employed. At last, we demonstrate the experimental results of our room temperature cavity electromechanical system.

3.1 Mechanical Motion Detection

The detection of mechanical motion from tiny mechanical objects with high precision remains a difficult task. It is due to the fact, that the displacement amplitude of such nanomechanical resonators are found in the order of 10^{-12} m to 10^{-9} m. In our group we employ the dielectrical detection scheme to determine the frequency and displacement amplitude of the mechanical oscillation. In the following, we provide a description about the working principle of our well-established cavity-assisted detection technique using heterodyne IQ-mixing.

3.1.1 Sideband Generation

In the field of cavity optomechanics [90], the mechanical oscillator is trapped inside an optical cavity to enhance the light matter interaction. Due to the high finesse of the optical cavity, the injected photons can circulate and remain inside the cavity for a long time, increasing the chance to transfer the momentum of the photons into a mechanical motion or vice versa by radiation pressure mediated backaction. This mechanism leads to interesting phenomena such as amplification or damping (also known as cooling) of the mechanical motion. The parametric, dispersive coupling in the optomechanical system leads to the generation of sidebands in the response spectrum of the optical cavity providing information of the mechanical element inside the cavity.

The cavity electromechanical systems operate under the very same principle as their cavity optomechanical analogues. Cavity electromechanics often utilizes low-loss superconducting circuits that are easily cooled to temperatures below 100 mK. The compatibility of this system to dilution refrigerator environment provide a large advantage in ground state cooling of the mechanical motion [42, 136]. J. D. Teufel et al. demonstrate in their experiments large electromechanical coupling using a flexible vacuum gap capacitor to cool the mechanical motion to the quantum ground state [93] and to reach the quantum enable strong coupling regime [92]. Many groups implement these cavity electromechanical systems for microwave-to-optical conversion [24, 137] to obtain squeezing of a micromechanical resonator [138], for amplification of microwave signals [139], entanglement generation [140, 141], just to name a few.

Here, we employ in our experiment the cylindrical microwave 3D cavity geometry discussed in Sec. 2.3.3 to readout the motion of the mechanical oscillator. The coupling occurs via gold electrodes flanking the dielectric SiN string resonator (see Fig. 2.26). On the one hand, one electrode is wirebonded to a microwave dipole antenna which is located inside the cavity. In turn, the dipole antenna can receive the signals from a microwave electric field that is built up inside the cavity due to the resonance condition. On the other hand, the mechanical motion of the dielectric SiN string resonator periodically modulates the capacitance of the electrodes, generating sidebands in the microwave cavity response similar to cavity optomechanics. In the following, we explain the mechanism of the sidebands generation using a lumped-element circuit picture rather than the standard framework of cavity optomechanics [90]. This model conveniently describes the frequency modulation of the cavity resonance [142].

As illustrated in Fig. 3.1, the motion of the nanomechanical system temporarily modulates the capacitance of the tank circuit. Then the modulated resonance frequency is

$$\omega_{\mathrm{c}}(t) = \frac{1}{\sqrt{LC}} = \frac{1}{\sqrt{LC_s(1+\delta C_{\mathrm{m}}(t)/C_{\mathrm{s}})}} \approx \widetilde{\omega}_{\mathrm{s}}\left(1 - \frac{\delta C_{\mathrm{m}}(t)}{2C_{\mathrm{s}}}\right). \tag{3.1}$$

Here, $\widetilde{\omega}_{\mathrm{s}} = \sqrt{LC_{\mathrm{s}}}$ is the unmodulated resonance frequency that results from the static part of the capacitance $C_{\mathrm{s}} = C_{\mathrm{Ant}} + C_0$. For the expression on the right hand side of Eq. (3.1), we use the series

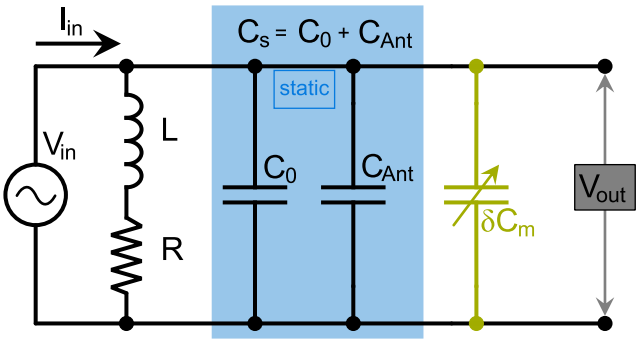

Figure 3.1 | Frequency Modulation of Cavity Resonance.
Simple tank circuit model that explains sidebands generation via capacitive coupling of a mechanical resonator to LCR-circuit. The capacitance of the tank circuit can be divided to static part, that consists of the circuit's intrinsic capacitance C_0 and the coupling capacitance via antenna C_{Ant}. The dynamical part $\delta C_{\mathrm{m}}(t)$ represents the demodulation via mechanical element.

expansion, since the relation $\delta C_{\mathrm{m}} \ll C_{\mathrm{s}}$ is generally valid in our system. The time-dependent part for the mechanical motion along x-direction is

$$\delta C_{\mathrm{m}}(t) = \frac{\partial C_{\mathrm{m}}}{\partial x} x(t) = C_{\mathrm{m}}^{'} x_{\mathrm{m}} \cos(\Omega_m t). \tag{3.2}$$

With C_{m} the capacitance of the gold electrodes, x_{m} is displacement amplitude of the mechanical resonator and Ω_{m} is the mechanical resonance frequency. The instantaneous frequency from Eq. (3.1) then takes the form

$$\omega_{\mathrm{c}}(t) \approx \widetilde{\omega}_{\mathrm{s}} \left(1 - \frac{C_{\mathrm{m}}^{'} x_{\mathrm{m}} \cos(\Omega_m t)}{2C_{\mathrm{s}}}\right) = \widetilde{\omega}_{\mathrm{s}} - \frac{C_{\mathrm{m}}^{'} x_{\mathrm{m}} \widetilde{\omega}_{\mathrm{s}}}{2C_{\mathrm{s}}} \cos(\Omega_m t). \tag{3.3}$$

The corresponding phase can be calculated by the integral

$$\begin{aligned} \phi(t) &\approx \int \left(\widetilde{\omega}_{\mathrm{s}} - \frac{C_{\mathrm{m}}^{'} x_{\mathrm{m}} \widetilde{\omega}_{\mathrm{s}}}{2C_{\mathrm{s}}} \cos(\Omega_{\mathrm{m}} t)\right) \mathrm{d}t \\ &= \widetilde{\omega}_{\mathrm{s}} t + \frac{C_{\mathrm{m}}^{'} x_{\mathrm{m}} \widetilde{\omega}_{\mathrm{s}}}{2C_{\mathrm{s}} \Omega_{\mathrm{m}}} \sin(\Omega_{\mathrm{m}} t) + \phi_0 \\ &= \widetilde{\omega}_{\mathrm{s}} t + \mathcal{A}(x_{\mathrm{m}}) \sin(\Omega_{\mathrm{m}} t) + \phi_0, \end{aligned} \tag{3.4}$$

where ϕ_0 is the initial phase of the system and the amplitude

$$\mathcal{A}(x_{\mathrm{m}}) = \frac{C_{\mathrm{m}}^{'} x_{\mathrm{m}} \widetilde{\omega}_{\mathrm{s}}}{2C_{\mathrm{s}} \Omega_{\mathrm{m}}}. \tag{3.5}$$

If the drive frequency is close enough to cavity resonance, we can write the output voltage of the tank circuit as

$$V_{\mathrm{out}}(t) \approx I_{\mathrm{in}} Q R \cos(\phi(t)) = I_{\mathrm{in}} Q R \cos[\widetilde{\omega}_{\mathrm{s}} t + \mathcal{A} \sin(\Omega_{\mathrm{m}} t) + \phi_0]. \tag{3.6}$$

The expression for the output voltage from Eq. (3.6) is well-known in the frequency modulation analysis, where a cosine wave signal with the carrier frequency $\widetilde{\omega}_{\mathrm{s}}$ is modulated by a sine function with frequency Ω_{m}. In this case the expression can be expanded using Bessel functions identity [143]

$$V_{\mathrm{out}}(t) = I_{\mathrm{in}} Q R \sum_{n=-\infty}^{\infty} J_n(\mathcal{A}) \cos[(\widetilde{\omega}_{\mathrm{s}} + n\Omega_{\mathrm{m}})t], \tag{3.7}$$

where $J_n(\mathcal{A})$ is the n^{th} Bessel function. We can write the first few terms for the cavity's output voltage

$$V_{\text{out}}(t) = I_{\text{in}} Q R \{ \underbrace{J_0(\mathcal{A}) \cos(\widetilde{\omega}_{\text{s}} t)}_{\text{cavity resonance}} + \underbrace{J_{-1}(\mathcal{A}) \cos[(\widetilde{\omega}_{\text{s}} - \Omega_{\text{m}})t]}_{1^{\text{st}} \text{ red sideband}} + \underbrace{J_{+1}(\mathcal{A}) \cos[(\widetilde{\omega}_{\text{s}} + \Omega_{\text{m}})t]}_{1^{\text{st}} \text{ blue sideband}} + \dots \}. \quad (3.8)$$

Here, Eq. (3.8) describes the cavity output with the pure cavity and the first sideband terms. In the absence of the mechanical resonator or for small displacement $\mathcal{A}(x_{\text{m}}) = 0$, all sidebands vanish and $J_0(0) = 1$, where only the cavity resonance persists. The modulation of the mechanical resonator creates a time-varying capacitance $\delta C_{\text{m}}(t)$. This serves to frequency modulate the microwave cavity resonance and create new susceptibilities that are multiples of the mechanical frequency above and below the uncoupled cavity resonance $\omega = \widetilde{\omega}_{\text{s}} \pm n\Omega_{\text{m}}$. Typically, only $n = 1$ is taken into account. So the observation of the microwave cavity's response will give us direct access to the mechanical properties.

3.1.2 Heterodyne IQ-Mixing Technique

In previous works, the mechanical motion detection was conducted using a co-planar $\lambda/4$ waveguide resonator [56, 63, 70, 130], which exhibits broad cavity linewidth of $\approx 36\,\text{MHz}$. The mechanical resonators, in turn, are designed to operate mostly from $5\,\text{MHz} - 10\,\text{MHz}$. Hence, the system is in the unresolved sideband regime and it is not possible to observe the mechanical response which is overlapped with the cavity spectrum in gigahertz regime. Additionally, in experiments that are performed by my colleague J. Ochs to explore nonlinearity effects of the nanomechanical resonators such as thermal squeezing [144], resonant amplification and absorption [145] and broken symmetry in the resonant nonlinear response [146], require the lock-in amplifier[1] that operates mainly in the megahertz range. Devices with the same functionalities in gigahertz range will become more cost-intensive and is much more difficult to control due to the large bandwidths that require fast electronics. For these reasons, the motions of the nanomechanical string resonators are detected with the heterodyne in-phase quadrature (IQ) mixing technique to down convert the sidebands from gigahertz to megahertz regime. Figure 3.2 shows the schematic of the heterodyne down-conversion procedure. A microwave tone from a signal generator[2] is applied to the single port of the cylindrical microwave 3D cavity. The input microwave signal is then phase-modulated due to the interaction with the mechanical resonator as discussed above. By using a microwave circulator[3], we can separate the input and output microwave signals. These microwave circulators (also isolators) are nonreciprocal devices that only allow the signal to propagate in one direction and protect the microwave source and the 3D cavity from back reflection. The output and demodulated cavity signal is then fed into an in-phase quadrature (IQ) mixer[4] together with a local oscillator (LO) of the very same microwave source. Let us first recall the trigonometric identity

$$\cos(A)\cos(B) = \frac{1}{2}(\cos(A+B) + \cos(A-B)). \quad (3.9)$$

By mixing the two signals

$$\cos(\omega_{\text{RF}} + \varphi) \cdot \cos(\omega_{\text{LO}}) = \frac{1}{2}[\cos(\omega_{\text{RF}} + \omega_{\text{LO}} + \varphi) + \cos(\omega_{\text{RF}} - \omega_{\text{LO}} + \varphi)], \quad (3.10)$$

[1] Zurich Instrument lock-in amplifier HF2LI
[2] Rohde&Schwarz SMA 100 A
[3] MCLI CS-19 4-8 GHz
[4] Marki Microwave IQ-0307 LXP

we will get a high frequency component $\omega_+ = \omega_{RF} + \omega_{LO} + \varphi$ and a low frequency component $\omega_{IF} = \omega_{RF} - \omega_{LO} + \varphi$. Here, ω_{RF} is the carrier frequency that contains the mechanical modulation with the phase shift φ and ω_{LO} is the frequency of a continuous local oscillator coming from the same microwave source. In the worst case scenario, the cavity phase modulation becomes $\varphi = \omega_{LO} - \omega_{RF} + \pi/2$ causing destructive interference of the two mixed signals. To overcome this phase dependent procedure, we use the before mentioned double-balanced IQ-mixer that consists of two hybrids (0°/0°) and (0°/90°) power splitter as well as two mixers (see Fig. 3.2). At the output of the mixer we will obtain the time-dependent in-phase and quadrature of the high frequency part $\mathcal{I}_+(t)$, $\mathcal{Q}_+(t)$ and the low intermediate frequency (IF) part $\mathcal{I}_{IF}(t)$ and $\mathcal{Q}_{IF^*}(t)$ with a well-defined 90° phase shift to each other

$$\mathcal{I}_{IF}(t) = \mathcal{A}(t)\cos\left(\omega_{IF} + \varphi(t)\right) \tag{3.11}$$

$$\mathcal{Q}_{IF^*}(t) = \mathcal{A}(t)\sin\left(\omega_{IF} + \varphi(t)\right). \tag{3.12}$$

So Eqs. (3.11) and (3.12) show that one of the output after the IQ-mixer is always non-zero and independent of the phase difference of the two input signals. The two demodulated quadrature components are then combined using another (0°/90°) power combiner/splitter[5]. Hence, the combined output signal is

$$\mathcal{S}(t) = \sqrt{\mathcal{I}_{IF}^2(t) + \mathcal{Q}_{IF^*}^2(t)}. \tag{3.13}$$

Depending on the phase of the two input signals from Eqs. (3.11) and (3.12), there is at least one of these signals that is non-zero. Thus, the sum of the two signal is completely independent of the phase relation of the two input signals and this helps us to avoid readjustments of the phase after each measurement. The combined output signal is subsequently low-pass[6] and high-pass[7] filtered to get rid of the high frequency component ω_+ and to reduce the noise contributions. The filtering procedure allows us to conduct measurements in a frequency window from 120 kHz to 81 MHz. This range is suitable to observe the mechanical oscillation since the eigenfrequency of the string resonator operates in megahertz regime. The signal is then amplified[8] and fed to the network analyzer[9] to reconstruct the amplitude and phase response of the mechanical signal in the dielectric driven measurement that will be discussed in the next section.

[5]Mini-Circuits JSPQ-65W+
[6]Mini-Circuits VLFX-80+
[7]Mini-Circuits ZFHP-0R75+
[8]MITEQ AU-1464-R Amplifier +35 dB
[9]Rohde & Schwarz ZNB 8

3.2 Dielectrical Actuation

One of the most efficient and highly integrable way to locally actuate nanomechanical resonator, is the capacitive actuation scheme. However, the major limitation of this system is the large dissipation due to the dominant loss mechanism of the metal layer deposited on the surface of the resonator [134, 147]. To overcome the strong metallic induced damping, the system needs to operate at low temperature environment and the thin metallic film needs to become superconductor [139, 148]. Since we want to conduct experiments at room temperature, we need to come up with an alternative transduction scheme. To this end, Q. Unterreithmeier et al. introduced an universal transduction scheme for the nanomechanical resonators based on dielectric interactions [70]. When a polarizable material is placed in an inhomogeneous electric field, it experiences an attractive force towards the maximum field strength. So the two electrodes flanking the polarizable dielectric SiN string resonator (see Fig. 2.26) can be utilized for both coupling to the microwave cavity, and at the same time for dielectrical transduction. The static voltage applied to the adjacent electrodes by a DC voltage source generates a strong, confined electric field, which in turn causes a change in the charge distribution in the dielectric silicon nitride string resonator. This voltage induced polarization can be approximated by an electric dipole that aligns along the field gradient and hence, exerts an electrostatic gradient force on the resonator. To this end, the resonator is pulled towards one of the electrodes, bringing it out of its equilibrium position. This leads directly to a change in the restoring force and thus, to a change in the resonant frequency of the respective string resonator. We will discuss the frequency tuning behaviour in more detail in Sec. 5.1.2. In addition to the DC voltage, we can further apply a weak periodic RF drive voltage $U_{\mathrm{RF}} = U_{\mathrm{d}} \cos(\omega_{\mathrm{d}} t)$ generating a periodic force [70]

$$F[U_{\mathrm{DC}} + U_{\mathrm{RF}}] \propto (U_{\mathrm{DC}} + U_{\mathrm{RF}})^2 \approx U_{\mathrm{DC}}^2 + 2V_{\mathrm{DC}} U_{\mathrm{d}} \cos(\omega_{\mathrm{d}} t), \tag{3.14}$$

that periodically drives the voltage-induced dipole, thus, actuating the nanomechanical string resonator at the drive frequency ω_{d}. Beside U_{DC} and U_{RF}, the microwave term $U_{\mu w}$ originated from the microwave 3D cavity the can contribute to the dielectric tuning effects (see discussion in Sec. 3.3.2). Note that we have neglected the quadratic term V_{RF}^2 that describes the resonator's actuation at twice the drive frequency. Due to small drive amplitude, the contribution of this term remains relatively small. The effect of the quadratic term may become pronounced in experiments exploring the resonators nonlinearity. We illustrate the dielectrical actuation scheme in Fig. 3.2, where the DC source and the RF drive from the network analyzer are combined with a bias tee[10] and applied to the electrodes via a single layer capacitor[11] (SLC). At the same time the SLC serves as a ground potential for the microwave cavity establishing a microwave bypass.

3.3 Sideband-Resolved Cavity Electromechanical System

The main motivation for this work, in which we replace the coplanar microstrip resonator with 3D cavity architectures, is to improve the quality factor of the microwave cavity. In previous works [95, 130], coplanar waveguide resonators used for cavity-assisted detection are imprinted on printed circuit boards (PCB), where the power dissipation is significant due to the dielectric material of the PCB. Hence, the linewidth (κ) of such cavities typically exceed the resonance frequency (Ω_{m}) of the mechanical resonator and mitigate the optomechanical coupling and detection sensitivity. 3D microwave cavities structures, on the other hand, offer strong confined electric and magnetic field distributions that are enclosed by the cavity walls and hence, the radiation loss is reduced substantially. At room temperature,

[10] Mini Circuits ZFBT-6 GW+
[11] JOHANSON TECHNOLOGY SLC Microwave Capacitor U70, 1800 pF

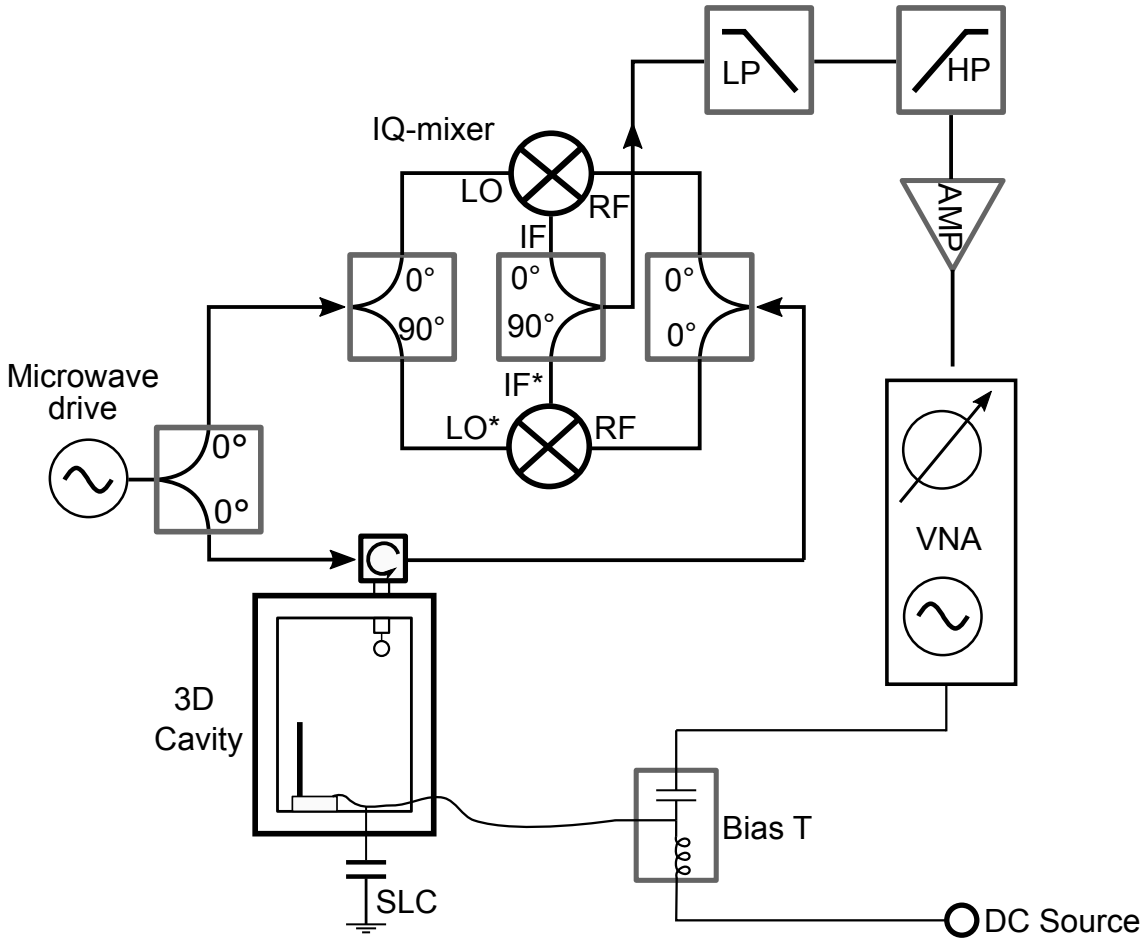

Figure 3.2 | Electrical Schematic for Mechanical Actuation and Detection.
Cavity-assisted displacement sensing and dielectrical actuation of nanomechanical silicon nitride string resonators. A microwave pump tone is applied to the cavity single port via a circulator that separates the input and output signal. A single layer capacitor (SLC) provides a ground path for the microwave signal and at the same time enables RF drive (supplied by the vector network analyzer (VNA)) and the control of the inhomogeneous electrical field between the two gold electrodes by a DC source. Both signals are combined using a bias tee. The mechanical detection is realized via a microwave loop antenna which is bonded to one of the electrodes to inductively couple to one of the cavity resonance's mode. At the same time, the mechanical motions periodically modulate the capacitance $C_{\mathrm{m}}(t)$ of the two electrodes, generating sidebands in the microwave cavity signal due to the loop antenna coupling. The electromechanically modulated cavity reflected signal from the single port is then fed into an IQ-mixer with a reference signal (LO) for the frequency down-conversion. The output intermediate 90° phased-shifted frequencies IF and IF* are merged with a $(0°/90°)$ power combiner and subsequently low-, high-pass (LP, HP) filtered and amplified (AMP) before feeding the signal back into the VNA.

the main loss mechanism for these types of geometry is conduction loss. Nevertheless, the quality factor of a 3D cavity can exceed that of a microstrip cavity by a few orders of magnitude. As a result, the optomechanical coupling and detection efficiency are improved. The high quality factor, thus, enable the operation in the sideband-resolved limit, where the cavity photon lifetime exceeds the mechanical oscillation period [149–151] ($\kappa < \Omega_{\mathrm{m}}$). In this regime, the injected photons can remain trapped inside the cavity for many oscillation periods where it is more likely to interact with the mechanical element.

3.3.1 Room Temperature Cavity-Assisted Detection

Figure 3.3 (a) depicts a photograph of the cylindrical cavity. It consists of two parts which have been machined from bulk copper (Cu > 99 %) and which can be closed using screws. The cavity has a radius of 35 mm and a height of 70 mm, it supports both transverse electric (TE) and transverse magnetic (TM) modes (see Sec. 2.3). As the modes reside in the hollow cylinder, they are slightly affected by dielectric and conductor losses, which enables high quality factor even at room temperature [106]. The coupling to the cavity is realized by injecting the microwave signal from a coaxial line through a loop coupler via a 3.6 mm sized hole in the cavity top [see Fig. 3.3 (a) and (c)]. In all our measurements, we use a circulator to physically separate the input and output signals of the single port reflection cavity and to avoid back reflections and interference effects. Figure 3.3 (b) (left) displays the reflection coefficient $|S_{11}|$ of the TM_{110} mode which is found at $\omega_c/(2\pi) \approx 5.147\,\mathrm{GHz}$ with a linewidth of $\kappa/(2\pi) = 2.824\,\mathrm{MHz}$ for the empty cavity, in good agreement with finite element simulations (now shown here). This corresponds to a cavity quality factor of 1.800, exceeding the state of the art in microwave-cavity-assisted nanomechanical displacement sensing at room temperature by more than an order of magnitude [56]. The nanomechanical resonator under investigation is a strongly pre-stressed nanostring fabricated from LPCVD silicon nitride on a fused silica wafer, which is flanked by two gold electrodes for dielectric transduction (see Sec. 2.4). The reflection coefficient of the same mode of the cavity including the resonator chip is shown in Fig. 3.3 (b) (right). Upon insertion of the resonator, the eigenfrequency of the TM_{110} mode shifts to $\omega_{\mathrm{c}}/(2\pi) = 5.226\,\mathrm{GHz}$. The linewidth increases by a factor of 2 to $\kappa/(2\pi) = 5.572\,\mathrm{MHz}$.

We use the circle fit technique discussed in Sec. 2.3.6 to fit of the amplitude and phase of the cavity's reflection coefficient. The fit reveals an external dissipation rate of $\kappa_e/(2\pi) = 1.361\,\mathrm{MHz}$. This leads to a coupling efficiency $\eta = \kappa_e/\kappa = 0.244$, indicating that the cavity is undercoupled. Figure 3.3 (c) shows the physical realization of the cavity electromechanical system. The sample holder with the resonator chip is placed inside the cavity. One of the electrodes is connected to an antenna to inductively couple to the TM_{110} of the cavity. It consists of a looped silver wire on top of a coaxial cable which places the loop into the electromagnetic field near the center of the hollow cylinder. The other electrode is bonded across a single layer capacitor acting as capacitive ground [130] and connected to an RF signal generator through a 1.5 mm wide hole in the cavity wall for dielectric actuation of the resonator [152–157]. The nanostring under investigation is $w = 250\,\mathrm{nm}$ wide, $t = 100\,\mathrm{nm}$ thick and $L = 57\,\mu\mathrm{m}$ long, similar to the one depicted in Fig. 3.3 (d).

While the cavity characterization is done under ambient conditions, the experiments discussed in the following involve the vibrational excitation of the nanostring and air damping needs to be excluded. Hence, the entire cavity electromechanical system consisting of the string resonator as well as the microwave cavity is placed inside a vacuum chamber below $5 \times 10^{-4}\,\mathrm{mbar}$. As indicated above, all measurements are performed at room temperature. The nanomechanical resonator is characterized by dielectrically driving its fundamental out-of-plane mode with a vector network analyzer (VNA). The response of the nanomechanical resonator is characterized using heterodyne cavity-assisted displacement detection discussed in Sec. 3.2 using the 3D microwave cavity. The microwave cavity is driven

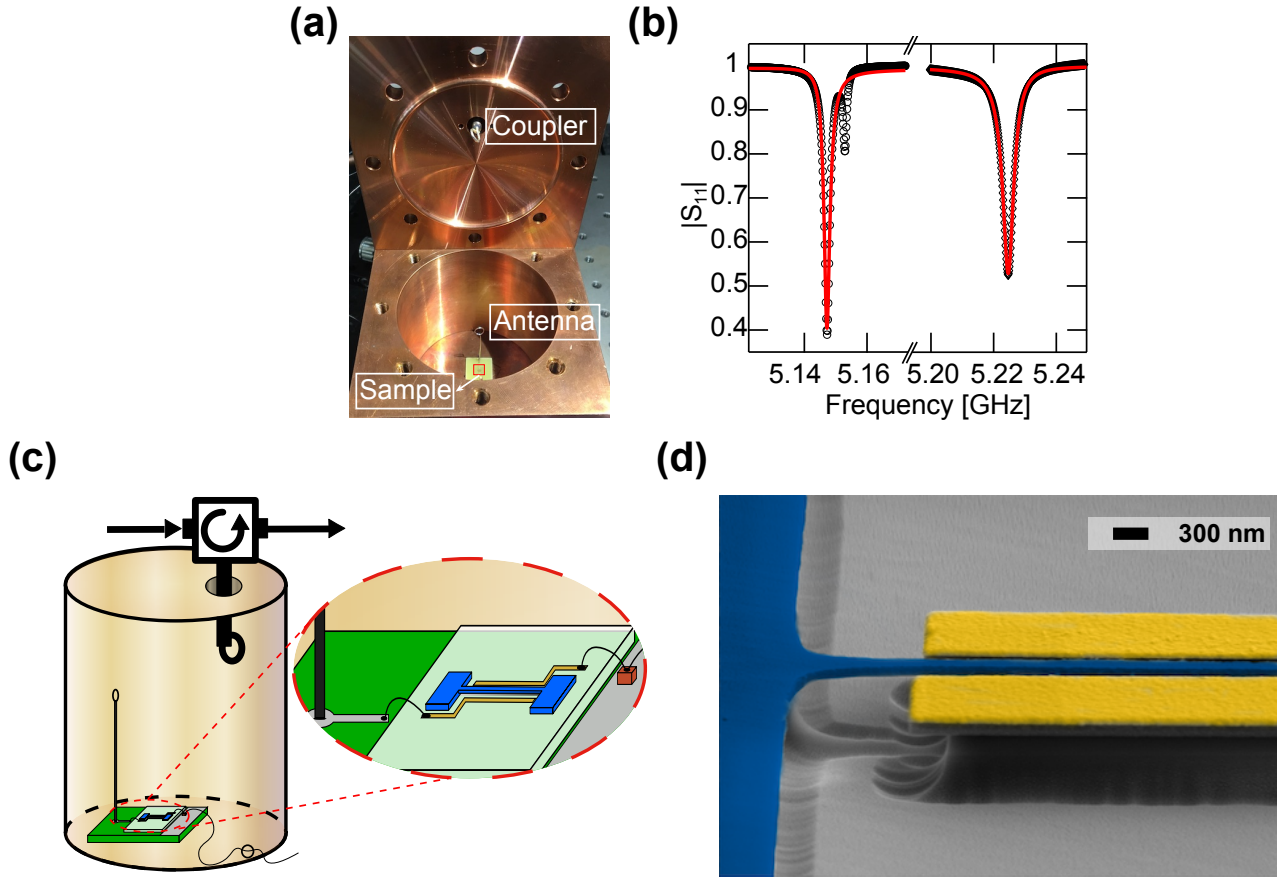

Figure 3.3 | Experimental Setup for Room Temperature Cavity Electromechanics.
(a), Photograph of the (open) cylindrical microwave 3D cavity machined from bulk copper. The microwave signal is inductively injected into the cavity via a loop coupler. The sample holder including the antenna is visible on the cavity floor. **(b)**, Reflection coefficient $|S_{11}|$ of the TM_{110} mode (black) along with fit to the data (red), showing the response of both the empty cavity (left) and the cavity including the sample (right). Upon insertion of the sample the frequency of the TM_{110} mode shifts by $\sim 80\,\mathrm{MHz}$. The second dip in the cavity response (left) belongs to the TE_{112} mode (see Fig. 2.11). Furthermore, an increase of the linewidth by a factor of 2 is observed. **(c)**, Schematic visualizing the physical implementation of the cavity electromechanical system. The doubly clamped silicon nitride string resonator (blue) is situated between two elevated gold electrodes (yellow). The resonator chip (light green) is glued to a printed circuit board (green) and placed inside the cavity (beige). The circuit board also hosts a looped dipole antenna which is bonded to one of the electrodes to inductively couple to the TM_{110} mode. The other electrode is connected to a single layer capacitor (brown) which serves as a capacitive ground for frequencies in the microwave frequency range, and to a wire which is fed through a hole in the cavity wall. This allows to apply DC voltages and RF signals to dielectrically drive the resonator inside the cavity. **(d)**, Scanning electron micrograph of a doubly clamped pre-stressed nanomechanical resonator between two gold electrodes for dielectric actuation as well as coupling to the three-dimensional microwave cavity. **Adapted and reprinted from Ref. [107], with the permission of AIP Publishing.**

exactly on resonance $\omega_d = \omega_c$, such that the periodic modulation of the capacitance induced by the dielectric nanostring vibrating between the two electrodes induces sidebands at $\omega_c \pm \Omega_m$ on the cavity response. The reflected signal of the cavity is demodulated by an in-phase quadrature (IQ) mixer, filtered and amplified as previously described in Sec. 3.2. The resulting signal is fed back into the VNA. The response of the fundamental out-of-plane mode of the resonator is displayed in Fig. 3.4.

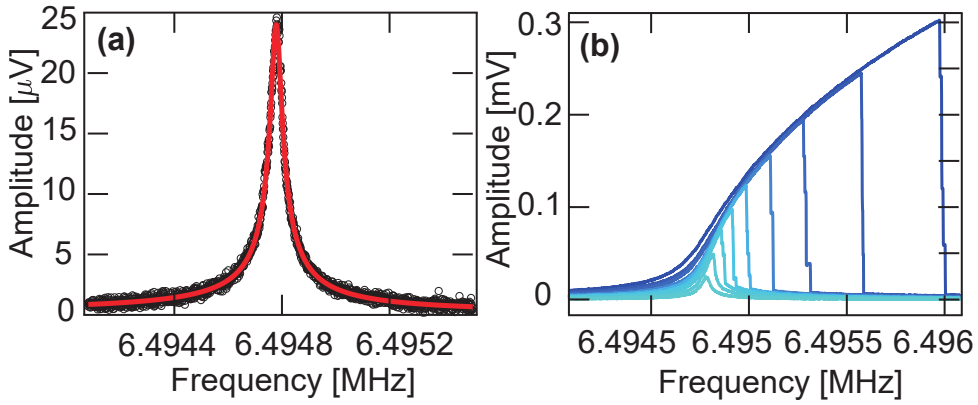

Figure 3.4 | Characterization of the nanostring resonator.
(a), Linear response of the fundamental out-of-plane mode of the nanostring (black) and Lorentzian fit (red) for a drive power of $P_m = -36\,\mathrm{dBm}$. **(b)**, Response of the nanostring by increasing drive power from $P_m = -36\,\mathrm{dBm}$ to $-14\,\mathrm{dBm}$ showing the transition to the nonlinear Duffing regime. **Adapted and reprinted from Ref. [107], with the permission of AIP Publishing.**

Figure 3.4 (a) shows the Lorentzian resonance curve observed in the linear response regime for a drive power $P_m = -36\,\mathrm{dBm}$. Fitting allows to extract the resonance frequency $\Omega_m/(2\pi) = 6.494\,8\,\mathrm{MHz}$, as well as a linewidth $\Gamma/(2\pi) = 42\,\mathrm{Hz}$ which gives rise to a quality factor of $Q \approx 150.000$. Given the cavity linewidth $\kappa/(2\pi) = 5.572\,\mathrm{MHz}$ the condition for sideband resolution, $\Omega_m > \kappa$, is fulfilled for the TM_{110} mode. The sweep response of the resonator toward higher frequencies for increasing drive power between $-36\,\mathrm{dBm}$ to $-14\,\mathrm{dBm}$ is depicted in Fig. 3.4 (b). Clearly, the transition from the linear, Lorentzian response to an asymmetric response curve, which is well described by the cubic nonlinearity αx^3 of the Duffing model with a stiffening $\alpha > 0$, is observed [158]. This demonstrates that the cavity-assisted displacement detection is not impeded even under strong driving of the nanomechanical resonator inside the 3D cavity.

3.3.2 Dielectrical and Optomechanical Backaction

Following the characterization of the microwave cavity and the nanomechanical resonator, we discuss the electromechanical coupling between the two systems. Here, we explore how the cavity detuning affects the mechanical eigenfrequency of the resonator.

Optomechanical Backaction The radiation pressure of the power circulating in the microwave cavity acts back on the mechanical resonator, causing a mechanical eigenfrequency shift which depends on the microwave drive power P_d and detuning $\Delta = \omega_d - \omega_c$. This so-called optical spring effect leads to a detuning-dependent softening or hardening of the resonator. In case of a high-Q mechanical oscillator with small linewidth, where $\Gamma \ll \kappa$, the frequency shift of the mechanical oscillator is given by [159]

$$\delta\Omega_{m,\mathrm{opt}} = g^2\left(\frac{\Delta-\Omega_m}{\frac{\kappa^2}{4}+(\Delta-\Omega_m)^2}+\frac{\Delta+\Omega_m}{\frac{\kappa^2}{4}+(\Delta+\Omega_m)^2}\right). \tag{3.15}$$

which is valid for $g \ll \kappa \ll \Gamma$. Here, $g = g_0 \cdot \sqrt{n_d}$, the electromechanical coupling strength which depends on the single photon coupling strength g_0 and the number of photons n_d circulating in the cavity. In order to define the intra-cavity photon number we need to distinguish between two cases.

Following Eq. (E45) in the Supplementary of Clerk et al. [160] the input power for single-side driven cavity can be defined as

$$P_d = \hbar\omega_d\frac{\kappa_e}{4}\cdot\bar{n}_d \tag{3.16}$$

The driven single-sided intra-cavity photon number is found to be [102]

$$\bar{n}_d = \frac{P_d}{\hbar\omega_d}\cdot\frac{\kappa_e}{\frac{\kappa^2}{4}+\Delta^2} \tag{3.17}$$

In the case of a driven two-sided cavity, where the incoming power can be sent either through the left or the right port $\kappa_e = \kappa_L + \kappa_R$, we can relate the incoming power with the photon number (i.e for the left input port)

$$P_d = \hbar\omega_d\frac{\kappa_e^2}{4\kappa_L}\cdot\bar{n}_d \tag{3.18}$$

Assuming symmetric coupling $\kappa_e = \kappa_L + \kappa_R$ we can re-write Eq. (3.18)

$$P_d = \hbar\omega_d\frac{\kappa_e}{2}\cdot\bar{n}_d \tag{3.19}$$

Hence, the driven two-side intra-cavity photon number is defined as [56, 92]

$$\bar{n}_d = \frac{2\cdot P_d}{\hbar\omega_d}\cdot\frac{\kappa_e}{\kappa^2+4\Delta^2} \tag{3.20}$$

In this work, we will use Eq. (3.17) to calculate the intra-cavity photon number since the input power is sent into a single port.

Note that the number of intra-cavity photons strongly depend on the drive power P_d *and* the cavity detuning $\Delta = \omega_d - \omega_c$. The presence of an average radiation pressure inside the cavity causes static shift in the mechanical displacement that, in turn, modifies the resonance frequency of the cavity leading to a new *effective* detuning [90, 161]

$$\bar{\Delta} = \Delta + \frac{g_0}{x_{\mathrm{ZPF}}}\bar{x}, \tag{3.21}$$

where $x_{\mathrm{ZPF}} = \sqrt{\frac{\hbar}{m_{\mathrm{eff}}\Omega_{\mathrm{m}}}}$ is the zero-point fluctuation amplitude of the mechanical oscillator and $\bar{x}$ is the static mechanical displacement. In our case, the static mechanical displacement of the resonator arising from the radiation pressure force is negligibly small, hence, the detuning Δ is employed rather than the effective detuning $\bar{\Delta}$ in Eq. (3.15).

Dielectrical Frequency Tuning In addition to the optomechanical backaction, we also expect a quasi-static dielectric force acting on the mechanical resonator. This force results from the root-mean-square (RMS) electrical field which builds up inside the microwave cavity and contributes to the dielectric frequency tuning (see discussion in Sec. 3.2) of the nanostring [130]. The RMS cavity field exhibits the same detuning-dependence as the intracavity photon number $\bar{n}_d$ defined in Eq. (3.17). This translates into a change in eigenfrequency of the mechanical oscillator as the cavity is detuned from its resonance. We will start the derivation of the dielectrical frequency tuning by defining the electrostatic energy of an induced dipole at position $\boldsymbol{r}_0$ in an electrical field. That is

$$W_{el} = -\frac{1}{2}\boldsymbol{p}\boldsymbol{E}(\boldsymbol{r}_0) = -\frac{1}{2}\alpha E^2(r_0) \tag{3.22}$$

with the polarizability of the dielectric material α. Now, consider only the $z-$component (for the mechanical OOP mode) of the electric field (or alternatively only $y-$component for the IP mode) that can be treated as a scalar. For small displacement z around the equilibrium position z_0 (which is valid in our case, because the displacement is $\sim$ fm). We can use the Taylor expansion

$$E(z_0+z) = \underbrace{E(z_0)}_{E_0} + \underbrace{\frac{\partial E}{\partial z}\bigg|_{z_0}}_{E_1}\cdot z + \underbrace{\frac{1}{2}\frac{\partial^2 E}{\partial^2 z^2}\bigg|_{z_0}}_{E_2}\cdot z^2 + O(z)^n \tag{3.23}$$

to express the electrostatic energy

$$\begin{aligned} W_{\mathrm{el}} &\approx -\frac{\alpha}{2}\Big(E_0 + E_1 z + E_2 z^2\Big)^2 \\ &= -\frac{\alpha}{2}\Big(E_0^2 + 2E_0E_1 z + 2E_0E_2 z^2 + E_1^2 z^2 + 2E_1E_2 z^3 + E_2^2 z^4\Big). \end{aligned} \tag{3.24}$$

The force acting in the $z-$direction is defined as

$$\begin{aligned} F &= -\frac{\partial W_{\mathrm{el}}}{\partial z} \\ &= +\frac{\alpha}{2}\Big(2E_0E_1 + \Big(4E_0E_2 + 2E_1^2\Big)z + 6E_1E_2z^2 + 4E_2^2z^3\Big). \end{aligned} \tag{3.25}$$

And hence,

$$F = \underbrace{\alpha E_0E_1}_{\text{constant offset}} + \underbrace{\alpha\Big(2E_0E_2 + E_1^2\Big)z}_{\text{dielectrical induced spring constant}} + \underbrace{3E_1E_2z^2 + 2E_2^2z^3}_{\text{dielectrical induced higher nonlinear terms}} . \tag{3.26}$$

Now consider the contribution of DC, RF and microwave signals. Assuming $E_2 = 0$ as linearized description. The dielectric force can be rewritten as

$$F = \alpha E_0E_1 + \alpha E_1^2 z \tag{3.27}$$

where $E_0 = E(z_0)$ and $E_1 = \frac{\partial E}{\partial z}\Big|_{z_0}$ as defined above.
The eigenfrequency of the resonator is determined by its spring constant

$$k = -\frac{\partial F}{\partial z} = -\alpha E_1^2 \tag{3.28}$$

$$\Omega_{m,\text{dielectric}} = \sqrt{\frac{k_0 + k}{m_{\text{eff}}}} = \sqrt{\frac{k_0}{m_{\text{eff}}}} \cdot \sqrt{1 + \frac{k}{k_0}} \underbrace{\approx}_{\text{for } k \ll k_0} \sqrt{\frac{k_0}{m_{\text{eff}}}} \cdot \left(1 + \frac{k}{2k_0}\right) = \Omega_m - \frac{\alpha E_1^2}{2m_{\text{eff}}\Omega_m} \tag{3.29}$$

The electric field and also its derivatives are expressed in terms of voltage applied between the electrodes. Assuming the resonator only reacts to the static component of the applied voltage

$$\boldsymbol{E}(z) \sim U, \tag{3.30}$$
$$\langle \boldsymbol{E}(z) \rangle \sim U_{\text{DC}} + U_{\text{RF}}^{\text{rms}} + U_{\mu w}^{\text{rms}}, \tag{3.31}$$

and accordingly

$$\langle \boldsymbol{E_1}(z) \rangle \sim U_{\text{DC}} + U_{\text{RF}}^{\text{rms}} + U_{\mu w}^{\text{rms}}. \tag{3.32}$$

The same is applied for all other derivatives of the electric field. The eigenfrequency shifts can be expressed as

$$\delta\Omega_{m,\text{dielectric}} = \Omega_{m,\text{dielectric}} - \Omega_m = -\frac{\alpha E_1^2}{2m_{\text{eff}}\Omega_m} = -\frac{\alpha}{2m_{\text{eff}}\Omega_m} \cdot \left(U_{\text{DC}} + U_{\text{RF}}^{\text{rms}} + U_{\mu w}^{\text{rms}}\right)^2. \tag{3.33}$$

Generally, we assume $U_{\text{DC}} > U_{\mu w}^{\text{rms}} > U_{\text{RF}}^{\text{rms}}$. In our experiment the static field U_{DC} is mainly used for large mechanical eigenfrequency tuning $\delta\Omega_{m,\text{dielectric}}/(2\pi) \approx 200\,\text{kHz}$. The term $U_{\mu w}^{\text{rms}}$ is the field built up inside the 3D microwave cavity. Its strength depends on the pump power and detuning of the cavity. Typically, the mechanical resonance eigenfrequency shift induced by the rms microwave field is one order of magnitude smaller $\delta\Omega_{m,\text{dielectric}}/(2\pi) \approx 20\,\text{kHz}$ if compared to the static DC frequency tuning. And finally, the RF drive field $U_{\text{RF}}^{\text{rms}}$ is employed for amplifying the resonator's amplitude and, if necessary, brings the system into the nonlinear regime. The contribution in the eigenfrequency tuning of the RF drive field is negligible small compared to the other two effects. Now, we only consider the effect of the microwave cavity where $U_{\text{DC}} = 0$ and $U_{\text{RF}}^{\text{rms}} = 0$

$$\delta\Omega_{m,\text{dielectric}} = c_{\mu w} \cdot \left(U_{\mu w}^{\text{rms}}\right)^2 \tag{3.34}$$

where $c_{\mu w} = -\frac{\alpha}{2m_{\text{eff}}\Omega_m}$. Hence, the dielectrical frequency detuning induced by the microwave cavity pump tone can be defined as

$$\delta\Omega_{m,\text{dielectric}} = c_{\mu w} R \cdot P_d = c_{\mu w} R\hbar\omega_d \kappa \cdot \bar{n}_d = c_{\mu w} R\hbar\omega_d \kappa \cdot \frac{\kappa_e}{\frac{\kappa^2}{4} + \Delta^2} \cdot \frac{P_d}{\hbar\omega_d}. \tag{3.35}$$

And finally we get the expression

$$\delta\Omega_{m,\text{dielectric}} = c_{\mu w} \cdot \left(U_{\mu w}^{\text{rms}}(\Delta)\right)^2 = c_{\mu w} R \frac{\kappa\kappa_e}{\frac{\kappa^2}{4} + \Delta^2} P_d. \tag{3.36}$$

The calibration factor $c_{\mu w}$ converts the change of the effective RMS voltage $U_{\mu w}^{\text{rms}}$ inside the cavity into a frequency change, and $R = 50\,\Omega$ is the impedance of the circuit, which allows to express the RMS voltage in terms of the power circulating in the cavity. In total, the detuning dependence of the mechanical resonance is

$$\Omega_m' = \Omega_m + \delta\Omega_{m,\text{dielectric}} + \delta\Omega_{m,\text{opt}}, \tag{3.37}$$

where Ω_m is the unperturbed mechanical eigenfrequency, $\delta\Omega_{m,\text{dielectric}}$ is the frequency tuning due to the quasi-static dielectric force and $\delta\Omega_{m,\text{opt}}$ is the optomechanical back-action effect from Eq. (3.15).

In Fig. 3.5 (a) the nanomechanical resonator's eigenfrequency is plotted as a function of detuning (black circles) for a cavity drive power of $P_d = 15\,\text{dBm}$. The data is well described by Eq. (3.37), which is apparent from a fit to the data (red line). However, the fit yields an overwhelming contribution of the dielectric frequency shift and only negligible optomechanical backaction such that the optomechanical coupling strength g can not be determined. The inset of Fig. 3.5 (a) shows the theoretical prediction of the eigenfrequency according to Eq. (3.37) using the parameters of the experiment for three different values of g_0: The grey solid line illustrates the eigenfrequency shift for zero optomechanical coupling $g_0/(2\pi) = 0\,\text{Hz}$.

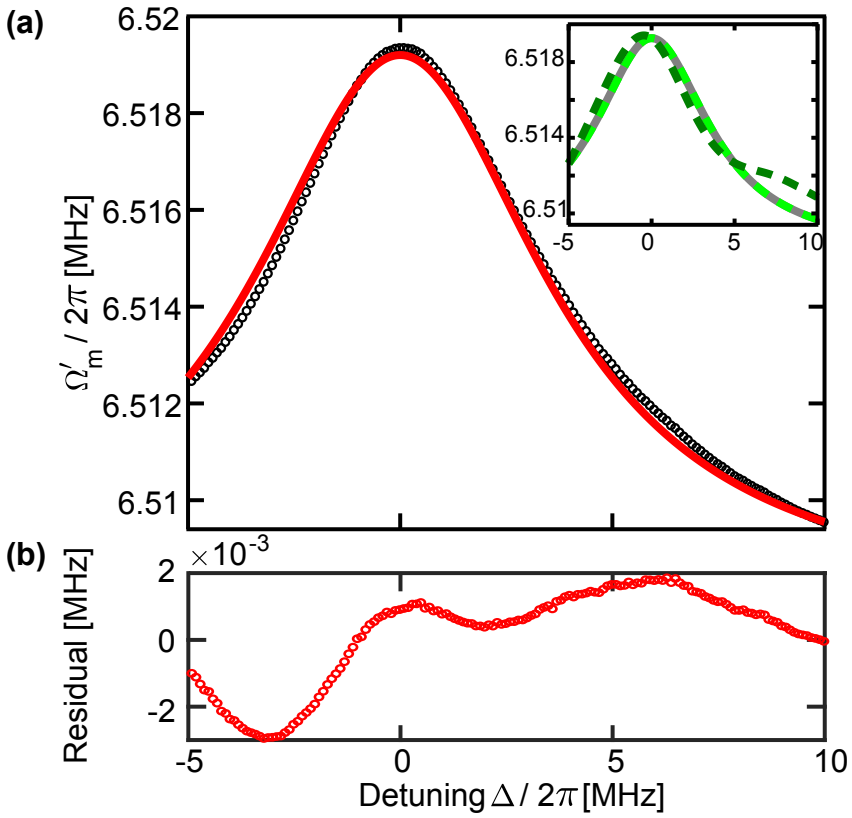

Figure 3.5 | Cavity-Induced Eigenfrequency Shift.
(a), Experimental data for a cavity drive power of $P_d = 15\,\text{dBm}$ are shown as black circles, the fit of Eq. (3.37) is indicated as a red solid line. The observed detuning dependence of the mechanical eigenfrequency is dominated by the dielectric shift, which overwhelms the contribution of the optomechanical backaction. Inset: Theoretical prediction of the eigenfrequency shift according to Eq. (3.37) for $g_0 = 0\,\text{Hz}$ (grey), 200 µHz (light green) and 20 mHz (dark green). **(b)** Residual of the data shown in (a). **Adapted and reprinted from Ref. [107], with the permission of AIP Publishing.**

As Eq. (3.36) does not depend on the sign of Δ, it is mirror symmetric with respect to the y-axis. The light green dashed line corresponds to $g_0/(2\pi) = 200\,\mu\text{Hz}$, which is the value of the single photon coupling rate estimated from the data in Fig. 3.7. The line completely coincides with the grey line, confirming that the optomechanical coupling has no measurable effect on the eigenfrequency shift. Minute deviations start becoming apparent from $g_0/(2\pi) = 2\,\text{mHz}$ which we thus estimate as an upper bound of the single photon coupling rate. The dark green dashed line for $g_0/(2\pi) = 20\,\text{mHz}$ already shows a sizable deviation of the eigenfrequency shift resulting from optomechanical coupling. Our

observation of a negligible optomechanical eigenfrequency shift is supported by the nearly mirror-symmetric shape of the measured eigenfrequency shift of the resonator around zero detuning in Fig. 3.5 (a). The slight deviation shifting the maximum to a small positive detuning is likely caused by a slight drift of the mechanical eigenfrequency from slow polarization effects within the nanostring during the cavity frequency sweep. The opposite effect would be expected from radiation pressure effects. Figure 3.5 (b) shows the residual of the data vs. the fit. We attribute the observed pattern to the same slow polarization effects. The small value of g_0 is consistent with our observation that the mechanical linewidth does not yield any measurable detuning dependence in our experiment (not shown).

3.3.3 Optomechanically Induced Reflection

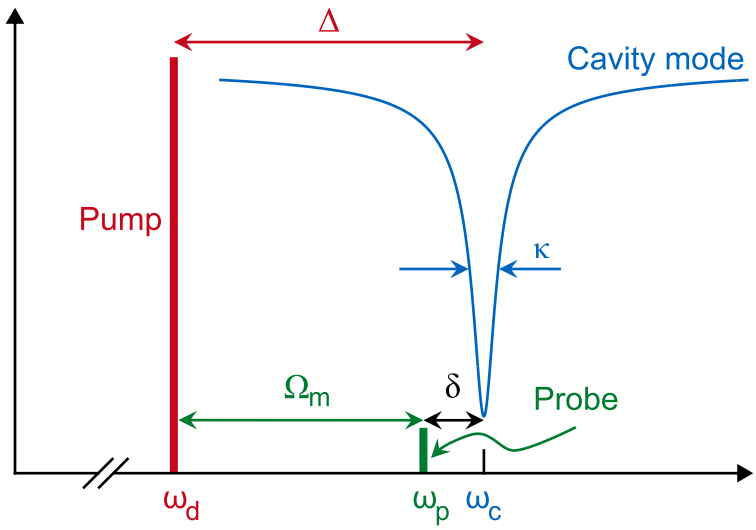

Figure 3.6 | Schematic Diagram for the Optomechanically Induced Reflection Experiment.
The pump tone ω_d defines the detuning from the cavity resonance frequency $\Delta = \omega_c - \omega_d$. The probe tone ω_p is used to determine the cavity's response that has a linewidth κ. The drive is detuned so that its uppder mechanical sideband is in the vicinity of the cavity resonance $\delta = \Delta - \Omega_m$.

In order to obtain a better estimation of the electromechanical coupling strength, we apply a second technique to characterize the parametric coupling between the nanostring and the three-dimensional cavity. It is based on the optomechanically induced transparency (OMIT) [92, 162, 163], which arises from the coherent interaction of two microwave tones with the mechanical resonator in the resolved sideband regime [101]. Figure 3.6 illustrates the pump scheme of an OMIT experiment. The cavity is strongly pumped by a drive tone at $\omega_d = \omega_c - \Delta$ which is red detuned from the cavity resonance by $\Delta = \delta + \Omega_m$. The cavity response is measured by a second, weak probe tone ω_p that is scanned across the cavity resonance. The beating between the two microwave tones induces a radiation pressure force coherently driving the mechanical resonator. In turn, the resonator imprints sidebands on the drive, which interfere constructively with the probe. This opens a transparency window in the cavity transmission or, as in our case, the cavity reflection, strictly speaking, leads to optomechanically induced reflection (OMIR) [101]. According to the standard theory of OMIT, the height of the transparency peak allows to directly extract the cooperativity $C = 4g^2/(\kappa\Gamma)$, rendering OMIT an important tool in cavity opto- and electromechanics.

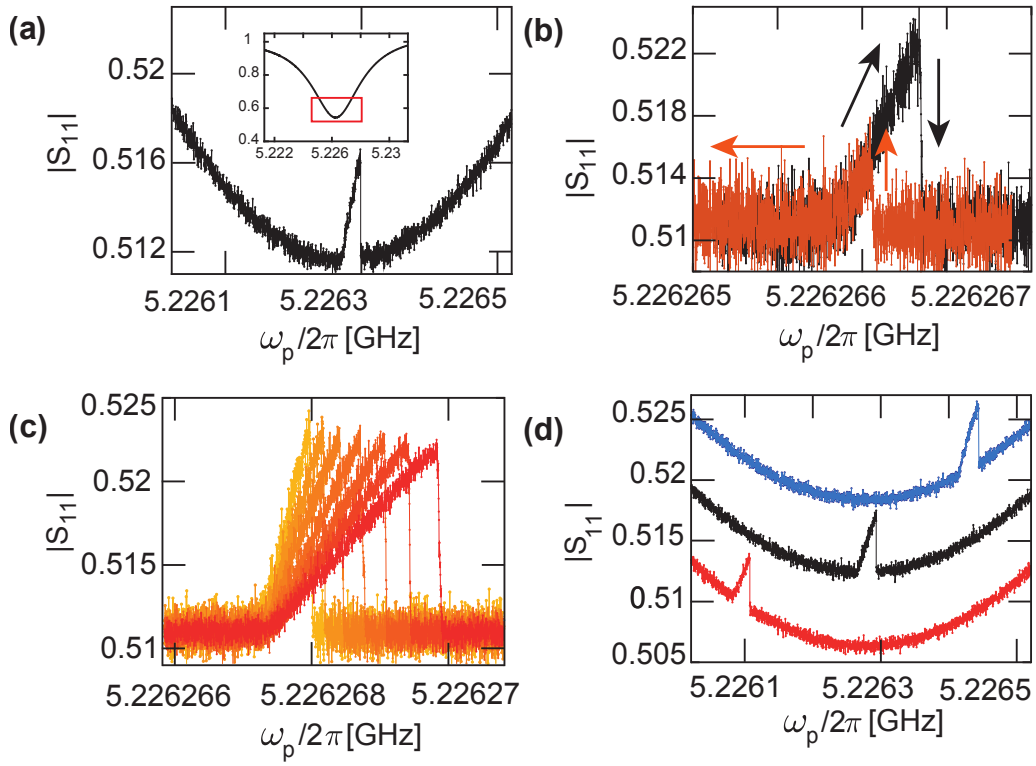

Figure 3.7 | Optomechanically induced reflection (OMIR).
(a), Cavity reflection coefficient $|S_{11}|$ showing an OMIR peak of the undercoupled cavity in response to a weak probe tone $\omega_p \approx \omega_c$ in the presence of an additional strong, red-detuned drive $\omega_d = \omega_c - \Omega_m$. The asymmetric shape of the OMIR feature reveals the nonlinearity of the mechanical resonator. The inset displays the full cavity resonance (red box illustrates area shown in main panel). **(b)**, Forward (blue) and reverse (red) sweeps of the probe tone reveal a hysteresis of the OMIR feature reflecting the bistability of the nonlinear mechanical system. **(c)** OMIR feature as a function of the probe power. For increasing probe power, the OMIR feature broadens, while its amplitude slightly decreases. **(d)** OMIR feature as a function of the drive detuning. For a drive tone red- or blue-shifted from the red sideband condition (red and blue trace, respectively) the OMIR feature shifts to the left or right of the cavity resonance. The situation for a drive on the red sideband is also included (black trace). Red and blue trace are vertically offset for clarity. **Adapted and reprinted from Ref. [107], with the permission of AIP Publishing.**

In Fig. 3.7 (a) we plot the response of the microwave cavity as a function of the probe frequency ω_p for a drive applied at optimal detuning $\Delta = \omega_d - \omega_c = -\Omega_m$. The drive and probe power are 15 dBm and −25 dBm, respectively. A transparency feature at ω_c is clearly apparent in the center of the cavity resonance. Note that the peak is not symmetric. Its asymmetry reflects the nonlinear response of the mechanical resonator to the radiation pressure drive exerted by the two microwave tones [161, 164, 165]. In agreement with the standard model for OMIR for the case of an undercoupled cavity driven on the red sideband, the shape of the nonlinear transparency peak directly follows the response of the Duffing resonator [161, 164].

This is also reflected in the hysteretic behavior of the OMIR feature displayed in Fig. 3.7 (b) for a forward (black) as well as a reverse (red) sweep of the cavity probe at a somewhat lower probe power. Figure 3.7 (c) illustrates the dependence of OMIR peak on the probe power. The curves (from left to right) correspond to an increasing probe power from −46 dBm to −39 dBm. As expected, the width of the nonlinear feature broadens with increasing probe power while its amplitude slightly decreases[161]. Finally, the effect of a detuning δ of the cavity drive from the red sideband condition, $\Delta = -\Omega_m + \delta$, is explored in Fig. 3.7 (d) for a constant probe power of −25 dBm. For a drive tone red- or blue-shifted from the red-sideband condition ($\delta = \pm 180$ kHz red and blue trace, respectively), the OMIR peak moves away from the minimum of the cavity response at ω_c [161]. The data for the drive matched to the red sideband is also included ($\delta = 0$ Hz, black trace). For clarity, the red and blue trace are vertically offset from the black trace.

According to the standard theory of OMIR, the height of the transparency peak S_{11}^0 allows to quantify the cooperativity. For the case of an undercoupled cavity driven on the red sideband, $C = (2\eta)/(1 - S_{11}^0) - 1$. Neither the nonlinear regime nor a poor sideband resolution greatly affect the magnitude of the OMIR feature [161, 166]. Using the yellow trace in Fig. 3.7 (c), we extract an approximate value of $C \approx 0.025$. This translates into an optomechanical coupling strength of $g/(2\pi) = 1.2$ kHz, and, given a cavity photon number of $4.0 \cdot 10^{13}$ at a drive power of 15 dBm on the red sideband, to a single photon coupling rate of $g_0/(2\pi) = 200$ µHz.

It is noteworthy to mention that such a feeble single photon coupling can produce observable features in the OMIT experiment at all. This is enabled by the large number of photons supported by the three-dimensional microwave cavity, which exceeds photon numbers achieved in planar microwave resonators at low temperatures [92, 101] by at least four orders of magnitude and is at present only limited by the maximum output power of our microwave generator. The observed weak single photon coupling strength is attributed to our cavity design, as the loop antenna could not be precisely positioned in the cavity in our experiment and presumably only weakly couples to the TM_{110} cavity mode. As apparent from Fig. 2.11, the cylindrical cavity geometry exhibits a large number of TM and TE modes with very similar resonance frequencies. Hence, multimode coupling can not be avoided in this case. At the same time, the electromechanical coupling of the nanostring to the electrodes is limited by a relatively large electrode-electrode separation of approx. 600 nm for the sample under investigation. For future work on the room temperature cavity electromechanics platform, an improved control of the antenna position as well as a smaller electrode gap will enable to significantly increase g_0. Furthermore, we attribute the strongly suppressed OMIR peak and the corresponding underestimation of the cooperativity to a large population of approx. 7500 thermal photons in the cavity, which is not accounted for in the standard theory. We further hypothesize that the reduced magnitude of the OMIR peak can be employed to independently probe the number of thermal photons in the cavity, which may also be of interest for cavity electromechanics at cryogenic temperatures where a small but finite thermal cavity population typically exists.

3.4 Conclusion

In conclusion, we have demonstrated a cavity electromechanical system that operates in the sideband resolved regime at room temperature. This was accomplished by introducing a three-dimensional, non-superconducting microwave cavity made of copper which replaces the previously employed copper microstrip cavity, the quality factor of which is outperformed by more than an order of magnitude. In our experiment a non-metallized silicon nitride nanostring resonator was dielectrically coupled to the TM_{110} mode of the cavity which offers almost perfect sideband resolution $\kappa \leq \Omega_m$. Electromechanical coupling was observed and characterized in one- and two-microwave tone experiments. While the mechanical eigenfrequency shift is dominated by dielectric frequency tuning, the optomechanically induced transparency (in reflection geometry) establishes a clear proof of dynamical backaction. Despite the minute single photon coupling rate of our first implementation of the room temperature cavity electromechanical platform in the sub-mHz regime, a measureable coupling is enabled by the large number of photons circulating in the three-dimensional microwave cavity. As a result of the required strong red-detuned cavity drive, the response of the mechanical resonator is nonlinear in our proof-of-principle experiment.

Our results translate the thriving field of cavity electromechanics from the millikelvin realm to room temperature. For future exploitation, the electromechanical vacuum coupling rate $g_0/(2\pi)$ will need to be increased. This can be accomplished by an improved positioning of the loop antenna providing the coupling between the cavity mode and the control electrodes. Furthermore, the coupling can be enhanced by increasing the dielectric transduction efficiency, i.e. by reducing the lateral gap between the electrodes. Following these technical improvements, we expect to reveal the electromechanical cooling or pumping of the mechanical mode. Finally, the quality factor or the TE_{011} mode exceeds that of the TM_{110} mode by another order of magnitude, which offers the prospect of entering the deep-sideband-resolved regime of cavity electromechanics at room temperature. In the following, we replace the cylindrical cavity geometry with a coaxial cavity (see discussion in Sec. 2.3.4). This type of cavity proves to be a more suitable candidate for the cavity-assisted detection scheme because it provides a remarkably clean frequency spectrum to avoid multimode coupling. Due to its small size, the coaxial cavity can be integrated into future experiments at cryogenic temperatures.

Table 3.1 | Parameters in Cavity Electromechanics Experiment.
Overview of the most important parameters and devices for the room temperature cavity electromechanics experiment.

Nanomechanical String Resonator		
Dimensions	$(w \times t \times L)$	$(250 \times 100 \times 57000)$ nm
Eigenfrequency	$\Omega_m/(2\pi)$	6.494 8 MHz
Linewidth	$\Gamma/(2\pi)$	42 Hz
Quality factor	Q	150.000
Cylindrical 3D Cavity		
Resonance Frequency (TM_{110})	$\omega_c/(2\pi)$ & 5.226 GHz	
Linewidth	$\kappa/(2\pi)$	5.572 MHz
External Coupling Rate	$\kappa_e/(2\pi)$	1.361 MHz
Coupling Efficiency	$\eta = \kappa_e/\kappa$	0.244
Dimensions	$(r \times H)$	(35×70) mm
Drive Power	P_d	31.623 mW
Drive Frequency	$\omega_d/(2\pi)$	
Cavity Detuning	$\Delta = \omega_d - \omega_c$	
Intra-Cavity Photons	$n_d(\Delta = 0)$	$2.5486 \cdot 10^{14}$
Intra-Cavity Photons	$n_d(\Delta = -\Omega_m)$	$3.9607 \cdot 10^{13}$

4 Coherent Sensing Protocol for Short Signals

The following chapter is based on our manuscript:

A. Chowdhury, A. T. Le, E. M. Weig and Hugo Ribeiro, "Iterative Adaptive Spectroscopy of Short Signals", *arXiv preprint arXiv:2204.04736 (2022)*. Reference [167]

The theoretical model has been developed in collaboration with Prof. H. Ribeiro from the University of Massachusetts Lowell and Dr. A. Chowdhury. The original theoretical model is printed under permission of Prof. H. Ribeiro. Certain passages of the original publication are printed under permission of Dr. A. Chowdhury and Prof. H. Ribeiro.

A quantum coherent sensor utilizes its fragile quantum nature to probe extremely small changes of a certain physical quantity, e.g. electric or magnetic field, and allows one to increase spatial resolutions and to measure with high sensitivity. Generally, the precision of any coherent sensor, classical or quantum, is limited by the maximal measurement time-window t_w over which a signal of interest can be sampled. This limitation originates from unwanted interactions of the sensor with noisy environment degrees of freedom, which lead to decoherence and thus, to the decay of the measured signals.[1]

Strategies extending the coherence time [168–173] or using states with no classical analogs [174–179], e.g., entangled or squeezed states, to improve the precision have been put forward. However, these strategies do not guarantee that the sensor operates with the highest precision attainable. This is only possible, if all steps involved in the sensing protocol are optimized [180].

In this chapter, we provide the theoretical development of a sensing protocol for frequency estimation with high precision. We employ the strong coupling nature of a nanomechanical two-mode system to implement an iterative, adaptive frequency sensing scheme based on Ramsey interferometry [51]. Typically, Ramsey sequences in quantum two-level systems, e.g. spin [181] or superconducting [182] quantum bit (qubit), are performed with a finite qubit-drive detuning. It enables one to measure the beating pattern (the Ramsey fringes) as a function of detuning in the rotating frame of the drive field. In our case, it is not necessary to implement a drive tone to bring our system into superposition states. Thus, we obtain a beating pattern that is due to the coherent exchange in excitation energy of the nanomechanical two-mode system in the laboratory frame (more details can be found in Sec. 4.1). Note that our protocol is applicable to any two-level systems in both classical and quantum regime and that it is particularly suited for short and finite signals.

We start with the implementation of the ubiquitous Ramsey interferometry [183] of a two-mode system to sense the unknown coupling strength $\Omega_0/2$ from a signal with short waiting time t_w. The waiting time (often referred to as dark time) denotes the free evolution period of the two-mode system in the Ramsey interference experiment. There are two reasons to impose a short t_w: First, it is experimentally simpler to sample short signals (smaller number of data points required) and second, from a signal

[1] Note that the term measured signal refers to the data recorded by the sensor, whereas the signal of interest represents the quantity to be detected.

processing point of view, it is easier to deal with non-decaying signals [2] to enhance the frequency estimation through the application of window functions [184]. Note that the coupling strength is the key element that we want to estimate with high precision, since the change in $\Omega_0/2$ is a direct consequence of the coupling of the sensor to the physical quantity that we want to measure.

Additionally, we introduce a strategy to enhance the Ramsey interferometry by correcting the control pulses, that come with experimental constraints such as bandwidth limitations and noisy environment. The correction allows us to prepare the sensing and readout states with high-fidelity. To find frequency control yielding high fidelity state preparation, we use the recently proposed Magnus-based strategy for control [185, 186]. Furthermore, we describe the signal processing technique to deal with finite and short signals to mitigate spurious effects such as spectral leakage and scalloping when transforming the signals from the time into frequency domain using discrete Fourier transform (DFT). And finally, we explain the working principle of our developed iterative, adaptive sensing protocol to estimate unknown frequency with high precision.

4.1 Ramsey Interferometry

The scope of this chapter is to develop a sensing protocol with a sensor element that uses coherence (i.e., wavelike spatial or temporal superposition) to probe a physical quantity. To follow the definitions in the review of Degen et al., a system needs to fulfill certain criteria in order to function as a coherent sensor [183]

1. The system has discrete, resolvable energy levels that are separated by a transition $E = \hbar\Omega_0$.
2. It is possible to initialize the system in a well-known state and to read-out the state accordingly.
3. The system can be coherently manipulated.
4. The coherent sensor interacts with relevant physical quantities, i.e. electric or magnetic field. The interaction translates into a change in energy levels or to transition between energy levels.

Generally, quantum two-level systems (TLS) are natural coherent sensor candidates that can fulfill all of these criteria. Furthermore, it has been shown that coherent manipulation and control are possible in both the quantum [187] and classical regime [47, 188]. In order to perform a coherent sensing experiment, we typically follow certain sequences that includes control and free evolution steps. Our goal is to develop a sensing protocol whose duration is short, i.e., $(\Omega_0/2\pi)t_\mathrm{r} < 5$ [shortest time scale possible to apply Blackman-Harris window, also see Fig. 4.9 (j) and (k)], where Ω_0 is the transition frequency of the two distinguishable modes and t_r is the time sequence to conduct a sensing experiment. To this end, we employ the ubiquitous Ramsey interferometry of a two-mode system to estimate an unknown frequency from a signal with a short waiting time t_w.

Commonly, the Ramsey interferometry can be divided into five individual steps [183]. Assuming the system has two distinguishable states that are $\mathbf{a}_1$ and $\mathbf{a}_2$ (i.e. the qubit's natural eigenstates $|g\rangle$ and $|e\rangle$ or the classical nanomechanical IP and OOP flexural modes), (I) the coherent sensor can be initialized into one of the states, i.e. $\mathbf{a}_1$. (II) A fast control pulse is applied to transform the coherent sensor into the superposition state with high fidelity. Alternatively, an adiabatic detuning combined with a $\pi/2$ pulse (see step I') can be used to bring the system into superposition state (see for instance Ref. [47]).

[2] The decay envelope of the signal can be viewed as an "uncontrolled" window function applied to the signal oscillating component. The presence of an "uncontrolled" window function can negate all the benefits of using specific window functions tailored to enhance frequency estimation.

(III) The system can evolve for a certain waiting time t_w, where the superposition state picks up a phase $\varphi = \Omega_0 t_w$ during the evolution. (IV) By applying a second control pulse, one can convert the system back to the measureable state $\mathbf{a}_1$. (V) The last step is the final read-out of the state to record the return probability

$$P(t_w) = |\boldsymbol{a}_1^T \exp(-i\Omega_0 t_w \sigma_x)\boldsymbol{a}_1|^2 = \cos^2(\Omega_0 t_w/2) = \frac{1}{2}[1 + \cos(\Omega_0 t_w)], \tag{4.1}$$

where σ_x is the Pauli matrix. So by measuring the return probability as a function of time t_w, we obtain an oscillatory signal with a frequency given by $\Omega_0/2$. In Fig. 4.1 (a), we illustrate the five individual steps of the Ramsey sequence. Consequently, the Ramsey measurement of a two-mode system provides us direct access to the energy splitting $E = \hbar\Omega_0$. If the system interacts with a relevant physical quantity $\mathcal{V}(t)$ (e.g. electric or magnetic fields), we should be able to observe a relative change in transition frequency due to the coupling of the form $\gamma = \frac{\partial^q \Omega_0}{\partial \mathcal{V}^q}$. The coupling can be linear ($q = 1$) or quadratic ($q = 2$).

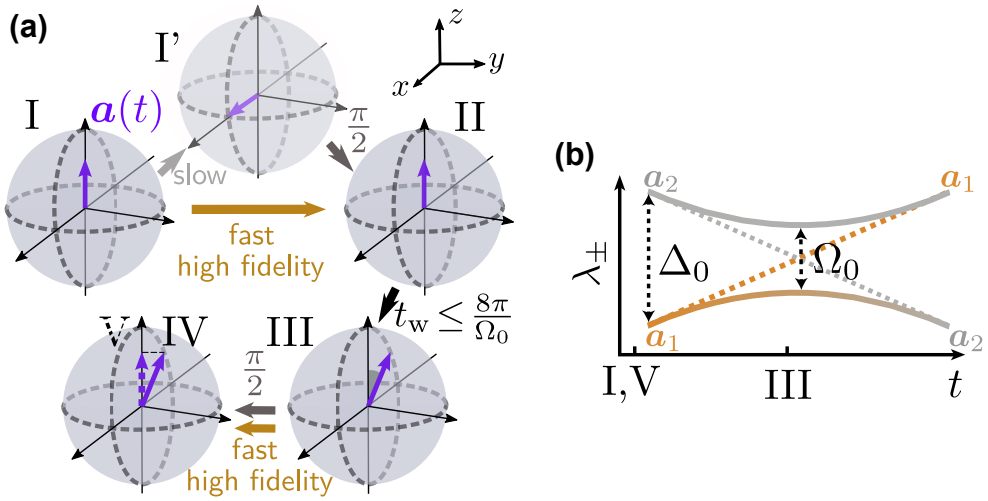

Figure 4.1 | Ramsey Interferometry with a Two-Mode System.
(a), The five steps of a Ramsey sequence to sense the coupling strength $\Omega_0/2$. The normal (slow) sequence is indicated by gray arrows, while the enhanced (fast, high-fidelity) sequence follows the orange arrows. **(b)**, The eigenfrequencies of the parametrically coupled two-mode system showing an avoided crossing with the frequency splitting Ω_0. **Reprinted from Ref. [167]**

4.1.1 Parametrically Coupled Two-Mode System as Coherent Sensor

We consider a parametrically coupled two-mode system as the coherent sensing element [see for instance Fig. 4.1 (b)]. The dynamical matrix (effective Hamiltonian) describing the coupled modes has been previously discussed in Sec. 2.2.4 (or see, e.g., Ref. [63]).

$$D(t) = \frac{1}{2}(\Delta(t)\sigma_z + [\Omega_0 + \delta\Omega(t)]\sigma_x), \tag{4.2}$$

where σ_j, $j \in \{x, y, z\}$, are the Pauli matrices, $\Delta(t) = \omega_2(t) - \omega_1(t)$ is the controllable frequency difference between mode 1 and 2 [see Fig. 4.1 (b)], $\Omega_0/2$ is the unknown coupling strength we seek to estimate [see Fig. 4.1 (b)], and $\delta\Omega(t)$ is a real stochastic process describing how noise arising, e.g., from thermal fluctuations or fluctuations of the fields the system is subjected to, affects the coupling

between the modes. By neglecting the noise contribution, the eigenfrequencies of Eq. (4.2) are given by $\lambda_{\pm}(t) = \pm\frac{1}{2}\sqrt{\Delta^2(t) + \Omega_0^2}$ [see Fig. 4.1 (b)].

The dynamical matrix $D(t)$ is formally equivalent to a quantum two-level Hamiltonian $\hat{H}(t)$ [47, 77, 188] subject to classical noise. The model we use, thus, describes both coherent classical systems [56, 63, 92, 189–194] and quantum systems [195–202]. Since our goal is to develop a sensing protocol whose duration t_r is short, i.e., $(\Omega_0/2\pi)t_r < 5$, we assume that $\delta\Omega(t) \approx \delta\Omega$ does not change appreciably for one realization of the protocol (frozen environment approximation). Within this framework, averaged Ramsey signals are obtained by performing statistical averaging, i.e.,

$$\langle s(t)\rangle_{\delta\Omega} = \int_{-\infty}^{\infty} \mathrm{d}(\delta\Omega)\, p(\delta\Omega)\, s(t), \tag{4.3}$$

where $s(t)$ is the oscillatory output of the Ramsey sequence and $p(\delta\Omega)$ is the probability distribution of $\delta\Omega$. Here, we assume $p(\delta\Omega)$ to be a Gaussian distribution with zero mean and standard deviation $\sigma_{\delta\Omega}$,

$$p(\delta\Omega) = \frac{1}{\sqrt{2\pi}\sigma_{\delta\Omega}} \exp\left[-\frac{1}{2}\frac{\delta\Omega^2}{\sigma_{\delta\Omega}^2}\right]. \tag{4.4}$$

Here, we further assume $\sigma_{\delta\Omega} = \Omega_0/10$.

4.1.2 Sensing and Readout State Preparation

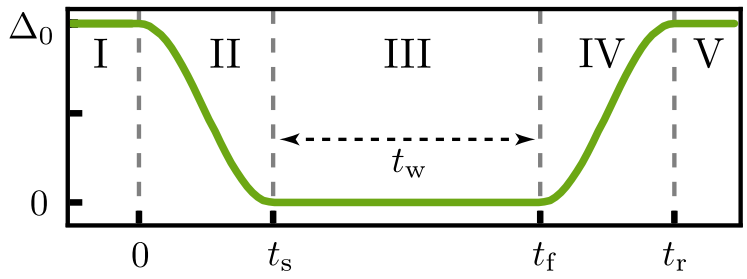

Figure 4.2 | Generic Sweep for the Ramsey Interferometry.
Time dependent frequency-sweep to generate a Ramsey sequence. (I) Sensing state ($\boldsymbol{a}_1$) initialization. (II) Control pulse to transform the coherent sensor into superposition state. (III) Free evolution during the time interval t_w. (IV) Second control pulse to convert the sensor back to the measurable state $\boldsymbol{a}_1$. (V) Sensing state readout. **Reprinted from Ref. [167]**

We consider a generic frequency-sweep for the Ramsey interferometry given by

$$\Delta(t) = \begin{cases} \Delta_s(t) = \Delta_0 f(t), & \text{for } 0 \le t \le t_s, \\ 0, & \text{for } t_s < t < t_f, \\ \Delta_r(t) = \Delta_0[1 - f(t - t_f)], & \text{for } t_f \le t \le t_r, \end{cases} \tag{4.5}$$

where $t_s = t_r - t_f$, $\Delta(0) = \Delta(t_r) = \Delta_0$ is the initial (final) value of the frequency difference of $\boldsymbol{a}_1$ and $\boldsymbol{a}_2$ [see Fig. 4.1 (b)] and $f(t)$ is a smooth sweep function obeying $f(0) = f(t_r) = 1$ and $f(t_s) = f(t_f) = 0$. We define the measurement time-window $t_w = t_f - t_s$ and the total sensing time $t_r = 2t_s + t_w$, where we choose the duration of both the sensing and readout state preparation protocols to be t_s (see Fig. 4.2).

By choosing $\Delta_0 \gg \Omega_0$, we can initialize the system in state $\boldsymbol{a}_1 = (0, 1)^{\mathsf{T}}$ at $t = 0$ [see step (I) in Fig. 4.1 (a) and Fig. 4.2]. This is also the sensing state $\boldsymbol{a}_s$ we would like to use to probe Ω_0, i.e.,

$\boldsymbol{a}_s = \boldsymbol{a}_1$. At the avoided crossing, $\boldsymbol{a}_1$ can be expressed as an equal superposition of the eigenmodes of Eq. (4.2), which is the state maximizing the visibility of the Ramsey fringes. To give an example, we can define the superpositions of the eigenmodes $\boldsymbol{a}_1$ and $\boldsymbol{a}_2$ as

$$\boldsymbol{a}_\pm = \frac{1}{\sqrt{2}}(\boldsymbol{a}_1 \pm \boldsymbol{a}_2). \tag{4.6}$$

Instead using one of the superposition states in Eq. (4.6), we can choose the basis

$$\boldsymbol{a}_1 = \frac{1}{\sqrt{2}}(\boldsymbol{a}_+ - \boldsymbol{a}_-). \tag{4.7}$$

Similarly, we can also choose $\boldsymbol{a}_2$ as the basis vector as the sensing state.

Using $\boldsymbol{a}_1$ as Sensing State We can verify the advantage of using $\boldsymbol{a}_1$ to maximize the visibility of the Ramsey signal by assuming that one can prepare with unit fidelity both the sensing and readout state. In this case the Ramsey signal is given by

$$s(t) = |\boldsymbol{a}_1^\mathsf{T} \exp(-i\Omega_0 t\sigma_x)\boldsymbol{a}_1|^2 = \cos^2[(\Omega_0/2)t], \tag{4.8}$$

which is a function oscillating between 0 and 1, and thus with unit visibility.

To understand why this property is important in the context of frequency estimation from short signals, let us consider the situation where we prepare any arbitrary state at $t = t_s$. We model this situation by describing the evolution generated by $D(t)$ [see Eq. (4.2)] between $t = 0$ and $t = t_s$ as a rotation $R_{\boldsymbol{n}}(\theta)$ of angle θ around an axis $\boldsymbol{n} = (\sin\alpha\cos\beta, \sin\alpha\sin\beta, \cos\alpha)^\mathsf{T}$. We have

$$R_{\boldsymbol{n}}(\theta) = \cos(\theta/2)\mathbb{1} - i\sin(\theta/2)\boldsymbol{n}\cdot\boldsymbol{\sigma}, \tag{4.9}$$

with $\boldsymbol{\sigma} = (\sigma_x, \sigma_y, \sigma_z)^\mathsf{T}$ the vector of Pauli matrices. Similarly, we assume that the preparation of the readout state is described by the rotation $R_{\boldsymbol{n}}(-\theta)$. Within this framework, the Ramsey signal is given by

$$\begin{aligned} s_\theta(t) &= |\boldsymbol{a}_1^\mathsf{T} R_{\boldsymbol{n}}(-\theta)\exp(-i\Omega_0 t\sigma_z)R_{\boldsymbol{n}}(\theta)\boldsymbol{a}_1|^2 \\ &= 1 + \left[\sin^2\alpha\left(2\cos\alpha\cos\beta\sin^2(\theta/2) + \sin\beta\sin\theta\right)^2 - 1\right]\sin^2[(\Omega_0/2)t] \\ &= 1 + v(\alpha,\beta,\theta)\sin^2[(\Omega_0/2)t] \end{aligned} \tag{4.10}$$

For $\alpha = 0$ with β and θ arbitrary, we have $s_\theta(t) = s(t)$ since this corresponds to a rotation around the z-axis which only imprints a global phase to mode $\boldsymbol{a}_1$. Another situation that leads to $s_\theta(t) = s(t)$ is setting $\alpha = \pi/2$, $\beta = 0$ and θ arbitrary, which corresponds to a rotation around the x-axis. This does also not affect the Ramsey signal since the Ramsey signal is obtained by letting the state vector precess freely around the x-axis.

For any other rotation, the Ramsey signal can be viewed as the sum of two signals: A constant signal $s_1(t) = 1$ and an oscillating signal $s_2(t) = v(\alpha,\beta,\theta)\sin^2[(\Omega_0/2)t]$ with visibility $0 \leq |v(\alpha,\beta,\theta)| < 1$. Thus, we can write the discrete Fourier spectrum as

$$|\mathcal{F}[s_\theta(t)]|^2 = |\mathcal{F}[s_1(t)]|^2 + |\mathcal{F}[s_2(t)]|^2 + 2\mathrm{Re}[\mathcal{F}[s_1(t)]\mathcal{F}[s_1(t)]^*]. \tag{4.11}$$

Equation (4.11) shows that one can interpret the spectrum of a finite $s_\theta(t)$ as an interferometric pattern. As a result, $|\mathcal{F}[s_\theta(t)]|^2$ does not necessarily have a maximum located at $\omega = \Omega_0$. This is yet a type of systematic error in the sensing result which cannot be eliminated unless one knows exactly what the values of α, β, and θ are.

Finally, we note that in the infinite measurement-time window limit, i.e., $t_w \to \infty$, this issues vanishes since the discrete Fourier transform of $s_1(t)$ would reduce to the Kronecker delta function. Consequently, in the limit defined by $\Omega_0 t_w \gg 1$, the induced systematic error is negligible. So by choosing $\boldsymbol{a}_1$, we would obtain the maximum contrast in the Ramsey fringe with unit visibility [see Eq. (4.8)]. Any arbitrary state would generate an additional signal leading to an interferometric pattern and hence, degrades the unit visibility in the Ramsey fringe.

Bandwidth Limitation in Pulse Generation To prepare the sensing state $\boldsymbol{a}_s = \boldsymbol{a}_1$ at $t = t_s$ and the readout state $\boldsymbol{a}_r$ at $t = t_r$ (step II and IV in Figs. 4.1 (a) and 4.2, respectively) one needs to choose $f(t)$ such that the evolution generated by Eq. (4.2) corresponds to the identity in the intervals $0 \le t \le t_s$ and $t_f \le t \le t_r$. This can theoretically be realized with a frequency-sweep whose leading and trailing edge duration fulfills the condition $\Omega_0 t_s \ll 1$ (quasi instantaneous sweep). However, faithful reproduction of fast sweeps in the lab environment are limited by the maximum bandwidth of wave generators. The Landau-Zener model [53–55, 203], where one sets the sweep function to be linear in time, $f(t) = 1 - t/t_s$, is a perfect example: Faster and faster sweeps require more and more Fourier components to accurately reproduce $f(t)$. This problem becomes apparent when dealing with the generation of a linear ramp.

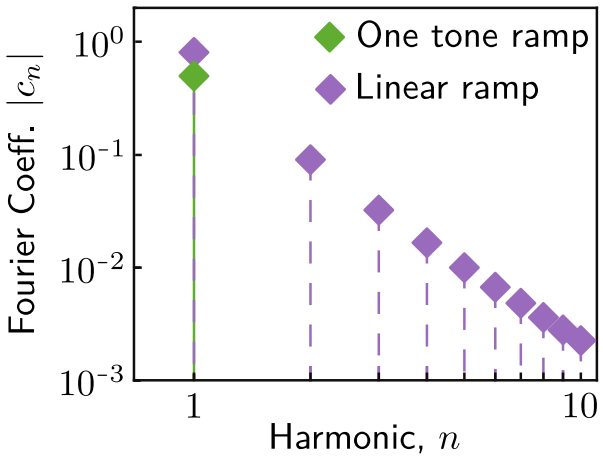

Figure 4.3 | Fourier Components of Linear Ramp versus One Tone Ramp.
Plot of the Fourier amplitudes $|c_n|$ [see Eq. (4.12)] as a function of the harmonic n, for one tone (green) and linear ramp $s_{\text{triangle}}(t)$ (purple). **Reprinted from Ref. [167]**

Generally, linear ramps are generated by approximating a triangular wave with a period equal to T. The linear ramp is then obtained by considering the time-interval $t \in [0, t_s = T/4]$. The Fourier series of the triangle wave is given by

$$\begin{aligned} s_{\text{triangle}}(t) &= \sum_{n=1}^{\infty} c_n \sin\left(2\pi(2n-1)\frac{t}{T}\right), \\ c_n &= -\frac{8}{\pi^2}\frac{(-1)^n}{(2n-1)^2}. \end{aligned} \tag{4.12}$$

This indicates that one needs to use an infinite number of harmonics to faithfully reproduce a linear ramp (see Fig. 4.3), that is impossible to implement in an experiment because of the bandwidth limitation of the signal generators. Instead of the smooth linear ramp, we would obtain a step-like function due to the absence of high frequency components.

The alternative is to use a frequency-sweep with an adiabatic leading edge followed by a $\pi/2$ pulse [see, e.g., Ref. [47] and extra step I' in Fig. 4.1 (a)]. While such a protocol is not limited by bandwidth constraints, it is limited by adiabaticity of the sweep and the fidelity of the resonant $\pi/2$ pulse. A high-fidelity adiabatic sweep must fulfill the condition $\Omega_0 t_s \gg 1$. This renders high fidelity preparation of the sensing state in the presence of noise unsustainable [204]. For systems with short decay time T_1, the implementation of an adiabatic sweep is not feasible.

So the challenge in this work is to design a fast and, at the same time, bandwidth-limited protocol that still yields a high-fidelity state preparation [orange arrows in Fig. 4.1 (a)]. For this purpose, we first start with the generation of the single-tone function for frequency detuning

$$f(t) = \frac{1}{2}\left[1 + \cos\left(\frac{\pi}{t_s}t\right)\right]. \tag{4.13}$$

Here, we choose a sweep time t_s which respects the bandwidth limitation imposed by various experimental components including arbitrary waveform generators (AWG), filters, amplifiers, and other passive and active circuit components in a laboratory environment. This implies that the allowed maximal t_s in Eq. (4.13) is in general still too slow to realize a quasi instantaneous sweep, but yet much shorter than the t_s required to fulfill the adiabatic criterion. In this intermediate regime, where the generated evolution is coherent, it is possible to applied the single tone function defined in Eq. (4.13) for state preparations in the Ramsey sequence. To further improve the visibility of the Ramsey fringe, we use the recently proposed Magnus-based strategy for control [185, 186] to cancel, on average, transitions to mode $\boldsymbol{a}_2$. This strategy provides a solution that modifies the simple single-tone control function (4.13) within the framework of bandwidth limitation. In the following section, we provide the fundamental idea of the Magnus-based corrections to overcome experimental constraints in order to faithfully prepare the sensing and readout states of the Ramsey sequence with high fidelity.

4.2 Strategy for High Fidelity Sensing State Preparation

From the previous sections we depicted the challenges in the implementation of a coherent sensing protocol. On the one hand, the bandwidth limitation of any AWG puts an upper bound on how well one can faithfully generate a control pulse in an experiment. On the other hand, the noise contribution will set the lower bound for the adiabaticity strategy. To overcome these experimental constraints, we follow the framework proposed by T. F. Roque and H. Ribeiro [185, 186] to construct control fields that are fast and allow one to realize the desired state flow that is compatible with all experimental constraints.

4.2.1 Magnus-Based Corrections

The generic strategy is to develop a specific time-dependent dynamical matrix (with all experimental constraints) to produce (at time t_f) a desired state evolution. We first define the generic dynamical matrix

$$D(t) = D_0(t) + \varepsilon V(t). \tag{4.14}$$

Here, we choose $D_0(t)$ such that when we completely neglect $V(t)$ [$\varepsilon \to 0$] Eq. (4.14) is exactly solvable. $V(t)$ represents the unwanted interaction that disrupts ideal dynamics and can be treated as perturbation with $\varepsilon \ll 1$. In this work, we focus on the classical dynamical matrix (instead of describing the system's Hamiltonian) and the classical flow (instead of time evolution operators). The basic strategy follows two steps

- We choose the control field for the simple dynamical matrix $D_0(t)$ so that the desired operation can be realized in the absence of the error term $V(t)$.
- The presence of $V(t)$ disrupts the ideal evolution of the system. Nevertheless, we desire a flow at time t_f that corresponds to the flow generated by $D_0(t)$ only. This, in general, can be achieved by modifying the control sequence so that the impact of $V(t)$ is averaged out over the evolution times.

Following the dynamical matrix in Eq. (4.14), we can define the corresponding time-dependent flow that describes the state evolution (see for instance Eq. (10) in [63])

$$\Phi(t) = \Phi_0(t)\Phi_I(t). \tag{4.15}$$

Here, $\Phi_0(t)$ is the ideal flow generated by the undisturbed dynamical matrix $D_0(t)$

$$\Phi_0(t) = \exp\left[-i\int_0^t d\tau D_0(\tau)\right]. \tag{4.16}$$

The contribution of the error term $V(t)$ to the system dynamics is given by $\Phi_I(t)$, which is defined as

$$\Phi_I(t) = \exp\left[-i\varepsilon\int_0^t d\tau V_I(\tau)\right]. \tag{4.17}$$

Here, the dynamics of the spurious term is transformed to the interaction picture generated by $\Phi_0(t)$ that is

$$V_I(t) = \Phi_0^\dagger(t)V(t)\Phi_0(t) - i\Phi_0^\dagger(t)\dot{\Phi}_0(t). \tag{4.18}$$

It is apparent from Eq. (4.15) that the presence of a nonzero error term $V(t)$ prevents the system to evolve at $t = t_f$ to a desired state, since in general $\Phi_I(t) \neq \mathbb{1}$.

Thus, the strategy to correct the unitary flow at $t = t_f$ is to modify the dynamical matrix in Eq. (4.14) by adding a control term $W(t)$ in order to cancel the unwanted effect of $V(t)$

$$D_{mod}(t) = D_0(t) + \varepsilon V(t) + W(t). \tag{4.19}$$

The corresponding flow generated by $D_{mod}(t)$ is given by $\Phi_{mod}(t) = \Phi_0(t)\Phi_{mod,I}(t)$. Here

$$\Phi_{mod,I}(t) = \exp\left[-i\int_0^t dt_1 D_{mod,I}(t_1)\right] \tag{4.20}$$

is the time-dependent unitary flow generated by the modified dynamical matrix

$$D_{mod,I}(t) = \varepsilon V_I(t) + W_I(t) \tag{4.21}$$

in the interaction picture with respect to $D_0(t)$ [see Eq. (4.18)].

The desired unitary evolution at $t = t_f$ is obtained if $\Phi_{mod,I} = \mathbb{1}$, i.e., $\Phi_{mod}(t_f) = \Phi_0(t_f)$. Obviously, the trivial solution here is $W(t) = -\varepsilon V(t)$. This solution demands the cancellation of the spurious term $V(t)$ at all times and is almost infeasible, since the correction term $W(t)$ will be constrained by the experimental apparatus and the interaction to the environment.

A more elegant solution consists in cancelling the error term on average. The correction is chosen to average out the effects of $V(t)$, meaning that during the intermediate time the evolution will defer from that generated by $D_0(t)$, but at the final time t_f we will have $\Phi(t_f) = \Phi_0(t_f)$. To follow the procedure

in Refs. [185, 186], we seek the control term $W(t)$ using a series representation, which allows one to treat the problem perturbatively

$$W(t) = \sum_{n=1}^{\infty} \varepsilon^n W^{(n)}(t). \tag{4.22}$$

By inserting Eq. (4.22) into Eq. (4.21) and (4.20), we obtain an equation system with time-ordered exponential (Dyson series). A more convenient approach is to use the Magnus expansion [205], where we can replace the complicated time-ordered exponential by the Magnus Ansatz [186]

$$\Phi_{\mathrm{mod,I}}(t) = \exp \sum_{l=1}^{\infty} \mathcal{M}_l(t). \tag{4.23}$$

The Magnus expansion terms $\mathcal{M}_l(t)$ are recursively defined by differential equations [185, 186, 205]. The first two terms are given as

$$\begin{aligned} \partial_t \mathcal{M}_1(t) &= -\mathrm{i} D_{\mathrm{mod,I}}(t), \\ \partial_t \mathcal{M}_2(t) &= \frac{1}{2}[\partial_t \mathcal{M}_1(t), \mathcal{M}_1(t)], \end{aligned} \tag{4.24}$$

where $[A, B] \equiv AB - BA$ is the matrix commutator of A and B. The main strategy here is to choose terms in the series for $W(t)$ in Eq. (4.22) to correct the dynamics up to order $O(\varepsilon^m)$. In Ref. [185] it has been demonstrated that the correction can be achieved by truncation of $W(t)$ up to order m and to satisfy the relation

$$\varepsilon^n \int_0^{t_\mathrm{f}} \mathrm{d}t W_\mathrm{I}^{(n)}(t) = -\mathrm{i} \sum_{l=1}^{n} \Omega_l^{(n-1)}(t_\mathrm{f}). \tag{4.25}$$

Here, $\Omega_l^{(n)}(t)$ is the lth term of the Magnus expansion computed from the partially modified dynamical matrix

$$D_{\mathrm{mod,I}}^{(n)}(t) = \varepsilon V_\mathrm{I}(t) + \sum_{l=1}^{n} \varepsilon^l W_\mathrm{I}^{(l)}(t). \tag{4.26}$$

From Eqs. (4.25) and (4.26) we can determine the Magnus expansion up to mth order, i.e. for $m = 1$ we obtain

$$\Omega_1^{(0)}(t) = -\mathrm{i} \int_0^{t_\mathrm{f}} \mathrm{d}t V_\mathrm{I}(t). \tag{4.27}$$

For the requirement $\Omega_1^{(1)}(t_\mathrm{f}) = 0$ we find the expression for the first order correction term to be given by

$$\int_0^{t_\mathrm{f}} \mathrm{d}t W_\mathrm{I}^{(1)}(t) = -\int_0^{t_\mathrm{f}} \mathrm{d}t V_\mathrm{I}(t). \tag{4.28}$$

And hence, the 1$^{\mathrm{st}}$ order Magnus expansion is given by

$$\Omega_1^{(1)}(t) = -i \int_0^{t_\mathrm{f}} \mathrm{d}t \left[V_\mathrm{I}(t) + W_\mathrm{I}^{(1)}(t) \right]. \tag{4.29}$$

The higher orders can be calculated using Eqs. (4.25) and (4.26) recursively.

The substantial limitation of this perturbative approach is that it often demands terms in $W(t)$ that are not realizable due to experimental restrictions. Therefore, Roque et al. introduced a way to find terms in the series expansion of $W(t)$ that are always compatible with all experimental constraints [186]. This can be done by performing a basis decomposition of the control terms in Eq. (4.22), and then further decompose the time-dependent coefficients of $W^{(n)}(t)$ into a Fourier series.

First, the system is decomposed by a set of N_H time-independent Hermitian matrices A_j. These matrices are chosen to form a basis such that any matrix can be uniquely decomposed into that basis. We define for $D_0(t)$, $V(t)$ and $W(t)$

$$D_0(t) = \sum_j d_j(t) A_j, \tag{4.30}$$

$$V(t) = \sum_j v_j(t) A_j, \tag{4.31}$$

$$W^{(n)}(t) = \sum_j w_j^{(n)}(t) A_j. \tag{4.32}$$

Here, $d_j(t)$, $v_j(t)$ and $w_j^{(n)}(t)$ are real control fields associated with the decomposition of $D_0(t)$, $V(t)$ and $W^{(n)}(t)$. To give an example, the set of Hermitian matrices A_j for a two-mode system are the Pauli matrices $\boldsymbol{\sigma}_j$ with $j \in \{x, y, z\}$. Similarly, we can transform (4.31) and (4.32) to the interaction picture defined by the unperturbed dynamical matrix $D_0(t)$

$$V_\mathrm{I}(t) = \sum_j \widetilde{v}_j(t) A_j, \tag{4.33}$$

$$W_\mathrm{I}^{(n)}(t) = \sum_j \widetilde{w}_j^{(n)}(t) A_j. \tag{4.34}$$

The tildes describe the control fields in the interaction picture

$$\widetilde{v}_j(t) = \sum_l a_{lj}(t) v_\mathrm{I}(t), \tag{4.35}$$

$$\widetilde{w}_j^{(n)}(t) = \sum_l a_{lj}(t) w_\mathrm{I}^{(n)}(t), \tag{4.36}$$

where the functions $a_{lj}(t)$ fully encode the action of the interaction picture transformation on the basis $A_{j,l}(t) = \sum_l a_{jl}(t) A_l$.

In order to determine the first-order correction control term we can substitute Eqs. (4.33) and (4.34) to (4.28) to obtain an equation system that can be divided into a set of N_H equations

$$\int_0^{t_\mathrm{f}} \mathrm{d}t \widetilde{w}_j^{(1)}(t) = -\int_0^{t_\mathrm{f}} \mathrm{d}t \widetilde{v}_j(t). \tag{4.37}$$

For a two-mode system we would obtain a system of three coupled integral equations. Each equation is associated to a Pauli matrix ($\boldsymbol{\sigma}_x$, $\boldsymbol{\sigma}_y$ and $\boldsymbol{\sigma}_z$) or in other words the basis decomposition. The difficulty in solving these coupled integral equations can be overcome by choosing appropriate decomposition for the functions $w_j^{(1)}(t)$ that have support in the interval $[0, t_\mathrm{f}]$. Hence, we can use a finite Fourier series decomposition

$$w_j^{(1)}(t) = \sum_{k=1}^{k_{\max,j}} c_{jk}^{(1)} \cos(\omega_k t) + d_{jk}^{(1)} \sin(\omega_k t), \tag{4.38}$$

with $\omega_k = 2\pi k/t_\mathrm{f}$ and $d^{(1)}_{j0} = 0$. With the parametrization defined in Eq. (4.38), we can calculate the time integration over the duration of the protocol and use free Fourier coefficients c_{jk} and d_{jk} to fulfill Eq. (4.37). Note that all experimental constraints should be imposed in Eq. (4.38), hence, c_{jk} and d_{jk} should be zero if one does not have control over a certain operation $A_{j'}$. It is often required in the protocol that $w^{(1)}_{j'}(0) = w^{(1)}_{j'}(t_\mathrm{f}) = 0$, hence we find in Eq. (4.38) that the coefficient $c^{(1)}_{j'k}$ must obey $\sum_{k=0}^{k_{\max,j}} c^{(1)}_{j'k} = 0$. For this requirement, the truncated series for $w^{(1)}_{j'}(t)$ has the form

$$w^{(1)}_{j'}(t) = \sum_{k=1}^{k_{\max,j'}} c^{(1)}_{j'k}[1 - \cos(\omega_k t)] + d^{(1)}_{j'k} \sin(\omega_k t). \tag{4.39}$$

Since we know the explicit time dependence of $w^{(1)}_{j'}(t)$ in the control sequence, we can perform the time integration and this simply leads us to a system of N_H time-independent linear equations that can be solved analytically.

Summary:
Generally, fast and high-fidelity control of the system is a complex task, which is this case reduces to find correction terms $W(t)$. Here, we use an analytical approach based on physical intuition, which can be summarized in three main steps. **(1)** The perturbative expansion of the correction term $W(t)$ in Eq. (4.22). **(2)** The decomposition of the system by a set of time-independent Hermitian matrices showed in Eqs. (4.30), (4.31) and (4.32). **(3)** The final Fourier expansion [see Eq. (4.38)] of the control fields with associated Fourier coefficients as free parameters to satisfy system of equations given by Eq. (4.37).

Singular Corrections Sometimes, experimental restrictions can put limitations in the control capability of $W(t)$. For example, there can be a bandwidth limitation, which would restrict the values of "k" when decomposing the field or maybe the problem is such that the coefficients associated to σ_z is a constant and the one associated to σ_y is zero. These are a typical situations where the corrections of the dynamical matrix become singular and the standard strategy described above is not applicable, due to the missing correction terms.

A naive solution would be to simply drop the terms that one can not implement, which makes the system's dynamics somewhat uncontrollable and it is indeed not the optimal approach. This problem, however, can be solved by using the commutation relation of the Hermitian basis to dynamically generate the missing terms, i.e. $[A_1, A_2] \propto \mathrm{i}A_3$. Here, the key point is to choose a basis that also has a closed Lie algebra structure. To use this property for the first order, we need to look for $W^{(1)}_\mathrm{I}(t)$ so that

$$\Omega^{(1)}_1(t_\mathrm{f}) + \Omega^{(1)}_2(t_\mathrm{f}) = 0. \tag{4.40}$$

We can further substitute the expressions for the first two Magnus expansion terms in Eq. (4.24) to Eq.(4.40) and obtain

$$-\mathrm{i}\int_0^{t_\mathrm{f}} \mathrm{d}t_1 D^{(1)}_{\mathrm{mod,I}}(t_1) - \frac{1}{2}\int_0^{t_\mathrm{f}} \mathrm{d}t_1 \int_0^{t_\mathrm{f}} \mathrm{d}t_2 \left[D^{(1)}_{\mathrm{mod,I}}(t_1), D^{(1)}_{\mathrm{mod,I}}(t_2)\right] = 0. \tag{4.41}$$

The commutation in the double integral in Eq. (4.41) will generate terms that are proportional to the missing term A_3 that is associated with $W^{(1)}_\mathrm{I}(t)$. So the price to pay in order to generate the missing correction terms in the singular case is to solve a nonlinear equation in $W^{(1)}_\mathrm{I}(t)$ [186].

When scaling up the strategy with arbitrary dimension N_{H}, we can write the Magnus expansion associated to $D^{(1)}_{\mathrm{mod}}(t) = \varepsilon V_{\mathrm{I}}(t) + W^{(1)}_{\mathrm{I}}(t)$ as

$$\sum_{l=1}^{\infty} \Omega^{(1)}_{\mathrm{I}}(t_{\mathrm{f}}) = \sum_{l=1}^{\infty} \left[\Omega^{(0)}_{l}(t_{\mathrm{f}}) + \delta\Omega^{(1)}_{l}(t_{\mathrm{f}}) \right]. \tag{4.42}$$

Here, $\Omega^{(0)}_{l}(t_{\mathrm{f}})$ are the Magnus terms that are only related to the uncorrected dynamical matrix $D^{(0)}_{\mathrm{mod,I}} = \varepsilon V_{\mathrm{I}}(t)$, and $\delta\Omega^{(1)}_{l}(t_{\mathrm{f}})$ contains higher-order commutators that generate the missing terms in $W^{(1)}_{\mathrm{I}}(t)$. The truncation of the summation in Eq. (4.42) will follow in case all the missing terms A_j in $W^{(1)}(t)$ are found. Assuming we generate the missing terms at $l = l_c$ with $\sum_{l=1}^{l_c} \delta\Omega^{(1)}_{l}(t_{\mathrm{f}})$, we can express Eq. (4.42) as

$$\sum_{l=1}^{l_c} \Omega^{(1)}_{l}(t_{\mathrm{f}}) = 0. \tag{4.43}$$

In order to solve Eq. (4.43), we follow the procedures described above for the standard linear strategy. $W^{(1)}(t)$ should be decomposed into a finite Fourier series [see Eq. (4.38)] and transformed to the interaction picture before inserting in Eq. (4.43). However, with the singular corrections the obtained system of Eqs. (4.43) are intrinsically nonlinear. Here, we have to solve polynomial equations that contain the coefficients c_{jk} and d_{jk} from Eq. (4.38).

4.2.2 Modified Pulse Sequence for the Two-Mode System

Now we use the Magnus-based strategy discussed above to enhance the sensing and readout states preparation of our two-mode system. We want to cancel the transitions from mode $\boldsymbol{a}_1$ to mode $\boldsymbol{a}_2$ on average [see Fig. 4.1 (b)]. Note that the mode transitions are the unwanted effects that we want to prevent, since we desire to initialize and prepare $\boldsymbol{a}_1$ as the sensing state $\boldsymbol{a}_s$, as mentioned above. In order to find the corrected leading and trailing edges of the frequency sweep [see step (II) and (IV) in Fig. 4.2], we need to seek the dynamical matrix $D(t) = D_0(t) + V(t)$. Here, $D_0(t)$ generates the desired dynamics that detunes the initial state $\boldsymbol{a}_1(t = 0)$ to the sensing state $\boldsymbol{a}_1(t = t_{\mathrm{f}}) = \boldsymbol{a}_s$. $V(t)$, however, is the spurious coupling that disrupts the desired dynamics. For the problem at hand (see Eq. (4.2)), and neglecting noise, we have

$$D_0(t) = \frac{1}{2}\Delta(t)\sigma_z, \tag{4.44}$$

and

$$V(t) = \frac{1}{2}\Omega_0(t)\sigma_x. \tag{4.45}$$

To follow the strategy, we introduce a control term $W(t)$, which cancels on *average* the spurious effects generated by $V(t)$. Formally, this leads to a modified dynamical matrix

$$D_{\mathrm{mod}}(t) = D(t) + W(t), \tag{4.46}$$

which generates a flow $\Phi_{\mathrm{mod}}(t)$. The control $W(t)$ must be chosen so that

$$\Phi_{\mathrm{mod}}(t_{\mathrm{f}}) = \Phi_0(t_{\mathrm{f}}), \tag{4.47}$$

where $\Phi_0(t)$ is the flow generated by $D_0(t)$ [see Eq. (4.44)].

From Eq. (4.39), we define $W(t) = \Delta_{\mathrm{corr}}(t)\sigma_z$, which is compatible with the constraints of the problems, where we are only able to control in time the field coupling to σ_z. Taking advantage of the mirror symmetry of the frequency-sweep around $t = t_\mathrm{r}/2$, we can express $\Delta_{\mathrm{corr}}(t)$ as

$$\Delta_{\mathrm{corr}}(t) = \begin{cases} \Delta_{\mathrm{even}}(t) + \Delta_{\mathrm{odd}}(t) & \text{for } 0 \leq t \leq t_\mathrm{s}, \\ 0 & \text{for } t_\mathrm{s} < t < t_\mathrm{f}, \\ \Delta_{\mathrm{even}}(t) - \Delta_{\mathrm{odd}}(t) & \text{for } t_\mathrm{f} \leq t \leq t_\mathrm{r}, \end{cases} \tag{4.48}$$

where $\Delta_{\mathrm{even}}(t)$ and $\Delta_{\mathrm{odd}}(t)$ are parametrized as finite Fourier series

$$\begin{aligned} \Delta_{\mathrm{even}}(t) &= \sum_{k=1}^{k_{\max}} c_k \left[1 - \cos\left(2\pi k \frac{t}{t_\mathrm{f}}\right)\right], \\ \Delta_{\mathrm{odd}}(t) &= \sum_{l=1}^{l_{\max}} d_l \sin\left(2\pi l \frac{t}{t_\mathrm{f}}\right). \end{aligned} \tag{4.49}$$

Here, c_k and d_l are the free Fourier coefficients one must find in order to fulfill Eq. (4.47). The number of free coefficients is set by choosing appropriate values for $k_{\max}$ and $l_{\max}$, e.g., one might want to constrain the bandwidth. We emphasize, that we parametrize Eq. (4.48) so that the coefficients c_k and d_l are the same for the leading and trailing edge of $\Delta_{\mathrm{corr}}(t)$.

Equations for c_k and d_l are found by transforming $D_{\mathrm{mod}}(t)$ to the interaction picture defined by $\Phi_0(t)$, i.e., $D(t) \rightarrow D_{\mathrm{mod,I}}(t) = \Phi_0^\dagger(t) D_{\mathrm{mod}}(t)\Phi_0(t) - \mathrm{i}\Phi_0^\dagger(t)\dot{\Phi}_0(t)$. We find $D_{\mathrm{mod,I}}(t) = V_\mathrm{I}(t) + W_\mathrm{I}(t)$, where

$$V_\mathrm{I}(t) = \frac{\Omega_0}{2}\left[\cos\left(\int_0^t \mathrm{d}t_1 \Delta(t_1)\right)\sigma_x - \sin\left(\int_0^t \mathrm{d}t_1 \Delta(t_1)\right)\sigma_y\right] \tag{4.50}$$

and

$$W_\mathrm{I}(t) = W(t). \tag{4.51}$$

By comparing $W_\mathrm{I}(t)$ with $V_\mathrm{I}(t)$, we notice that the control dynamical matrix $W(t)$ is singular [186]. Thus, we follow the strategy outlined in section 4.2.1 and in Ref. [186] to obtain a set of nonlinear equations for the coefficients c_k and d_l.

Here, we look for the coefficients c_k and d_l which fulfill the coupled equations

$$\begin{aligned} \frac{1}{2}\mathrm{Tr}\left[\sum_{k=1}^{4} \Omega_k^{(1)}(t_\mathrm{f})\sigma_x\right] &= 0, \\ \frac{1}{2}\mathrm{Tr}\left[\sum_{k=1}^{4} \Omega_k^{(1)}(t_\mathrm{f})\sigma_y\right] &= 0, \end{aligned} \tag{4.52}$$

where $\Omega_k^{(1)}(t_\mathrm{f})$ are the elements of the Magnus series generated by $D_{\mathrm{mod,I}}(t)$. Since we only want to prevent (coherent) transitions on average from mode $\boldsymbol{a}_1$ to mode $\boldsymbol{a}_2$ and vice versa, we only look for the coefficients c_k and d_l that cancel the off-diagonal elements of the Magnus expansion up to fourth order.

Since the non-linear system of equations in Eq. (4.52) generally has more than one solution, one can choose the solution that minimizes the norm of the vector of free parameters, i.e., the function $g = \sum_{k,l}(c_k^2 + d_l^2)$. In particular, it is numerically more efficient to directly minimize g under the constraints defined by Eq. (4.52).

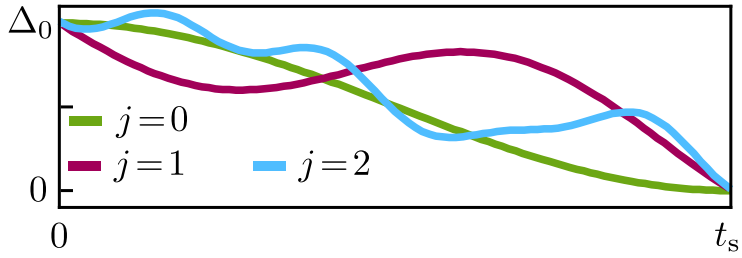

Figure 4.4 | Corrections of the Leading Edge.
Comparison of the leading edge of the uncorrected (green) and modified (red and blue) frequency-sweep allowing one to prepare the sensing state [step (II) in Fig. 4.2]. For $j = 1$ (red line), only a single harmonic component $k_{\max} = l_{\max} = 1$ is used. For $j = 2$, the correction terms in Eq. (4.49) are added up to the forth harmonics $k_{\max} = l_{\max} = 4$. **Reprinted from Ref. [167]**

In Fig. 4.4 we plot the pulse form of the leading edge that dynamically changes the detuning of the two-mode system from Δ_0 to 0 (at avoided crossing) as a function of time $t = [0, t_s]$. The green line in Fig. 4.4 represents the uncorrected single-tone function $f(t)$ of Eq. (4.13), that we assign with the index $j = 0$.

The Magnus strategy yields the function f_{mod} for the leading edge that is

$$f_{\text{mod}}(t) = f(t) + \Delta_{\text{even}}(t) + \Delta_{\text{odd}}(t). \tag{4.53}$$

Equation (4.53) defines a modified frequency sweep, where $\Delta_{\text{even}}(t)$ and $\Delta_{\text{odd}}(t)$ are the parametrized Fourier series in Eq. (4.49). We consider here two different modified frequency-sweeps. For $j = 1$ (red line in Fig. 4.4) is the case, where we only add a single harmonic component $k_{\max} = l_{\max} = 1$ to the Fourier series. For $j = 2$, we use $k_{\max} = l_{\max} = 4$ (see blue line in Fig. 4.4). In the following, we will label Mod1 as the modified frequency sweep associated with $j = 1$ (red) and $j = 2$ with Mod2 (blue), respectively.

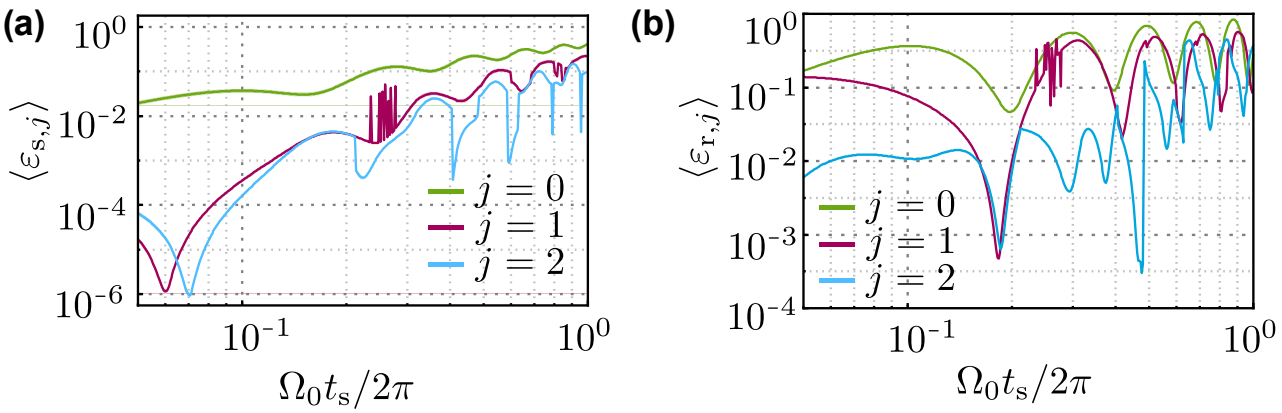

Figure 4.5 | Fidelity in State preparation.
(a) Comparison of the averaged sensing state error fidelity [see Eq. (4.54)] between the uncorrected (green), correction by adding one harmonic component $k_{\max} = l_{\max} = 1$ (red, Mod1), and corrections with 4 harmonic components $k_{\max} = l_{\max} = 4$ (blue, Mod2) frequency-sweeps as a function of t_s. **(b)** Same as (a) for the readout state. **Reprinted from Ref. [167]**

To compare the performance of the different frequency-sweeps, we consider the state fidelity errors

$$\begin{aligned}\varepsilon_{\mathrm{s},j} &= 1 - |\boldsymbol{a}_1^{\mathsf{T}}\Phi_j(t_\mathrm{s})\boldsymbol{a}_1|^2,\\ \varepsilon_{\mathrm{r},j} &= 1 - |\boldsymbol{a}_1^{\mathsf{T}}\Phi_j^{\mathsf{T}}(t_\mathrm{f})\Phi_j(t_\mathrm{r})\boldsymbol{a}_1|^2,\end{aligned} \tag{4.54}$$

associated to the preparation of the sensing and readout state. Again, $j \in \{0, 1, 2\}$ labels the different frequency-sweeps: $j = 0$ is the uncorrected detuning sweep [see Eqs. (4.5) and (4.13)], and $j = 1, 2$ are associated to the modified frequency-sweeps Mod1 and Mod2, respectively. The flow $\Phi_j(t)$ allows one to find the state vector at time t, e.g. $\boldsymbol{a}(t) = \Phi_j(t)\boldsymbol{a}(0)$, and obeys the equation of motion (see, e.g., Ref. [63])

$$i\dot{\Phi}_j(t) = D_j(t)\Phi_j(t), \tag{4.55}$$

with $D_j(t)$ given by Eq. (4.2).

Fig. 4.5 (a) and (b) display the averaged errors in the preparation for the sensing state $\langle\varepsilon_{\mathrm{s},j}\rangle$ and the readout state $\langle\varepsilon_{\mathrm{r},j}\rangle$ [obtained by averaging $\varepsilon_{\mathrm{s},j}$ and $\varepsilon_{\mathrm{r},j}$ over noise, see Eq. (4.3)] as a function of t_s, respectively. To achieve error fidelities on the order of 10^{-3} with the uncorrected frequency-sweep (green trace), one would need to fulfill $\Omega_0 t_\mathrm{s}/(2\pi) \ll 10^{-2}$, which would require an AWG with a very large bandwidth. In stark contrast, the corrected detuning-sweeps (red and blue traces) allow one to achieve error fidelities smaller than 10^{-3} for values of $\Omega_0 t_\mathrm{s}$ that are much larger than the ones required for a quasi instantaneous sweep, which reduces the bandwidth requirements associated with such a sweep. In the appendix A.1, we further discuss the effects of noise and low fidelity state preparation on the sensing protocol.

4.2.3 Inaccuracy in Frequency Estimation with trivial Signal Processing

Although our modified frequency-sweeps allow us to prepare the ideal sensing and readout states, they do not allow us to correctly estimate unknown frequencies from short-time signals, i.e., $2 \leq (\Omega_0/2\pi)t_\mathrm{w} \leq 4$.

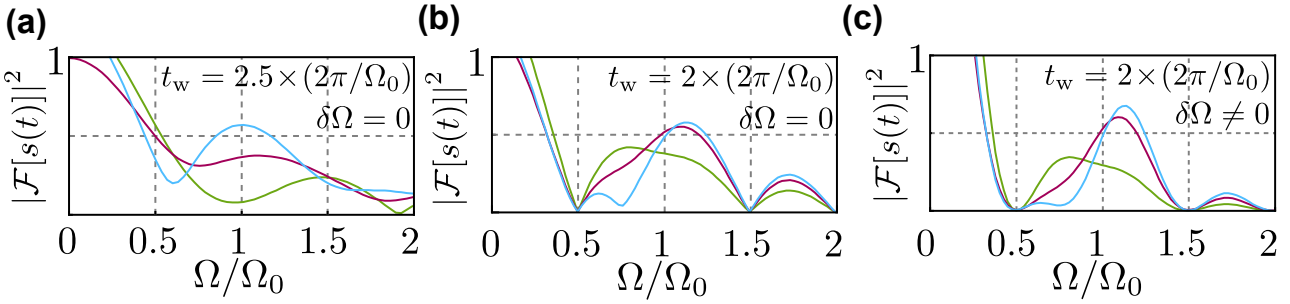

Figure 4.6 | Frequency Estimation with Trivial Signal Processing.
(a) Discrete spectral density $|\mathcal{F}\langle s(t)\rangle|^2$ obtained from signals generated with the uncorrected ($j = 0$, green), Mod1 ($j = 1$, red) and Mod2 ($j = 2$, blue) frequency-sweep for $t_\mathrm{w} = 2.5 \times (2\pi/\Omega_0)$ and no noise contribution that is $\delta\Omega = 0$. **(b)** Same as (a) for $t_\mathrm{w} = 2 \times (2\pi/\Omega_0)$. **(c)** Same as (b) for $\delta\Omega \neq 0$ [see Eqs. (4.3) and (4.4)]. **Reprinted from Ref. [167]**

We illustrate this in Fig. 4.6 (a)-(c) where we compare the modulus squared of the discrete signal Fourier transform (spectral density), $|\mathcal{F}[\langle s(t)\rangle]|^2$, for different case scenarios. We stress that, unlike for the case of a sensing experiment, the spectra were obtained assuming that we know exactly the value of Ω_0 to capture only the effects of the shortcomings associated to Fourier transforms of short-time signals.

The modified frequency-sweeps (red and blue traces) lead to spectra where the global maximum (with the 0-frequency peak excluded) can be more easily identified. However, the global maximum is not located at $\Omega/\Omega_0 = 1$. Our results also show that small changes in t_w can result in different spectra with maxima located at very different frequencies, which obviates a correct frequency estimation.

In the following section, we discuss on the shortcoming associated with the Fourier transform of a short and finite signal and the procedure utilizing windowing functions to enhance the estimation of the unknown frequency.

4.3 Signal Processing Technique

In this section, we briefly describe the fundamental and most important technique in signal processing that is based on Fourier analysis to transform signals from the time into the frequency domain. The motivation for the transformation is the direct visibility in contributions of all frequency components in the frequency domain and hence, they can easily be extracted. In the time domain, where the "Ramsey fringes" are measured, it is difficult to estimate frequency distributions with high precision due to the absence of a precise analytic function to fit the data.

Fourier analysis and the corresponding Fourier transform are among the most important algorithms used for image and audio compression, high performance scientific computing and signal processing. A continuous-time periodic (and aperiodic) signal can be simply expressed by a sum of harmonically related sine and cosine waveforms. These are generally known as the Fourier series expansion of the signal, which involves the decomposition of periodic (aperiodic) signals into their individual frequency components [184]. Generally, the continuous-time Fourier series of a aperiodic signal can be defined as

$$\mathcal{F}(\omega) = \int_{\infty}^{\infty} s(t) \mathrm{e}^{-\mathrm{i}\omega t} \, \mathrm{d}t. \tag{4.56}$$

Here, the complex exponential $\mathrm{e}^{-\mathrm{i}\omega t}$ provides the frequency components that are used as the orthogonal basis functions. $s(t)$ is the analytic function that can be decomposed into individual Fourier coefficients and is also known as the inverse Fourier transform

$$s(t) = \frac{1}{2\pi} \int_{\infty}^{\infty} \mathcal{F}(\omega) \mathrm{e}^{\mathrm{i}\omega t} \, \mathrm{d}\omega. \tag{4.57}$$

We want to highlight a very useful property of the Fourier transform that is the convolution theorem. A convolution is an integral expressing the degree of overlap of a function s_1 with another function s_2.

$$s_1 * s_2 \equiv \int_{-\infty}^{\infty} s_1(\tau) s_2(t - \tau) \, \mathrm{d}t. \tag{4.58}$$

The theorem states that the convolution of the two signals in the time domain is a point wise product of their Fourier transform counterparts in the frequency domain and vice versa

$$s_1(t) * s_2(t) \longleftrightarrow \mathcal{F}_1(\omega) \cdot \mathcal{F}_2(\omega). \tag{4.59}$$

This theorem allows us to apply the so-called window functions to the measured signal in order to suppress unwanted spurious effects, such as spectral leakage that hinders precise frequency estimation.

4.3.1 Discrete Fourier Transform (DFT) of Short Signals

Most of the time, data obtained from experiments in the laboratory or from simulations are sampled with a finite rate. Consequently, there exists no analytic function required to perform the Fourier transform. Furthermore, it is also apparent that it is not possible to implement the Fourier transform for general purpose digital signal processing. The integral sign in Eq. (4.56) requires an infinite amount of computational effort. These difficulties can be overcome by the so-called discrete Fourier transform (DFT), that is more accessible for digital implementation.

The DFT is defined for n_{samp} samples of x_n at n_{samp} equally spaced frequencies ω_k. Note that n is the discrete location with the corresponding amplitude x_n. Given a periodic signal with period T and n_{samp} sampling points, the DFT is defined as [184]

$$\mathcal{F}[k] = \sum_{n=0}^{n_{\text{samp}}-1} s[n] \mathrm{e}^{-\mathrm{i}\frac{2\pi}{T}kn}, \quad \text{for } k = 0, 1, \ldots, n_{\text{samp}} - 1. \tag{4.60}$$

In other words, the DFT is the method to transform the data vector $x[n]$ into its sine and cosine components by Fourier expansion instead of transforming an analytic function $s(t)$. The inverse DFT is defined as

$$s[n] = \frac{1}{T} \sum_{k=0}^{N-1} \mathcal{F}[k] \mathrm{e}^{\mathrm{i}\frac{2\pi}{T}kn}, \quad \text{for } n = 0, 1, \ldots, n_{\text{samp}} - 1. \tag{4.61}$$

4.3.2 Zero-Padding

The main goal of our work is to find a simple way to estimate the frequency of an oscillating signal in the time domain, namely the Ramsey fringe, with high precision. But when dealing with signals that are constructed from a finite number of sampling points, we need to take additional systematic errors into account. One source of such error is due to small n_{samp} that will lead to *scalloping loss*. This loss mechanism is produced by the inability of the DFT to observe the spectrum as a continuous function because the Fourier transform spectrum is limited to integer multiple of the fundamental frequency ω_k. In the worst case scenario, if the spectral component of interest is located, e.g., between ω_{k-1} and ω_k, the component will then be seen by both frequencies and the maximum of interest is distributed among these wrong frequencies. So the lack in resolution does not allow the Fourier transform to resolve the real maxima of the spectrum any further than the frequency spacing

$$\delta\omega = \frac{\omega_s}{n_{\text{samp}}}, \tag{4.62}$$

where ω_s is the sampling rate and n_{samp} is the number of sampling points of the signal. This source of error is, however, relatively simple to fix by using the zero-padding technique, as described in signal processing textbooks, e.g., in Ref. [184]. Zero-padding consist in extending the signal with n_{pad} zeros yielding a $\left[\left(n_{\text{samp}} + n_{\text{pad}}\right)/2\right]$-points discrete Fourier transform. To further reduce the effects of scalloping loss we use interpolation of the padded discrete spectrum [206].

4.3.3 Spectral Leakage

The second source of error that mitigates the high precision in frequency estimate is related to the selection of a finite-time interval, e.g. the waiting time t_{w} in the Ramsey sequence (see Sec. 4.1). The coherence time of the sensor defines an upper limit for the time window in which a measurement is possible. By performing the DFT, we project the time signal into a set of orthogonal trigonometric

basis functions. From the all possible frequencies, only those which coincide with the basis will project into a single basis vector. All other frequencies will exhibit non-zero projection on the entire basis set. This behaviour is often referred to as spectral leakage [207].

Rectangular Window (no window) To follow the discussion in the text book [184], the spectral leakage is often related to the effect of *windowing*. The obtained spectrum in the time domain can always be expressed as the convolution of the measured signal and a window function. Now assuming the case, where we directly analyze measured data. Even thought there is "no (extra) window" involved, this situation still corresponds to a "rectangular window", simply because the data set has a beginning and a finite end. We illustrate this for the case of the rectangular window, which is the situation encountered when directly analyzing a measured signal, and show how this inevitably leads to the creation of new frequency components. This is apparent by Fourier transforming a cosine function that is truncated by a rectangular window function. We define a continuous-time cosine function as

$$s(t) = \cos(\omega_0 t), \quad \text{for } -\infty < t < \infty. \tag{4.63}$$

The continuous-time Fourier transform of Eq. (4.63) is given by

$$\mathcal{S}(\omega) = \pi[\delta(\omega + \omega_0) + \delta(\omega - \omega_0)], \tag{4.64}$$

which can be considered as two Dirac-delta impulses located at $\pm\omega_0$. In a real experiment, however, we need to record a finite number of data samples over a duration $0 < t < t_\mathrm{w}$. That effectively creates a rectangular window

$$w(t) = \begin{cases} 1, & \text{for } 0 \le t \le t_\mathrm{w}, \\ 0 & \text{elsewhere .} \end{cases} \tag{4.65}$$

The Fourier transform of the rectangular function in Eq. (4.65) is the sinc function

$$\mathcal{W}(\omega) = t_\mathrm{w}\,\mathrm{sinc}\left(\frac{\omega t_\mathrm{w}}{2\pi}\right)\mathrm{e}^{\frac{-\mathrm{i}\omega t_\mathrm{w}}{2}}, \quad \text{for } -\infty < \omega < \infty. \tag{4.66}$$

Altogether, the truncated cosine function can be expressed as

$$s_w(t) = s(t)w(t) = \begin{cases} \cos(\omega_0 t), & \text{for } 0 \le t \le t_\mathrm{w}, \\ 0 & \text{elsewhere .} \end{cases} \tag{4.67}$$

From the convolution theorem [see Eq. (4.59)] the DFT of $s_w(t)$ is found to be

$$\begin{aligned} \mathcal{S}_w(\omega) &= \mathcal{S}(\omega) * \mathcal{W}(\omega) \\ &= \pi t_\mathrm{w}[\mathrm{sinc}((\omega+\omega_0)t_\mathrm{w}/2\pi) + \mathrm{sinc}((\omega-\omega_0)t_\mathrm{w}/2\pi)]\mathrm{e}^{\frac{-\mathrm{i}\omega t_\mathrm{w}}{2}}, \quad \text{for } -\infty < \omega < \infty. \end{aligned} \tag{4.68}$$

The discrete Fourier transform of a finite-time cosine function truncated by a rectangular window exhibits two sinc-function components centered at $\pm\omega_0$ with a series of side-lobes that slowly decay (see e.g. blue curves in Fig. 4.7). This spurious peaks occur due to the truncation of the signal and is unavoidable when applying DFT. The resulted spectral leakage is a combination of the before mentioned sinc side-lobes and the transform of the sinusoidal components, whose frequencies are not integer multiples of the reciprocal of the period $T = 2\pi/\omega_0$. Consider a finite input signal to the DFT $f[n] = A\mathrm{e}^{\mathrm{i}\omega_0 n\delta t}$, where $\delta t = t_\mathrm{w}/n_\mathrm{samp}$. The DFT can be computed as [184]

$$\begin{aligned} \mathcal{F}[k] &= \sum_{n=0}^{n_{samp}-1} f[n]\mathrm{e}^{\frac{-\mathrm{i}2\pi nk}{n_\mathrm{samp}}}, \quad k = 0, 1, \ldots, n_\mathrm{samp} - 1 \\ &= A\mathrm{e}^{\left[\mathrm{i}\frac{n_\mathrm{samp}-1}{2}\left(\omega_0\delta t - \frac{2\pi k}{n_\mathrm{samp}}\right)\right]} \cdot \frac{\sin\left[\frac{n_\mathrm{samp}}{2}\left(\omega_0\delta t - \frac{2\pi k}{n_\mathrm{samp}}\right)\right]}{\sin\left[\frac{1}{2}\left(\omega_0\delta t - \frac{2\pi k}{n_\mathrm{samp}}\right)\right]}. \end{aligned} \tag{4.69}$$

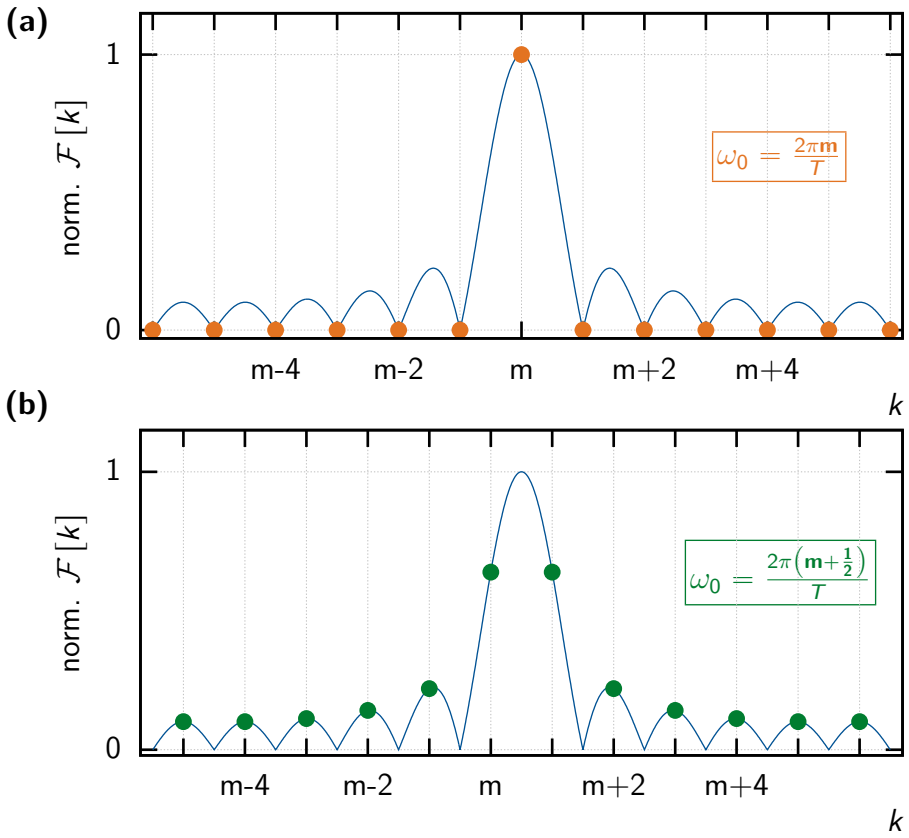

Figure 4.7 | Spectral Leakage.
(a), Zero leakage for frequency $\omega_0 = \frac{2\pi m}{T}$ which is an integer multiple m of reciprocal of the period T. The frequency response of the sinc function [blue lines in both (a) and (b)] is added for comparison. The DFT outputs (orange dots) show a maximum for $\mathcal{F}[k = m]$ that exactly coincides with the maximum of the sinc function. The adjacent output points are zero. **(b)**, The distribution of the discrete Fourier spectrum (green dots) when ω_0 is not an integer (here: $m + 1/2$). The amplitude of the main output point $\mathcal{F}[m = k]$ is not at the maximum of the sinc function. The response of the adjacent points, however, is non zero and coincides with the maxima of the sidelobes. This spreading of energy to the sidelobes is referred to as spectral leakage.

In Fig. 4.7, we plot the normalized DFT in Eq. (4.69) for two cases. Fig. 4.7 (a) illustrates the frequency spectrum with zero leakage for $\omega_0 = m\frac{2\pi}{T}$ (orange dots) for a same length that equals an integer m of the period T. For comparison, we plot the sinc-function (blue lines) of the corresponding continuous Fourier transform. The response has a maximum amplitude at $k = m$, which coincides with the main-lobe and the remaining frequency contribution is zero at the side-lobes. Spectral leakage occurs, when ω_0 is not an integer multiple of the reciprocal of T. Figure 4.7 (b) illustrates the situation of maximum spectral leakage which occurs for $\omega_0 = \left(m + \frac{1}{2}\right)\frac{2\pi}{T}$. The contribution to the side-lobes are non zero and there are two local maxima. This spread of energy is referred to as frequency leakage, which leads to a wrong estimation in frequency.

Blackman-Harris Window Another intuitive way to understand the mechanism of spectral leakage is that the frequency components in the measured signal do not match with those from the basis set in the DFT. Hence, the periodic extension of the signal will cause discontinuities at the boundaries of the observation. These discontinuities are responsible for the spectral leakage over the entire basis set. A very common way to minimize the effect of spectral leakage is to apply weighting functions (also known as window functions) to the data in the time domain. This approach effectively reduces the discontinuity at the boundary of the periodic extension [207]. In other words, an appropriate

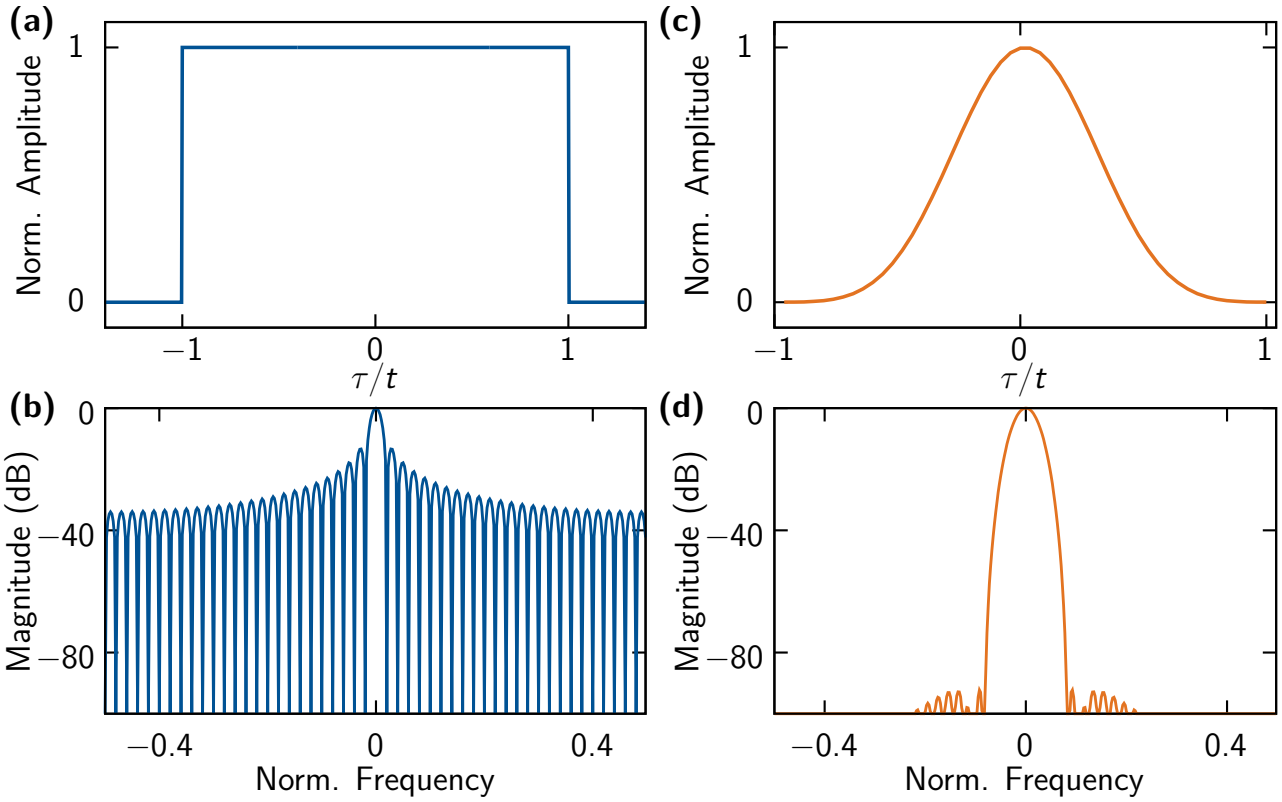

Figure 4.8 | Rectangular Window vs. Blackman-Harris Window.
(a), The scheme of the rectangular window (no window) function defined in Eq. (4.65). **(b)**, The continuous-time Fourier spectrum of the rectangular window shows a moderate decrease in the side-lobes by −6 dB per octave. **(c)**, The Blackman-Harris window function (see Eq. (4.70)). **(d)**, The continuous-time Fourier spectrum of the Blackman-Harris window shows strongly suppressed side-lobes and broadened main-lobe as a direct consequence of the reduced amplitude at the leading and trailing edges.

window function will suppress the contribution of the side-lobes (in frequency domain) to minimize the leakage.

Among the numerous window functions, the so-called Blackman-Harris (BH) window function is known to strongly suppress the sidelobes, thus greatly minimizing the effect of the spectral leakage. The BH window is defined as the sum of four-terms [184]

$$w_{\mathrm{BMH}}(t) = \begin{cases} a_0 + a_1 \cos\left(\frac{\pi t}{\tau}\right) + a_2 \cos\left(\frac{2\pi t}{\tau}\right) + a_3 \cos\left(\frac{3\pi t}{\tau}\right), & \text{for } |t| \le \tau \\ 0, & \text{elsewhere .} \end{cases} \tag{4.70}$$

With the coefficients $a_0 = 0.35875$, $a_1 = 0.48829$, $a_2 = 0.14128$ and $a_3 = 0.01168$. The corresponding Fourier transform is given by

$$\begin{aligned} \mathcal{W}_{\mathrm{BMH}}(\omega) = 2a_0 \frac{\sin(\omega\tau)}{\omega} &+ a_1 \left[\frac{\sin((\omega+\pi/\tau)\tau)}{(\omega+\pi/\tau)} + \frac{\sin((\omega-\pi/\tau)\tau)}{(\omega-\pi/\tau)} \right] \\ &+ a_2 \left[\frac{\sin((\omega+2\pi/\tau)\tau)}{(\omega+2\pi/\tau)} + \frac{\sin((\omega-2\pi/\tau)\tau)}{(\omega-2\pi/\tau)} \right] \\ &+ a_3 \left[\frac{\sin((\omega+3\pi/\tau)\tau)}{(\omega+3\pi/\tau)} + \frac{\sin((\omega-3\pi/\tau)\tau)}{(\omega-3\pi/\tau)} \right], \quad \text{for } -\infty < \omega < \infty. \end{aligned} \tag{4.71}$$

In Fig. 4.8, we demonstrate the effectiveness in side-lobe suppression of the Blackman-Harris window compared to the rectangular (or no window) function. From Eqs. (4.65) and (4.66) we know the Fourier transform of a rectangular window [see Fig. 4.8 (a)] exhibits a frequency spectrum with the sinc distribution (Fig. 4.8 (b)). The first side-lobes in the continuous-time Fourier spectrum show a reduction in amplitude by only -13 dB compared to the main-lobe. All the subsequent side-lobes fall off at -6 dB per octave, which is expected from a function with an abrupt discontinuity [184, 207]. The Blackman-Harris window illustrated in Fig. 4.8 (c), on the other hand, has a smooth transition at the beginning and the end of the window. Remarkably, the side-lobes suppression is substantial that is -92 dB compared to the main-lobe (Fig. 4.8 (d)). The price to pay is a trade-off between the side-lobes suppression and the broadening in the width of the main-lobe. The discrete-time Fourier transform of the Blackman-Harris window exhibits a width in the main-lobe that is four times larger than that of the rectangular window.

Summary In the following, we summarize the shortcomings associated with Fourier transforms for short signals discussed above (see Fig. 4.9). We employ the cosine function in Eq. (4.63) over a finite interval of time. We consider two different intervals of time defined as $t_{1,\max} = 4T$ and $t_{2,\max} = 4.5T$, where $T = 2\pi/\omega_0$ [see Fig. 4.9 (a)-(b)]. Let us first consider a situation where one could continuously measure the signal. A finite-time signal is equivalent to the pointwise multiplication of an infinite signal with a rectangular window. The corresponding Fourier transform produces a spectrum, whose value at $\omega = \omega_0$ is the sum of all the spectral contributions of the signal weighted by the spectrum of the window centered at ω_0 (convolution theorem). As a result, even a simple, single frequency spectrum appears with multiple frequency components [see Fig. 4.9 (c)].

Experimentally, however, it is not always possible to measure a continuous signal, but it can be sampled at certain rates [Fig. 4.9 (d) and (e)]. In this situation, one uses the discrete Fourier transform (DFT) to extract information of frequency components (also see discussion in Sec. 4.3.1). This results in a spectrum with a finite number of points [dotted points in Fig. 4.9 (f)], from which frequency estimation is limited due to a finite frequency resolution set by $\delta f = 1/t_{\max}$. This is known as scalloping loss (see Sec. 4.3.2).

For the sake of visibility, we illustrate the continuous lines in Fig. 4.9 (f) showing the discrete-time Fourier transform (DTFT) associated to the sampled signals in (d-e). Note that the DTFT is the Fourier transform of a discrete time signal but the number of sampling point n_{samp} is allowed to approach infinity. Hence, the output of the DTFT can be seen as a continuous function. In contrast, the discrete Fourier transforms [dots in Fig. 4.9 (f)] sample the continuous spectrum generated by the discrete-time Fourier transform with a frequency interval δf.

To minimize scalloping losses, the common practice requires one to use zero-padding [Fig. 4.9 (g)-(h)], which effectively reduces δf. Additionally, zero-padding forces the signal to appear aperiodic, which mitigates spectral leakage when the time interval is not an integer multiple of the period [see Fig. 4.9 (i)]. However, the accuracy of the frequency estimate is still limited by the use of a rectangular window (or no-window), which as we discussed above, also induces spectral leakage [inset in Fig. 4.9 (i)].

Using specific window functions, e.g., the Blackmann-Harris window [Fig. 4.9 (j)-(k)] [207], one further mitigates spectral leakages. This leads to a better estimate of the signal frequency as seen in Fig. 4.9 (l). As mentioned in Sec. 4.3.2, using interpolation of the Fourier spectrum further enhances the accuracy of the frequency estimate.

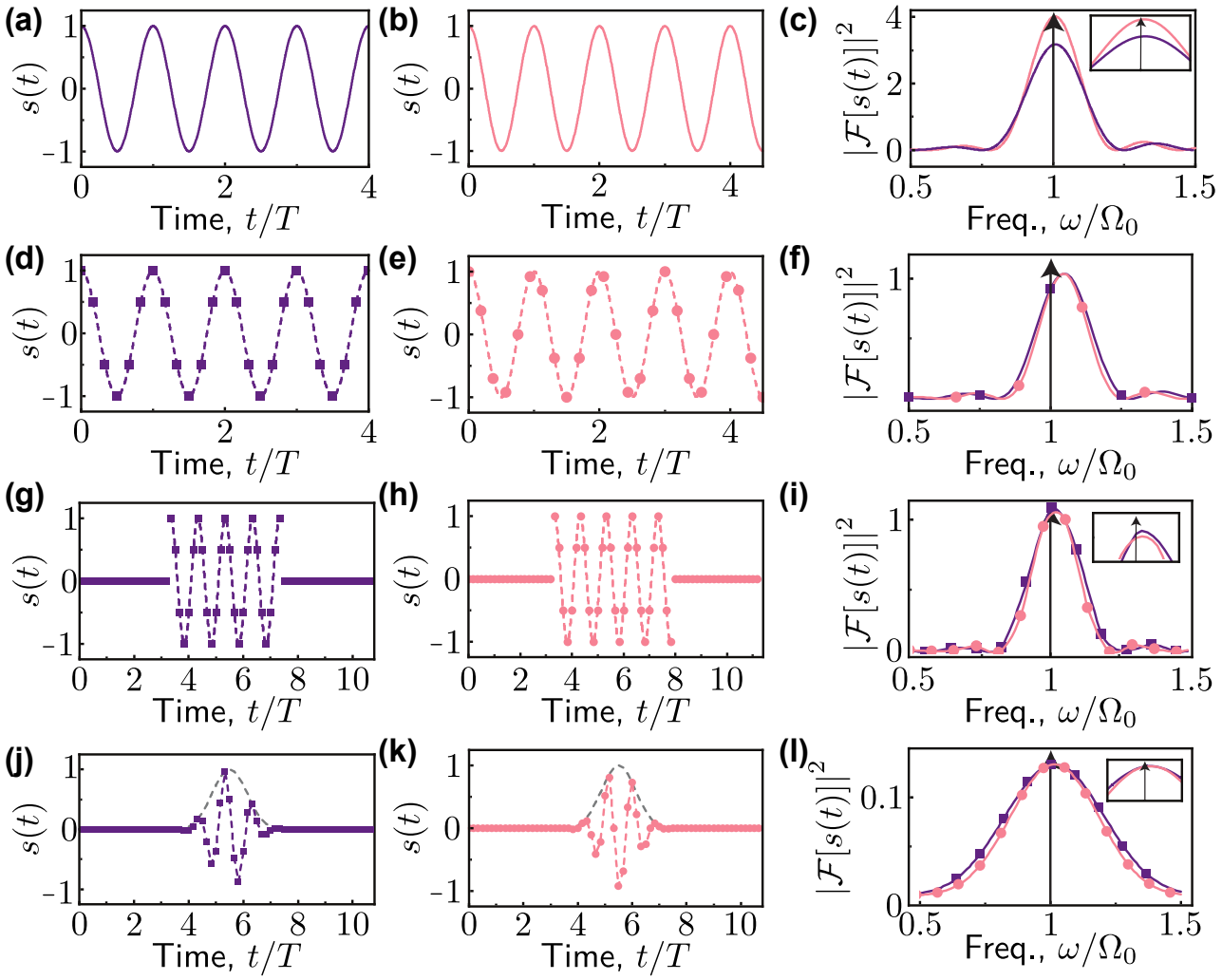

Figure 4.9 | Spectral Leakage and Scalloping Losses.
Time and frequency domain representation of $s(t) = \cos(\omega_0 t)$ for a time interval of $4T$ (purple) and $4.5T$ (pink). **(a-b)**, Continuous time measurement with finite time windows and their corresponding continuous Fourier transform in **(c)**. **(d-e)**, Discrete sampling of a continuous signal for both time intervals. The associated discrete Fourier transform (dots) and discrete-time Fourier transforms (solid lines) are shown in **(f)**. **(g-h)** Zero-padding of the sampled signal and corresponding interpolated discrete Fourier transforms in **(i)**. Post-processing of the sampled signal with a Blackmann-Harris window and zero-padding **(j-k)**. The resulting discrete Fourier transform is less susceptible to spectral leakage **(l)**. **Reprinted from Ref. [167]**

4.4 Iterative Adaptive Spectroscopy for Frequency Estimation

Beside the corrections in state preparations with the Magnus-based strategy, we show how an iterative procedure combining both an update on the estimate for Ω_0 and different windowing schemes [184] to process the measured signal solves the issues outlined above and yields a high-precision estimate of the unknown frequency.

From the discussion in Sec. 4.3, we know that windows (sometimes also referred to as tapers) are weighting functions designed to simplify the analysis of harmonic signals. In particular, the window functions apply selective weights to reduce spectral leakage associated with finite measurement windows [184, 207].

As apparent in Figs. 4.8 (c) and (d) the Blackman-Harris window [184, 207] is constructed to effectively reduce spectral leakage. However, as a downside, the width of the main-lobe from the BH window is substantially broadened. Additionally, we must choose the measurement-time window with at least four periods of oscillations: $(\Omega_0/2\pi)t_w \geq 4$. This is due to the fact that the BH window effectively suppresses the oscillations of the left and right sides of the signal [compare for instance Figs. 4.9 (g) and (j)]. Hence, the total number oscillations are reduced to two, which is the minimum number required for the frequency estimation. The reduction in oscillation period leads to a decrease in amplitude of the spectral density [see Figs. 4.9 (i) and (l)], which can render frequency detection problematic, specially for short-time, noisy signals. Finally, and we cannot stress this enough, while windowing reduces spectral leakage, it can never completely suppress it. Thus, even with windowing, high-precision frequency estimation is still limited by artifacts linked to discrete Fourier transforms of short-time signals.

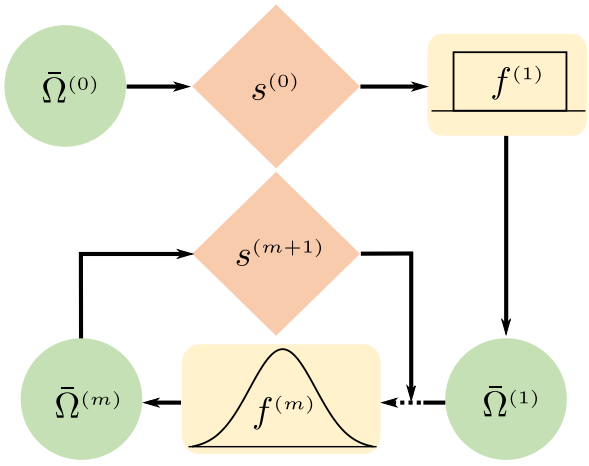

Figure 4.10 | Iterative Adaptive Spectroscopy of Short Signals.
Flow chart illustrating the steps involved at each iteration. From the first frequency estimation $\bar{\Omega}^{(0)}$, i.e. obtained from a spectroscopy measurement, the Ramsey interferometry $s^{(0)}$ is performed. The resulting Ramsey fringe in the time-domain is subsequently transformed into the frequency domain using DFT with zero-padding and rectangular windowing. From the new estimated frequency $\bar{\Omega}^{(1)}$ we repeat the procedure by updating the Magnus-based correction to calculate the Fourier components c_k and d_l [see Eq. (4.49)]. Note that by performing the 2nd DFT of the Ramsey fringe to estimate $\bar{\Omega}^{(2)}$, we introduce the Blackman-Harris window function to suppress spectral leakage and scalloping effects. The iterative procedure can be repeated arbitrarily. **Reprinted from Ref. [167]**

To overcome this limitation we use the iterative, adaptive sensing (IAS) protocol depicted in Fig. 4.10. Each interaction consists in performing Ramsey interferometry (see Sec. 4.1) involving the Magnus-based (see Sec. 4.2.1) high fidelity state transfer (rhombi in Fig. 4.10) with a frequency-sweep that takes into account our current knowledge of the frequency estimate [circles in Fig. 4.10]. This way we can iteratively suppress systematic frequency shift errors originating from spectral leakage when t_{w} (step III in Fig. 4.2) is not an integer multiple of the period. This is done by updating after each iteration the measurement-time window

$$t_{\mathrm{w}}^{(m+1)} = n_{\mathrm{p}} \times \frac{2\pi}{\bar{\Omega}^{(m+1)}} \quad m \in \mathbb{N}_0, \tag{4.72}$$

where $\bar{\Omega}^{(m)}$ denotes the frequency estimate obtained at iteration m and $n_{\mathrm{p}} \geq 4$ is an integer that defines how many periods are in the measurement-time window.

We assume in Eq. (4.72) that a prior estimate of the frequency, which we denote by $\bar{\Omega}^{(0)}$, is known. This quantity can, e.g., be obtained with "standard" Ramsey interferometry or by using spectroscopic methods. We also update after each iteration the leading and trailing edge of the modified detuning-sweeps since the Magnus-based strategy for control requires one to know the parameters entering the equations of motion [see Eqs. (4.2) and (4.55)]. Thus, we decrease at each iteration the error in preparing both the sensing and readout state.

A new estimate of the frequency is obtained by processing the acquired signal either with a window function tailored to either enhance the amplitude of the Fourier spectrum for the first iteration or the quality of the frequency estimation for all subsequent iterations (rectangles in Fig. 4.10). The window functions for signal processing are chosen according to

$$f^{(m)}(t) = \begin{cases} \Theta(t) - \Theta(t - t_{\mathrm{w}}^{(1)}) & \text{for } m = 1, \\ f_{\mathrm{BH}}(t/t_{\mathrm{w}}^{(m)} - 1/2) & \text{for } m \geq 1, \end{cases} \tag{4.73}$$

where $\Theta(t)$ denotes the Heaviside function and $f_{\mathrm{BH}}(t)$ is the Blackman-Harris window function [see Eq. (4.70)]. We deliberatively choose not to process the signal after the first iteration (we use a rectangular window) [3] in order to generate a spectral density with larger amplitudes, from which maxima are easier to extract.

The other source of systematic errors arise when dealing with a signal which is constructed from a finite number of sampling points (measurements) n_{samp}. A small n_{samp} will lead to scalloping, i.e., the $\lfloor n_{\mathrm{samp}}/2 \rfloor$-point discrete Fourier transform does not resolve the real maxima of the spectrum [see Fig. 4.7 (b)]. This is, however, easily fixable by using zero-padding, as described in Sec. 4.3.2.

Fig. 4.11 shows the relative error of the frequency estimate

$$\varepsilon_{\Omega}^{(1)} = |1 - \bar{\Omega}_{(1)}/\Omega_0| \tag{4.74}$$

as a function of n_{samp} for $n_{\mathrm{p}} = 4$ for the first iteration [$m = 1$ in Eqs. (4.72) and (4.73)] of our iterative sensing scheme. Here n_{pad} is chosen such that $n_{\mathrm{samp}} + n_{\mathrm{pad}} = 1000$. Independently of the frequency-sweep used, doubling n_{samp} only leads to a small variation of the relative error. This allows us to identify $\lceil n_{\mathrm{samp}}/n_{\mathrm{p}} \rceil = 8 > 2$ as a good compromise between the error and experimental cost, i.e., the number of measurements required. The results show the advantage of using the modified frequency-sweeps Mod1 (red trace) and Mod2 (blue trace) over the uncorrected one (green trace); the smaller the error in preparing both the sensing and readout state the smaller the relative error of the first frequency estimate for a signal of identical duration.

[3] From the point of view of signal processing applying a rectangular window is the same as applying no window.

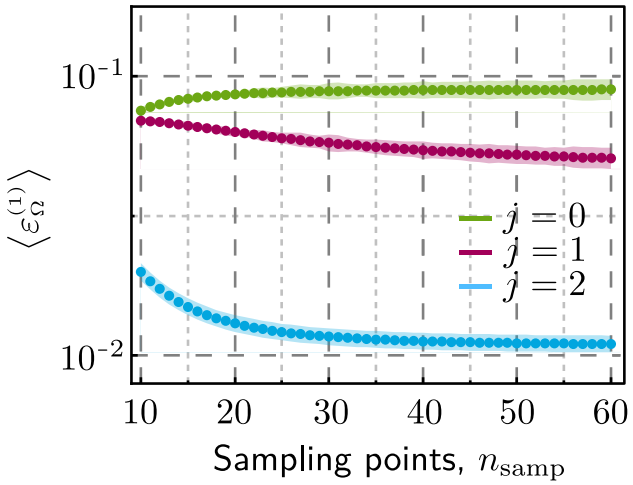

Figure 4.11 | Frequency Estimation Error versus Sampling points.
Comparison of the relative error $\varepsilon_\Omega^{(1)}$ of the frequency estimation as a function of sampling points n_{samp} for the uncorrected ($j = 0$, green), corrected Mod1 ($j = 1$, red), and Mod2 ($j = 2$, blue) detuning-sweeps. The shaded region shows the error on the measurement. **Reprinted from Ref. [167]**

In Fig. 4.12 (a) we plot the relative error $\varepsilon_\Omega^{(m)}$ after each iteration of our adaptive scheme (IAS 1, light blue squares). We also include the error on our prior estimate $\bar{\Omega}^{(0)}$ (see definition for standard deviation $\sigma_{\delta\Omega}$ in Sec. 4.1.1) for reference (orange circle). The iterative procedure converges to a value of the frequency estimate whose error is significantly smaller than the initial estimate. The fast convergence indicates that we have reached the spectral resolution allowed by our measurement time-window after just a few iterations.

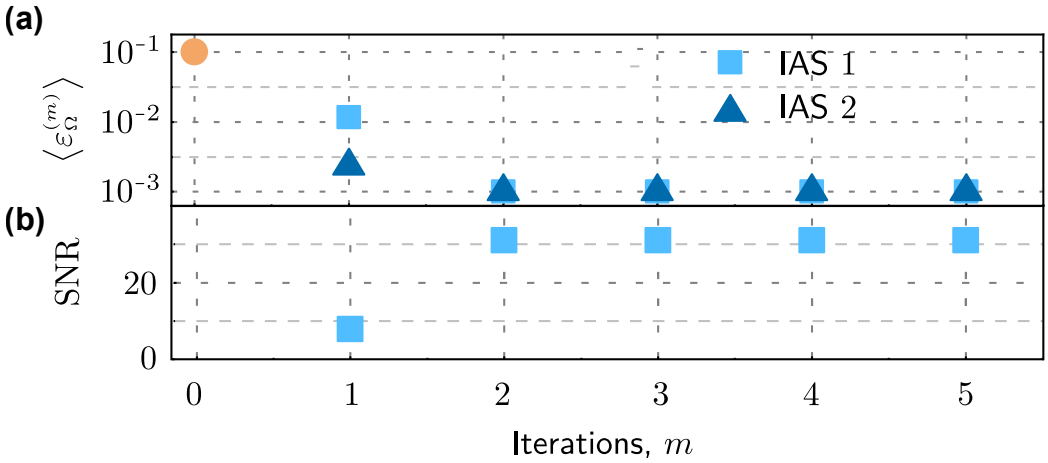

Figure 4.12 | Results of the Iterative Adaptive Spectroscopy.
(a) Relative error $\varepsilon_\Omega^{(m)}$ in frequency estimation as a function of iterations for IAS 1 (light blue squares) and IAS 2 (dark blue triangles). **(b)** Signal to noise ratio (SNR) [see Eq. (4.75)] as a function of iterations for IAS 1. Note that the error in both (a) and (b) is smaller than the symbols. Otherwise specified, we use $t_{\mathrm{w}} = 4 \times \left(2\pi/\bar{\Omega}^{(m)}\right)$, $t_{\mathrm{f}} = 0.5 \times \left(2\pi/\bar{\Omega}^{(m)}\right)$, $n_{\mathrm{samp}} = 30$ and $n_{\mathrm{pad}} = 970$. **Reprinted from Ref. [167]**

To show that the choice of window for the first iteration has no influence on the results, we also plotted in Fig. 4.12 (a) the relative error obtained by using at every step the Blackman-Harris window for

signal processing (IAS 2, dark blue triangles). Finally, we plot in Fig. 4.12 (b) the signal-to-noise (SNR) ratio defined as

$$\mathrm{SNR} = \frac{\sqrt{N}\mathcal{F}[\langle s^{(m)}(t) f^{(m)}(t)\rangle]}{\left[\sum_{j=1}^{N}\left(\mathcal{F}[s_j^{(m)}(t) f^{(m)}(t)] - \mathcal{F}[\langle s^{(m)}(t) f^{(m)}(t)\rangle]\right)^2\right]^{1/2}}, \tag{4.75}$$

which is a measure of the confidence level on the frequency estimate. More precisely, in this context, the SNR quantifies the degree of confidence we have in identifying the global maximum of the spectral density (zero-frequency component excluded). Our results show that as the relative error on the frequency estimate decreases, we become more and more confident in identifying the frequency associated to the global maximum of the spectral density in spite of having a noisy signal.

4.5 Conclusion

To sum up, we have theoretically developed an iterative, adaptive sensing protocol based on enhanced Ramsey interferometry of two-mode systems. Our scheme allows one to get precise estimates of an unknown frequency by considering short, finite-time signals under realistic assumptions of experimental bandwidth limitations. Specifically, our scheme avoids shortcomings both related to dealing with decaying signals and experimental constraints related to the sampling and could be implemented, e.g., in coupled mechanical oscillators [56, 63, 189, 190], optomechanical systems [92, 191], hybrid optomechanical systems [192], coupled optical modes [193], and qubits [58, 208] under the influence of classical noise, just to name a few.

The main ingredients of our method are the use of the Magnus-based strategy discussed in Sec. 4.2.1 and 4.2.2 for control to find frequency-sweeps that allow one to prepare with high fidelity both the sensing and readout state and an iterative procedure (see Sec.4.4) built to mitigate systematic errors showed in 4.3.3 and 4.3.2 when using Fourier transforms to extract frequency components. We stress that independently of how the sensing and readout state are prepared, our iterative, adaptive sensing protocol can always be applied to enhance frequency estimates. In the following chapter, we will demonstrate the experimental implementation of our theoretical work.

5 A Classical Nanomechanical Two-Level System as Coherent Sensor

The following chapter is based on our unpublished manuscript that is in preparation:

A. T. Le, A. Chowdhury, H. Ribeiro and E. M. Weig, "Fast iterative adaptive frequency sensing scheme of a two-level system", Unpublished manuscript.

The theoretical model has been developed in collaboration with Prof. H. Ribeiro from the University of Massachusetts Lowell and Dr. A. Chowdhury. The experiment was performed by the author of this work. The data evaluation relies on discussions between E. M. Weig, A. Chowdhury and H. Ribeiro. The theoretical model and certain passages of the original publication is printed under permission of Dr. A. Chowdhury and Prof. H. Ribeiro.

Motivated from the theoretical development of the coherent sensing protocol in Chapter 4, we implement this idea into an experimental realization. Here, we need a two-level system (either classical or quantum) that satisfies the criteria of a Ramsey protocol (see section 4.1) and, at the same time, dynamically couples to a physical quantity that we wish to determine in order to use it as a coherent sensing element. It has been theoretically demonstrated [77, 188], that classically coupled harmonic oscillators can be coherently controlled and manipulated in the same way as their quantum mechanical two-level system analogues.

T. Faust et al. showed in the experiment with a classical nanomechanical two-mode system that the coherent dynamics of two strongly coupled flexural modes can be fully controlled and described in a Bloch sphere representation [47]. By employing pulse schemes that are well-known from coherent spin control, e.g. Rabi, Ramsey and Hahn Echo sequences, it is possible to simulate the coherent dynamics of a quantum system by a classical two-mode system.

Another classical to quantum analogy based on coherence has been demonstrated by Seitner et al. in the Stückelberg interferometry experiment [62, 63] with the very same classical nanomechanical two-level system. The Stückelberg interferometry usually describes the dynamics of a quantum two-level system that undergoes a double passage through an avoided crossing. The phase accumulation during the double passage leads to self-interference and creates an oscillating pattern in the return probability of the quantum two-level system [208–210]. The coherent exchange in excitation energy of the two mechanical modes represents an analogy to the quantum mechanical interference.

This chapter provides a natural follow-up of these prior works from the chair by implementing the enhanced Ramsey protocol proposed in Sec. 4.1 on the nanomechanical two-mode system under investigation. We are going to employ the strong coupling nature of the mechanical in-plane and out-of-plane flexural modes. Our aim is to develop a testbed applicable for quantum sensing protocols that is fast and allows frequency estimate with high precision.

The chapter is organized as follows: first, we discuss in depth the challenges to experimentally realize the theoretically proposed sensing protocol using the platform described in Sec. 4.4. In Sec. 5.1, we demonstrate the experimental implementation in the development of voltage combiners and pulse

generation, which must meet certain requirements for precise implementation of the Magnus control pulses. Second, we re-introduce the nanomechanical system and the dielectrical frequency tuning mechanism that we exploit for implementation of the sensing protocol (see Sec. 5.1.2). Sec. 5.2 briefly demonstrates the simple single passage experiment that can be described by the Landau-Zener model. This experiment serves as a simple proof of state control of the two-mode system, and to test the readout. In Sec. 5.3 and Sec. 5.4, we show the experimental results of the Ramsey protocol based on the proposed iterative adaptive spectroscopy (IAS) and compare them to the theoretically model. And finally, as a first proof of principle, we demonstrate a coherent sensing experiment in Sec. 5.5, where we utilize fast and high precision in frequency estimation to observe a frequency shift in coupling strength Ω_0 of the classical two-level system due to the change in the electrical field environment. In the last section 5.6, the experimental work and the corresponding results are summarized.

5.1 Experimental Realization

We implement the sensing protocol using nanomechanical resonator in a vacuum chamber with relative moderate pressure of about $< 10^{-4}$ mbar and at room temperature. Here, we study a nanomechanical two-mode system, i.e. the dynamics of two distinguishable strongly coupled, classical mechanical modes that can be seen as two collective phononic ensembles that can coherently exchange excitation energies. Here, our sample consists of a freely suspended doubly-clamped, pre-stressed silicon nitride string resonator with a high quality factor of $Q \approx 250.000$. The resonator used in this experiment exhibits a length of $L = 55\,\mu\text{m}$, the width is $w = 250\,\text{nm}$ and the thickness is about $t = 100\,\text{nm}$. The eigenfrequencies of such a mechanical resonator are typically in the radio frequency (RF) domain. In Sec. 2.4, we described the fabrication procedure and illustrated the scanning electron microscopy (SEM) image (see Fig. 2.26) of such nanomechanical resonator. As discussed in Sec. 2.1, the rectangular cross-section of such a doubly-clamped string resonator leads to a frequency offset between the two orthogonally polarized fundamental modes due to the difference in the moment of inertias, respectively [see Eqs. (2.5) and (2.6)]. This resonant frequency offset can be compensated by dielectric frequency tuning. In addition, the spatially inhomogeneous electric field causes the two modes to hybridize into normal modes in the near resonance condition [56]. We will discuss the dielectrical frequency tuning and mode coupling mechanism in more details further below in Sec. 5.1.2.

We show the device schematic of this experiment in Fig. 5.1. Additionally, we illustrate in Fig. 5.2 a complete overview of our experimental setup, including detection, noise and RF drive, as well as dielectrical frequency tuning and the coherent control capability using pulse sequences for the Ramsey interferometry experiment.

Again, we employ the microwave cavity-assisted detection scheme combined with the heterodyne mixing technique described in Sec. 3.1. The mechanical motion is detected by placing adjacent gold electrodes in the vicinity of the dielectrical string resonator. One of the electrodes is connected to an antenna that capacitively (C_{Ant}) couples to the electric field of the three dimensional (3D) coaxial $\lambda/4$ microwave cavity (see Fig. 5.1) that we representatively illustrate as a simple LC-circuit with inductance L_0 and capacitance C_0 (see blue box in Fig. 5.2). Note that the antenna is placed right above the inner conductor of the 3D cavity, where the electric field distribution of the fundamental TEM mode has its maximum [see Fig. 2.14 (a)]. With the sample and the coupling antenna inside, the cavity resonance of the fundamental mode is found to be $\omega_c/(2\pi) = 3.0\,\text{GHz}$. The geometrical illustration of such a cavity can be found in Fig. 2.13. We emphasize, that we have switched from the cylindrical geometry to the coaxial cavity due to the simple and clean spectral mode distribution. As apparent in Fig. 2.14, the second TEM harmonic mode of the cavity starts to emerge at 10.8 GHz that

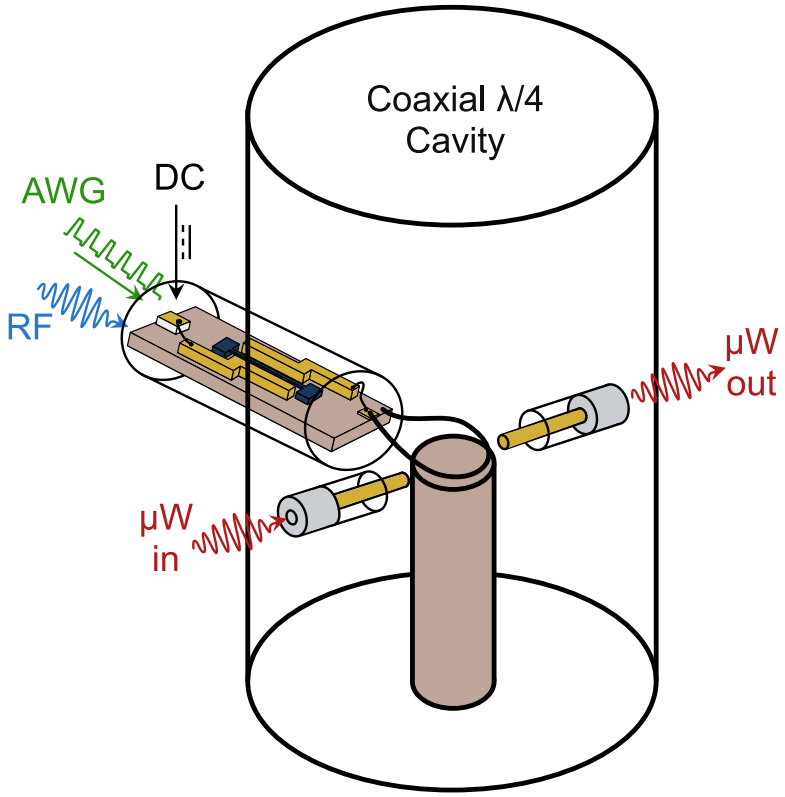

Figure 5.1 | Device Schematic.
Coaxial $\lambda/4$ microwave 3D cavity made of cooper support a microwave resonance of $\omega_c/(2\pi) = 3.0\,\mathrm{GHz}$. The sample with the nanomechanical string resonator is coupled to the cavity via an microwave loop antenna that is connected to one of the gold electrode. The mechanical RF drive tone, the pulse generated by an AWG and the DC voltage can be applied on the second electrode via a single layer capacitor. The microwave cavity is continuously pumped and measured in transmission.

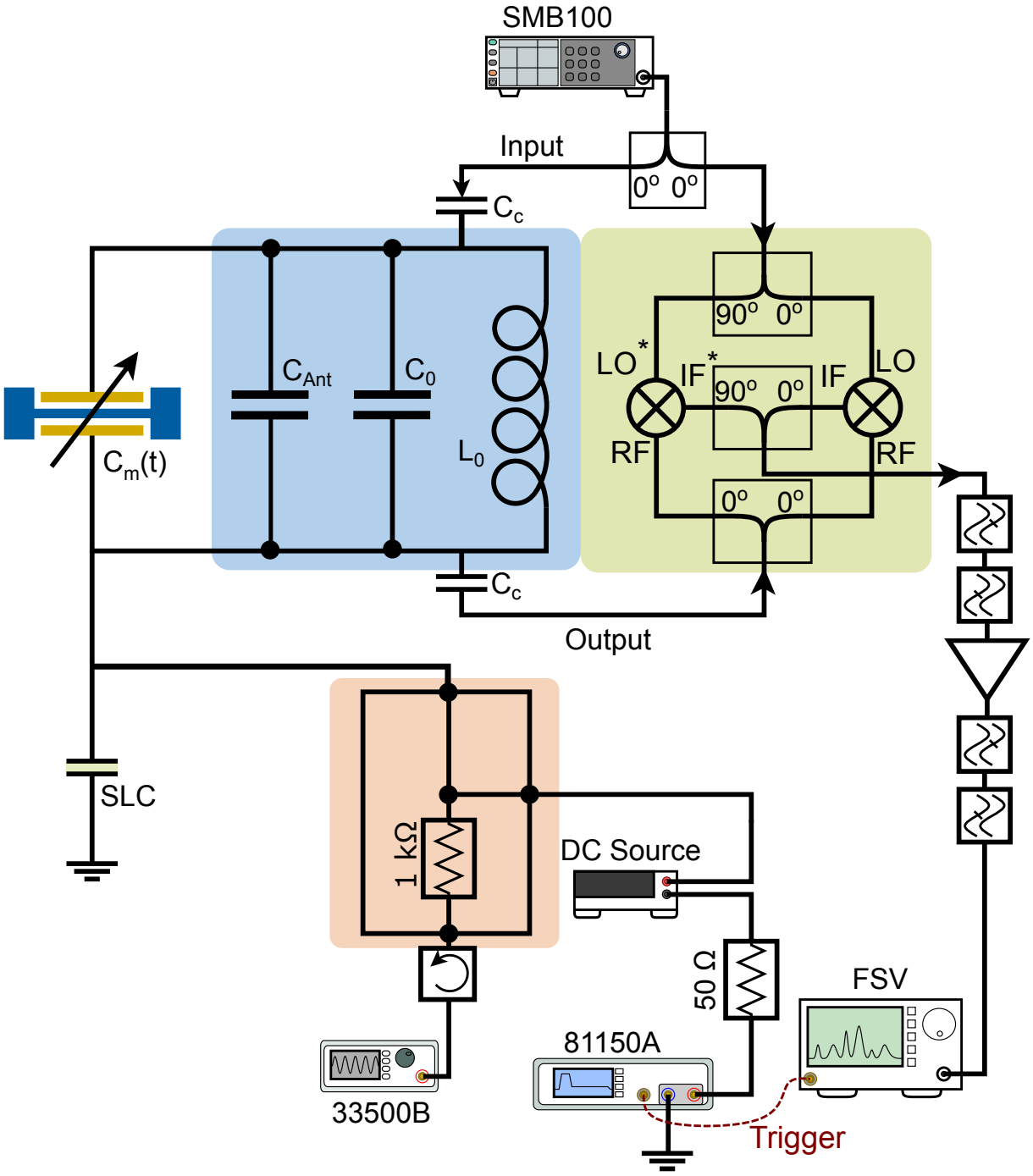

Figure 5.2 | Experimental Setup for the Iterative Adaptive Spectroscopy Experiment.
The 3D microwave coaxial $\lambda/4$ cavity (blue box) is driven on resonance by a signal generator to avoid unwanted optomechanical effects. The capacitance ($C_m(t)$) of the electrodes is periodically modulated by the mechanical motion and at the same time, one of the electrode is capacitively coupled to the 3D cavity via microwave antenna (C_{Ant}). The cavity output is down-converted using heterodyne mixing technique (green box) using a local oscillator (LO). The down-converted signal is then filtered and amplified before feeding into a spectrum analyzer for observation. Additionally, we utilize a custom made voltage combiner (orange box) in order to merge the outputs of a DC source, an arbitrary waveform generator and RF drive source into a single output to feed them to the electrodes via a single layer capacitor (SLC). In the Ramsey experiment, where the pulse sequence are generated, it is necessary to synchronize the function generators (33500B and 81150A) with the spectrum analyzer by the internal 10 MHz clock. Additionally, the arbitrary wave function generator provides a trigger signal to the FSV to start the ring-down measurement.

is three times higher than the fundamental mode and the cylindrical waveguide mode is at even much higher frequency that is 14.7 GHz.

As described in Sec. 3.1.1, the mechanical motion periodically modulates the capacitance $C_m(t)$ of the electrodes and, simultaneously, induce sidebands in the cavity response of the resonantly driven cavity at frequencies $\omega_c \pm \omega_m$. Here, the cavity resonance is $\omega_c/(2\pi) = 3.0\,\text{GHz}$ and the mechanical fundamental frequencies of the flexural modes are roughly $\omega_m/(2\pi) \approx 7.3\,\text{MHz}$. Note, that the second electrode is wirebonded to a single layer capacitor[1] (SLC) that provides the ground plane for the high frequency mode of the microwave cavity and at the same time, it enables the application of the DC and RF signal from various sources[2] [3] [4] to the electrodes for the drive and coherent frequency tuning. Throughout the experiment, the microwave 3D coaxial cavity is driven using a signal generator[5] precisely on resonance to avoid unwanted electromechanical interactions [56, 92, 102, 107]. Note that the resonance frequency of the 3D cavity is extracted at the maximum position of the cavity transmission. This is simple enough due to the clean frequency spectrum and high signal-to-noise ratio. The resulting electromechanical sidebands can be resolved using heterodyne IQ-mixing[6] technique (see green box in Fig. 5.2) with subsequent low-[7] and high-pass[8] filtering and amplification[9]. Finally, the down-converted signal is fed into a spectrum analyzer[10] to observe either the noise driven frequency response of the mechanical resonator in the frequency domain or the decaying (ring-down) signal in the time domain.

5.1.1 Voltage and Pulse Control Technique

One of the challenges in this work is to develop a precise and reliable voltage control scheme to manipulate the tuning speed and the shape of the ramp function in a coherent control experiment. In order to implement the theoretically calculated pulse shape to the experiment, we quire a reliable implementation of the generated voltage function on the sample. In this section, we discuss the different possibilities to combine the output of a DC voltage source with the output of an arbitrary wave function generator (AWG) and the requirement for the combiner to meet certain experimental criteria. Additionally, we describe the working principle of our self developed Matlab script that controls all the devices in this experiment.

Voltage Combiners The frequency tuning of the nanomechanical two-mode system can be realized by applying control DC voltages to the two adjacent electrodes. We will discuss the dielectrical tuning behaviour (already addressed in Ch. 3) in more detail in the following section 5.1.2. In order to perform the Ramsey scheme, discussed in Sec. 4.1, we should be able to initialize the two-mode system to fulfill the requirement of step (I) in Fig. 4.2.This can be achieved in the experiment by setting the DC voltage to a fixed value. To satisfy step (II) and (IV) in Fig. 4.2, where we have to detune the system to the sensing state and readout state, we need to generate additional control pulses on top of the DC voltage, which bring the system to the desired operation points. The challenge here is to create a voltage combiner, that superimposes an arbitrary waveform (consisting of multiple frequency

[1] JOHANSON TECHNOLOGY SLC Microwave Capacitor U70, 1800 pF
[2] Keithley SourceMeter 2410
[3] Keysight Trueform Waveform Generator 33500B
[4] Keysight Pulse Function Arbitrary Noise Generator 81150A
[5] Rohde & Schwarz Signal Generator SMB100
[6] Marki Microwave IQ-0307 LXP
[7] Mini-Circuits VLFX-80+
[8] Mini-Circuits ZFHP-0R75+
[9] MITEQ AU-1464-R +35 dB
[10] Rohde & Schwarz FSV Signal and Spectrum Analyzer

components) on top of a DC voltage. We require a combiner that works with large DC offsets. It should support signals from DC to a few tens of megahertz (DC - MHz) range to faithfully reproduce the Magnus-based correction pulses, and most importantly, by adding and removing the arbitrary pulse form of the AWG, we require a smooth transition without the switch-on and switch-off spikes. In the experiment, such spikes can lead to an unwanted detuning behaviour and hence, mitigate the fidelity in preparation of the sensing and readout states.

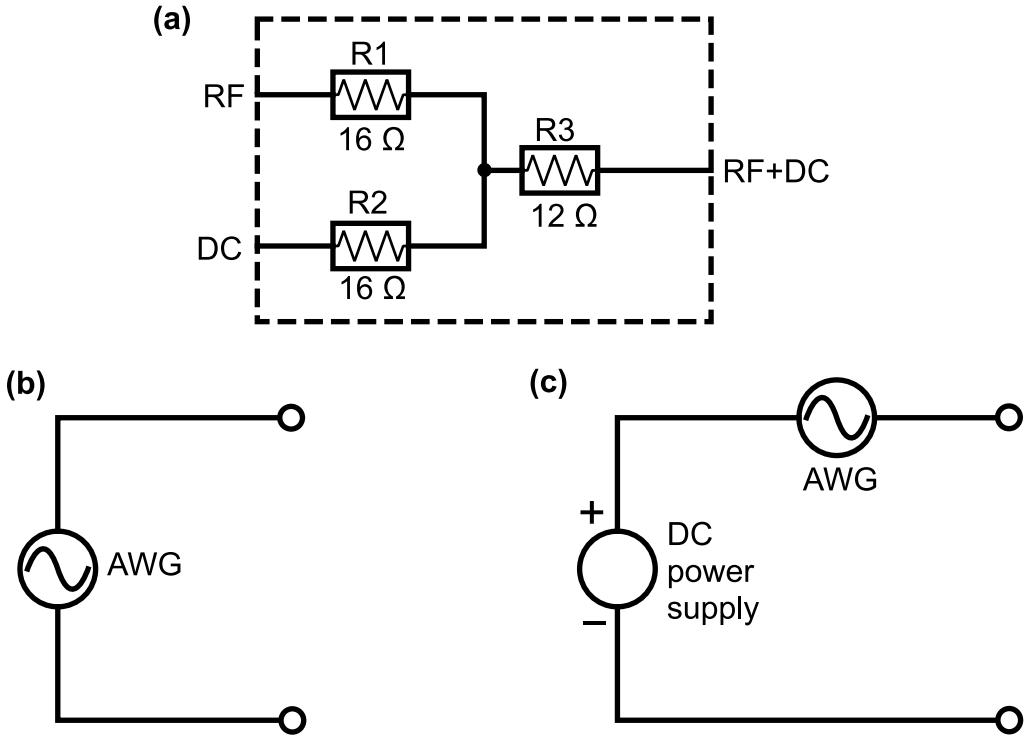

Figure 5.3 | Combine DC and RF Signals.
(a) Combining DC and RF using resistive RF-splitter/combiner. The resulting circuitry leads to a division in the voltage (attenuation) of ≈ 6 dBm, hence the maximum amplitude range of the devices cannot be fully exploited. **(b)** Generation of an arbitrary wave function with the build-in offset of the function generator itself. This configuration is not suitable for our pulse scheme experiment and the DC offset provided by the device is limited (mostly ±5 V). **(c)** Producing DC+RF by putting the AWG and the DC source in series. This technique allows full range operation of the DC voltage source and the large bandwidth (DC - 50 MHz) of the AWG.

In previous works [62, 211], an active operational amplifier (OpAmp) has been used to combine the DC voltage with the linear ramp function. Due to the high demands on signal accuracy (large DC offsets, large frequency range and no voltage spikes) the operational amplifier is not a valid option for our experiment. It is known that such devices create voltage offsets, frequency and phase shifts in the combined signal.

Another possibility is to combine the signals using a resistive RF power splitter/combiner [see Fig. 5.3 (a)]. The disadvantage of this system, however, is the strong attenuation of the input signals of about 6 dBm which is undesirable since we require large DC offsets.

A simple and convenient method is to use only the function generator by itself. Many AWG have the ability to produce a DC offset in conjunction with their output waveform [see Fig. 5.3 (b)]. Unfortunately, due to the application of internal attenuators and also the limited DC offset range of the devices itself, it is impossible for us to utilize this option. Most of the devices offer DC offsets superimposed with waveform signal voltage only in the range of −5 V to 5 V into 50 Ω load impedance,

which is equivalent to the range from −10 V to 10 V into an open circuit. Moreover, this option is compatible only with experiments using continuous waveform and offset. In a finite time experiment with pulsed sequences, it is not possible to initialize the system and hence we cannot conduct the Ramsey sequence.

In order to generate a signal or pulse sequences riding on top of a DC offset and, at the same time, require an offset that is greater than the function generator can provide, we can put the DC power supply in series with the function generator output [see Fig. 5.3 (c)]. This technique offers several advantages, i.e. full bandwidth capabilities of the function generator and the flexibility in setting the DC level delivered by the voltage source. Note, it is important to make sure that the devices in this series should either have the same ground potential or one of them should be internally isolated (float) from the earth ground. In our case, the DC voltage source *Keithley 2410* is isolated from the earth ground and we can float the output off the ground up to ±240 V. This means we can apply the full range of voltage from the DC source, that is ±21 V.

Additionally, the AWG [11] used in our setup operates with two different types of amplifiers [212] in the channel output. One amplifier (*high bandwidth amplifier*) is optimized for high bandwidth (up to 120 MHz), but provides a smaller output voltage window (±5 V). The second one (*high voltage amplifier*) is optimized for high output voltage (±10 V) but the downside of this amplifier type is the lower bandwidth that allows us to operate with frequencies only up to 50 MHz instead of the full range to 120 MHz. Nevertheless, we are not limited by the restriction of the bandwidth since we only require the operation up to a few megahertz. In our experiment, we choose the second option to employ the full voltage range of the AWG.

Altogether, with this technique we are able to apply DC voltages that can go up to $U_{\mathrm{max}} = \pm 31\,\mathrm{V}$, which is a combination of AWG $U_{\mathrm{AWG,max}} = \pm 10\,\mathrm{V}$ and the DC source $U_{\mathrm{DC,max}} = \pm 21\,\mathrm{V}$. We can generate arbitrary pulses with a bandwidth that ranges from DC to 50 MHz. The simple circuitry from our custom made voltage combiner box is illustrated in Fig. 5.4 (a). The output of the AWG is put in series with the DC voltage source using a custom made BNC cable [see Fig. 5.4 (b)]. The cable provides a proper shielding that is connected to the HF housing of the combiner box with the connection to the ground. Furthermore, we can add a second wave function generator [12] that can supply the sinusoidal or white noise drive to the nanomechanical resonator to implement mechanical frequency regulations in the measurement routine (for detail discussion see Sec. 5.1.3). Note, the input of this drive source (33500B) is heavily attenuated by adding a resistor of 1 kΩ to the device output port (see Fig. 5.4), however, the combined signal from the AWG (81150A) and the DC voltage source remains unaffected. This is desirable for our purposes, because we want to keep the drive power weak in order to operate the resonator in the linear regime. For the coherent control, however, we should be able to operate in a larger range of voltage (combined voltages of AWG 81150A and DC source) so we can reliably separate the initial and sensing states.

[11] Keysight 81150A Pulse Function Arbitrary Noise Generator
[12] Keysight Trueform Waveform Genrator 33500B

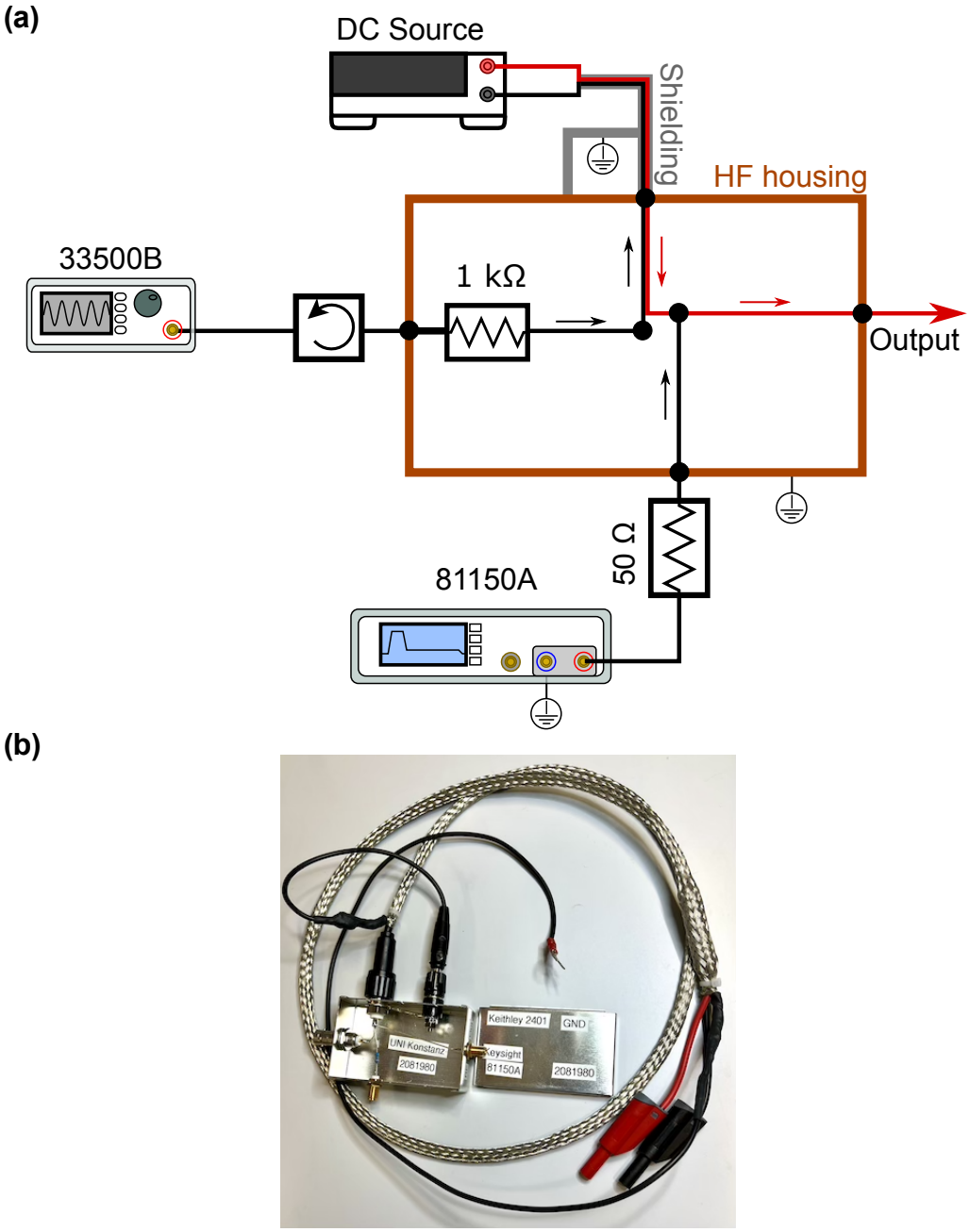

Figure 5.4 | Schematic of the Power Combiner Box.
(a) Graphical illustration of the power combiner box used to combine the DC voltage source and the arbitrary noise generator (AWG 81150A) in series, together with the second wave function generator (33500B). Due to the difference in the output impedance, the signal from the wave function generator (33500B) that we use for sinusoidal and noise drive is heavily attenuated by ($\approx -24\,\mathrm{dBm}$). The combined signal from the DC voltage source and the AWG (81150A), that we used for coherent control, remains relatively unchanged. The voltage combiner box is made out of the HF housing Teko 372.16 that is commercially available to protect the signal from unwanted interaction with the environment in the laboratory. **(b)** Photograph of the (open) box and the custom made BNC cable for the series circuitry. The cable has the outer shielding that is connected to the HF housing of the box for proper grounding.

Pulse Generation In addition to the conventional waveforms, such as square, ramp and sine ect., the AWG (*Keysight 81150A*) offers the possibility to create arbitrary waveforms that can be custom made. This option is essential for the Ramsey interferometry experiments, since we need to customize the control pulse provided by the Magnus-based corrections discussed in Sec. 4.2. Conveniently, the provider Keysight offers a commercial software[13] that reliably supports the design of such an arbitrary waveform. The waveform builder is a Microsoft Windows-based program that provides creation tools, e.g. the equation editor, waveform math and drawing tools, which can be used to create custom signals [213]. The created waveform can be fed into the AWG either by direct link or via USB drive. The disadvantage of this method, however, is the lack in flexibility to dynamically adapt the waveform during the measurement protocol. The waveform always has to be loaded into the AWG manually, since there is no posibility to connect the waveform builder software to our Matlab control script.

An alternative method to generate arbitrary waveforms is the implementation of the Matlab based application tool the so-called *IQtools*, that is also provided by Keysight. Note that the IQtools is a part of Keysight's *IO Library Suite*, and hence, it is important to install both the library and the tool's source code into the Matlab working directory. The IQtools application allows direct communication and streaming of data to the AWG via predefined Matlab codes, which we can incorporate directly into our measurement routine. This type of device communication is therefore the key element that allows automation of our measurement process without manual adjustment in the control script. In Fig. 5.5 we illustrate a typical numerically created Ramsey pulse sequence recorded from the output of the arbitrary wave function generator.

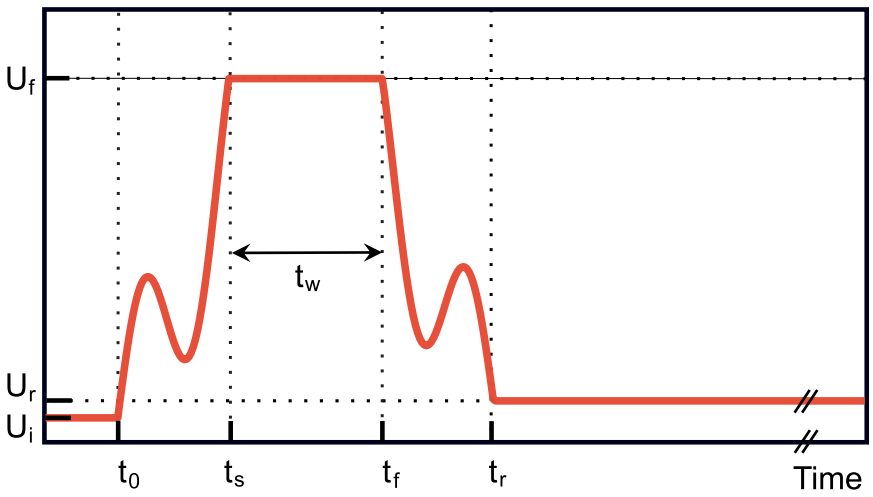

Figure 5.5 | Pulse Generation.
A typical pulse form as a function of time generated by the arbitrary wave function generator (Keysight 81150A) in the Ramsey interferometry experiment.

The total pulse length consists of $N_{\text{tot}} = 500.000$ sample points (500 kSa) and is typically divided into five different time windows (Ramsey sequence). The first region from $0 \longrightarrow t_0$ is a short time window with $U_{\text{i}} = 0\,\text{V}$, before the actual voltage ramp [14]. Here, we set the time $t_0 = 2\pi \times \frac{N_0}{N_{\text{tot}}} \frac{1}{\omega_{\text{AWG}}}$, with $N_0 = 1$

[13] 33503A BenchLink Waveform Builder Pro Software
[14] A constant DC voltage is applied during the entire sequence. Both voltages from the DC source and the AWG are combined using the combiner box as described above

kSa and $\omega_{\mathrm{AWG}}/(2\pi)$ is the frequency that is defined by the AWG itself. The second time window is extended from t_0 to

$$t_{\mathrm{s}} - t_0 = 2\pi \times \frac{50\ \mathrm{Sa}}{500\ \mathrm{kSa}} \cdot \frac{1}{\omega_{\mathrm{AWG}}}, \tag{5.1}$$

that is the period to bring the initial state to the sensing state by ramping up the voltage $U_{\mathrm{i}} \rightarrow U_{\mathrm{f}}$. Note, we choose the ratio $\frac{N_{\mathrm{tot}}}{N_{\mathrm{s}}} = 10^4$ for the sensing state preparation, i.e. by setting $\omega_{\mathrm{AWG}}/(2\pi) = 1\,\mathrm{Hz}$ in the AWG. With that, we obtain the sweep frequency for the sensing state

$$\beta_{\mathrm{AWG}} = \frac{N_{\mathrm{tot}}}{N_{\mathrm{s}}} \cdot \frac{\omega_{\mathrm{AWG}}}{2\pi} = 10\,\mathrm{kHz}. \tag{5.2}$$

The third region of our pulse scheme with a time window $t_{\mathrm{w}} = t_{\mathrm{f}} - t_{\mathrm{s}}$, is designed for the system to evolve freely, where the two flexural modes can coherently exchange their excitation energy. Here, we keep the voltage constant at U_{f}. Subsequently, the forth region in Fig. 5.5, defined by the time between t_{r} and t_{f}, is employed to detune the system to the readout state. We emphasize that the exponential decay of the returning excitation must be measured with a finite offset with respect to the initial frequency. This is due to the fact that the resonant sinusoidal drive tone used to prepare the initial frequency is always on throughout the sequence. The difference in the initial and readout states can be realized by introducing an offset in the applied voltage that is $U_{\mathrm{off}} = U_{\mathrm{r}} - U_{\mathrm{i}}$. We choose the offset to be large enough to avoid re-excitation by the sinusoidal drive tone using in the initial state preparation. Subsequently, in the fifth region ($t > t_{\mathrm{r}}$), we measure the exponential decay of the returned excitation after tuning U_{f} to U_{r}. After the measurement, the absolute voltage is ramped from U_{r} back to the initial voltage U_{i} (not shown).

As mentioned in the previous section, the arbitrary wave function generator (*Keysight 81150A*) offers two different types of amplifiers. We choose to operate with the high voltage amplifier option to exploit the full range in the voltage output ($\pm 10\,\mathrm{V}$). Note that most function generators are designed with $50\,\Omega$ output impedance to minimize signal reflections when the output is connected to a coaxial cable that also has a characteristic impedance of $50\,\Omega$ and is terminated with a $50\,\Omega$ load. Consequently, the $50\,\Omega$ output impedance and the $50\,\Omega$ load form a 2:1 voltage divider and the actual internal output of the function generator is twice the set voltage value in the AWG. By reducing the output impedance of our AWG to $0\,\Omega$, we can obtain an even larger voltage range from $-20\,\mathrm{V}$ to $20\,\mathrm{V}$. Another important fact to consider, when feeding the numerically designed pulse scheme into the AWG, is that the device will always generate an output voltage that ranges from $-U_{\mathrm{f}}$ to $+U_{\mathrm{f}}$. Therefore, it is necessary to add an offset $+U_{\mathrm{f}}$ to the device to compensate the negative value and to enable the pulse sequence to start from $0\,\mathrm{V}$. With the introduced offset and the $0\,\Omega$-output impedance, the total voltage output of the AWG is $U_{\mathrm{AWG}} = 4U_{\mathrm{f}}$. In order to obtain the right output voltage, we need to readjust the output voltage at the AWG to $U_{\mathrm{AWG}} = U_{\mathrm{f}}/4$ to compensate both before mentioned effects.

5.1.2 Dielectric Frequency Tuning and Two-Mode Coupling

To follow the discussion in Sec. 3.3.2, where we have described the quasi-static dielectric detuning of the nanomechanical resonator from the cavity's RMS electrical field, we can treat the detuning effect resulted from the applied DC voltage in the similar manner. The static and inhomogeneous electric field from the gold electrodes induces a polarization in the dielectric material of the nano resonator. As a result, the string is pulled towards the maximum of the electric field and therefore, experiences a different field gradient which can be seen as an additional spring constant [56, 70, 130]

$$\boldsymbol{F}_{\mathrm{el}} = -\nabla(\boldsymbol{p} \cdot \boldsymbol{E}). \tag{5.3}$$

Here, $\boldsymbol{p} = \alpha \boldsymbol{E}$ is the electric dipole moment and α is the polarizability of the dielectric material (SiN) of the nanomechanical string resonator. From Sec. 2.1, we know that the string supports two fundamental flexural vibrational modes. The in-plane (IP) mode describes the mechanical motion along the x-axis and the out-of-plane (OOP) mode is the perpendicular polarized vibration mode along the z-axis (see Fig. 2.1). Due to the difference in dimension of the string's rectangular cross-section, where the 250 nm beam width exceeds its thickness of 100 nm, the IP mode exhibits a slightly higher rigidity than the OOP mode which leads to a higher eigenfrequency of the IP mode.

From Eq. (3.26), we show that the force gradient, experienced by the string resonator, is proportional to the square of the applied DC voltage and thus, we expect a quadratic dependence in the detuning behaviour of the resonator resonance frequency with respect to the applied DC voltage. In the investigated geometry, where the string is lower than electrodes, the respective eigenfrequencies of the IP and OOP modes can be detuned in opposite directions [130]. Thus, by tuning the applied DC voltage, we can compensate the frequency difference of the two respective modes and bring them on resonance.

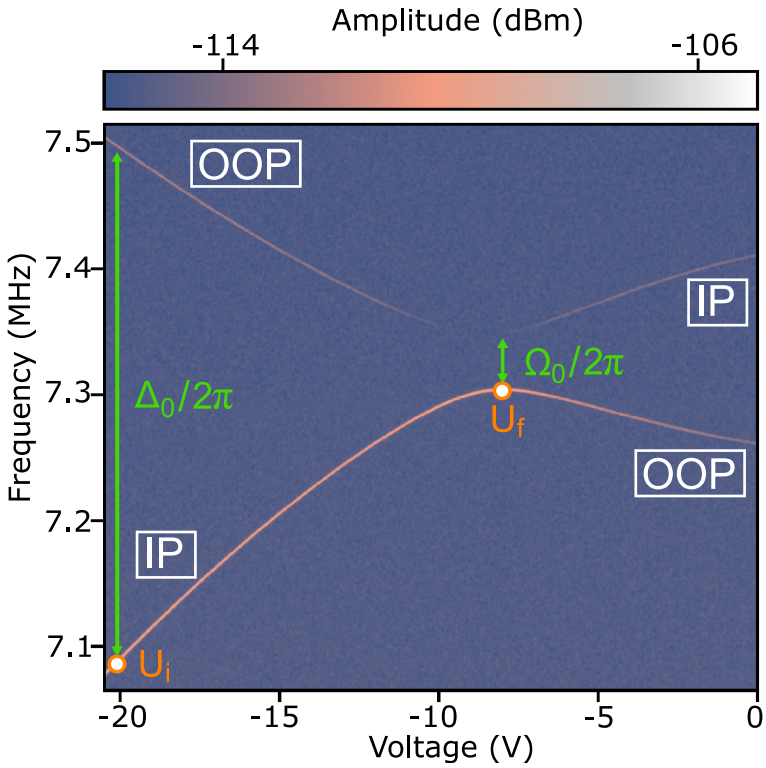

Figure 5.6 | Dielectric Tuning and Strong Coupling.
Color-coded and noise driven frequency spectrum versus the applied DC voltage. The resonance frequency of the IP mode decreases quadratically as a function of the DC voltage. The resonance frequency of the OOP mode, on the other hand, increases quadratically. The strong coupling of the two flexural modes and the resulting avoided crossing with a level splitting Ω_0 is apparent. The orange circles denote the initial and final voltages of the Ramsey protocol that we will discuss later in Sec. 5.3. Δ_0 is the initial level splitting of the two flexural modes. The green arrows illustrate the differences in frequency splitting in both cases.

In case of strong coupling, these two fundamental flexural modes hybridize into normal modes that can be expressed as a superpositon of the two modes. The resulting avoided crossing near resonance is the characteristic fingerprint of strong coupling with the corresponding level splitting Ω_0. As shown in Fig. 5.6, the IP mode has a higher eigenfrequency than the OOP mode at $U_{\mathrm{DC}} = 0\,\mathrm{V}$. By increasing the DC voltage to $\approx -8\,\mathrm{V}$ the two modes can be tuned into resonance, where the avoided crossing

with a level splitting of Ω_0 can be observed. Note that the coupling of the two modes is mediated by the strong inhomogeneous electric field $\boldsymbol{E}$ between the electrodes that induces force gradient to the beam due to asymmetry in the geometry [56]

$$\Omega_0/2\pi \propto \frac{\partial F_x}{\partial z} = \frac{\partial}{\partial z}\left(-\frac{\partial \alpha E^2}{\partial x}\right) = -\alpha \frac{\partial^2 E^2}{\partial z \partial x}. \tag{5.4}$$

The non-zero cross derivative in Eq. (5.4) ensures that a displacement in x-direction modifies both the IP and OOP modes and is responsible for the mode coupling. The strong coupling allows coherent exchange in excitation energy of the two normal modes, where coherent control experiments such as Rabi, Ramsey and Hahn Echo sequences can be conducted [47, 77]. By further increasing the voltage ($U_{\mathrm{DC}} \approx -20.5\,\mathrm{V}$), we can strongly tune the two modes out of resonance to obtain pure IP and OOP modes again. By tuning the nanomechanical flexural modes in and out of resonance, we can mediate the coupling behaviour of the system.

5.1.3 Measurement Protocol

The frequency tuning of the nanomechanical flexural modes to implement the theoretical proposed iterative adaptive sensing protocol (see Sec. 4.4) requires very reliable and precise control in DC voltage supply and pulse generation. Therefore, it is essential to generate a measurement script to implement the sequences and commands to control all the devices showed in Fig. 5.2. The communication between AWG (*Keysight 81150A*) that is used to prepare the sensing and readout states during the measurement and the spectrum analyzer (*R&S FSV*) that measures the exponential decay in a ring-down measurement, is of particular importance. The synchronization of the two devices can be realized using the so-called "*trigger mode*". When operating in the trigger mode, the AWG (*81150A*) will simultaneously send the pre-defined waveform and a trigger signal to the output ports (see Fig. 5.2). The spectrum analyzer, on the other side, will start to record the data within a certain time window once it receives the trigger signal from the AWG. To achieve a good synchronization, we need to implement a certain delay time between the trigger output and the beginning of the measurement. The delay time will compensate the transient time of the triggered signal that travels through the cable at certain length. In Fig. 5.7, we illustrate the working principle of our Matlab control script. The Matlab source codes can be found in the GitHub repository [214].

Generally, we start our Matlab script by defining important device parameters, the working directory in which the final results can be saved and the eigenfrequency f_{init} of the nanomechanical IP mode for measurement's initialization. Note that the initial eigenfrequency of the IP mode and the corresponding intial voltage can be roughly estimated using the spectroscopy measurement depicted in Fig. 5.6 (orange dot at roughly $-20.5\,\mathrm{V}$). The microwave cavity pump is kept constant at $P_{\mu\mathrm{w}} = 22\,\mathrm{dBm}$ throughout the measurement. To get the exact initial frequency f_{init}, we implement a noise driven characterization measurement using the spectrum analyzer. Here, the nanomechanical eigenfrequency is regulated by the applied voltage U_{i} inside a feedback loop until the desired eigenfrequency f_{init} is obtained. Note that the initial voltage U_{i} must be re-adjusted after each measurement to keep f_{init} constant, since the resonator experiences eigenfrequency shifts due to temperature fluctuations and the large sudden change in control voltage.

In the next step, we calculate the voltage offset $\delta U = U_{\mathrm{f}} - U_{\mathrm{i}}$ and Ω_0 that are necessary to create the leading and trailing edges of the Ramsey sequence. The results from the spectroscopy measurement serve as a first rough estimate (see orange dot (U_{f}) in Fig. 5.6) to find the appropriate final voltage U_{f} and to reach the avoided crossing region. In Appendix A.3, we show our routine to fit the avoided crossing in order to extract all the important parameters. Additionally, we use the prior knowledge of

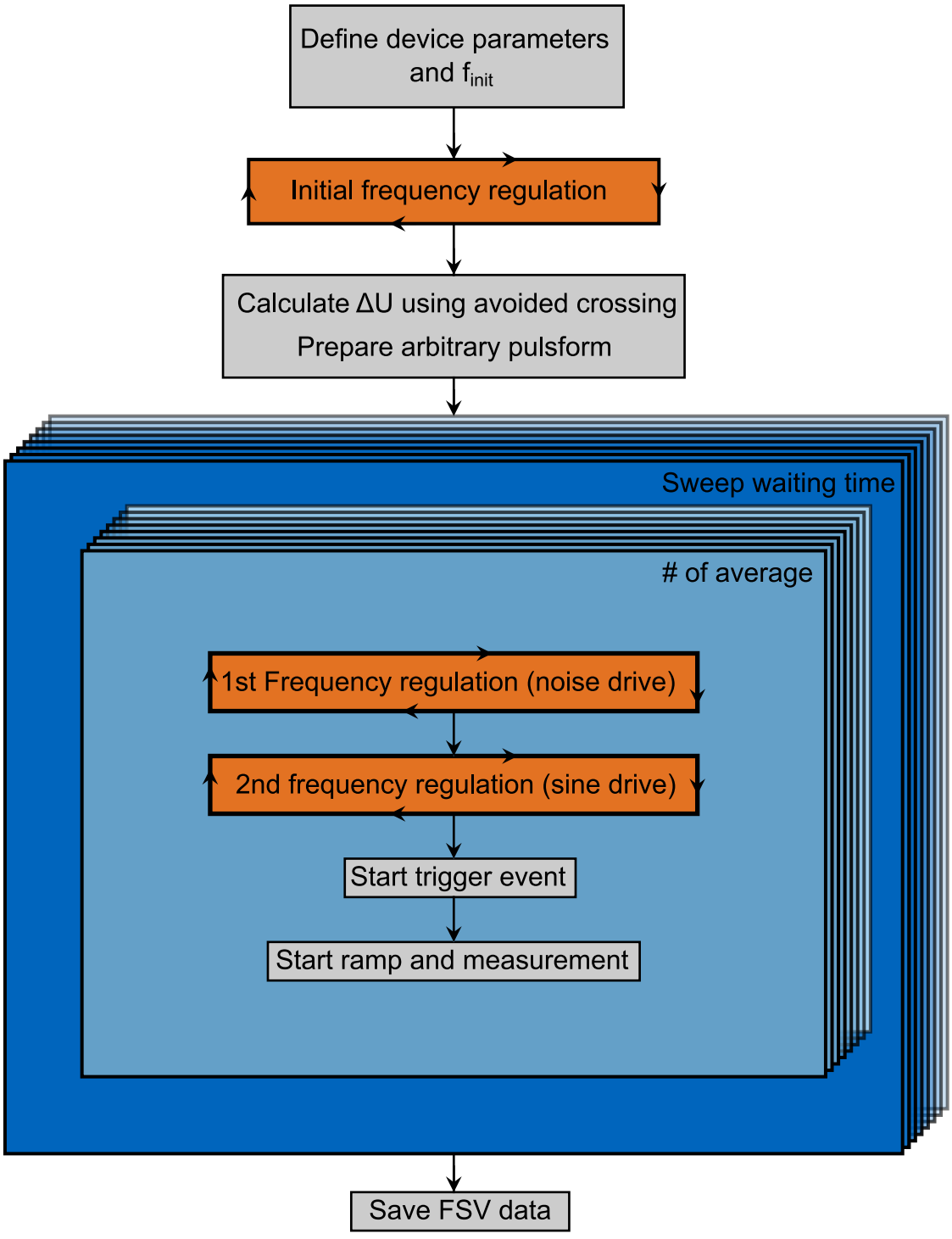

Figure 5.7 | Working Principle of the Matlab Control Script.
The Matlab script is the key element that controls all the devices for frequency regulations and ring-down measurements. It dynamically changes the input parameters to generate data for the Ramsey protocol.

the level splitting Ω_0 to calculate the Fourier coefficients c_k, d_l [see Eq. (4.49)] in the Magnus-based corrections and to adjust the proper time window such that $(\Omega_0/2\pi)t_w = 4$ to improve the frequency estimation procedure. The numerically designed correction pulse with Magnus-based correction for the leading and trailing edges can then be fed into the AWG using the *IQtools* source code.

We start the actual measurement routine by creating a set of waiting times to dynamically modify the pulse form. Before each measurement, we again introduce two steps of frequency regulations to always start at the right frequency f_{init}. This is particularly important because our system experiences frequency drift as the ambient temperature inside the lab changes over time. Furthermore, the detuning in the voltages also leads to a slow drift in the mechanical eigenfrequency that we need to compensate. [15] In the first step, we employ the noise driven frequency regulation scheme that is similar to the initial frequency regulation described above. To obtain a better accuracy, we add the 2$^{\text{nd}}$ frequency regulation step. Here, we apply a single frequency sinusoidal drive at f_{init} and, again, re-adjust U_i to fine tune the maximum amplitude of the mechanical response. In case both frequency regulations are satisfied, the script will switch the AWG and FSV into trigger mode operation. Subsequently, the AWG initiates a trigger event and, simultaneously, sends the arbitrary pulse to the main output port to start the ring-down measurement in the FSV. Note, for each set of waiting time, we repeat the measurement 30 times, respectively. The data generated by the spectrum analyzer is then stored in the predefined working directory for subsequent data analysis.

Setup Characterization Since we want to operate the coupled two-mode system in the linear regime, it is important to find out the threshold of drive power, where the mechanical response becomes nonlinear. For that purpose we characterize the nanomechanical amplitude response by varying the sinusoidal drive power from $-50\,\text{dBm}$ to $0\,\text{dBm}$. The sinusoidal drive frequency is kept constant and the amplitude is readout using the spectrum analyzer in the time domain at the very same drive frequency. Note that the initial frequency is regulated with the very same voltage regulation procedures discussed above. The results are illustrated in Fig. 5.8 (a). Each measurement point represented the average amplitude measured over 1 s time window. For low drive power up to $\approx -25\,\text{dBm}$, we observe a linear increase in the amplitude response of the resonator. Above the threshold, the response of the mechanical resonator enters the nonlinear regime, hence, the output amplitude starts to saturate since we only measure at the same frequency.

Additionally, we show in Fig. 5.8 (b) a typical result of the voltage regulation procedure during the experiments. Here, we choose a waiting time period that contains 30 data points. Each individual point is then repeated 30 times to obtain statistical distributions for a better frequency estimate. The voltage regulation procedure needs to be re-adjusted after each measurement point. It is apparent, that the system experiences a large drift at the beginning of the experiment. That is due to the strong tuning of the applied DC voltage to find the initial frequency. Note that the cavity pump at $P_{\mu w} = 22\,\text{dBm}$ is always kept constant and we usually wait for 2-3 days before performing the measurement for the system to stabilized in order to avoid long term drift due to microwave cavity pump. From Fig. 5.8 (b), it is apparent that the voltage adjustment can compensate a much slower drift that is attributed to the change in the temperature inside the lab environment.

We would like to emphasize that the voltage regulation procedures are essential for our data analysis. It is very important to always start with the same condition and the same initial frequency (f_{init}) to ensure reproducibility.

[15] Note that the measured the frequency drift due to temperature fluctuation is 2 Hz over 40 hours. The slow drift due to the change in cavity pump power or applied voltages is roughly 1.2 kHz

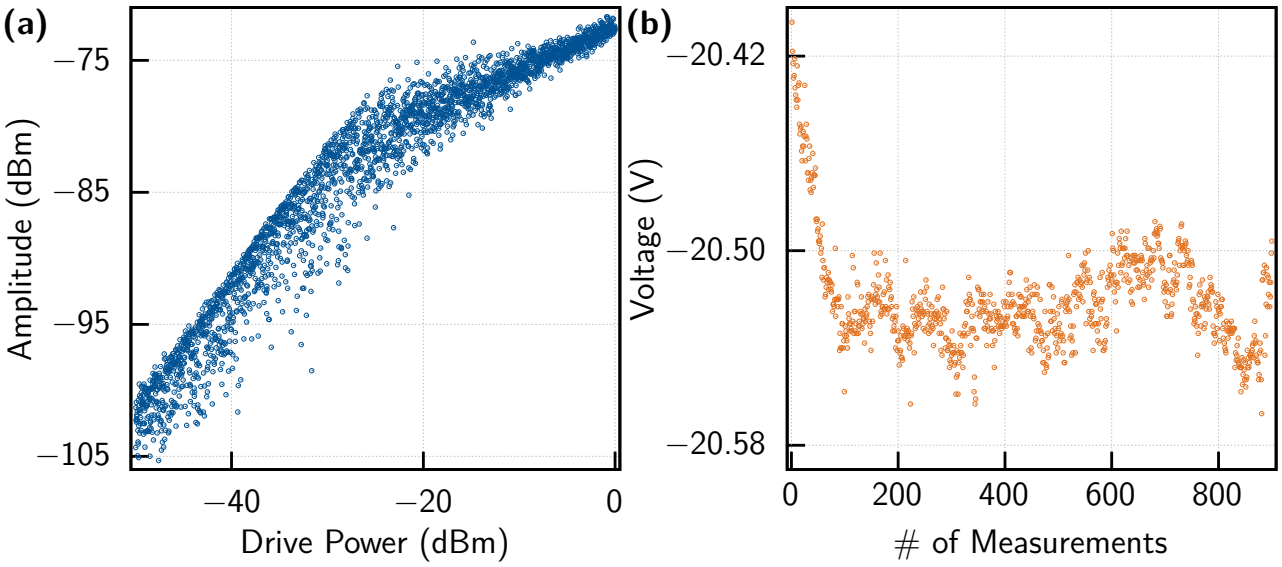

Figure 5.8 | Measurement Setup Characterizations.
(a) Nanomechanical resonator amplitude response versus the applied sinusoidal drive power. Linear increase in the amplitude response up to −25 dBm defines the threshold in the driven experiment before the resonator starts to enter the nonlinear regime. **(b)** The voltage regulation from a set of measurement consists of a time period ($(\Omega_0/2\pi)t_w = 4$) with 30 measurement points and each measurement point is repeated by 30 times to obtain statistical distributions.

5.2 Landau-Zener Transitions

The observation of an avoided crossing in the dielectric detuning experiment in Sec. 5.1.2 is a characteristic fingerprint of strong coupling. Now, we can further study the time dynamics of these two strongly coupled flexural IP and OOP modes. When tuning the flexural modes through the avoided crossing region (see Fig. 5.6), the modes undergo a transition that strongly depends on the tuning speed. This behaviour follows the well-known Landau-Zener model, that is often used to describe nonadiabatic transitions of quantum mechanical modes, e.g. quantum dots [208], superconducting qubits [215], and nitrogen-vacancy centers in diamonds [216].

In Figs. 5.9 (a) and (b), we depict the dielectric frequency detuning scheme to sweep the system through the coupling region. Note that we utilize the same measurement protocol discussed in Sec. 5.1.3.The mechanical resonator is initialized at frequency f_{init} by applying a sinusoidal drive tone at the mechanical eigenfrequency $\omega_{\mathrm{IP}}/(2\pi)$ in the lower branch or $\omega_{\mathrm{OOP}}/(2\pi)$ in the upper branch [see green circles in Fig. 5.9 (a)] together with a static DC bias voltage $U_{\mathrm{i,LZ}}$ to the electrodes. At time $t = 0$, we add a third tone that contains a simple linear ramp function provided by the AWG to increase the voltage up to $U_{\mathrm{f,LZ}}$ within a time interval τ [red solid line in Fig. 5.9 (b)]. By changing the frequency of the linear ramp function, we are able to modify the tuning speed and therefore, we expect to observe a change in the transition probability [188]. After the ramp and a short delay time $\tau + \delta$, we start to record the decaying signal a_{r} [blue solid line in Fig. 5.9 (b)] of the mechanical oscillator. In this measurement, we initialize the system either in the lower branch with the IP mode and $\omega_{\mathrm{IP}}/(2\pi)$ or in the upper branch using the OOP mode with $\omega_{\mathrm{OOP}}/(2\pi)$. In both cases, we use the initial voltage $U_{\mathrm{i,LZ}} \approx -17\,\mathrm{V}$. We measure in both cases at the lower branch after sweeping the initial frequencies through the avoided crossing at $U_{\mathrm{f,LZ}} \approx -1\,\mathrm{V}$ [see red circle in Fig. 5.9 (a)]. Note, it is necessary to add a delay time to avoid transient artifacts in the pulse scheme. As shown in Fig. 5.9 (b), we extrapolate the exponential decay back to the beginning of the linear ramp (blue dashed line) to determine the resonator's amplitude a_0 at $t = 0$. Note that the decay in amplitude between $t = 0$ and

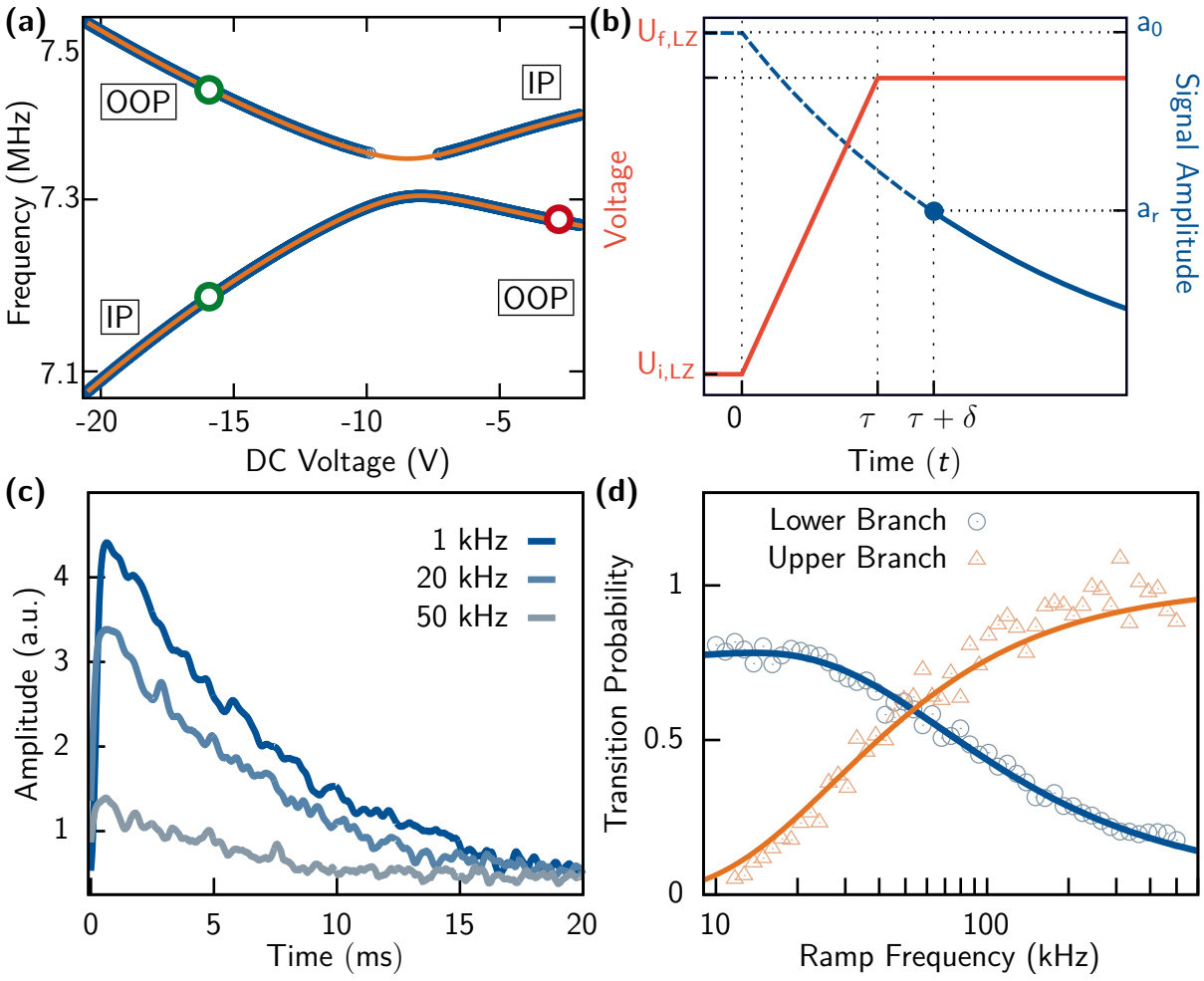

Figure 5.9 | Adiabatic and Diabatic Dynamics of the classical Two-Level System.
(a) Dielectric tuning of the mechanical modes reveals a clear avoided crossing at $\approx -8\,\mathrm{V}$. The eigenfrequencies are extracted from the spectroscopic measurement illustrated in Fig. 5.6. Green circles indicate the initialization either in the IP mode or OOP mode at $U_{\mathrm{i,LZ}} \approx -17\,\mathrm{V}$ and the red circle denotes the measured position ($U_{\mathrm{f,LZ}} \approx -1\,\mathrm{V}$) to determine Landau Zener transitions. **(b)** The pulse and measurement sequence of the time resolved experiment to demonstrate Landau-Zener transitions. At $t = 0$ The initial DC voltage U_{i} (red solid line) is ramped up to U_{f} during the time span τ to sweep the mechanical modes through the avoided crossing region. We start to record the mechanical decay (dark blue solid line) after a delay time δ. The exponential fit (dark blue dashed line) is used to extrapolate the decaying signal back to $t = 0$ to extract the magnitude of the mechanical resonator for normalization. **(c)** Exponential decays of the mechanical amplitude for different sweep frequencies $\beta_{\mathrm{AWG}} = \{1, 20, 50\}\,\mathrm{kHz}$. Here, the initial frequency $\omega_{\mathrm{IP}}(U_{\mathrm{i}})/(2\pi)$ and final frequency $\omega_{\mathrm{OOP}}(U_{\mathrm{f}})/(2\pi)$ are in the same lower branch [see Fig. 5.9 (a)]. **(d)** The probability of traversing the avoided level crossing for different ramp speed ω_{AWG}, i.e. going from a mode initialized in the OOP mode of the upper branch into the OOP mode of the lower branch on the other side of the avoided crossing (light blue circles). The transition probability, when initializing the IP mode in the lower branch and sweeping through the avoided crossing into the OOP mode in the lower branch, is indicated by the light orange circles. The blue and orange solid lines illustrate theoretical predictions obtained from Eq. (5.9).

$t = \tau + \delta$ has to be accounted in the theoretical model in order to determine the correct transition probability. In our case, we introduce the an additional term in the normalization procedure

$$P_{\mathrm{LZ}} = \frac{a_0}{a_{\mathrm{init}}} \exp\left(\frac{\Gamma}{\beta_{\mathrm{AWG}}}\right). \tag{5.5}$$

Here a_0 is the extrapolated amplitude extracted from the exponential fit, a_{init} is the initial amplitude from the sinusoidal drive prepared at $U_{\mathrm{i,LZ}}$, Γ is the mechanical decay term and β_{AWG} is the sweep frequency. For the initialization in the lower branch using the IP mode, we find $1/\Gamma_{\mathrm{IP}} = 5.9\,\mathrm{ms}$. In the upper branch the decay is $1/\Gamma_{\mathrm{OOP}} = 6.8\,\mathrm{ms}$.

For a small tuning speed, the excitation energy remains in the same branch. In other words, it is very likely to transfer the energy from one vibrational mode to the other in the adiabatic limit. When the frequency detuning speed becomes faster, the system is dominated by the diabatical behaviour and there is no mixing between the two modes. The excitation energy is more likely to remain at the same flexural mode and hence, there is a transition from one branch to another. This is the classical behaviour [188] of the Landau-Zener transition that is analogous to the quantum mechanical counterparts. We can define the transition probabilities for both quantum and classical case as

$$P_{\mathrm{dia}} = \exp\left(-\frac{\pi\Omega_0^2}{2\alpha}\right). \tag{5.6}$$

The transition probability for the adiabatic case is simply

$$P_{\mathrm{adia}} = 1 - P_{\mathrm{dia}}. \tag{5.7}$$

We define the detuning speed in Eq. (5.6) as

$$\alpha\left[\frac{Hz}{s}\right] = c_{\mathrm{eff}} \cdot \delta U \cdot \beta_{\mathrm{AWG}}, \tag{5.8}$$

with $c_{\mathrm{eff}} = 43.363\,\mathrm{kHz/V}$ the voltage to frequency conversion factor obtained from the avoided crossing, $\delta U = U_{\mathrm{f}} - U_{\mathrm{i}}$ and $\beta_{\mathrm{AWG}} = 10^4 \cdot \frac{\omega_{\mathrm{AWG}}}{(2\pi)}$ the sweep frequency that we can adjust from the AWG to change the detuning speed. In Fig. 5.9 (c), we plot the exponential decays, where the initial IP mode and the readout mode (OOP) are in the same lower branch, as a function of time for different sweep frequencies $\beta_{\mathrm{AWG}} = \{1, 20, 50\}\,\mathrm{kHz}$, respectively. As expected, most of the excitation in the IP mode is adiabatically transferred to the OOP mode in the same branch for low detuning speed. At higher speed, $\omega_{\mathrm{AWG}}/(2\pi) = 50\,\mathrm{kHz}$, the excitation energy is more likely to end up in the upper branch. This measurement is repeated for many different ramp frequencies.

We show the final result for the Landau-Zener transitions in Fig. 5.9 (d). Note that in this experiment, we prepare the initial states either in the upper or lower branch [see green circles in Fig. 5.9 (a)] and monitor the decay of the mechanical resonator in the lower branch after sweeping through the avoided crossing at the final voltage $U_{\mathrm{f},LZ} \approx -1\,\mathrm{V}$ [see red circle in Fig. 5.9 (a)]. The results in Fig. 5.9 (d) clearly demonstrate the expected behaviour. For slow ramp frequencies, the adiabatic behaviour dominates. For faster detuning, the transition probabilities interchange the roles for both cases. Note that we do not obtain unity transition probability for the case, which we initialize the system in the lower branch [light blue circles in Fig. 5.9 (d)]. We refer this behavior to the fact that we can not prepare the initial mode as a pure state due to the mode hybridization of the two modes over the operated DC voltage range. Hence, this mitigates the contrast in the transition probability. Since

we do not operate with pure mechanical flexural modes (IP and OOP) but with hybridized modes, we use a modified transition probability [217]

$$P_{\mathrm{dia,mod}} = \left[\sqrt{P_{\mathrm{dia}}} \cdot v + \sqrt{1 - P_{\mathrm{dia}}} \cdot (1 - v)\right]^2 \tag{5.9}$$

with v is the visibility equal to 1 for pure state preparation. Note, from the fit using Eq. (5.9) we can extract the level splitting for the case of frequency initialization in the upper branche [light orange triangles in Fig. 5.9 (d)] $\Omega_0/(2\pi) = 40.02\,\mathrm{kHz}$. When initializing the system in the lower branch [light blue cirlcles in Fig. 5.9 (d)] , we obtain $\Omega_0/(2\pi) = 56.06\,\mathrm{kHz}$ and from the avoided crossing (see Fig. 5.6 and Appendix A.3), we get $\Omega_0/(2\pi) = 41.31\,\mathrm{kHz}$. These results demonstrate the difficulty to extract the level splitting of our strongly coupled flexural modes of the nanomechanical resonator with high accuracy. In the following section, we introduce the experimental realization of the theoretically developed iterative adaptive sensing protocol (see Sec.4.4) based on Ramsey interferometry (discussed in Sec. 4.1) that allows frequency estimates with high precision. The precise estimation of the level splitting is essential for the development of the coupled two-mode system as a coherent sensor.

5.3 Ramsey Protocol

As mentioned in the beginning of this chapter, we employ the coherent nature of the resolvable and strongly coupled modes to implement the enhanced Ramsey protocol proposed in Sec. 4.1. The key quantity in this protocol is the phase, $\varphi(t_{\mathrm{w}}) = \Omega_0 t_{\mathrm{w}}$, emerged during the coherent transitions. Thus, the recorded phase provides direct access to the level splitting Ω_0. In contrast to conventional Ramsey interferometry, we replace the $\pi/2$-pulse [see step I' in Fig. 4.1 (a)] used for sensing state preparation by a fast-tuning pulse generated from the AWG to directly implement the Ramsey protocol [fast process indicated by orange arrows in Fig. 4.1 (a)]. This pulse performs an unitary mapping of the initialized state into the sensing state at the avoided crossing. The fidelity of generating an ideal sensing state is proportional to the speed of the unitary evolution, which is limited by experimental constraints (see Sec. 4.1.2). We overcome this limitation by introducing the Magnus-based corrected protocol discussed in Sec. 4.2. These corrected pulses ensure high-fidelity sensing and readout state preparations while working intermediate regime. The Ramsey interferometry can thus be implemented by the following pulse scheme

$$U(t) = \begin{cases} U_{\mathrm{i}}, & \text{for } t < t_0, \\ U_{\mathrm{i}} + \delta U \cdot \Delta_{0\mathrm{s}}(t), & \text{for } t_0 \le t < t_{\mathrm{s}}, \\ U_{\mathrm{f}}, & \text{for } t_{\mathrm{s}} \le t < t_{\mathrm{f}}, \\ U_{\mathrm{f}} - \delta U \cdot [1 - \Delta_{\mathrm{fr}}(t)], & \text{for } t_{\mathrm{f}} \le t < t_{\mathrm{r}}, \\ U_{\mathrm{r}}, & \text{for } t_{\mathrm{r}} \le t. \end{cases} \tag{5.10}$$

Here, $U_{\mathrm{i}}, U_{\mathrm{f}}$ are the initial and final voltages [see Fig. 5.10 (a)] and $\delta U = U_{\mathrm{f}} - U_{\mathrm{i}}$. Furthermore, we define the time dependent detuning

$$\Delta_{jk}(t) = f_{jk}(t) + \Delta_{jk,\mathrm{corr}}(t), \tag{5.11}$$

where $j \in \{0, \mathrm{f}\}$, $k \in \{\mathrm{s}, \mathrm{r}\}$. The single tone function $f_{jk}(t)$ requires the pulse scheme to fulfill the condition $f(t = 0) = f(t = t_{\mathrm{r}}) = 0$ and hence, we define

$$f_{jk}(t) = \frac{1}{2}\left[1 - \cos\left(\pi \frac{t - t_j}{t_k - t_j}\right)\right]. \tag{5.12}$$

The correction term

$$\Delta_{jk,\mathrm{corr}}(t) = \Delta_{jk,\mathrm{even}}(t) + \Delta_{jk,\mathrm{odd}}(t) \tag{5.13}$$

is obtained from the Magnus-based strategy with the corresponding first harmonic in the Fourier series

$$\begin{aligned} \Delta_{jk,\mathrm{even}}(t) &= c_1\left[1 - \cos\left(2\pi\frac{t-t_\mathrm{j}}{t_\mathrm{k}-t_\mathrm{j}}\right)\right], \\ \Delta_{jk,\mathrm{odd}}(t) &= d_1\left[\sin\left(2\pi\frac{t-t_\mathrm{j}}{t_\mathrm{k}-t_\mathrm{j}}\right)\right], \end{aligned} \tag{5.14}$$

where c_1 and d_1 are the free Fourier coefficients associated with the first harmonic correction one must find to fulfill Eq. (4.47). Figure 5.10 (a) illustrates the typical Ramsey pulse scheme that includes the following sequence

(I) Initialization: the state $\boldsymbol{a}_1 = \begin{bmatrix} 0 \\ \omega_\mathrm{ip}(t_0) \end{bmatrix}$ is prepared by applying a constant voltage U_i to obtain the IP mode with the corresponding eigenfrequency ω_IP at initial time t_0 (in the lower branch) to satisfy the condition $\Delta_0/\Omega_0 \gg 1$ (see Fig. 5.6). Note, the mode is driven continuously on resonance during the entire sequence.

(II) Sensing state preparation: implementation of the leading edge with Magnus-based corrections [see Eq. (5.10)] to frequency-sweep the system to the sensing state $\boldsymbol{a}_\mathrm{s} = \boldsymbol{a}_1$ at $t = t_\mathrm{s}$. To obtain a reference measurement for the corrected protocol, we can prepare the sensing state without any correction.

(III) Coherent evolution: for a time $t_\mathrm{w} = t_\mathrm{f} - t_\mathrm{s}$ where the system picks up a phase $\phi = \Omega_0 t_\mathrm{w}$.

(IV) Read-out state preparation: implementation of the trailing edge with (or without) Magnus-based corrections to sweep the system to the read-out state $\boldsymbol{a}_\mathrm{r}$ at $t = t_\mathrm{r}$.

(V) Readout of the ring-down signal as described in Sec. 5.2 to determine the system's return probability.

Ideally, the initial and readout states should be identical in order to correctly map the return probability from the Ramsey sequence. Since the initial state is driven continuously, it is necessary to introduce a finite offset $a_1(t_\mathrm{r}) - a_1(t_0) \neq 0$ that enables the readout state to decay rather than being re-excited (see solid blue line in Fig. 5.10 (a). Additionally, the exponential decay is extrapolated back to t_0 (see dashed blue line in Fig. 5.10 (a) to compensate mechanical damping during the evolution times $t_\mathrm{s}, t_\mathrm{w}$ and t_r. By keeping the ratio $\{\omega_\mathrm{ip}(t_\mathrm{r}) - \omega_\mathrm{ip}(t_0)\}/\Delta_0 \ll 1$, we assume the offset has no significant impact on the determination of the return probability. Fig. 5.10 (b) illustrates the typical ring-downs of the readout mode for waiting times $t_\mathrm{w} = 0$ (circles) and $t_\mathrm{w} = 2\pi/\Omega_0 \times \frac{1}{2}$ (diamonds), respectively. The corresponding exponential decay fits are extrapolated back to t_0 and the resulting return amplitude is normalized to the signal amplitude during the initialization procedure (see step I) where the eigenfrequency of the in-plane mode $\omega_\mathrm{ip}(t_0)$ is continuously driven. The measured return probability is thus defined as [see also Eq. (4.1)]

$$P_\mathrm{r}(t_\mathrm{w}) = |\boldsymbol{a}_1^\mathrm{T} \exp\left(-\mathrm{i}\Omega_0 t_\mathrm{w}\sigma_x\right)\boldsymbol{a}_1|^2 = 1 - v\,\sin^2\left[\left(\bar{\Omega}_0^{(m)}/2\right) + \varphi\right]. \tag{5.15}$$

Here, v is the visibility equal to 1 for ideal state preparation.

In the following, we demonstrate the outputs of our experimental results. First, we conduct the Ramsey interferometry protocol with the simple control term $\Delta_{jk}(t) = f_{jk}(t)$ that contains only a

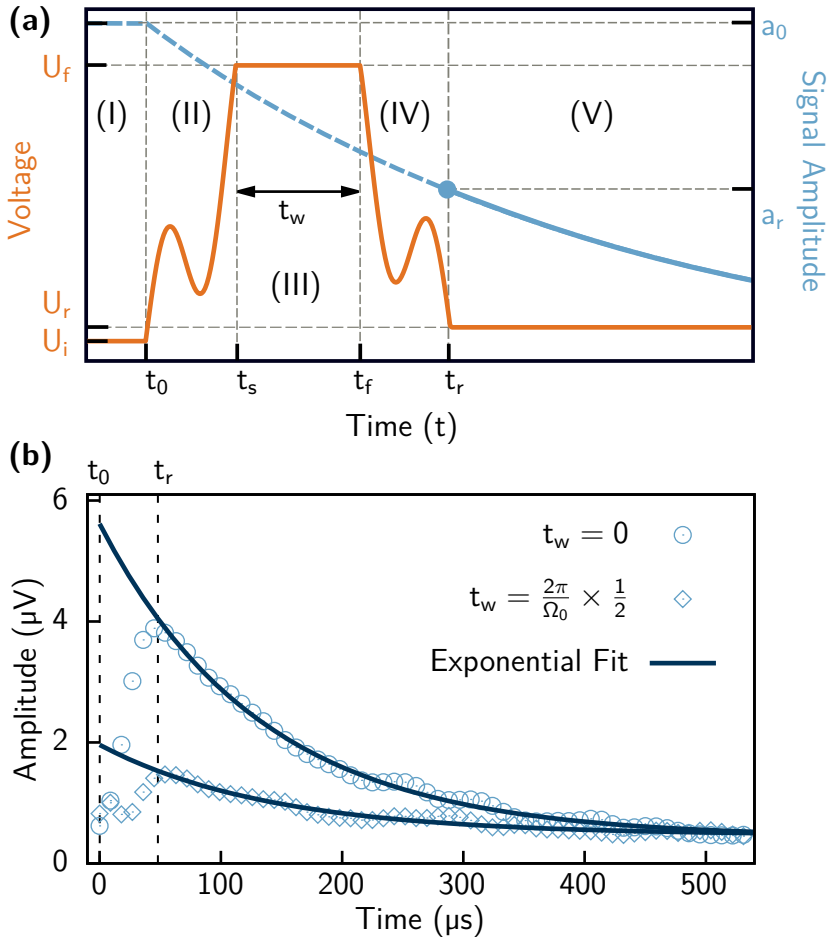

Figure 5.10 | Implementation of the Ramsey Interferometry.
(a) Ramsey pulse sequence with the corresponding first harmonic Magnus-based correction for $j = 1$ (Mod1) (see Sec. 4.2.2) of the leading (I) and trailing (IV) edges for the frequency-sweep. Note that we introduce a finite offset $U_r - U_i \neq 0$, that allows the readout state $\boldsymbol{a}_r(t_r)$ to decay while the initial state $\boldsymbol{a}_1(t_0)$ is continuously driven. **(b)** Experimental ring-downs for different waiting times t_w of the Ramsey sequence (light blue). The exponential fits are extrapolated back to t_0 to compensate the decay caused by the mechanical damping during the evolution time. The black dashed lines indicate the positions of t_0 and t_r in (a), respectively. Note that due to the different waiting times t_w, there is a small deviation in the readout times t_r . However, this is not clearly observable since the difference is only $\approx 10\,\mu s$.

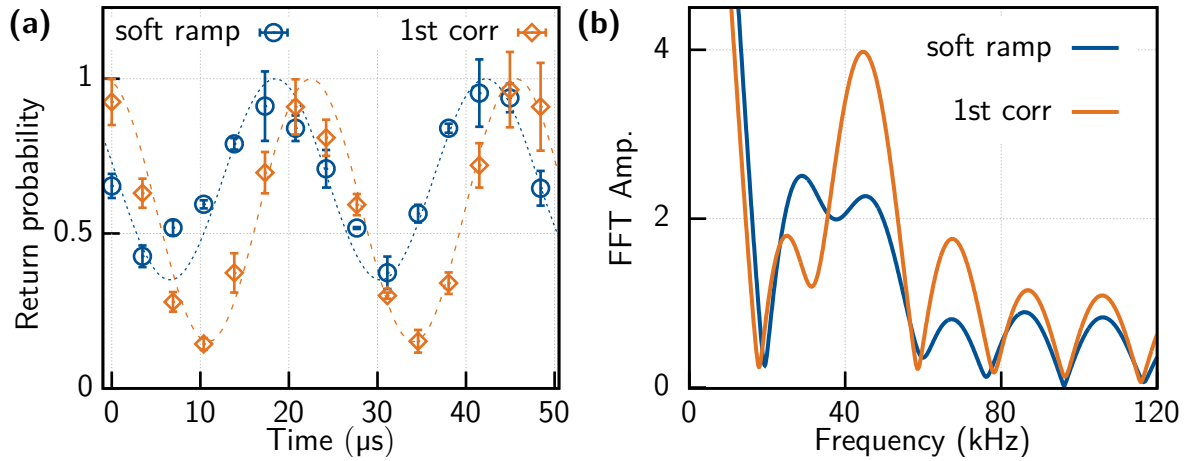

Figure 5.11 | Control Pulse with Magnus-Based Corrections versus Soft Ramp.
(a) The outputs of the Ramsey interferometry showing the return probability as a function of waiting time with the typical oscillatory behaviour (Ramsey fringes) for both uncorrected control pulses, denoted soft ramp, (blue circles) and the Magnus-based modified control pulses (orange diamonds). The measurement time window is $t_w = n_p\left(\frac{2\pi}{\Omega_0}\right)$, with $n_p = 2$ is the number of the expected cycles. **(b)** The discrete oscillatory outputs in the time domain in (a) is transformed into the frequency domain using DFT. In the soft ramp case (blue solid line), no distinct global maximum is observed (ignoring the zero-frequency peak), whereas the Magnus-based corrected frequency-sweep (orange solid line) leads to a frequency distribution with a pronounced global maximum. Due to the added zero-padding (see discussion in Sec. 4.3.2), the resolution of the DFT in the frequency domain is greatly enhanced. We choose $n_{pad} = 2000$.

single frequency component in the cosine function [see Eq. (5.12)]. We refer to this configuration as the "soft ramp" case which serves as a reference measurement for the corrected protocol.

Second, we add the correction terms from the Magnus-based strategy, that contains the first harmonic in the Fourier series [see Eqs. (5.13) and (5.14)], to the control pulse $\Delta_{jk}(t) = f_{jk}(t) + \Delta_{jk,\mathrm{corr}}(t)$. We refer this case as the "1st corr". Figure 5.10 (a) illustrates a typical pulse form whose leading and trailing edges are modified using the first harmonic corrections.

Here, we choose the measurement time window such that $t_w = 2\left(\frac{2\pi}{\Omega_0}\right)$. The tuning speed in our case is defined by the sweep frequency that is

$$\beta_{\mathrm{AWG}} = \frac{c_{\mathrm{eff}} \cdot \delta U \cdot \Omega_0}{\Delta_0 \cdot \xi}. \tag{5.16}$$

Here, $\delta U = U_f - U_i = 13.012\,\mathrm{V}$ is the voltage required to detune the initial state into the sensing state, $c_{\mathrm{eff}} = 43.363\,\mathrm{kHz/V}$ is the voltage to frequency conversion factor obtained from the dielectric tuning measurement in Sec. 5.1.2, $\Omega_0/(2\pi) = 41.311\,\mathrm{kHz}$ is the level splitting of the two coupled mechanical modes in the avoided crossing region, $\Delta_0/(2\pi) = 463.153\,\mathrm{kHz}$ is the initial frequency splitting at $t = t_0$ and

$$\xi = \frac{\Omega_0 t_s}{2\pi} \tag{5.17}$$

is a dimensionless parameter in Eq. (5.16) with a sweep time t_s dependence. In the theoretical prediction [see Fig. 4.5 (a) and (b)], the uncorrected frequency sweep needs to fulfill $\Omega_0 t_s/(2\pi) \ll 10^{-2}$ in order to achieve error fidelities on the order of 10^{-3}. This requirement translates into a sweep frequency output that is $\beta_{\mathrm{AWG}} \approx 5.777\,\mathrm{MHz}$. Although this requirement is well-suited in the operation bandwidth of our AWG (0 MHz – 50 MHz) in the *high voltage amplifier* mode, it is still not possible for us to perform control pulses in this frequency range. In this experiment, the voltage combiner box

together with the single layer capacitor (see Fig. 5.2) ultimately put an upper limit in the frequency operation at 100 kHz (see discussion in appendix A.4).

Conveniently, we can soften the frequency requirement with the Magnus-based strategy, e.g. we can choose control pulses with the first harmonic corrections such that $\xi = \Omega_0 t_s/(2\pi) \equiv \frac{1}{2}$ [see Fig. 4.5 (a) and (b)]. In this case, the error fidelities in state preparations is on the order of 10^{-2}. At the same time, we can strongly reduce the sweep frequency requirement in Eq. (5.16) to $\beta_{\mathrm{AWG}} \approx 100\,\mathrm{kHz}$.

In Fig. 5.11 (a), we plot the return probabilities [see Eq. (5.15)] of the initial state $\boldsymbol{a}_1$ as a function of waiting time t_w for the uncorrected "*soft ramp*" case and the corrected "1st corr" case. Note, we perform 30 averages for each measurement point to obtain a mean value and the corresponding statistical error. We observe the oscillatory behaviour in the time domain which is the characteristic finger print of the Ramsey interferometry in both cases. In stark contrast, the corrected pulse scheme exhibits an oscillatory signal with a much higher peak to peak amplitudes and exhibits a corrected phase shift compared to the soft ramp. This result indeed indicates the strong suppression of the spurious coupling during the sensing and readout state preparations when adding Magnus-based correction terms to the control pulses.

The effect of the corrected dynamics becomes even more apparent when transforming the Ramsey interferometry outputs to the frequency domain. In Fig. 5.11 (b), we show the corresponding discrete Fourier transform of the obtained Ramsey fringes. In order to reduce the effect of scalloping loss due to a small number of sampling points $n_{\mathrm{samp}} = 30$, we use the zero-padding technique discussed in Sec. 4.3.2. Here, we add $n_{\mathrm{pad}} = 2000$ zero-valued sampling points on both sides of the oscillatory signals to enhance the frequency resolutions. The modified control pulse with correction terms leads to a frequency spectrum (orange solid line), where a global maximum can easily be identified (the zero-frequency peak is excluded). In the case of the soft ramp (blue solid line), however, no distinct global maximum is observed.

We emphasize that despite the good control in sensing and readout state preparations, we still observe the effect of spectral leakage in the frequency distribution. From the discussion in section 4.3.3, we know that this effect can lead to a shift of the maxima of the Fourier transform and hence, mitigates the precision in frequency estimate. In the following section, we show how the iterative, adaptive procedure proposed in Ch. 5, that combines the windowing schemes and the update of the previously estimated frequency Ω_0, will minimize the unwanted effects in the discrete Fourier transform and thus, yields a high precision estimate of the level splitting Ω_0.

5.4 Iterative Adaptive Spectroscopy for Frequency Estimation

To determine the level splitting Ω_0 with high fidelity, we follow the theoretically proposed "Iterative Adaptive Spectroscopy" protocol (IAS) discussed in section 4.4. The protocol first follows an initial estimate of Ω_0, e.g. extracted from spectroscopy measurement, which is done by fitting the avoided crossing (see Appendix A.3). We define this initially estimated splitting as $\bar{\Omega}_0^{(0)}$. This measurement is then used to define the measurement time window $t_{\mathrm{w}}^{(1)} = n_{\mathrm{p}}\left(2\pi/\bar{\Omega}_0^{(0)}\right)$ and the correction coefficients $c_1^{(1)} := c_1^{(1)}\left[\bar{\Omega}_0^{(0)}, \Delta_0\right]$ and $d_1^{(1)} := d_1^{(1)}\left[\bar{\Omega}_0^{(0)}, \Delta_0\right]$ for the iteration step, $m = 1$. Again, c_1 and d_1 are the free Fourier coefficients associated with the first harmonic correction one must find to fulfill Eq. (4.47). Δ_0 is the initial detuning at t_0 shown in Fig. 5.6 (c) fixed by the choice of our initialization frequency $\boldsymbol{a}_1(t_0)$ and the number of cycles $n_p = 4$. The initial estimate for this system from the spectroscopic measurement (see appendix A.3) gives a splitting of $\bar{\Omega}_0^{(0)}/(2\pi) = 41(1)$ kHz from the fitting and the error is given by the least squares in the regression analysis. The modified Ramsey protocol with these parameters then yield an oscillatory signal following

$$P_{\mathrm{r}}^{(m)} = 1 - v\ \sin^2\left[\left(\bar{\Omega}_0^{(m)}/2\right) + \varphi\right] \tag{5.18}$$

where, v is the visibility equal to 1 for ideal state preparation. The coupling then can be estimated by performing a fast Fourier transform (FFT) on the zero-padded Ramsey data [184]. On each iteration step ($m > 1$) we then:

(a) update the measurement window with $t_{\mathrm{w}}^{(m)} = n_{\mathrm{p}}\left(2\pi/\bar{\Omega}_0^{(m-1)}\right)$,

(b) update the corrected control pulses with the adapted Fourier coefficients $c_1^{(m)} := c_1^{(m)}\left[\bar{\Omega}_0^{(m-1)}, \Delta_0\right]$ and $d_1^{(m)} := d_1^{(m)}\left[\bar{\Omega}_0^{(m-1)}, \Delta_0\right]$,

(c) convolute the Ramsey signal with the Blackmann-Harris (BH) window to reduce the effect of signal processing artifacts, such as spectral leakage and scalloping losses (see discussions in Sec. 4.3.3).

For instance, we show in Fig. 5.12 (a) the Ramsey signal with no windowing (blue) and Blackman-Harris windowing (orange) for iteration step $m = 8$. The Ramsey signal is then padded and Fourier transformed which gives us an estimate of the splitting for this particular instance [see Fig. 5.12 (b)]. We would like to stress that for each iteration step m the estimation of $t_{\mathrm{w}}^{(m)}$, $c_1^{(m)}$, $d_1^{(m)}$ is performed with $\bar{\Omega}_0^{(m-1)}$ evaluated by Blackman-Harris window function in the previous iteration. However, we display the result of the estimation at each iteration step m (for $m > 1$) with both BH and rectangular window (or no window) as shown in Fig. 5.12 (c). Note the missing point in BH window for iteration $m = 1$. Only the rectangular window can be applied for this particular case, that is due to the small number of cycle $n_{\mathrm{p}} = 2$ (see Fig. 5.11). Since the BH window function strongly suppresses the side lobes of the signal in the time domain [see Fig. 5.12 (a)], it is necessary to employ $n_{\mathrm{p}} \geq 4$ in order to be able to estimate the signal in the Fourier frequency domain. For each iteration m, the measurements are performed statistically on 30 Ramsey signals. To obtain a statistical distribution in the frequency domain, we estimate the frequency of each Ramsey oscillation before averaging. Here, we assume that the noise contribution does not appreciably change the level splitting for one realization of the protocol (frozen environment approxiamtion).

As seen in Fig. 5.12 (c), the Blackman-Harris window results in a well distinguishable estimate of the splitting compared to the rectangular window with an accuracy better than the standard errors of the

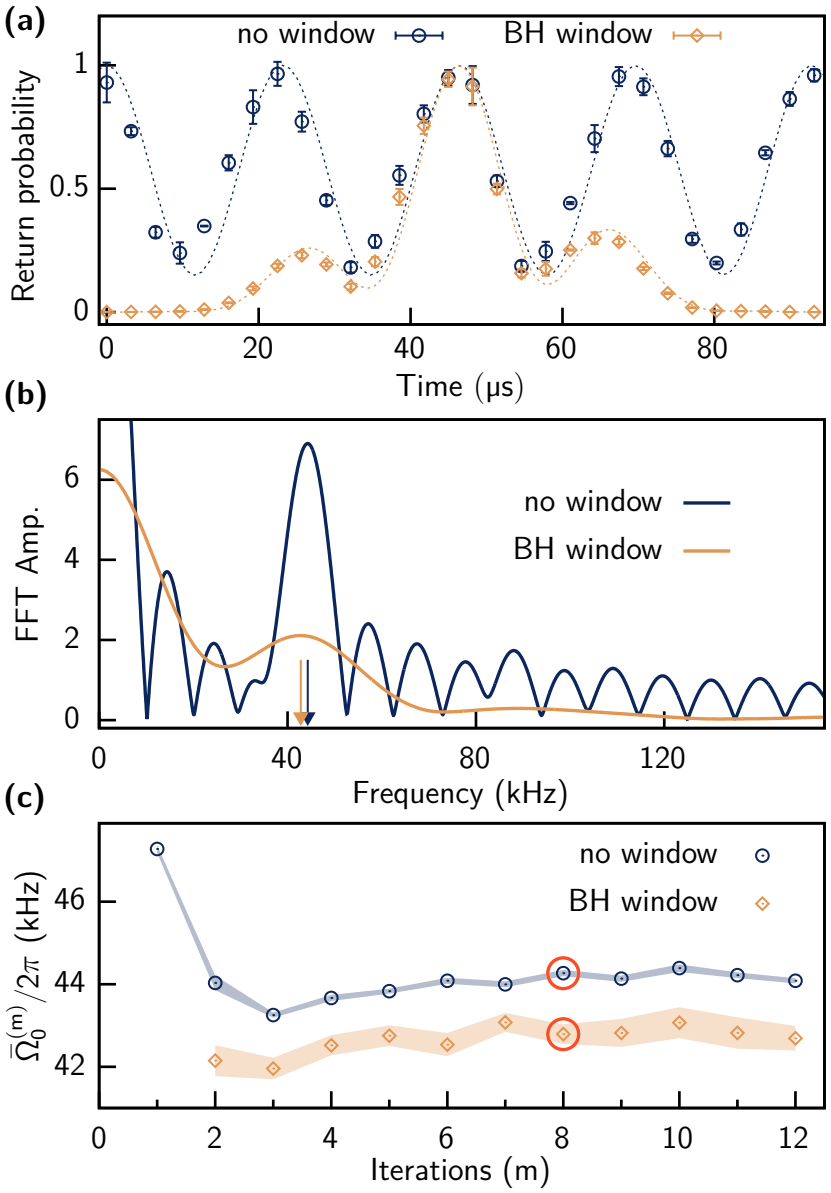

Figure 5.12 | Iterative Adaptive Spectroscopy for Short and Finite Signals.
(a) Return probability of the state $\boldsymbol{a}_1$ as a function of time in the Ramsey interferometry experiment (blue circles). Similar to Fig. 5.11 (a), we obtain the typical Ramsey fringe that oscillates at Ω_0 in the chosen time window $t_\mathrm{w} = 4\left(\frac{2\pi}{\Omega_0}\right)$. Point-wise product of the Ramsey fringe with the Blackmann-Harris window (orange dots). Each point indicates the mean value and the corresponding error bars indicate the statistical distribution over 30 measurements. The dotted blue and orange lines serve as guide to the eye. **(b)** Fourier spectra of zero-padded Ramsey signal with rectangular window (no window) function (dark blue) and Blackmann-Harris window function (orange). The dark blue and orange arrows indicate the maximum positions for frequency estimations using the respective windows. **(c)** Frequency estimations of the level splitting $\bar{\Omega}_0{}^{(m)}$ for each subsequently updated iteration step m. The red circles at $m = 8$ indicate the frequency estimates from panels (a) and (b) using no window and BH window functions, respectively. For $m = 1$, we choose the number of cycle $n_\mathrm{p} = 2$ for the Ramsey oscillation. Since the BH window function strongly suppresses the beginning and the end of a signal in time domain [see (a)], it is not possible to determine frequencies in Fourier domain for $n_\mathrm{p} = 2$. Thus, only the no window function is applicable in this case.

individual estimations. Although the iteration saturates for $m > 3$ and then stays within the standard errors of further estimations, we show here until $m = 12$ to display the stability of our measurement scheme. For $m = 8$ (red circles), corresponding to the situation shown in Fig. 5.12 (a) and (b), the frequency estimations with the corresponding standard errors from Blackman-Harris and rectangular window are $\bar{\Omega}^{(8)}_{0,\mathrm{BH}}/(2\pi) = 42.79(24)$ kHz and $\bar{\Omega}^{(8)}_{0,\mathrm{RW}}/(2\pi) = 44.27(8)$ kHz, respectively.

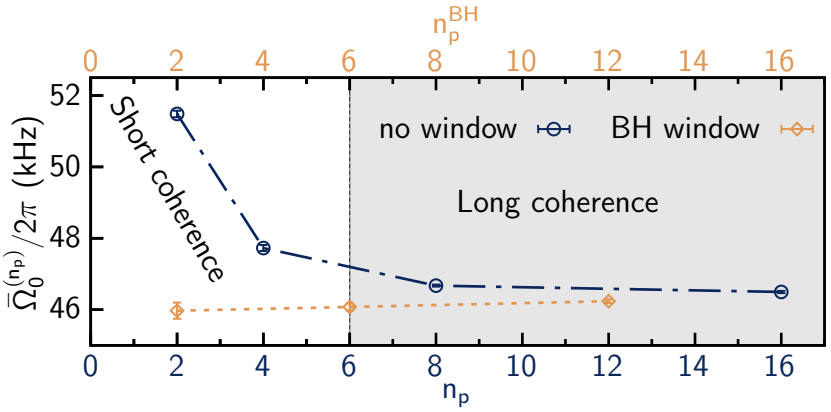

Figure 5.13 | Frequency Estimation versus Number of Cycles.
Frequency estimation with high precision is possible for systems with long coherent time. For system with short coherence our IAS sequence with BH window (orange) yields a much better frequency estimate than the rectangular window function(dark blue). For the sake of comparison, we introduce a new x-axis showing the effective number of cycles $n_\mathrm{p}^{\mathrm{BH}}$. This is again due to the fact, that the BH window strongly suppresses the amplitude at the beginning and the end of the oscillatory signal in the time domain [see Fig. 5.12]. The vertical dashed black line separates the regimes with long (gray box) and short (white box) coherence times.

A natural and simple way to suppress spectral leakage and scalloping is to increase the number of cycles n_p and number of data points (i.e. zero-padding) in the measurement. Here, we again employ the iterative adaptive method mentioned above and, at the same time, vary the number of cycles n_p to update the measurement window. Additionally, we add $n_\mathrm{pad} = 2000$ to increase the spectral solution in the Fourier frequency domain. As apparent in Fig. 5.13, the frequency estimate using the rectangular window (dark blue) has strong variations for small n_p, whereas the BH window (orange) remains relatively unchanged. By increasing the number of cycles, the effects of spectral leakage is strongly suppressed and the frequency estimate of the rectangular window approaches the BH method. Note, however, that this type of measurement with large number of measurement cycles n_p is only possible for systems with long coherence time.

Nevertheless, precise frequency estimate for short finite signals (i.e. low n_p) is still achievable with our developed iterative adaptive spectroscopy. For the sequence, we employ Magnus-based corrections for high fidelity state preparation and BH window filter function to suppress spectral leakage. Once again, we want to emphasize the advantage of our quasi-instantaneous high precision IAS measurement over conventional coherent control techniques e.g. spin-echo [52] or Carr-Purcell-Meiboom-Gill (CPMG) sequence [218]. These dynamical-decoupling techniques were implemented to mitigate noise and extend the coherence of the two-level system by generating train of control $\pi-$pulses [219]. In order to reliably generate these pulses, good knowledge of the level splitting Ω_0 and long coherence time T_1 are strongly required. Furthermore, the applied square pulses have finite rise times that are limited by the bandwidth of the pulse generator, and again, degrade the precise control of the coherent dynamics. Our method, however, is not constrained by systematic noise, decoherence sources or limitations such as the bandwidths of the experimental apparatus and thus, enables fast and high precision in frequency estimate even applicable for systems with short coherence times, where only a small number of cycles

n_p can be measured (see Fig. 5.13). Note that we indeed conduct frequency estimate experiments using a nanomechanical system with long coherence time $T_1 \approx 6\,\text{ms}$. Nevertheless, we can mimic the operation of the system with short coherence time simply by reducing the number of oscillation periods n_p in the experiments to demonstrate the advantage of our developed IAS protocol in frequency estimation with high precision.

5.5 Coherent Sensing

The high fidelity state preparation and precise frequency estimate allow us to employ the coupled nanomechanical two-level system as a coherent sensor to determine small changes of physical quantities, e.g electric or magnetic field, in the surround environment, where the two-level system is embedded.

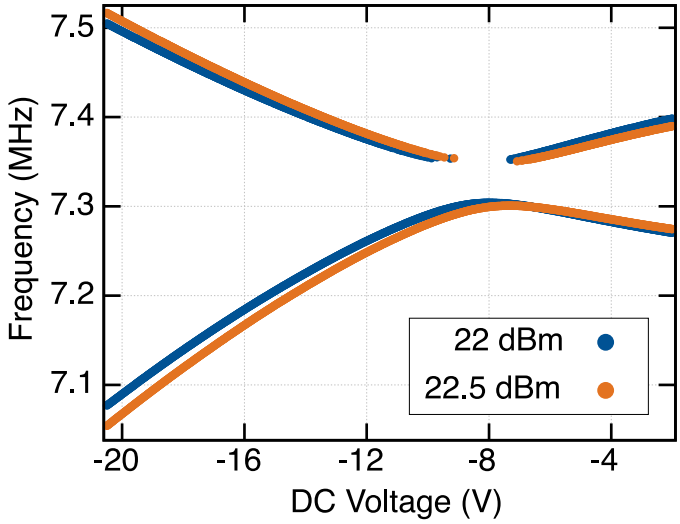

Figure 5.14 | Dielectric Tuning and Cavity Pump Power.
Eigenfrequencies of the IP and OOP modes versus DC bias voltage. The dots are values extracted from Lorentzian fits of the spectroscopic measurements (see for instance Fig. 5.6). The modification of the cavity's pump power leads to a small deviation in the tuning behaviour of the respective modes.

.

Modification of the Level Splitting In Ref. [56], it has been demonstrated that the strong coupling Ω_0 of the two flexural modes arises from the asymmetry of the beam and the two adjacent electrodes. The effective electric field exhibits a gradient in x and z direction [see Eq. (5.4)] that governs the coupling strength of the in-plane and out-of-plane modes. In our specific case, we modify the root-mean-square (RMS) electric field that builds up inside the microwave cavity [95, 107] by varying the microwave cavity's pump power $P_{\mu w}$ and hence, changing the electrical environment around the dielectrical resonator. As a result, we expect the coupling strength Ω_0 of the two flexural modes to shift according the change in the field's strength. In Fig. 5.14, we illustrate the dielectrical eigenfrequency tuning behaviour of the flexural IP and OOP modes as a function of the applied DC voltage for two different cavity pump powers $P_{\mu w} = 22\,\text{dBm}$ and $P_{\mu w} = 22.5\,\text{dBm}$, respectively. The slight change in the pump power of the microwave cavity results in a small deviation in eigenfrequency tuning. The modification in the eigenfrequency tuning and the corresponding level splitting Ω_0 can be verified using COMSOL simulations (see discussion in appendix A.5).

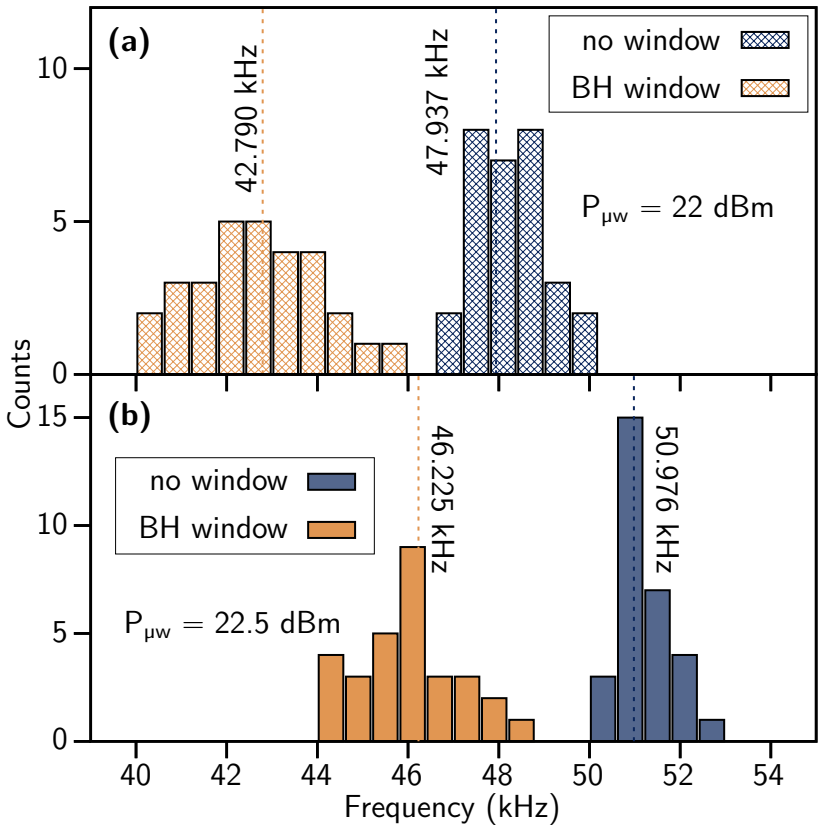

Figure 5.15 | Nanomechanical Two-Level System as a Coherent Sensor.
(a) Statistical frequency distributions of 30 Ramsey signals for both window functions with $n_{\mathrm{p}} = n_{\mathrm{p}}^{BH} = 2$ and cavity pump power $P_{\mu w} = 22\,\mathrm{dBm}$. **(b)** By increasing cavity pump power to $P_{\mu w} = 22.5\,\mathrm{dBm}$ we can clearly observe absolute shifts in frequency distributions in both no window and BH window cases. However, there is a small deviation in the relative offset $\xi^{(\mathrm{rel})}$. This indicates, that the precision in frequency estimate indeed differs depending on the applied window functions.

Sensing Capability In the following, we record the Ramsey fringes after modifying the RMS electric field and apply our IAS scheme to estimate the new level splitting. Fig.5.15 (a) shows the statistical frequency distribution of the 30 Ramsey signals and the corresponding mean values for both rectangular and BH windows with $P_{\mu w} = 22\,\mathrm{dBm}$. Here, we choose the Ramsey signal with $n_p = 2$ for rectangular window. The point wise product of the Ramsey signal (with $n_p = 4$) and the BH window function suppresses the side lobes and effectively reduces the number of cycles to $n_p^{BH} = 2$ [see Fig. 5.12 (a)]. The measurement results can thus be compared for an effective number of 2 cycles in both cases. The frequency distributions in both cases are well separated. From the previous Sec. 5.4, we know that the BH windows yields a reliable frequency estimate of $\bar{\Omega}_{0,BH}^{22\,\mathrm{dBm}}/(2\pi) = 42.79(24)\,\mathrm{kHz}$ due to mitigation of the spectral leakage, and hence, suppresses systematic frequency shift errors. The rectangular window, however, gives a relative offset of

$$\xi_{(rel)}^{22\,\mathrm{dBm}}/(2\pi) = \left(\bar{\Omega}_{0,RW}^{22\,\mathrm{dBm}} - \bar{\Omega}_{0,BH}^{22\,\mathrm{dBm}}\right)/(2\pi) = 5.15(39)\,\mathrm{kHz} \tag{5.19}$$

which is $\approx 12\%$ deviation compared to the result from BH window.

In order to quantify the sensing ability of the nanomechanical two-level system, we increase the cavity pump power by $\Delta P_{\mu w} = 0.5\,\mathrm{dBm}$. Figure 5.15 (b) shows significant shifts in the statistical frequency distribution in both cases. We obtain a new frequency estimate using BH window $\bar{\Omega}_{0,BH}^{22.5\,\mathrm{dBm}}/(2\pi) = 46.23(19)\,\mathrm{kHz}$. Again, we can find the relative offset due to the estimate using rectangular window

$$\xi_{(rel)}^{22.5\,\mathrm{dBm}}/(2\pi) = \left(\bar{\Omega}_{0,RW}^{22.5\,\mathrm{dBm}} - \bar{\Omega}_{0,BH}^{22.5\,\mathrm{dBm}}\right)/(2\pi) = 4.75(30)\,\mathrm{kHz}. \tag{5.20}$$

Note that besides the absolute shifts after the modification of the electric field strength, there is a small deviation in the relative offsets before and after the sensing procedure that is $\xi_{(rel)}^{22.5\,\mathrm{dBm}} - \xi_{(rel)}^{22\,\mathrm{dBm}} \neq 0$. Based on our prior knowledge about the high precision in frequency estimate (both theoretical and experimental) of the BH window technique, we claim that the deviation in the relative offset results from the rectangular window.

The frequency shift using BH window is

$$\Delta\bar{\Omega}_{0,BH}/(2\pi) = \left(\bar{\Omega}_{0,BH}^{22.5\,\mathrm{dBm}} - \bar{\Omega}_{0,BH}^{22\,\mathrm{dBm}}\right)/(2\pi) = 3.44(43)\,\mathrm{kHz}. \tag{5.21}$$

It is noteworthy to mention that the statistical distributions [see Figs. 5.15 (a) and (b)] in frequency estimate using BH window (orange bars) are wider spread compared to the ones with rectangular window (blue bars). This is due reduction in the amplitude and the broadening of the main lobe in the frequency domain when applying the BH window to the measured signal as discussed in Sec. 5.4. Nevertheless, the strong suppression of spectral leakage of the BH window still allows one to improve the frequency estimation in the DFT, whereas the results using rectangular window are intrinsically subject to error [see for instance Fig. 5.12 (a) and (b) for comparison].

Thus, despite the downside of the BH window technique, where the measurement time window needs to fulfill the condition $(\Omega_0/2\pi)t_w \geq 4$ and the reduction in the spectral amplitude, the result confirms the robustness and high precision of the frequency estimate using Blackman-Harris windowing function compared to the conventional no-windowing method.

5.6 Conclusion

In conclusion, we demonstrate the experimental realization of the iterative adaptive spectroscopy based on the enhanced Ramsey interferometry that allows frequency estimate with high precision. Experimental constraints such as bandwidth limitation of the AWG that hinders high fidelity sensing and readout state preparation can be overcome using Magnus-based strategy for frequency sweep control. When continuously updating the control pulses we can mitigate systematic errors in the Fourier transform to extract the frequency components. Additionally, the application of the Blackman-Harris window filter function to the time domain Ramsey signal further suppresses spectral leakage and scalloping effects for short finite signal and enables precise estimates of the unknown level splitting Ω_0. As a proof of principle, we perform the sensing experiment by modifying the electrical field around the strongly coupled nanomechanical two-level system and at the same time, survey the shift of the level splitting in the Fourier frequency domain. We stress that our experimental method is not limited to classical but can also be applied to any quantum two-level systems and is particularly well-suited for systems with short coherence time. We believe our experimental results provide an additional contribution in the field of quantum sensing and quantum computation, where fast and high fidelity parameter estimation is required.

6 Summary and Outlook

In this chapter, we sum up the key results of this thesis in Sec. 6.1 and give an outlook towards future experiments in Sec. 6.2. In Sec. 6.2.2, we discuss the possibilities to improve the coupling between the microwave cavity and the nanomechanical string resonator to enhance the detection efficiency and the optomechanical interactions. In section 6.2.3, we show the perspective of moving our nanomechanical two-level system from the classical into the quantum regime and we provide a brief outlook in the development of a novel quantum coherent sensor using Ramsey interferometry with non-classical squeezed states.

6.1 Summary

One of the main scopes of this thesis is the development of a cavity-assisted displacement sensing scheme of the nanomechanical resonator at room temperature. The mechanical element used in this work is a freely suspended doubly-clamped, pre-stressed silicon nitride string resonator with a length of $L = 55\,\mu\text{m}$, the width is $w = 250\,\text{nm}$ and the thickness is about $t = 100\,\text{nm}$ that is placed between a pair of gold electrodes used for dielectrical actuation and detuning as well as detection. The eigenfrequencies of the nanomechanical resonator are typically in the radio frequency domain.

The vibrational motion detection of the nanomechanical string resonator is accomplished by coupling the two adjacent gold electrodes to the electric or magnetic field of the microwave cavity via microwave antenna. The mechanical motion of the dielectrical SiN string resonator periodically modulate the capacitance between the two gold electrodes, and hence, generating sidebands in the microwave cavity response.We introduce in this work three-dimensional, non-superconducting microwave cavities to replace the previously employed copper microstrip cavity. We provide studies on different geometries, e.g. rectangular, cylindrical and coaxial $\lambda/4$ resonators, and the various coupling mechanisms to these types of 3D cavity. In particular, the novel coaxial $\lambda/4$ cavity is a promising candidate that is ideally suited for conducting further experiments towards the quantum regime. First, this type of cavity offers exceptionally high quality factors up to $Q \approx 10^8$ at cryogenic temperatures. Even room temperature, the quality factor of such cavity can still outperform the one of the microstrip cavity by more than an order of magnitude. Second, we can design the cavity such that the fundamental TEM mode is well below the waveguide cutoff frequency. As a result, the fundamental mode's energy density decreases exponentially into the waveguide section and hence, no light can leak outside the cavity. And third, the resonance frequencies of the higher TEM harmonics are sufficient far away from that of the fundamental mode. Thus, the coaxial $\lambda/4$ provides a remarkably clean frequency spectrum that allows us to avoid multi-mode coupling issues.

In Ch. 3, we demonstrate the operation of a cavity electromechanical system that consists of a nanomechanical string resonator embedded inside a cylindrical 3D microwave cavity. Here, the non-metallized silicon nitride nanostring resonator can be dielectrically coupled to the cavity's resonant modes. Even at room temperature, the high quality factor of the cylindrical 3D cavity allows us to conduct experiments in the sideband resolved regime ($\kappa < \Omega_\text{m}$). To this end, we are able to observe electromechanical coupling effects in single- and two-microwave tone experiments. While the

mechanical eigenfrequency shift is dominated by the dielectric frequency tuning, the optomechanically induced transparency (in reflection geometry) establishes a clear proof of dynamical backaction.

In the second part of this thesis, we focus on the study of the coherent dynamics of the two strongly coupled flexural modes of the nanomechanical string resonator. In Ch. 4, we show the theoretical development of the coherent sensing protocol that allows frequency estimate of short signals with high precision. First, we introduce the ubiquitous Ramsey interferometry scheme to sense the unknown coupling strength $\Omega_0/2$ of a two-level system. The coupling strength is the quantity of the coherent sensor that we want to estimate. The change of Ω_0 is a direct consequence of a sensor that couples to the physical quantities in the environment. Second, we introduce a strategy to enhance the Ramsey interferometry by modifying the control pulses that come with experimental constraints such as bandwidth limitations and noisy environments. The corrections enable the preparations of sensing and readout states with high fidelity. We find the frequency control scheme yielding high fidelity state preparations in the recently proposed Magnus-based strategy. Note that this strategy provides corrections in the control terms to cancel, on average, unwanted spurious effects in the system's dynamics during the time of evolution.

In order to improve the frequency estimation of the oscillatory output from the Ramsey interferometry, we need to solve two main issues associated to discrete Fourier transform (DFT). The first systematic error to deal with is the so-called scalloping loss. This type of loss mechanism occurs from a signal which is constructed from a finite number of sampling points n_{samp}. As a consequence, the Fourier transform can not resolve the real maxima of the spectrum due to the lack in frequency resolution. This is, however, relatively simple to fix by using zero-padding technique to extend the signal with n_{pad} zeros on both sides to increase the frequency resolution.

The second source of systematic error in the DFT is spectral leakage, which makes a simple spectrum with a single frequency appear to have multiple frequency components. Additionally, this effect can lead to a shift of the maxima in the frequency domain. The spectral leakage occurs when the oscillatory signal in the time domain does not match the multiple integer of the period.

To overcome this limitations, we combine the Blackman-Harris (BH) windowing technique with the iterative, adaptive sensing (IAS) protocol. To carry out the protocol, we repeatedly perform Ramsey interferometry with a frequency-sweep that takes prior knowledge of the frequency estimate into account. With the repetition and the BH windowing technique, we can iteratively suppress systematic frequency shift errors originating from spectral leakage. The IAS protocol is done by updating the measurement time $t_{\mathrm{w}}^{(m+1)}$ obtained from the frequency estimate $\Omega_0^{(m)}$ at step m after each iteration. Additionally, we update the leading and trailing edges of the modified detuning-sweep, since the Magnus-based strategy for control requires one to know the parameters entering the equations of motion. Thus, we decrease the error in preparing both the sensing and readout state after each iteration. Our theoretical result shows that we can reduce the relative error in frequency estimate by two orders of magnitudes compared to the initial estimate just after a few iterations.

Our iterative, adaptive sensing protocol is particularly suitable for frequency estimates of two-level systems with short coherence time. The theoretical model of the two-level system used in our work is valid for both coherent classical and quantum systems. We stress that independently of how the sensing and readout states are prepared, our IAS protocol can always be applied to enhance frequency estimates.

In Ch. 5, we demonstrate the experimental implementation of our theoretically developed IAS protocol. The main focus of the experiment is to develop a testbed which is applicable for quantum sensing that is fast and, at the same time, allows frequency estimate with high precision. Here, we employ the coherent nature of the two strongly coupled fundamental flexural in-plane and out-of-plane modes of

the nanomechanical string resonator that serves as the classical two-level system. Similar to Ch. 3, we employ the cavity-assisted displacement sensing scheme to detect the motion of the mechanical resonator. In this experiment, the cylindrical microwave cavity is replaced by a coaxial $\lambda/4$ microwave cavity, which exhibits an exceptionally clean frequency spectrum to avoid multimode coupling

By applying a DC voltage to the electrodes, we can induce an electric polarization in the silicon nitride string resonator which, in turn, couples to the inhomogeneous electric fields. The resulting force gradients, thus, alter the restoring force of the in-plane and out-of-plane flexural modes of the mechanical oscillator leading to quadratic resonance frequency tuning of the respective modes. Note that the rectangular cross-section of the mechanical resonator leads to a small offset in the eigenfrequencies of the two fundamental flexural modes. Since the electric field gradients along these flexural modes have opposing signs, we can compensate the frequency offset simply by changing the applied DC voltage to bring the two modes into resonance. The cross-derivative of the applied inhomogeneous electric fields induces a linear coupling of the two modes causing them to hybridize into normal modes in near resonance conditions. The resulting avoided crossing with level splitting Ω_0 is the characteristic fingerprint of the strong coupling, where the two modes can coherently exchange excitation energies.

To perform Ramsey interferometry on this classical two-level system, we need to initialize the system at voltage U_i in the lower branch that is far away from the avoided crossing region to fulfill the condition $\Delta_0 \gg \Omega_0$. On top of the static DC voltage, we need to add a dynamical control pulse provided by an arbitrary wave function generator to detune the system to the desired operation point at the avoided crossing and back. In order to create a reliable voltage control scheme to manipulate the frequency tuning speed, we build a custom made voltage combiner which puts the DC power supply in series with the function generator's output. This technique offers several advantages, i.e. the full bandwidth capabilities of the AWG and the flexibility in setting the DC level that is delivered by the voltage source. The only requirement for this configuration is that one of the device in the series need to be internally isolated from the earth ground. In our case, the DC voltage source *Keithley 2410* is floated up to ±240 V.

The experimental implementation of the proposed sensing protocol requires reliable and precise control over all types of apparatus simultaneously. Particularly, it is essential to establish good communication between the AWG used to prepare sensing and readout state and the spectrum analyser that records the exponential decay in energy of the mechanical resonator. The synchronization of the devices can be realized using the *trigger mode*. For this purpose, we create an all-in-one Matlab-based script to generate command sequences and to have full control over all of the devices. With the control script, we can directly stream the numerically generated pulse scheme into the AWG without usage of additional software. Furthermore, we can define several feedback loops for voltage regulation in the script to compensate drift effects in the mechanical eigenfrequencies due to fluctuations in the environmental parameters such as electric field and temperature. The voltage regulations ensure the reliability and reproducibility of the experimental outputs.

In the first time-resolved experiment, we show the capability to control the dynamics of the classical two-level system in both adiabatic and diabatic regimes that are well described by the Landau-Zener transitions. Subsequently, we demonstrate the return probability of the initial state as a function of waiting time t_w in the Ramsey sequence. As expected, we observe the oscillatory behaviour that is well-known as the Ramsey fringe with a frequency given by frequency splitting Ω_0. In stark contrast, the Magnus-based corrected Ramsey pulse scheme shows an oscillatory output with much higher peak to peak amplitudes compared to the uncorrected scheme with a single frequency component in the control pulse. The improvement in the Magnus-based corrections directly translates in the Fourier

transform in frequency domain, where a global maximum is clearly visible, whereas in the uncorrected case no distinct global maximum is observable.

To determine the level splitting Ω_0 with high fidelity, we implement the proposed iterative, adaptive sensing protocol to our experimental routine. The initial estimate level splitting $\bar{\Omega}_0^{(0)}$ can be obtained from the spectroscopy measurement. Subsequently, we update the measurement time window $t_{\mathrm{w}}^{(m)} = n_{\mathrm{p}}\left(2\pi/\bar{\Omega}_0^{(m-1)}\right)$, where $n_{\mathrm{p}} = 4$ is the number of cycles, and the corrected control pulses with the corresponding Fourier coefficients $c_1^{(m)}$, $d_1^{(m)}$ after each iteration step m. In addition, we apply zero-padding technique and the Blackman-Harris window function to the Ramsey signal to reduce the effect of spectral leakage and scalloping losses. The results with the Blackman-Harris window show a well distinguishable estimate of frequency splitting compared to the no window case with an accuracy better than the standard errors of the individual estimates. In accordance to theory prediction, we observe a saturation in frequency estimate after 3 iterations. By increasing the number of cycles n_{p} in the Ramsey interferometry, we can confirm the validity of precise frequency estimate for short time signals with our developed iterative adaptive method and the Blackman-Harris windowing technique.

At last, as a proof of principle, we demonstrate the ability of the classical two-level system to work as a coherent sensor. Since the strong coupling of the two flexural modes is governed by the strength of the inhomogeneous electric field, we expect the level splitting Ω_0 to change when modifying the electric field environment around the mechanical resonator. In this case, we modify the root-mean-square electric field that builds up inside the microwave cavity simply by increasing the microwave cavity's pump power. Indeed, we observe a distinct shift in the statistical frequency distribution that confirms the change in the frequency splitting of the two-level system due to the change in the electrical environment.

Our theoretical and experimental methods are not limited to classical but can also be applied to any quantum two-level system. Our results are very promising and we believe that we can perform further experiments operating deep in the quantum regime to contribute to the field of quantum sensing and quantum computation, where fast and reliable parameter estimation is required. In the upcoming sections, we discuss the possibilities to further optimize the experimental setups in order to operate in the quantum regime.

6.2 Outlook

6.2.1 Nanomechanical Resonator as Oscillator in the Quantum Regime

Recent development on mechanical oscillators in the quantum regime opens a plethora of possibilities in application of these devices in quantum technologies. The preparation of mechanical state close to its ground state of motion has been the motivation of several groups spreading around the world for the last decade. As we speak, there are several successful platforms which have been able to demonstrate ground state cooling of the mechanical state and demonstrate quantum state preparation of a mechanical resonator. The systems include micromechanical resonator [42], drum resonator [93], optomechanical crystal [220], nanospheres in an optical cavity [39] and ultra coherent resonator [221] to name a few.

In most of the above-mentioned devices the ground state is reached by overcoming the thermal fluctuations due to the finite temperature in the experimental environment using various techniques. These include passive (cryogenic) cooling high frequency GHz modes by placing them in a cryogenic bath with a fixed temperature [222, 223] or using techniques that utilize dynamical backaction cooling by cavity electro/optomechanical coupling [90, 93, 224, 225]. The product of the eigenfrequency and the quality factor (Q-factor) known as the Q-f product puts an upper limit to achievable thermal occupancy in the quantum regime. It can be found in systems range from membranes having resonance frequency in the sub-MHz regime to one dimensional doubly clamped beams in the sub-GHz to GHz frequency regime. At very low thermal occupation numbers (i.e. $n_{\mathrm{th}} < 1$), resolving the displacement of such oscillators becomes challenging. This requires efficient modulation of the coupled optical or microwave cavity frequency as a function of the fluctuation of the mechanical oscillator. This fundamental transduction parameter is often referred as vacuum (or single photon) optomechanical coupling rate, g_0. Another, less fundamental parameter is known simply as optomechanical coupling, defined as $g = \sqrt{n_{\mathrm{cav}}} g_0$, ($n_{\mathrm{cav}}$ is the average photon number in the cavity) is also of significant importance when discussing optomechanical systems. Particularly, it is important to carefully optimize the parameter g to realize a mechanical system at a considerably low phonon occupation and also to be have sufficient sensitivity to be able to resolve small displacements at such low phonon limits. In the following section, we discuss the 3D cavity-nanomechanical resonator coupling scheme to improve the optomechanical coupling rate g_0 in our experiment.

6.2.2 Improved Cavity-Nanomechanical Coupling

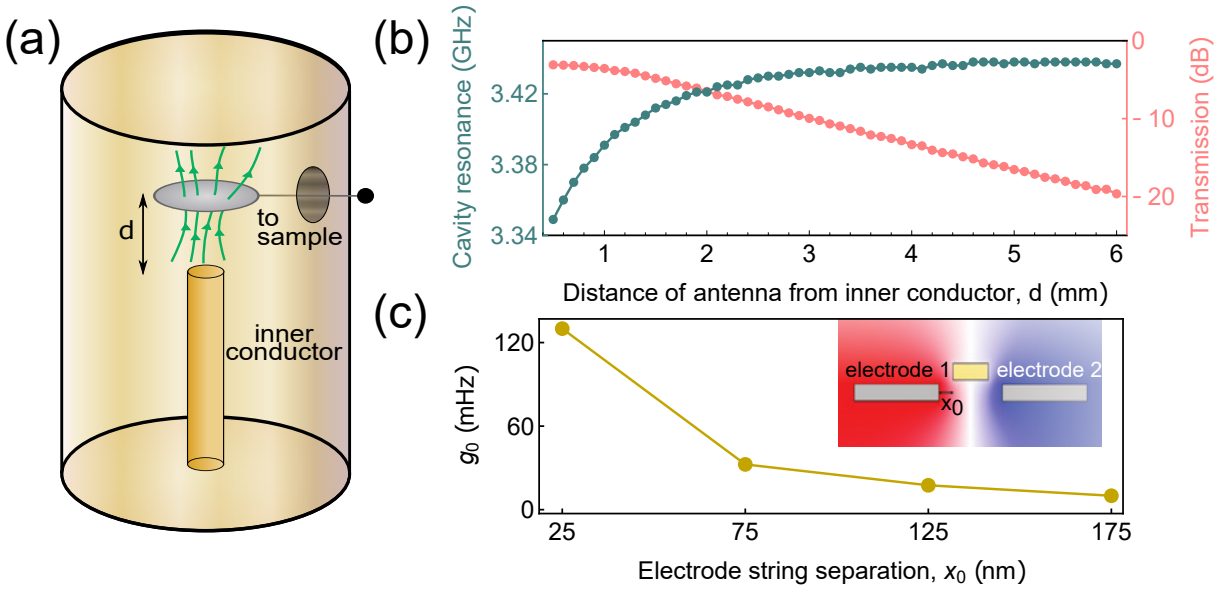

Figure 6.1 | Cavity Coupling with a Plate Antenna.
(a), Schematic of the antenna coupling of the cavity field to the sample. The antenna is capacitively coupled to the electric fields (green lines) and the antenna is shorted directly to one of the electrode that flanks the nanomechanical string resonator. **(b)**, Change of the cavity resonance frequency (green) and input-output transmission (red) as a function of the separation between the antenna the inner conductor. **(c)**, Numerical simulation of achievable optomechanical coupling, g_0 between cavity and the mechanical element as a function of electrodes-string separation, x_0. The plot show that it is possible to exponentially approach a very high optomechanical coupling without being constrained by fabrication limits. Inset shows the string-electrodes system and the field distribution.

The long term vision is to develop a novel quantum sensor on a nanomechanical two-level platform that is not limited by the standard quantum limit (SQL). The first step towards this challenging task is to reduce the thermal occupation of the system down to $n_{\mathrm{th}} < 1$ in order to operate in the quantum regime. This is experimentally achievable with a combination of passive and active cooling. For example, for a silicon nitride string resonator with a length of 5 µm and eigenfrequency of about 75 MHz, the thermal occupation at room temperature is $n_{\mathrm{th}} \approx 85.000$. However, we can reduce the average thermal phonon occupation n_{th} of the resonator to around 2 at a base temperature of 10 mK. With modern day dilution refrigerators, temperatures in this regime are easily accessible. At this level of thermal occupation, the energy levels are yet not sufficiently separated resulting in possible leakages in sensing experiments. Therefore, an additional optomechanical cooling is still required to further reduce the thermal occupation to $n_{\mathrm{th}} \leq 1$. As shown in Sec. 3.3.2, we can observe the dynamical backaction of the cylindrical 3D microwave cavity and the nanomechanical resonator in the optomechanically induced reflection measurement that reveals a weak single photon coupling rate of $g_0/(2\pi) = 200$ µHz at room temperature and high cavity drive power. In order to obtain optomechanical sideband cooling we need to further optimize the optomechanical coupling parameters to enhance interaction of the microwave cavity and the nanomechanical string resonator. To better compensate the mismatch between the model volumes of the cavity and the mechanical oscillator, we implement a novel design scheme to increase the coupling mechanism. In Fig. 6.1 (a), we show a plate capacitor that is capacitively coupled to a resonant mode of the coaxial $\lambda/4$ 3D microwave cavity. This in turn is capacitively coupled to the string resonator. A COMSOL simulation of the cavity coupling as a function of the antenna position is shown in Fig. 6.1 (b). We believe this result is extremely encouraging as it demonstrates very high

coupling between the microwave mode to the antenna. The next coupling element is the coupling between the electrodes (one is shorted to the antenna) and the string resonator. The electrodes-string resonator system creates an additional capacitor element in the LC circuit of the microwave resonator. The motion of the mechanical element periodically modulates the capacitance in the LC circuit and hence, creates sidebands in the cavity response (see discussion in section 3.1.1). The efficiency of this transduction is mostly dominated by the modulation of the capacitance between the electrodes as a function of the string position. As seen in Fig. 6.1 (c), this effect can be exponentially increased by bringing the electrodes as close to the string resonator as possible. With the modern clean room facility in TUM, we anticipate that the separation x_0 can be decreased to a value as small as 20 nm. However, as seen in Fig. 6.1 (c), even with nominal value of $x_0 = 25$ nm, it is possible to boost the single photon coupling g_0 by three order of magnitude compared to the previous result. We expect a $g_0/(2\pi) \sim 100 \times 10^{-3}$ Hz for a string resonator with the nominally defined parameters.

As mentioned above, it is important to, firstly, reduce the thermal occupation of the nanomechanical system to $n_{\mathrm{th}} < 1$ to enable experiments in the quantum regime. This could be done by a combination of passive cooling from the dilution refrigerator and optomechanical active cooling. At such low modal temperatures, the system becomes even more sensitive to external noises. Therefore, equipartition theorem cannot serve as a faithful indicator of quantum performance. An alternate quantum indicator is the so-called ratio between Stokes and anti-Stokes scattering field which frees itself from any calibration issues [226]. One can retrieve this quantum indicator directly from heterodyne measurements [227–229]. At such a level of thermal occupation, the displacement noise of the resonator is on the order of 10^{-15} m. Resolving displacement amplitudes of such orders also requires a high optomechanical coupling, g. Therefore, a careful analysis of the optomechanical coupling required to achieve desired goals is of fundamental importance to justify the proposed optomechanical system.

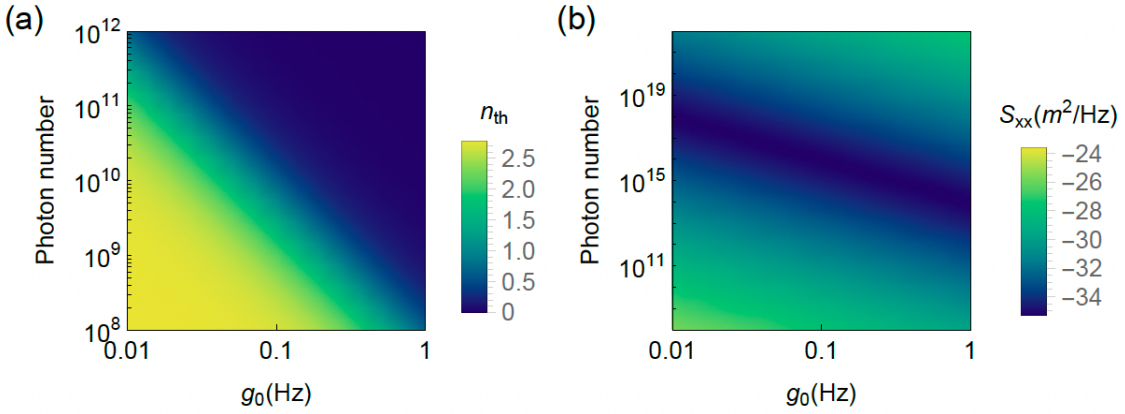

Figure 6.2 | Thermal Occupation and Thermal Noise.
(a), Color plot of thermal occupation of the nanomechanical resonator, n_{th} as a function of cavity photon occupation, n_{cav} and vacuum optomechanical coupling g_0. **(b)**, Total noise floor S_{xx} (in m/Hz^2) as a function of cavity photon occupation, n_{cav} and vacuum optomechanical coupling g_0.

In the following, we show the analysis of the proposed optomechanical system with nominal parameters following the dynamical backaction proposed by Aspelmeyer et al. [90]. With a careful estimate of system parameters, one can calculate the two most important parameters for the proposed optomechanical system, namely the thermal occupation n_{th} and the total noise S_{xx} in m/Hz^2 [see Eq. (72) in Ref. [90]]. The total noise S_{xx} is a combination of backaction noise, imprecision noise and thermal noise in the system. The evolution of n_{th} and S_{xx} as a function of g_0 and cavity photon number n_{cav} is shown in Fig. 6.2 (a) and (b), respectively. The results are indeed motivating, as with a

considerably moderate $g_0/(2\pi)$ $\left(\sim 100 \times 10^{-3}\text{Hz}\right)$ and n_{cav} $\left(\sim 10^{11}\right)$ it is possible to achieve a thermal occupation with $n_{\text{th}} \sim 1$ and a noise floor $S_{\text{xx}} \approx 10^{-32}\text{m}/\text{Hz}^2$. Here, n_{th} is low enough to have a system with significantly high "quantumness" and the noise floor is low enough to resolve displacements at such low phonon levels (which is expected to be around 10^{-15}m for zero point fluctuations). With cautious design parameters it is expected to achieve $g_0/(2\pi) \sim 10\times10^{-3}$ Hz as predicted by COMSOL simulations discussed previously. On the other hand, as seen on Fig. 6.1 (a) it is possible to achieve optimum coupling between the cavity field and the antenna by varying the position of the capacitive plate antenna with respect to the inner conductor.

6.2.3 Sensing Beyond Standard Quantum Limit

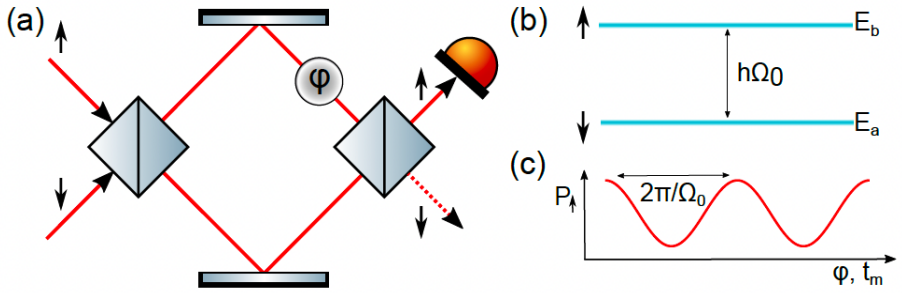

Figure 6.3 | Mach-Zehnder Interferometer and Ramsey Interferometry.
(a), Schematic of a Mach-Zehnder interferometer. One of the light path travels with an additional variable phase delay ϕ. This creates an interferometric pattern, varying as a function of the phase ϕ. **(b)**, Same effect can be observed for Ramsey interferometry with a two-level system. The interference effect in this case varies the probability of one of the state as the function of the measurement time t_{m}. The period of the oscillation gives direct estimate of the level splitting Ω_0. **(c)** Similar interference effects is observed for both Mach-Zehnder and Ramsey interferometer.

An interferometer is used to monitor differential phase changes between light beams going through two different optical paths. The sensitivity to monitor this small phase change ϕ, is limited from the Poissonian statistics of mutually independent photons. The Poissonian distribution is in fact an approximation of a Gaussian distribution for discrete sampling which scales with a standard deviation of $\sqrt{N}$, where N is the size of the statistical distribution. Since this statistics is a random process following a classical description, for photons such a statistical behavior is often referred as a semi-classical behavior. In short, this semiclassical description of photon counting puts an upper limit to the achievable sensitivity known as the shot noise limit. The very same effect happens while working with a Ramsey interferometer with a projective measurement. This in the community often referred as the Quantum Projection Noise (QPN) which also scales in same way due to similar statistical behavior. This limit could be surpassed by creating states that do not follow such Poissonian distribution. For quantum systems, one example of such states is the Squeezed state [230].

Squeezed states of lights have been extensively used in pioneering experiments and recently in the LIGO gravitational-wave interferometer [174, 177]. The use of squeezed resources becomes even more effective when radiation pressure shot noise plays a role in the observed quantum limits [231]. Squeezed states are generated by reducing standard deviation of one of the quadrature of the probe field at the expense of the other. For a coherent state (which follows Poissonian statistics) the smallest measurable phase difference in an interferometric measurement is given by $\Delta\phi = 1/\sqrt{N}$. While for a squeezed state, the smallest measurable phase difference scales as, $\Delta\phi = \mathrm{e}^{-r}/\sqrt{N}$, where r is called the squeezing parameter. It has been even shown that, with such non-classical states it is possible to achieve sensitivity which scales as $1/N$ and therefore yielding what is called the Heisenberg limit or Heisenberg scaling. Such states result in unprecedented sensitivity in metrology as shown in the work of Hosten et al. [232].

The phononic states follow the same bosonic operators as the photonic states used for laser interferometer. Moreover, the flow of Ramsey interferometry resemble closely to an optical interferometer like Mach-Zehnder interferometer as shown in Fig. 6.3 (a). The two input beams of an optical interferometer resemble two initial sensing states of any quantum sensor [Fig. 6.3 (b)]. The two input beams are combined through a 50/50 beam splitter, which is formally equivalent to generation of a superposition state for a two-level system. For a two-level system this is analogues to two distinct energy levels E_a

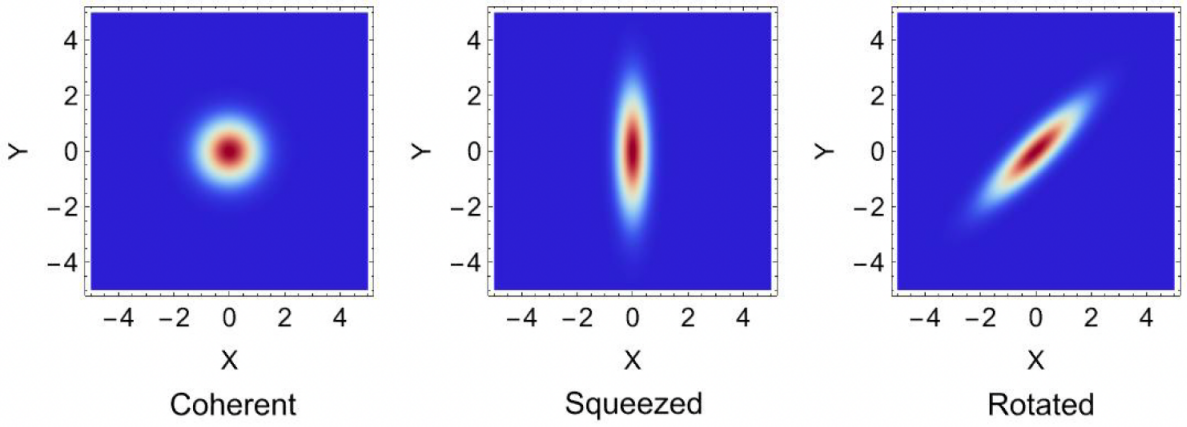

Figure 6.4 | Squeezed State Ramsey Interferometry.
State representation with respect to the Wigner probability distribution> First a coherent super position state is generated at the avoided crossing. It is followed by creation of squeezed state for example by parametrically modulating the resonator. Finally, a free evolution of the state vector will imprint a phase signature (ϕ) proportional to the energy difference of the two distinct energy levels.

and E_b separated by $\hbar\Omega_0$. Then one of the beam has a variable phase shifter, ϕ on its path which affects the interference pattern when they are finally recombined at the second beam splitter. This is equivalent to a Ramsey interferometer, where the higher energy state gathers phase proportional to the energy difference, $\hbar\Omega_0$ between two discrete energy levels. This interference effect generates a beating pattern at the frequency of the splitting Ω_0 when projection of one of the state vector is probed. In a classical or semi-classical picture the estimate of Ω_0 (as ϕ) will scale as $1/\sqrt{N}$ with a Poissonian distribution. However, with a squeezed state it is indeed possible to achieve a more accurate estimate of the frequency Ω_0. For many qubit systems with fermionics degrees of freedom (spin squeezing) squeezing has been successfully witnessed to enhance sensitivity of the measurement [232].
The usual protocol (see Fig. 6.4) for squeezed state Ramsey interferometry first follows system initialization by creation of a coherent state for the spin ensemble. This is followed by a $\pi/2$ pulse to create a superposition state, with indistinguishable quadratures (grey circle in Fig. 6.4). A squeezed state is then generated by employing a squeezed operator (ξ) on the superposition state. The state vector can then freely rotate around the z-axis on a Bloch sphere where it gathers phase ϕ proportional to the energy difference between the ground and excited state. Finally a projective measurement scheme is used to map back the sensing state. Taking inspiration from the spin states, we propose a Ramsey interferometry with squeezed states based on parametric modulation of the optical spring constant. This is achieved by firstly creating a displaced state by coherently modulating the mechanical degree of freedom. Following the suggestion by Roque et al. [186], a squeezed state is then created by generating an eigenstate of either $a^2 + \left(a^\dagger\right)^2$ or $-\mathrm{i}\left(a^2 - \left(a^\dagger\right)^2\right)$. Where $a^\dagger$ and a correspond to the creation and annihilation operator respectively. It can be achieved by parametrically modulating the nanomechanical resonator proportional to $\left(a + a^\dagger\right)^2$. This is followed by mapping the state back to a measurable state. However, as suggested in the work of Roque et al. [186], a strong parametric drive (high squeezing parameter) generates unwanted oscillations at high frequencies. These oscillations possibly can destroy the coherence of state evolution.

The challenge here is to find an eigenstate of $a^2 + \left(a^\dagger\right)^2$ or $-\mathrm{i}\left(a^2 - \left(a^\dagger\right)^2\right)$ with very high fidelity. One then has to devise a protocol that is able to generate the desired state with high precision. A detailed experimental investigation on the techniques to generate the squeezed states of one of the superposition

states will then have to carry out very carefully. The next step will deal with the implementation of the squeezed Ramsey with a cautious inspection of the sensing precision.

In conclusion, we theoretically proposed an iterative adaptive sensing protocol based on enhance Ramsey interferometry to estimate unknown frequency from short, finite signal with high precision. Our experimental results on coherent sensing of the nanomechanical two-mode system show excellent agreement with the theoretical prediction. In perspective, the theoretical and experimental results of this work can be applied to advanced coherent sensing experiments operating in the quantum regime.

A Appendix

A.1 State preparation errors

In this section we discuss how noise and low fidelity state preparation affects the sensing protocol.

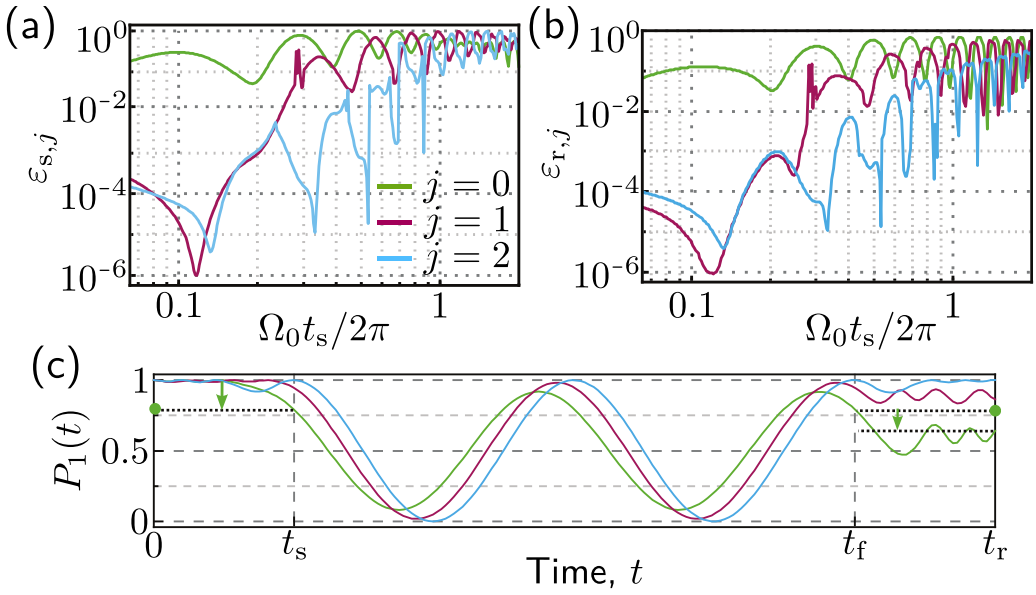

Figure A.1 | Noise Induced Errors.
(a) Comparison of the sensing state error fidelity for $\delta\Omega = 0$ between the uncorrected (green) Mod1 (red), and Mod2 (blue) frequency-sweeps as a function of t_s. **(b)** Same as (a) for the readout state. **(c)** Evolution of the probability $P_1(t)$ of measuring mode $\boldsymbol{a}_1$ as a function of time for $\Omega_0 t_s/2\pi = 0.5$. The green dots and arrows are a visual indicator to show how much the ideal coherent evolution is corrupted by coherent errors when using the uncorrected pulse in both sensing and readout state. **Reprinted from Ref. [167]**

A.1.1 Noise-induced errors

In Sec. 4.2.2, we showed the noise averaged sensing and readout state fidelity error [see Figs. 4.5 (a) and (b)]. Here, to give a sense on how noise hinders the preparation of both states, we present in Fig. A.1 (a) and (b) $\varepsilon_{s,j}$ and $\varepsilon_{r,j}$ [see Eq. (4.54)] obtained in the absence of noise ($\delta\Omega = 0$ in Eq. (4.2)).

Let us first consider the sensing state fidelity error for the uncorrected protocol [green trace in Fig. 4.5 (a) and Fig. A.1 (a)]. In this case, the presence of noise favors the state preparation by preventing the generation of the ideal coherent evolution and thus partially suppressing coherent transitions to mode $\boldsymbol{a}_2$. On the other hand, for the modified protocols [red and blue traces in Fig. 4.5 (a) and Fig. A.1(a)] that rely on coherent evolution to average out the effects of the spurious interaction [see Eqs. (4.45) and (4.50)] noise reduces the state preparation fidelity. However, as the results in Fig. 4.5 show, the fidelity errors obtained with the modified protocols in the presence of noise are still orders of magnitude smaller than the uncorrected one. This fact can be attributed to having protocols that are designed to be shorter than the decoherence time set by the noise.

For the readout state preparation, one would expect the same observations as above. This is, however, not the case. Comparison of Fig. 4.5(b) and Fig. A.1(b) reveals that noise hinders the readout state preparation to a much greater extent than it does for the sensing state preparation. This difference originates from the dependence of the state fidelity error on the initial state, which for preparing the sensing state is simply $\boldsymbol{a}_1$ and for preparing the readout state is $\boldsymbol{a}(t_\mathrm{f}) = \Phi_j(t_\mathrm{f})\boldsymbol{a}_1$. The latter is a coherent superposition state and is therefore more susceptible to noise-induced decoherence.

A.1.2 Coherent errors

To illustrate how low fidelity state preparation affects the sensing protocol, we plot in Fig. A.1(c) the probability $P_1(t_\mathrm{w}, t)$ of measuring mode $\boldsymbol{a}_1$ as a function of time for a fixed measurement-time window t_w. We note that the Ramsey signal $s(t_\mathrm{w})$ is constructed from the values of $P_1(t_\mathrm{w}, t_\mathrm{r})$ when t_w is varied, i.e., $s(t_\mathrm{w}) = P_1(t_\mathrm{w}, t_\mathrm{r})$. We have

$$P_{1,j}(t) = |a_1^T \Phi_j(t) a_1|^2, \tag{A.1}$$

where $j \in \{0, 1, 2\}$ labels, as in Fig. 4.4, which detuning sweep is used to obtain $\Phi_j(t)$. We recall that $j = 0$ labels the uncorrected detuning-sweep, while $j = 1, 2$ labels the detuning-sweep coined Mod1 and Mod2, respectively.

The uncorrected detuning-sweep [green trace in Fig. A.1(c)] shows how coherent errors propagate and lead to the "wrong" Ramsey signal. Using Mod1 (red trace) or Mod2 (blue trace) which allow for high fidelity state preparation of both the sensing and readout state, coherent errors are reduced and a more faithful Ramsey signal can be constructed.

A.2 Iterative procedure for an idealized Ramsey signal

In this section, we show that the iterative, adaptive sensing protocol we developed in Sec. 4.4 is less efficient when using rectangular windows only.

To show this, we use a toy model which assumes an ideal Ramsey signal, $s(t) = \cos^2[(\Omega_0/2)t]$ and consider three different IAS protocols. We consider the protocols IAS 1 and 2 discussed in Sec. 4.4 along with the protocol IAS 3, which consists in using only rectangular windows. For convenience, they are defined again below:

- **IAS 1** $f^{(m)} = \Theta(t) - \Theta(t - t_{\mathrm{w}}^{(1)})$ for $m = 1$ and $f^{(m)} = f_{BH}(t/t_{\mathrm{w}} - 1/2)$ for $m \geq 1$,
- **IAS 2** $f^{(m)} = f_{BH}(t/t_{\mathrm{w}}^{(m)} - 1/2)\ \forall m$,
- **IAS 3** $f^{(m)} = \Theta(t) - \Theta(t - t_{\mathrm{w}}^{(1)})\ \forall m$.

We assume the starting estimate to be $\bar{\Omega}^{(0)} = 1.1\Omega_0$ and, as in Sec. 4.2.3, after each iteration we update the measurement time-window t_{w} based on the new estimate.

In Fig. A.2 we show the relative error of the frequency estimate using the previously defined IAS protocols (see Sec. 4.4). Using IAS 3 results in a less accurate estimation due to using rectangular windows, which lead to spectral leakage. The results generated by IAS 1 and IAS 2 lead to the same relative error for $m > 1$, in agreement with the results shown in Fig. 4.12.

As explained in Sec. 4.4, we find IAS 1 to be the protocol of choice, since it allows one to make the first frequency estimate from a spectrum whose main frequency component has a larger Fourier amplitude.

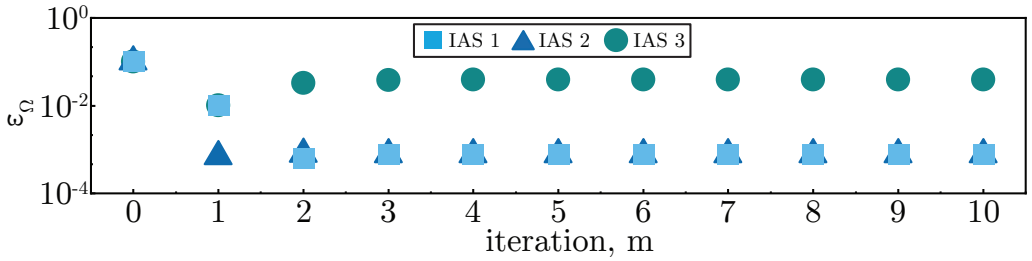

Figure A.2 | Iterative Procedure with Rectangular Window.
Relative error $\epsilon_\Omega^{(m)}$ as a function of iteration number, m for three different protocols. **Reprinted from Ref. [167]**

A.3 Fitting the Avoided Crossing

Follow the discussion in Sec. 2.2.3, where we described the dynamics of two linearly coupled harmonic oscillators with the masses m_A and m_B and the spring constants k_A and k_B. The solution for the eigenvalues in Eq. (2.19) can be expressed in a different way that is

$$\omega_{\pm}^2 = \frac{1}{2}\left(\omega_A^2 + \omega_B^2 \pm \sqrt{\left(\omega_A^2 + \omega_B^2\right)^2 + 4\Omega_0^2\omega_A\omega_B}\right)^2. \tag{A.2}$$

With the eigenfrequencies $\omega_j = \sqrt{\frac{k_j+\kappa}{m_j}}$ where $j \in \{A, B\}$ and $\Omega_0 = \frac{\sqrt{\kappa/m_A}\sqrt{\kappa/m_B}}{\sqrt{\omega_A\omega_B}}$ is the frequency splitting of the two coupled modes. Furthermore, we define $m_A = m_B = m_{\text{eff}} = \rho Lwt/2$ and $k_A = k_B = k_0$. When applied DC voltage to the electrodes the respective string constants are modified. The tuning behaviour, we use a second order series expansion of the parabolic frequency tuning to approximate

$$k_j = k_0 + \xi_j(U - U_{\text{f}}) + \lambda_j(U - U_{\text{f}})^2. \tag{A.3}$$

With U_{f} is the crossing voltage, ξ_j and λ_j are the frequency conversion factors.

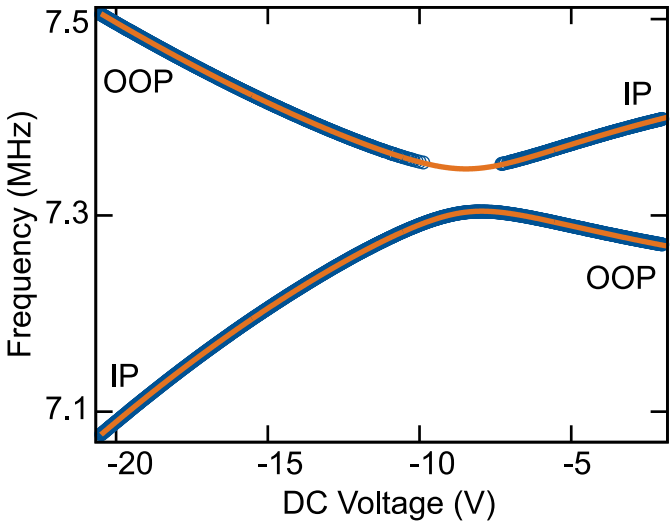

Figure A.3 | Mechanical Eigenfrequency versus DC Voltage.
Dielectrical tuning behaviour of the nanomechanical flexural IP and OOP modes extracted from Fig. 5.6 in the main text. Blue circles indicate the eigenfrequencies obtained from the Lorentzian fit and the orange lines are the corresponding fit using Eq. (A.2)

.

In Fig. A.3, we show the extracted data from the dielectric frequency tuning experiment described in Sec.5.1.2. Note, that in the region where the avoided crossing occurs, it is not possible to fit the data using Lorentzian function since the visibility is very low in the upper branche. Nevertheless, Eq. (A.2) provides a good fit to the experimental data. In table A.1, we indicate all the pre-defined and fit parameters.

A.3.1 Conversion Factor Calibration

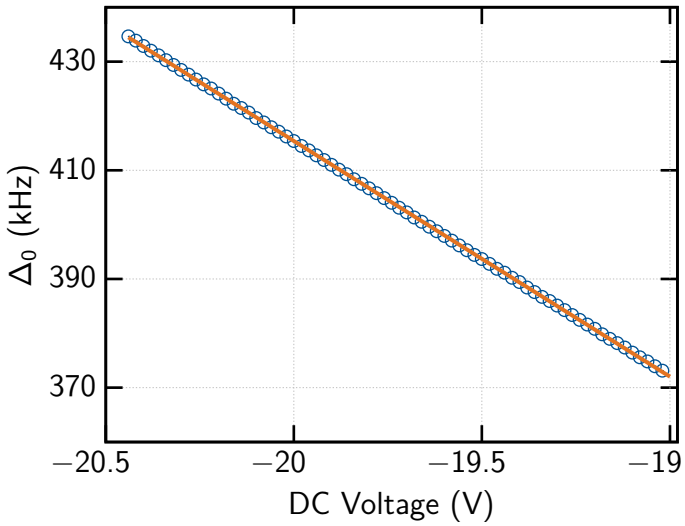

Figure A.4 | Calibration of the Conversion Factor.
Frequency difference of the two flexural modes (blue circles) extracted from Fig. A.3 and the corresponding linear fit (orange line) in the region where $\Delta_0/\Omega_0 \approx 10$.

.

In Fig. A.4, we illustrate the calibration of the voltage to frequency conversion factor c_{eff}. To keep it simple, we approximate the frequency tuning to be linear in time. We choose the frequency difference of the two flexural modes in the region that is far away from the avoided crossing, where the extracted slope from the linear fit gives a conversion factor of $c_{\text{eff}} = 43.363\,\text{kHz}$. Note that this procedure is only a rough approximation, since the resonance frequencies of the flexural modes are expected to be tuned with the applied DC voltage [see Eqs. (A.2) and (A.3)]. Despite the discrepancy in the quadratic frequency tuning by using linear approximation, the theoretical prediction and experimental results are in good agreement.

Table A.1 | Avoided Crossing Fitting Parameters.
Overview of the pre-defined and fit parameters to determine the avoided crossing.

Nanomechanical String Resonator		
Parameter	Symbol	Unit
SiN mass density	ρ	$2\,800\,\mathrm{kg/m^3}$
String's length	L	$49\,\mu\mathrm{m}$
String's width	w	$250\,\mathrm{nm}$
String's thickness	t	$100\,\mathrm{nm}$
String's effective mass	$m_{\mathrm{eff}} = \rho w t L/2$	$1.71 \cdot 10^{-15}\,\mathrm{kg}$
Fit Parameters		
Parameters	Symbol	Unit
Spring constant	$k_A = k_B = k_0$	$0.093\,\mathrm{N/m}$
1^{st} order frequency conversion factor	ξ_A	$-0.26 \cdot 10^{-3}\,\mathrm{N/(V\,m)}$
1^{st} order frequency conversion factor	ξ_B	$0.34 \cdot 10^{-3}\,\mathrm{N/(V\,m)}$
2^{nd} order frequency conversion factor	λ_A	$8.3 \cdot 10^{-6}\,\mathrm{N/(V^2\,m)}$
2^{nd} order frequency conversion factor	λ_B	$-11.5 \cdot 10^{-6}\,\mathrm{N/(V^2\,m)}$
Mutual coupling constant	κ	$0.52 \cdot 10^{-3}\,\mathrm{N/m}$
Crossing voltage	U_{f}	$-8.06\,\mathrm{V}$
Voltage offset	$\Delta U = U_{\mathrm{f}} - U_{\mathrm{i}}$	$12.8\,\mathrm{V}$
Initial detuning	$\Delta_0/2\pi$	$427\,\mathrm{kHz}$
Level splitting	$\Omega_0/2\pi$	$41.3\,\mathrm{kHz}$

A.4 Bandwidth Limitation

As explained in Sec. 4.2.2 and 5.3, we need to fulfill the condition $\Omega_0 t_s/(2\pi) \ll 10^{-2}$ in the "*uncorrected*" control scheme to achieve error fidelities in the order of 10^{-3} for sensing and readout state preparations. This condition translates to a sweep frequency of $\beta_{\mathrm{AWG}} \approx 5.777\,\mathrm{MHz}$ in the AWG output. The frequency range in megahertz, however, is not accessible in our experimental setup due to the bandwidth limitation defined by the custom made voltage combiner box and the single layer capacitor.

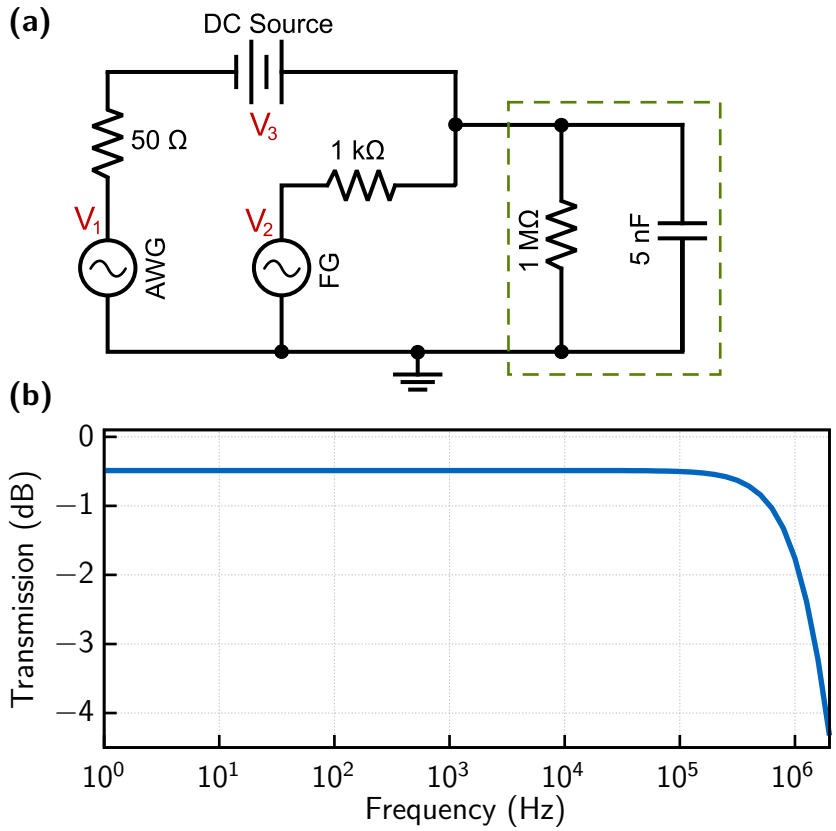

Figure A.5 | Limitation of the Voltage Combiner.

.

In Fig. A.5 (a), we show a circuit diagram demonstrating the dielectric control scheme of our experimental setup. The AWG (V_1) and the DC voltage Source (V_3) are connected in series, whose output is then combined with a function generator (V_2). Here, we assume that our sample (dashed green box) has a high impedance of 1 MΩ. The total capacitance is 5 nF, which results from the combination of a single-layer capacitor (SLC) and the electrodes. The Bode diagram in Fig. A.5 (b) illustrates the transmission of the AWG output voltage (V_1) as a function of frequency. Due to the strong ratio in the output impedance (50 Ω : 1 kΩ), the AWG output voltage only experiences a relatively small attenuation of $\approx -0.4\,\mathrm{dB}$ at low frequency. Above 100 kHz, however, the attenuation in V_1 becomes noticeable.

A.5 COMSOL Solid Mechanics/Electrostatics Simulations

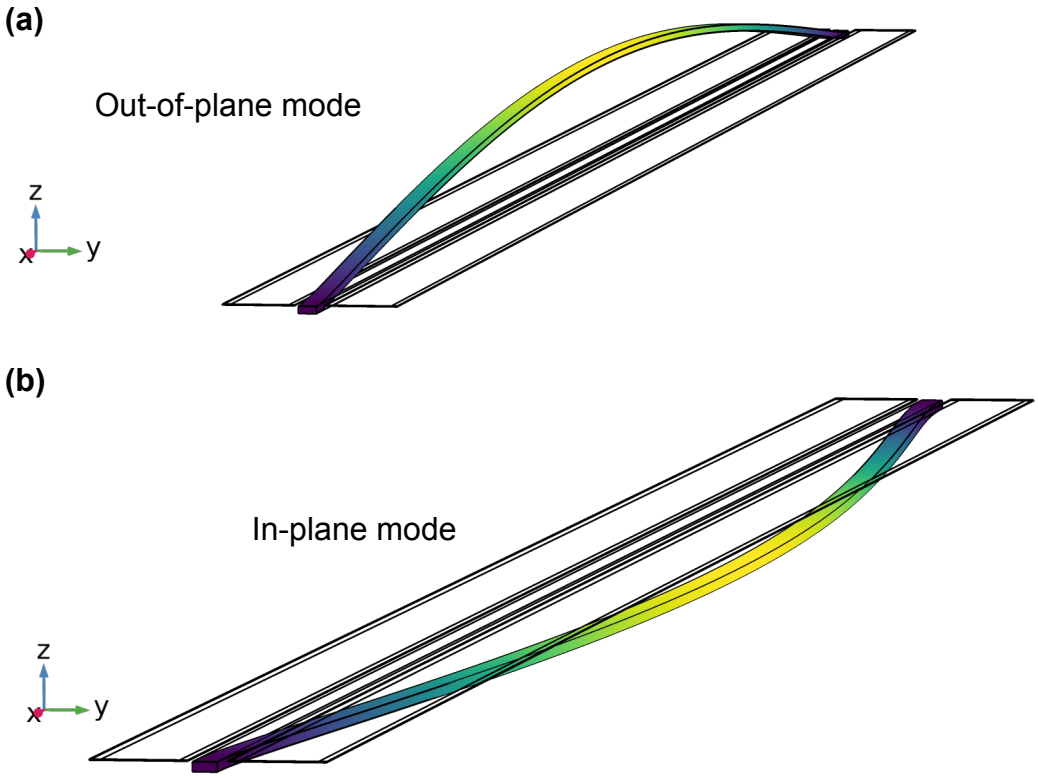

Figure A.6 | Flexural Modes of a Nanomechanical String Resonator.
COMSOL 3D simulations (using *Solid Mechanics/Electrostatic Modules*) illustrates the displacement profiles of the out-of-plane **(a)** and in-plane **(b)** flexural modes of the pre-stressed doubly clamped nanomechanical string resonator.

To verify the sensing capability of the nanomechanical two-level system, we model the dielectric tuning behaviour of the string resonator using FEM simulation. The geometry of the COMSOL model is shown in Fig. A.6. Here the dimension of the string resonator is $\{w \times t \times \ell\} = \{250\,\text{nm} \times 100\,\text{nm} \times 44\,\mu\text{m}\}$ and is embedded between two gold electrodes of dimension $\{w \times t \times \ell\} = \{1\,\mu\text{m} \times 10\,\text{nm} \times 44\,\mu\text{m}\}$. Note that the string is vertically offset from the electrodes to induce dielectric coupling via force gradient. In Fig. A.6 (a) and (b), we illustrate the displacement profiles of the out-of-plane and in-plane flexural modes. When no DC bias voltage is applied, the corresponding eigenfrequencies are found to be $\omega_{\text{OOP}}/(2\pi) = 7.256\,\text{MHz}$ and $\omega_{\text{OOP}}/(2\pi) = 7.514\,\text{MHz}$.

Both mechanical modes can be tuned in opposite directions by increasing the DC bias voltage (see Fig. A.7 (a)), where we can observe a clear avoided crossing of the two modes. To simulate the static contribution of the electric field that surrounds the string resonator, we modify the charge density in the dielectric material of the beam and repeat the DC bias voltage sweep. As apparent in Fig. A.7 (b), there is a deviation in the tuning behaviour of the two flexural modes. The frequency difference of the two modes $\Delta\omega$ as a function of applied DC voltage for three different charge densities is illustrated in Fig. A.7 (c), indicating a distinct shift in the level splitting Ω_0 depending on the strength of the electric field. In Fig. A.7 (d), we plot the level splitting Ω_0 as a function of charge densities. This COMSOL simulation confirms the change in the coupling strength of the two flexural modes as a direct consequence of the change in the electric field in the surrounding.

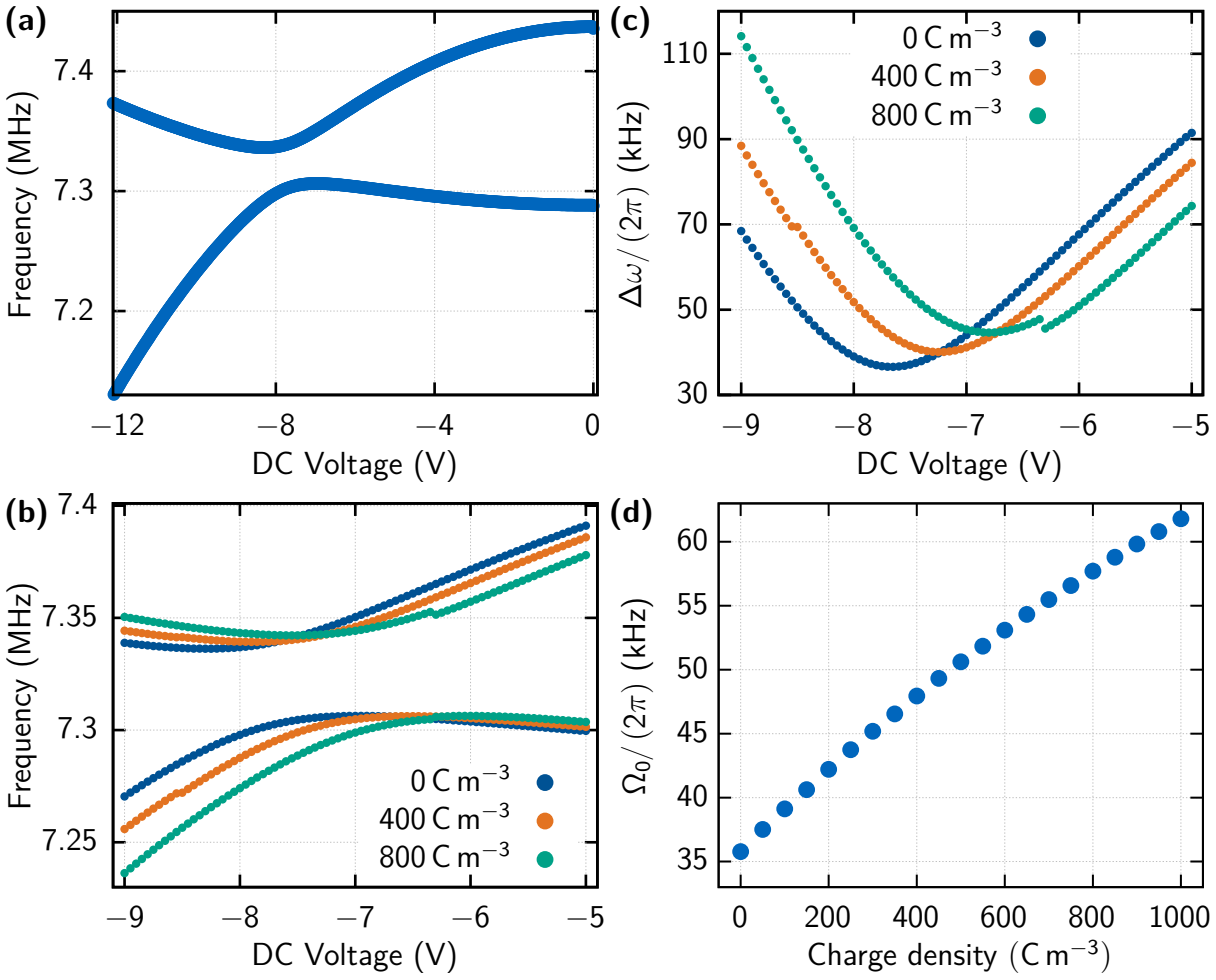

Figure A.7 | Modifications in Level Splitting of the Nanomechanical Flexural Modes.
(a) Eigenfrequency tuning of the mechanical IP and OOP flexural modes as a function of applied DC voltage reveals an avoided crossing. **(b)** Mechanical tuning behaviour can be modified by inducing charge densities to the nano beam. **(c)** Frequency difference of the upper and lower branch in (b) shows a shift in the minima depending on the induced charge density. **(d)** The level splitting in increases with increasing charge density indicating the electric field sensing capability of the silicon nitride nanomechanical resonator.

Acknowledgement

The success of this work was only possible due to the great support of many people and the years of prior research on which the present work is based.

First and foremost, I would like to express my deepest gratitude to you Prof. Dr. *Eva Weig* for being a great PhD supervisor and mentor. Your invaluable advice and constant support over the last five years have contributed significantly to the success of this work. You have always given me the creative freedom to bring my own ideas into this project, which is not taken for granted. Thank you for giving me the opportunity to do research in nanomechanics and to be a member of your group.

A special thanks to my colleague and dear friend Dr. *Avishek Chowdhury*. I am very grateful that we could start the sensing project together. Your experimental expertise and data analysis skills contributed significantly to this work. I really enjoy our daily discussions be it physics related or any other topics, e.g. your opinion towards Apple or the taste of music.

I also would like to thank our theoretical collaborator Prof. *Hugo Ribeiro* for the development of the amazing Magnus-based corrections and the insightful discussions on a weekly basis. You have always brought new ideas to the project, and your theory has become an essential part of this thesis. Thank you for the time and effort you put into the collaboration.

Another special thanks to the staff employees from the University of Konstanz. Thank you *Louis Kukk*, our former technician and the master of craft, for putting all my 3D cavity and antenna designs into reality. Thank you *Matthias Hagner* for organizing and the maintenance of the NanoLab. Thank you *Harald Richter* from the electronics workshop for your ideas to implement the voltage combiner.

I wish to thank all the members from the NQS group and the former members from Konstanz: *Susanne Maier, Berke Demiralp, Avishek Chowdhury, Felix David, Berke Yalaman, Jonny Qiu, Philipp Bredol, Ahmed Barakat, Maria Kallergi, Maximilian Bückle, Juliane Doster, Katrin Gajo, Felix Rochau, Alexandre Brieussel, Jana Ochs, Yannick Klaß, Irene Sanchez-Arribas* for the great working environment. I enjoyed our endless discussion on lunch breaks, bar and restaurant visits, the wine festivals and the trips to conferences.

Thank you *Irene, Ahmed, Philipp, Berke, Jana, Hugo and Avishek* for proof reading my thesis.

To you *Benita*, words are not enough to express my gratitude. Thank you for your emotional support along the journey of life and the motivation to push me forwards. Thank you for proofreading my work and finding all the grammar mistakes I made. I am just grateful to have you by my side and look forward to what is to come.

And finally, I wish to thank my beloved family for your lifetime support and your unconditional love .

Bibliography

[1] C. H. Mielke and A. V. Balatsky, "Crossing a bridge into the unknown", Nature Nanotechnology **3**, 129–130 (2008).

[2] K. Y. Billah and R. H. Scanlan, "Resonance, tacoma narrows bridge failure, and undergraduate physics textbooks", American Journal of Physics **59**, 118–124 (1991).

[3] X. L. Feng, C. J. White, A. Hajimiri, and M. L. Roukes, "A self-sustaining ultrahigh-frequency nanoelectromechanical oscillator", Nature Nanotechnology **3**, 342–346 (2008).

[4] S.-B. Shim, M. Imboden, and P. Mohanty, "Synchronized oscillation in coupled nanomechanical oscillators", Science **316**, 95–99 (2007).

[5] L. Huang, S. M. Soskin, I. A. Khovanov, R. Mannella, K. Ninios, and H. B. Chan, "Frequency stabilization and noise-induced spectral narrowing in resonators with zero dispersion", Nature Communications **10**, 10.1038/s41467-019-11946-8 (2019).

[6] A. N. Cleland and M. L. Roukes, "A nanometre-scale mechanical electrometer", Nature **392**, 160–162 (1998).

[7] M. D. LaHaye, O. Buu, B. Camarota, and K. C. Schwab, "Approaching the quantum limit of a nanomechanical resonator", Science **304**, 74–77 (2004).

[8] D. Rugar, R. Budakian, H. J. Mamin, and B. W. Chui, "Single spin detection by magnetic resonance force microscopy", Nature **430**, 329–332 (2004).

[9] Y. T. Yang, C. Callegari, X. L. Feng, K. L. Ekinci, and M. L. Roukes, "Zeptogram-scale nanomechanical mass sensing", Nano Letters **6**, 583–586 (2006).

[10] J. Chaste, A. Eichler, J. Moser, G. Ceballos, R. Rurali, and A. Bachtold, "A nanomechanical mass sensor with yoctogram resolution", Nature Nanotechnology **7**, 301–304 (2012).

[11] S. L. de Bonis, C. Urgell, W. Yang, C. Samanta, A. Noury, J. Vergara-Cruz, Q. Dong, Y. Jin, and A. Bachtold, "Ultrasensitive displacement noise measurement of carbon nanotube mechanical resonators", Nano Letters **18**, 5324–5328 (2018).

[12] F. W. Beil, A. Wixforth, W. Wegscheider, D. Schuh, M. Bichler, and R. H. Blick, "Shock waves in nanomechanical resonators", Phys. Rev. Lett. **100**, 026801 (2008).

[13] A. Cho, "Researchers race to put the quantum into mechanics", Science **299**, 36–37 (2003).

[14] K. C. Schwab and M. L. Roukes, "Putting mechanics into quantum mechanics", Physics Today **58**, 36–42 (2005).

[15] G. R. Conference, *Gordon research conference, frontiers of science*, https://www.grc.org/.

[16] J. Harris and A. Cleland, *Gordon research conference, mechanical systems in the quantum regime*, (2008) https://www.grc.org/mechanical-systems-in-the-quantum-regime-conference/2008/.

[17] C. Regal and C. Hammerer, *Gordon research conference. mechanical systems in the quantum regime, quantum photonics for fundamental measurements and quantum technology.* (2022) https://www.grc.org/mechanical-systems-in-the-quantum-regime-conference/2022/.

[18] B. P. Abbott, R. Abbott, T. D. Abbott, M. R. Abernathy, F. Acernese, K. Ackley, C. Adams, T. Adams, P. Addesso, R. X. Adhikari, V. B. Adya, C. Affeldt, M. Agathos, K. Agatsuma, and N. Aggarwal, "Observation of gravitational waves from a binary black hole merger", Physical Review Letters **116**, 10.1103/physrevlett.116.061102 (2016).

[19] H. Miao, S. Danilishin, H. Müller-Ebhardt, H. Rehbein, K. Somiya, and Y. Chen, "Probing macroscopic quantum states with a sub-heisenberg accuracy", Phys. Rev. A **81**, 012114 (2010).

[20] H. Müller-Ebhardt, H. Rehbein, R. Schnabel, K. Danzmann, and Y. Chen, "Entanglement of macroscopic test masses and the standard quantum limit in laser interferometry", Phys. Rev. Lett. **100**, 013601 (2008).

[21] A. R. Wade, G. L. Mansell, T. G. McRae, S. S. Y. Chua, M. J. Yap, R. L. Ward, B. J. J. Slagmolen, D. A. Shaddock, and D. E. McClelland, "Optomechanical design and construction of a vacuum-compatible optical parametric oscillator for generation of squeezed light", Review of Scientific Instruments **87**, 063104 (2016).

[22] J. A. Henry, Y. Wang, D. Sengupta, and M. A. Hines, "Understanding the effects of surface chemistry on mechanical energy dissipation in alkyl-terminated micromechanical silicon resonators", The Journal of Physical Chemistry B **111**, 88–94 (2006).

[23] S. Gröblacher, J. B. Hertzberg, M. R. Vanner, G. D. Cole, S. Gigan, K. C. Schwab, and M. Aspelmeyer, "Demonstration of an ultracold micro-optomechanical oscillator in a cryogenic cavity", Nature Physics **5**, 485–488 (2009).

[24] R. W. Andrews, R. W. Peterson, T. P. Purdy, K. Cicak, R. W. Simmonds, C. A. Regal, and K. W. Lehnert, "Bidirectional and efficient conversion between microwave and optical light", Nature Physics **10**, 321–326 (2014).

[25] J. P. Moura, R. A. Norte, J. Guo, C. Schäfermeier, and S. Gröblacher, "Centimeter-scale suspended photonic crystal mirrors", Optics Express **26**, 1895 (2018).

[26] A. Schliesser, O. Arcizet, R. Rivière, G. Anetsberger, and T. J. Kippenberg, "Resolved-sideband cooling and position measurement of a micromechanical oscillator close to the heisenberg uncertainty limit", Nature Physics **5**, 509–514 (2009).

[27] T. Botter, D. Brooks, S. Gupta, Z.-Y. Ma, K. L. Moore, K. W. Murch, T. P. Purdy, and D. M. Stamper-Kurn, "Quantum micro-mechanics with ultracold atoms", in Pushing the frontiers of atomic physics (Mar. 2009).

[28] M. O. Scully, M. S. Zubairy, and I. A. Walmsley, "Quantum optics", American Journal of Physics **67**, 648–648 (1999).

[29] M. O. Scully and A. A. Svidzinsky, "The super of superradiance", Science **325**, 1510–1511 (2009).

[30] S. Camerer, M. Korppi, A. Jöckel, D. Hunger, T. W. Hänsch, and P. Treutlein, "Realization of an optomechanical interface between ultracold atoms and a membrane", Phys. Rev. Lett. **107**, 223001 (2011).

[31] M. Bhattacharya, H. Uys, and P. Meystre, "Optomechanical trapping and cooling of partially reflective mirrors", Phys. Rev. A **77**, 033819 (2008).

[32] Z. Xu, X. Gao, J. Bang, Z. Jacob, and T. Li, "Non-reciprocal energy transfer through the casimir effect", Nature Nanotechnology **17**, 148–152 (2021).

[33] A. Buikema, C. Cahillane, G. L. Mansell, C. D. Blair, R. Abbott, C. Adams, R. X. Adhikari, A. Ananyeva, S. Appert, K. Arai, J. S. Areeda, Y. Asali, S. M. Aston, C. Austin, A. M. Baer, M. Ball, S. W. Ballmer, S. Banagiri, and Barker, "Sensitivity and performance of the advanced ligo detectors in the third observing run", Phys. Rev. D **102**, 062003 (2020).

[34] L. Magrini, P. Rosenzweig, C. Bach, A. Deutschmann-Olek, S. G. Hofer, S. Hong, N. Kiesel, A. Kugi, and M. Aspelmeyer, "Real-time optimal quantum control of mechanical motion at room temperature", Nature **595**, 373–377 (2021).

[35] A. Militaru, M. Rossi, F. Tebbenjohanns, O. Romero-Isart, M. Frimmer, and L. Novotny, "Ponderomotive squeezing of light by a levitated nanoparticle in free space", Phys. Rev. Lett. **129**, 053602 (2022).

[36] X. Zhang, C.-L. Zou, L. Jiang, and H. X. Tang, "Cavity magnomechanics", Science Advances **2**, 10.1126/sciadv.1501286 (2016).

[37] B. D. Hauer, K. Cicak, F. Lecocq, R. W. Simmonds, J. Aumentado, and J. D. Teufel, "Quantum optomechanics with millimeter wave photons", in Conference on lasers and electro-optics (2021).

[38] R. D. Delaney, M. D. Urmey, S. Mittal, B. M. Brubaker, J. M. Kindem, P. S. Burns, C. A. Regal, and K. W. Lehnert, "Superconducting-qubit readout via low-backaction electro-optic transduction", Nature **606**, 489–493 (2022).

[39] U. Delić, M. Reisenbauer, K. Dare, D. Grass, V. Vuletić, N. Kiesel, and M. Aspelmeyer, "Cooling of a levitated nanoparticle to the motional quantum ground state", Science **367**, 892–895 (2020).

[40] K. M. Backes, D. A. Palken, S. A. Kenany, B. M. Brubaker, S. B. Cahn, A. Droster, G. C. Hilton, S. Ghosh, H. Jackson, S. K. Lamoreaux, A. F. Leder, K. W. Lehnert, S. M. Lewis, M. Malnou, R. H. Maruyama, N. M. Rapidis, M. Simanovskaia, S. Singh, D. H. Speller, I. Urdinaran, L. R. Vale, E. C. van Assendelft, K. van Bibber, and H. Wang, "A quantum enhanced search for dark matter axions", Nature **590**, 238–242 (2021).

[41] J. S. Pedernales, K. Streltsov, and M. B. Plenio, "Enhancing gravitational interaction between quantum systems by a massive mediator", Phys. Rev. Lett. **128**, 110401 (2022).

[42] A. D. O'Connell, M. Hofheinz, M. Ansmann, R. C. Bialczak, M. Lenander, E. Lucero, M. Neeley, D. Sank, H. Wang, M. Weides, J. Wenner, J. M. Martinis, and A. N. Cleland, "Quantum ground state and single-phonon control of a mechanical resonator", Nature **464**, 697–703 (2010).

[43] S. M. de Vasconcellos, S. Gordon, M. Bichler, T. Meier, and A. Zrenner, "Coherent control of a single exciton qubit by optoelectronic manipulation", Nature Photonics **4**, 545–548 (2010).

[44] C. Roman, A. Ransford, M. Ip, and W. C. Campbell, "Coherent control for qubit state readout", New Journal of Physics **22**, 073038 (2020).

[45] M. Zanner, T. Orell, C. M. F. Schneider, R. Albert, S. Oleschko, M. L. Juan, M. Silveri, and G. Kirchmair, "Coherent control of a multi-qubit dark state in waveguide quantum electrodynamics", Nature Physics **18**, 538–543 (2022).

[46] E. Leonard, M. A. Beck, J. Nelson, B. Christensen, T. Thorbeck, C. Howington, A. Opremcak, I. Pechenezhskiy, K. Dodge, N. Dupuis, M. Hutchings, J. Ku, F. Schlenker, J. Suttle, C. Wilen, S. Zhu, M. Vavilov, B. Plourde, and R. McDermott, "Digital coherent control of a superconducting qubit", Phys. Rev. Applied **11**, 014009 (2019).

[47] T. Faust, J. Rieger, M. J. Seitner, J. P. Kotthaus, and E. M. Weig, "Coherent control of a classical nanomechanical two-level system", Nature Physics **9**, 485–488 (2013).

[48] E. M. Purcell, H. C. Torrey, and R. V. Pound, "Resonance absorption by nuclear magnetic moments in a solid", Phys. Rev. **69**, 37–38 (1946).

[49] F. Bloch, "Nuclear induction", Phys. Rev. **70**, 460–474 (1946).

[50] I. I. Rabi, "Space quantization in a gyrating magnetic field", Phys. Rev. **51**, 652–654 (1937).

[51] N. F. Ramsey, "A molecular beam resonance method with separated oscillating fields", Phys. Rev. **78**, 695–699 (1950).

[52] E. L. Hahn, "Spin echoes", Phys. Rev. **80**, 580–594 (1950).

[53] L. D. Landau, "Zur Theorie der Energieubertragung. II", Phys. Z. Sowjetunion **2**, 46 (1932).

[54] C. Zener, "Non-adiabatic crossing of energy levels", Proc. R. Soc. A **137**, 696 (1932).

[55] E. C. G. Stückelberg, "Theorie der unelastischen Stösse zwischen Atomen", Helv. Phys. Acta **5**, 239 (1932).

[56] T. Faust, J. Rieger, M. J. Seitner, P. Krenn, J. P. Kotthaus, and E. M. Weig, "Nonadiabatic dynamics of two strongly coupled nanomechanical resonator modes", Phys. Rev. Lett. **109**, 037205 (2012).

[57] M. Seitner, "Coherent dynamics and parametric effects in strongly coupled nanomechanical resonator modes", PhD thesis (University of Konstanz, 2017).

[58] W. D. Oliver, Y. Yu, J. C. Lee, K. K. Berggren, L. S. Levitov, and T. P. Orlando, "Mach-zehnder interferometry in a strongly driven superconducting qubit", Science **310**, 1653–1657 (2005).

[59] M. Mark, T. Kraemer, P. Waldburger, J. Herbig, C. Chin, H.-C. Nägerl, and R. Grimm, "'stückelberg interferometry" with ultracold molecules", Phys. Rev. Lett. **99**, 113201 (2007).

[60] S. Shevchenko, S. Ashhab, and F. Nori, "Landau Zener Stückelberg interferometry", Physics Reports **492**, 1–30 (2010).

[61] S. N. Shevchenko, S. Ashhab, and F. Nori, "Inverse Landau-Zener-Stückelberg problem for qubit-resonator systems", Phys. Rev. B **85**, 094502 (2012).

[62] M. J. Seitner, H. Ribeiro, J. Kölbl, T. Faust, J. P. Kotthaus, and E. M. Weig, "Classical Stückelberg interferometry of a nanomechanical two-mode system", Physical Review B **94**, 10.1103/physrevb.94.245406 (2016).

[63] M. J. Seitner, H. Ribeiro, J. Kölbl, T. Faust, and E. M. Weig, "Finite-time Stückelberg interferometry with nanomechanical modes", New Journal of Physics **19**, 033011 (2017).

[64] N. Ramsey, *Molecular beams* (Oxford University Press, New York, 1985).

[65] M. Brune, S. Haroche, J. M. Raimond, L. Davidovich, and N. Zagury, "Manipulation of photons in a cavity by dispersive atom-field coupling: quantum-nondemolition measurements and generation of "schrödinger cat" states", Phys. Rev. A **45**, 5193–5214 (1992).

[66] A. N. Cleland, *Foundations of nanomechanics* (Springer Berlin Heidelberg, 2003).

[67] S. Schmid, L. G. Villanueva, and M. L. Roukes, *Fundamentals of nanomechanical resonators* (© Springer International Publishing Switzerland, 2016).

[68] W. Weaver Jr, S. P. Timoshenko, and D. H. Young, *Vibration problems in engineering* (John Wiley & Sons, 1991).

[69] J. Rieger, A. Isacsson, M. J. Seitner, J. P. Kotthaus, and E. M. Weig, "Energy losses of nanomechanical resonators induced by atomic force microscopy-controlled mechanical impedance mismatching", Nature Communications **5**, 10.1038/ncomms4345 (2014).

[70] Q. P. Unterreithmeier, E. M. Weig, and J. P. Kotthaus, "Universal transduction scheme for nanomechanical systems based on dielectric forces", Nature **458**, 1001–1004 (2009).

[71] P.-L. Yu, T. P. Purdy, and C. A. Regal, "Control of material damping in high-q membrane microresonators", Phys. Rev. Lett. **108**, 083603 (2012).

[72] S. A. Fedorov, N. J. Engelsen, A. H. Ghadimi, M. J. Bereyhi, R. Schilling, D. J. Wilson, and T. J. Kippenberg, "Generalized dissipation dilution in strained mechanical resonators", Phys. Rev. B **99**, 054107 (2019).

[73] S. S. Verbridge, H. G. Craighead, and J. M. Parpia, "A megahertz nanomechanical resonator with room temperature quality factor over a million", Applied Physics Letters **92**, 013112 (2008).

[74] Y. Tsaturyan, A. Barg, E. S. Polzik, and A. Schliesser, "Ultracoherent nanomechanical resonators via soft clamping and dissipation dilution", Nature Nanotechnology **12**, 776–783 (2017).

[75] A. H. Ghadimi, S. A. Fedorov, N. J. Engelsen, M. J. Bereyhi, R. Schilling, D. J. Wilson, and T. J. Kippenberg, "Elastic strain engineering for ultralow mechanical dissipation", Science **360**, 764–768 (2018).

[76] A. Beccari, D. A. Visani, S. A. Fedorov, M. J. Bereyhi, V. Boureau, N. J. Engelsen, and T. J. Kippenberg, "Strained crystalline nanomechanical resonators with quality factors above 10 billion", Nature Physics **18**, 436–441 (2022).

[77] M. Frimmer and L. Novotny, "The classical bloch equations", American Journal of Physics **82**, 947–954 (2014).

[78] C. L. Garrido Alzar, M. A. G. Martinez, and P. Nussenzveig, "Classical analog of electromagnetically induced transparency", American Journal of Physics **70**, 37–41 (2002).

[79] S. Asztalos, E. Daw, H. Peng, L. J Rosenberg, C. Hagmann, D. Kinion, W. Stoeffl, K. van Bibber, P. Sikivie, N. S. Sullivan, D. B. Tanner, F. Nezrick, M. S. Turner, D. M. Moltz, J. Powell, M.-O. André, J. Clarke, M. Mück, and R. F. Bradley, "Large-scale microwave cavity search for dark-matter axions", Phys. Rev. D **64**, 092003 (2001).

[80] N. M. Rapidis, S. M. Lewis, and K. A. van Bibber, "Characterization of the HAYSTAC axion dark matter search cavity using microwave measurement and simulation techniques", Review of Scientific Instruments **90**, 024706 (2019).

[81] M. Reagor, W. Pfaff, C. Axline, R. W. Heeres, N. Ofek, K. Sliwa, E. Holland, C. Wang, J. Blumoff, K. Chou, M. J. Hatridge, L. Frunzio, M. H. Devoret, L. Jiang, and R. J. Schoelkopf, "Quantum memory with millisecond coherence in circuit qed", Phys. Rev. B **94**, 014506 (2016).

[82] A. Wallraff, D. I. Schuster, A. Blais, L. Frunzio, R.-S. Huang, J. Majer, S. Kumar, S. M. Girvin, and R. J. Schoelkopf, "Strong coupling of a single photon to a superconducting qubit using circuit quantum electrodynamics", Nature **431**, 162–167 (2004).

[83] G. Kirchmair, B. Vlastakis, Z. Leghtas, S. E. Nigg, H. Paik, E. Ginossar, M. Mirrahimi, L. Frunzio, S. M. Girvin, and R. J. Schoelkopf, "Observation of quantum state collapse and revival due to the single-photon kerr effect", Nature **495**, 205–209 (2013).

[84] L. Sun, A. Petrenko, Z. Leghtas, B. Vlastakis, G. Kirchmair, K. M. Sliwa, A. Narla, M. Hatridge, S. Shankar, J. Blumoff, L. Frunzio, M. Mirrahimi, M. H. Devoret, and R. J. Schoelkopf, "Tracking photon jumps with repeated quantum non-demolition parity measurements", Nature **511**, 444–448 (2014).

[85] E. Flurin, N. Roch, J. D. Pillet, F. Mallet, and B. Huard, "Superconducting quantum node for entanglement and storage of microwave radiation", Phys. Rev. Lett. **114**, 090503 (2015).

[86] A. Angerer, T. Astner, D. Wirtitsch, H. Sumiya, S. Onoda, J. Isoya, S. Putz, and J. Majer, "Collective strong coupling with homogeneous rabi frequencies using a 3d lumped element microwave resonator", Applied Physics Letters **109**, 033508 (2016).

[87] X. Zhang, C.-L. Zou, L. Jiang, and H. X. Tang, "Strongly coupled magnons and cavity microwave photons", Phys. Rev. Lett. **113**, 156401 (2014).

[88] M. Göppl, A. Fragner, M. Baur, R. Bianchetti, S. Filipp, J. M. Fink, P. J. Leek, G. Puebla, L. Steffen, and A. Wallraff, "Coplanar waveguide resonators for circuit quantum electrodynamics", Journal of Applied Physics **104**, 113904 (2008).

[89] M. Aspelmeyer, P. Meystre, and K. Schwab, "Quantum optomechanics", Physics Today **65**, 29–35 (2012).

[90] M. Aspelmeyer, T. J. Kippenberg, and F. Marquardt, "Cavity optomechanics", Reviews of Modern Physics **86**, 1391–1452 (2014).

[91] J. D. Teufel, T. Donner, M. A. Castellanos-Beltran, J. W. Harlow, and K. W. Lehnert, "Nanomechanical motion measured with an imprecision below that at the standard quantum limit", Nature Nanotechnology **4**, 820–823 (2009).

[92] J. D. Teufel, D. Li, M. S. Allman, K. Cicak, A. J. Sirois, J. D. Whittaker, and R. W. Simmonds, "Circuit cavity electromechanics in the strong-coupling regime", Nature **471**, 204–208 (2011).

[93] J. D. Teufel, T. Donner, D. Li, J. W. Harlow, M. S. Allman, K. Cicak, A. J. Sirois, J. D. Whittaker, K. W. Lehnert, and R. W. Simmonds, "Sideband cooling of micromechanical motion to the quantum ground state", Nature **475**, 359–363 (2011).

[94] R. W. Peterson, T. P. Purdy, N. S. Kampel, R. W. Andrews, P.-L. Yu, K. W. Lehnert, and C. A. Regal, "Laser cooling of a micromechanical membrane to the quantum backaction limit", Phys. Rev. Lett. **116**, 063601 (2016).

[95] T. Faust, P. Krenn, S. Manus, J. Kotthaus, and E. Weig, "Microwave cavity-enhanced transduction for plug and play nanomechanics at room temperature", Nature Communications **3**, 10.1038/ncomms1723 (2012).

[96] D. M. Pozar, *Microwave engineering* (John Wiley & Sons, 2012).

[97] H. Mooijweer, *Microwave techniques* (Macmillan Education UK, 1971).

[98] M. J. Reagor, "Superconducting cavities for circuit quantum electrodynamics", PhD thesis (Yale University, 2015).

[99] H. Paik, D. I. Schuster, L. S. Bishop, G. Kirchmair, G. Catelani, A. P. Sears, B. R. Johnson, M. J. Reagor, L. Frunzio, L. I. Glazman, S. M. Girvin, M. H. Devoret, and R. J. Schoelkopf, "Observation of high coherence in josephson junction qubits measured in a three-dimensional circuit QED architecture", Physical Review Letters **107**, 10.1103/physrevlett.107.240501 (2011).

[100] Y. Tabuchi, S. Ishino, A. Noguchi, T. Ishikawa, R. Yamazaki, K. Usami, and Y. Nakamura, "Coherent coupling between a ferromagnetic magnon and a superconducting qubit", Science **349**, 405–408 (2015).

[101] V. Singh, S. J. Bosman, B. H. Schneider, Y. M. Blanter, A. Castellanos-Gomez, and G. A. Steele, "Optomechanical coupling between a multilayer graphene mechanical resonator and a superconducting microwave cavity", Nature Nanotechnology **9**, 820–824 (2014).

[102] M. Yuan, V. Singh, Y. M. Blanter, and G. A. Steele, "Large cooperativity and microkelvin cooling with a three-dimensional optomechanical cavity", Nature Communications **6**, 10.1038/ncomms9491 (2015).

[103] A. Noguchi, R. Yamazaki, M. Ataka, H. Fujita, Y. Tabuchi, T. Ishikawa, K. Usami, and Y. Nakamura, "Ground state cooling of a quantum electromechanical system with a silicon nitride membrane in a 3d loop-gap cavity", New Journal of Physics **18**, 103036 (2016).

[104] T. Rylander, P. Ingelström, and A. Bondeson, *Computational electromagnetics* (Springer New York, 2013).

[105] S. E. Ratcliffe, "Developing a resonant waveguide cavity as a notch filter", MA thesis (Ludwig-Maximilians-Universität München, 2012).

[106] M. Reagor, H. Paik, G. Catelani, L. Sun, C. Axline, E. Holland, I. M. Pop, N. A. Masluk, T. Brecht, L. Frunzio, M. H. Devoret, L. Glazman, and R. J. Schoelkopf, "Reaching 10 ms single photon lifetimes for superconducting aluminum cavities", Applied Physics Letters **102**, 192604 (2013).

[107] A. T. Le, A. Brieussel, and E. M. Weig, "Room temperature cavity electromechanics in the sideband-resolved regime", Journal of Applied Physics **130**, 014301 (2021).

[108] C. Wang, Y. Y. Gao, P. Reinhold, R. W. Heeres, N. Ofek, K. Chou, C. Axline, M. Reagor, J. Blumoff, K. M. Sliwa, L. Frunzio, S. M. Girvin, L. Jiang, M. Mirrahimi, M. H. Devoret, and R. J. Schoelkopf, "A schrödinger cat living in two boxes", Science **352**, 1087–1091 (2016).

[109] N. Ofek, A. Petrenko, R. Heeres, P. Reinhold, Z. Leghtas, B. Vlastakis, Y. Liu, L. Frunzio, S. M. Girvin, L. Jiang, M. Mirrahimi, M. H. Devoret, and R. J. Schoelkopf, "Extending the lifetime of a quantum bit with error correction in superconducting circuits", Nature **536**, 441–445 (2016).

[110] R. W. Heeres, P. Reinhold, N. Ofek, L. Frunzio, L. Jiang, M. H. Devoret, and R. J. Schoelkopf, "Implementing a universal gate set on a logical qubit encoded in an oscillator", Nature Communications **8**, 10.1038/s41467-017-00045-1 (2017).

[111] W. Pfaff, C. J. Axline, L. D. Burkhart, U. Vool, P. Reinhold, L. Frunzio, L. Jiang, M. H. Devoret, and R. J. Schoelkopf, "Controlled release of multiphoton quantum states from a microwave cavity memory", Nature Physics **13**, 882–887 (2017).

[112] K. S. Chou, J. Z. Blumoff, C. S. Wang, P. C. Reinhold, C. J. Axline, Y. Y. Gao, L. Frunzio, M. H. Devoret, L. Jiang, and R. J. Schoelkopf, "Deterministic teleportation of a quantum gate between two logical qubits", Nature **561**, 368–373 (2018).

[113] S. Rosenblum, Y. Y. Gao, P. Reinhold, C. Wang, C. J. Axline, L. Frunzio, S. M. Girvin, L. Jiang, M. Mirrahimi, M. H. Devoret, and R. J. Schoelkopf, "A CNOT gate between multiphoton qubits encoded in two cavities", Nature Communications **9**, 10.1038/s41467-018-03059-5 (2018).

[114] C. J. Axline, L. D. Burkhart, W. Pfaff, M. Zhang, K. Chou, P. Campagne-Ibarcq, P. Reinhold, L. Frunzio, S. M. Girvin, L. Jiang, M. H. Devoret, and R. J. Schoelkopf, "On-demand quantum state transfer and entanglement between remote microwave cavity memories", Nature Physics **14**, 705–710 (2018).

[115] H. A. Bethe, "Theory of diffraction by small holes", Physical Review **66**, 163–182 (1944).

[116] D. Anic, "Mikrowellenhohlraumresonatoren in nanoelektromechanik bei raumtemperatur", MA thesis (Universität Konstanz, Feb. 2021).

[117] C. N. Works, "Resonant cavities for dielectric measurements", Journal of Applied Physics **18**, 605–612 (1947).

[118] H. Paik and K. D. Osborn, "Reducing quantum-regime dielectric loss of silicon nitride for superconducting quantum circuits", Applied Physics Letters **96**, 072505 (2010).

[119] M. Aspelmeyer, T. J. Kippenberg, and F. Marquardt, *Cavity optomechanics* (Springer-Verlag Berlin Heidelberg, 2014).

[120] P. J. Petersan and S. M. Anlage, "Measurement of resonant frequency and quality factor of microwave resonators: comparison of methods", Journal of Applied Physics **84**, 3392–3402 (1998).

[121] N. Chernov and C. Lesort, "Least squares fitting of circles", Journal of Mathematical Imaging and Vision **23**, 239–252 (2005).

[122] S. Probst, F. B. Song, P. A. Bushev, A. V. Ustinov, and M. Weides, "Efficient and robust analysis of complex scattering data under noise in microwave resonators", Review of Scientific Instruments **86**, 024706 (2015).

[123] K. L. Geerlings, "Improving coherence of superconducting qubits and resonators", PhD thesis (Yale University, Aug. 2013).

[124] C. Deng, M. Otto, and A. Lupascu, "An analysis method for transmission measurements of superconducting resonators with applications to quantum-regime dielectric-loss measurements", Journal of Applied Physics **114**, 054504 (2013).

[125] M. S. Khalil, M. J. A. Stoutimore, F. C. Wellstood, and K. D. Osborn, "An analysis method for asymmetric resonator transmission applied to superconducting devices", Journal of Applied Physics **111**, 054510 (2012).

[126] S. Probst, *Python implementation of the fitting algorithm*, (2015) https://www.phi.kit.edu/ustinov_downloads.php.

[127] D. Rieger, S. Günzler, M. Spiecker, A. Nambisan, W. Wernsdorfer, and I. M. Pop, "Fano interference in microwave resonator measurements", https://doi.org/10.48550/arXiv.2209.03036 (2023).

[128] R. B. Yalaman, "Fabrication and characterization of high q nanomechanical string resonators", MA thesis (Technical University of Munich, 2022).

[129] F. David, "Fabrication and characterization of nanomechanical string resonators based on silicon carbide", MA thesis (Technical University of Munich, 2022).

[130] J. Rieger, T. Faust, M. J. Seitner, J. P. Kotthaus, and E. M. Weig, "Frequency and q factor control of nanomechanical resonators", Applied Physics Letters **101**, 103110 (2012).

[131] K. Bordo and H.-G. Rubahn, "Effect of deposition rate on structure and surface morphology of thin evaporated al films on dielectrics and semiconductors", Materials Science **18**, 10.5755/j01.ms.18.4.3088 (2012).

[132] Y. Klass, "High q nanomechanical resonators fabricated from crystalline silicon carbide", PhD thesis (Technical University of Munich, 2022).

[133] M. Bückle, "Nanomechanical systems based on tensile-stressed crystalline indium gallium phosphide", PhD thesis (University of Konstanz, 2020).

[134] M. J. Seitner, K. Gajo, and E. M. Weig, "Damping of metallized bilayer nanomechanical resonators at room temperature", Applied Physics Letters **105**, 213101 (2014).

[135] N. C. Carvalho, J. Bourhill, M. Goryachev, S. Galliou, and M. E. Tobar, "Piezo-optomechanical coupling of a 3d microwave resonator to a bulk acoustic wave crystalline resonator", Applied Physics Letters **115**, 211102 (2019).

[136] C. A. Regal and K. W. Lehnert, "From cavity electromechanics to cavity optomechanics", Journal of Physics: Conference Series **264**, 012025 (2011).

[137] M. Forsch, R. Stockill, A. Wallucks, I. Marinković, C. Gärtner, R. A. Norte, F. van Otten, A. Fiore, K. Srinivasan, and S. Gröblacher, "Microwave-to-optics conversion using a mechanical oscillator in its quantum ground state", Nature Physics **16**, 69–74 (2019).

[138] J.-M. Pirkkalainen, E. Damskägg, M. Brandt, F. Massel, and M. A. Sillanpää, "Squeezing of quantum noise of motion in a micromechanical resonator", Phys. Rev. Lett. **115**, 243601 (2015).

[139] F. Massel, T. T. Heikkilä, J.-M. Pirkkalainen, S. U. Cho, H. Saloniemi, P. J. Hakonen, and M. A. Sillanpää, "Microwave amplification with nanomechanical resonators", Nature **480**, 351–354 (2011).

[140] T. A. Palomaki, J. D. Teufel, R. W. Simmonds, and K. W. Lehnert, "Entangling mechanical motion with microwave fields", Science **342**, 710–713 (2013).

[141] S. Barzanjeh, E. S. Redchenko, M. Peruzzo, M. Wulf, D. P. Lewis, G. Arnold, and J. M. Fink, "Stationary entangled radiation from micromechanical motion", Nature **570**, 480–483 (2019).

[142] M. Roukes, *Fns invited talk: microwave cavity optomechanics, parametrically-coupled nonlinear oscillators and single molecules analysis.* (2021) http://fns2021.icfo.eu/2020/12/18/michael-roukes/.

[143] M. Abramowitz and I. A. Stegun, *Handbook of mathematical functions with formulas, graphs, and mathematical tables*, Vol. 55 (US Government printing office, 1964).

[144] J. S. Huber, G. Rastelli, M. J. Seitner, J. Kölbl, W. Belzig, M. I. Dykman, and E. M. Weig, "Spectral evidence of squeezing of a weakly damped driven nanomechanical mode", Physical Review X **10**, 021066 (2020).

[145] J. S. Ochs, M. Seitner, M. I. Dykman, and E. M. Weig, "Amplification and spectral evidence of squeezing in the response of a strongly driven nanoresonator to a probe field", Physical Review A **103**, 013506 (2021).

[146] J. S. Ochs, G. Rastelli, M. Seitner, M. I. Dykman, and E. M. Weig, "Resonant nonlinear response of a nanomechanical system with broken symmetry", Physical Review B **104**, 155434 (2021).

[147] L Sekaric, D. Carr, S Evoy, J. Parpia, and H. Craighead, "Nanomechanical resonant structures in silicon nitride: fabrication, operation and dissipation issues", Sensors and Actuators A: Physical **101**, 215–219 (2002).

[148] K. L. Ekinci, X. M. H. Huang, and M. L. Roukes, "Ultrasensitive nanoelectromechanical mass detection", Applied Physics Letters **84**, 4469–4471 (2004).

[149] I. Wilson-Rae, N. Nooshi, W. Zwerger, and T. J. Kippenberg, "Theory of ground state cooling of a mechanical oscillator using dynamical backaction", Phys. Rev. Lett. **99**, 093901 (2007).

[150] F. Marquardt, J. P. Chen, A. A. Clerk, and S. M. Girvin, "Quantum theory of cavity-assisted sideband cooling of mechanical motion", Phys. Rev. Lett. **99**, 093902 (2007).

[151] A. Schliesser, R. Rivière, G. Anetsberger, O. Arcizet, and T. J. Kippenberg, "Resolved-sideband cooling of a micromechanical oscillator", Nature Physics **4**, 415–419 (2008).

[152] F. Chen, A. J. Sirois, R. W. Simmonds, and A. J. Rimberg, "Introduction of a dc bias into a high-q superconducting microwave cavity", Appl. Phys. Lett. **98**, 132509 (2011).

[153] S. E. de Graaf, D. Davidovikj, A. Adamyan, S. E. Kubatkin, and A. V. Danilov, "Galvanically split superconducting microwave resonators for introducing internal voltage bias", Applied Physics Letters **104**, 052601 (2014).

[154] Y. Hao, F. Rouxinol, and M. D. LaHaye, "Development of a broadband reflective t-filter for voltage biasing high-q superconducting microwave cavities", Applied Physics Letters **105**, 222603 (2014).

[155] W.-C. Kong, G.-W. Deng, S.-X. Li, H.-O. Li, G. Cao, M. Xiao, and G.-P. Guo, "Introduction of DC line structures into a superconducting microwave 3d cavity", Review of Scientific Instruments **86**, 023108 (2015).

[156] M. A. Cohen, M. Yuan, B. W. A. de Jong, E. Beukers, S. J. Bosman, and G. A. Steele, "A split-cavity design for the incorporation of a dc bias in a 3d microwave cavity", Applied Physics Letters **110**, 172601 (2017).

[157] M Stammeier, S Garcia, and A Wallraff, "Applying electric and magnetic field bias in a 3d superconducting waveguide cavity with high quality factor", Quantum Science and Technology **3**, 045007 (2018).

[158] A. H. Nayfeh and D. T. Mook, *Nonlinear oscillations* (Wiley, May 1995).

[159] M. Aspelmeyer, T. J. Kippenberg, and F. Marquardt, "Cavity optomechanics", Reviews of Modern Physics **86**, 1391–1452 (2014).

[160] A. A. Clerk, M. H. Devoret, S. M. Girvin, F. Marquardt, and R. J. Schoelkopf, "Introduction to quantum noise, measurement, and amplification", Reviews of Modern Physics **82**, 1155–1208 (2010).

[161] O. Shevchuk, V. Singh, G. A. Steele, and Y. M. Blanter, "Optomechanical response of a nonlinear mechanical resonator", Physical Review B **92**, 10.1103/physrevb.92.195415 (2015).

[162] G. S. Agarwal and S. Huang, "Electromagnetically induced transparency in mechanical effects of light", Physical Review A **81**, 10.1103/physreva.81.041803 (2010).

[163] S. Weis, R. Rivière, S. Deléglise, E. Gavartin, O. Arcizet, A. Schliesser, and T. J. Kippenberg, "Optomechanically induced transparency", Science **330**, 1520–1523 (2010).

[164] X. Zhou, F. Hocke, A. Schliesser, A. Marx, H. Huebl, R. Gross, and T. J. Kippenberg, "Slowing, advancing and switching of microwave signals using circuit nanoelectromechanics", Nature Physics **9**, 179–184 (2013).

[165] V. Singh, O. Shevchuk, Y. M. Blanter, and G. A. Steele, "Negative nonlinear damping of a multilayer graphene mechanical resonator", Physical Review B **93**, 10.1103/physrevb.93.245407 (2016).

[166] T. Bodiya, V. Sudhir, C. Wipf, N. Smith, A. Buikema, A. Kontos, H. Yu, and N. Mavalvala, "Sub-hertz optomechanically induced transparency with a kilogram-scale mechanical oscillator", Physical Review A **100**, 10.1103/physreva.100.013853 (2019).

[167] A. Chowdhury, A. T. Le, E. M. Weig, and H. Ribeiro, "Iterative adaptive spectroscopy of short signals", 10.48550/ARXIV.2204.04736 (2022).

[168] P. Fisk, M. Sellars, M. Lawn, C. Coles, A. Mann, and D. Blair, "Very high q microwave spectroscopy on trapped /sup 171/yb/sup +/ ions: application as a frequency standard", IEEE Transactions on Instrumentation and Measurement **44**, 113–116 (1995).

[169] K. Saeedi, S. Simmons, J. Z. Salvail, P. Dluhy, H. Riemann, N. V. Abrosimov, P. Becker, H.-J. Pohl, J. J. L. Morton, and M. L. W. Thewalt, "Room-temperature quantum bit storage exceeding 39 minutes using ionized donors in silicon-28", Science **342**, 830–833 (2013).

[170] M. Zhong, M. P. Hedges, R. L. Ahlefeldt, J. G. Bartholomew, S. E. Beavan, S. M. Wittig, J. J. Longdell, and M. J. Sellars, "Optically addressable nuclear spins in a solid with a six-hour coherence time", Nature **517**, 177–180 (2015).

[171] A. Barfuss, J. Kölbl, L. Thiel, J. Teissier, M. Kasperczyk, and P. Maletinsky, "Phase-controlled coherent dynamics of a single spin under closed-contour interaction", Nature Physics **14**, 1087–1091 (2018).

[172] J. Kölbl, A. Barfuss, M. S. Kasperczyk, L. Thiel, A. A. Clerk, H. Ribeiro, and P. Maletinsky, "Initialization of single spin dressed states using shortcuts to adiabaticity", Phys. Rev. Lett. **122**, 090502 (2019).

[173] E. D. Herbschleb, H. Kato, Y. Maruyama, T. Danjo, T. Makino, S. Yamasaki, I. Ohki, K. Hayashi, H. Morishita, M. Fujiwara, and N. Mizuochi, "Ultra-long coherence times amongst room-temperature solid-state spins", Nature Communications **10**, 3766 (2019).

[174] M. Tse and et al., "Quantum-enhanced advanced ligo detectors in the era of gravitational-wave astronomy", Phys. Rev. Lett. **123**, 231107 (2019).

[175] M. Malnou, D. A. Palken, B. M. Brubaker, L. R. Vale, G. C. Hilton, and K. W. Lehnert, "Squeezed vacuum used to accelerate the search for a weak classical signal", Phys. Rev. X **9**, 021023 (2019).

[176] T. L. scientific Collaboration, "A gravitational wave observatory operating beyond the quantum shot-noise limit", Nature Physics **7**, 962–965 (2011).

[177] J. Aasi and et al., "Enhanced sensitivity of the ligo gravitational wave detector by using squeezed states of light", Nature Photonics **7**, 613–619 (2013).

[178] M. Werninghaus, D. J. Egger, F. Roy, S. Machnes, F. K. Wilhelm, and S. Filipp, "Leakage reduction in fast superconducting qubit gates via optimal control", npj Quantum Information **7**, 14 (2021).

[179] B. J. Lawrie, P. D. Lett, A. M. Marino, and R. C. Pooser, "Quantum Sensing with Squeezed Light", ACS Photonics **6**, 1307–1318 (2019).

[180] J. Liu, M. Zhang, H. Chen, L. Wang, and H. Yuan, "Optimal scheme for quantum metrology", Advanced Quantum Technologies **5**, 2100080 (2022).

[181] L. M. K. Vandersypen and I. L. Chuang, "Nmr techniques for quantum control and computation", Rev. Mod. Phys. **76**, 1037–1069 (2005).

[182] D. Vion, A. Aassime, A. Cottet, P. Joyez, H. Pothier, C. Urbina, D. Esteve, and M. H. Devoret, "Manipulating the quantum state of an electrical circuit", Science **296**, 886–889 (2002).

[183] C. L. Degen, F. Reinhard, and P. Cappellaro, "Quantum sensing", Rev. Mod. Phys. **89**, 035002 (2017).

[184] K. M. M. Prabhu, *Window functions and their applications in signal processing* (CRC Press, Sept. 2018).

[185] H. Ribeiro, A. Baksic, and A. A. Clerk, "Systematic magnus-based approach for suppressing leakage and nonadiabatic errors in quantum dynamics", Phys. Rev. X **7**, 011021 (2017).

[186] T. F. Roque, A. A. Clerk, and H. Ribeiro, "Engineering fast high-fidelity quantum operations with constrained interactions", npj Quantum Information **7**, 10.1038/s41534-020-00349-z (2021).

[187] J. Clarke and F. K. Wilhelm, "Superconducting quantum bits", Nature **453**, 1031–1042 (2008).

[188] L. Novotny, "Strong coupling, energy splitting, and level crossings: a classical perspective", American Journal of Physics **78**, 1199–1202 (2010).

[189] H. Okamoto, A. Gourgout, C.-Y. Chang, K. Onomitsu, I. Mahboob, E. Y. Chang, and H. Yamaguchi, "Coherent phonon manipulation in coupled mechanical resonators", Nature Physics **9**, 480–484 (2013).

[190] F. R. Braakman, N. Rossi, G. Tütüncüoglu, A. F. i. Morral, and M. Poggio, "Coherent two-mode dynamics of a nanowire force sensor", Phys. Rev. Applied **9**, 054045 (2018).

[191] A. Ranfagni, P. Vezio, M. Calamai, A. Chowdhury, F. Marino, and F. Marin, "Vectorial polaritons in the quantum motion of a levitated nanosphere", Nature Physics **17**, 1120–1124 (2021).

[192] I Yeo, P.-L. de Assis, a Gloppe, E Dupont-Ferrier, P Verlot, N. S. Malik, E Dupuy, J Claudon, J.-M. Gérard, a Auffèves, G Nogues, S Seidelin, J.-p. Poizat, O Arcizet, and M Richard, "Strain-mediated coupling in a quantum dot-mechanical oscillator hybrid system.", Nature Nanotechnology **9**, 106–110 (2014).

[193] S. M. Thon, M. T. Rakher, H. Kim, J. Gudat, W. T. M. Irvine, P. M. Petroff, and D. Bouwmeester, "Strong coupling through optical positioning of a quantum dot in a photonic crystal cavity", Applied Physics Letters **94**, 111115 (2009).

[194] M. Pernpeintner, P. Schmidt, D. Schwienbacher, R. Gross, and H. Huebl, "Frequency control and coherent excitation transfer in a nanostring-resonator network", Phys. Rev. Applied **10**, 034007 (2018).

[195] C. H. Bennett, D. P. DiVincenzo, P. W. Shor, J. A. Smolin, B. M. Terhal, and W. K. Wootters, "Remote state preparation", Phys. Rev. Lett. **87**, 077902 (2001).

[196] J. Koch, T. M. Yu, J. Gambetta, A. A. Houck, D. I. Schuster, J. Majer, A. Blais, M. H. Devoret, S. M. Girvin, and R. J. Schoelkopf, "Charge-insensitive qubit design derived from the cooper pair box", Phys. Rev. A **76**, 042319 (2007).

[197] P. Rabl, S. J. Kolkowitz, F. H. L. Koppens, J. G. E. Harris, P. Zoller, and M. D. Lukin, "A quantum spin transducer based on nanoelectromechanical resonator arrays", Nature Physics **6**, 602–608 (2010).

[198] M. S. J. Barson, P. Peddibhotla, P. Ovartchaiyapong, K. Ganesan, R. L. Taylor, M. Gebert, Z. Mielens, B. Koslowski, D. A. Simpson, L. P. McGuinness, J. McCallum, S. Prawer, S. Onoda, T. Ohshima, A. C. B. Jayich, F. Jelezko, N. B. Manson, and M. W. Doherty, "Nanomechanical sensing using spins in diamond", Nano Letters **17**, 1496–1503 (2017).

[199] P. Kurpiers, P. Magnard, T. Walter, B. Royer, M. Pechal, J. Heinsoo, Y. Salathé, A. Akin, S. Storz, J.-C. Besse, S. Gasparinetti, A. Blais, and A. Wallraff, "Deterministic quantum state transfer and remote entanglement using microwave photons", Nature **558**, 264–267 (2018).

[200] A. Zrenner, E. Beham, S. Stufler, F. Findeis, M. Bichler, and G. Abstreiter, "Coherent properties of a two-level system based on a quantum-dot photodiode", Nature **418**, 612–614 (2002).

[201] J. M. Boss, K. S. Cujia, J. Zopes, and C. L. Degen, "Quantum sensing with arbitrary frequency resolution", Science **356**, 837–840 (2017).

[202] F. Poggiali, P. Cappellaro, and N. Fabbri, "Optimal control for one-qubit quantum sensing", Phys. Rev. X **8**, 021059 (2018).

[203] E. Majorana, "Atomi orientati in campo magnetico variabile", Nuovo Cimento **9**, 43 (1932).

[204] P. Nalbach and M. Thorwart, "Landau-Zener transitions in a dissipative environment: numerically exact results", Phys. Rev. Lett. **103**, 220401 (2009).

[205] W. Magnus, "On the exponential solution of differential equations for a linear operator", Communications on Pure and Applied Mathematics **7**, 649–673 (1954).

[206] M. Gasior and J. L. Gonzalez, "Improving fft frequency measurement resolution by parabolic and gaussian spectrum interpolation", AIP Conference Proceedings **732**, 276–285 (2004).

[207] F. Harris, "On the use of windows for harmonic analysis with the discrete fourier transform", Proceedings of the IEEE **66**, 51–83 (1978).

[208] J. R. Petta, H. Lu, and A. C. Gossard, "A coherent beam splitter for electronic spin states", Science **327**, 669–672 (2010).

[209] L. Gaudreau, G. Granger, A. Kam, G. C. Aers, S. A. Studenikin, P. Zawadzki, M. Pioro-Ladrière, Z. R. Wasilewski, and A. S. Sachrajda, "Coherent control of three-spin states in a triple quantum dot", Nature Physics **8**, 54–58 (2011).

[210] H. Ribeiro, G. Burkard, J. R. Petta, H. Lu, and A. C. Gossard, "Coherent adiabatic spin control in the presence of charge noise using tailored pulses", Phys. Rev. Lett. **110**, 086804 (2013).

[211] J. Kölbl, "Kohärente dynamik von gekoppelten nanomechanischen resonatormoden", MA thesis (Universität Konstanz, 2015).

[212] K. Technology, *Getting started guide: keysight 81150a and 81160a pulse function arbitrary noise generator*, (2014) https://www.keysight.com/us/en/assets/9018-03434/quick-start-guides/9018-03434.pdf.

[213] Keysight, *Data sheet: keysight 33503a benchlink waveform builder pro and basic software.* (2021) https://www.keysight.com/us/en/assets/7018-02919/data-sheets/5990-7569.pdf.

[214] A. T. Le, *Github website with Matlab source codes for control in Ramsey interferometry experiment with Magnus-based corrections.* (2022) https://github.com/ATLe88/Project_IAS.git.

[215] M. Sillanpää, T. Lehtinen, A. Paila, Y. Makhlin, and P. Hakonen, "Continuous-time monitoring of Landau-Zener interference in a cooper-pair box", Phys. Rev. Lett. **96**, 187002 (2006).

[216] G. D. Fuchs, G. Burkard, P. V. Klimov, and D. D. Awschalom, "A quantum memory intrinsic to single nitrogen–vacancy centres in diamond", Nature Physics **7**, 789–793 (2011).

[217] H. Ribeiro, A. Chowdhury, and A. T. Le, Unpublished, Private discussion with collaborators H. Ribeiro and A. Chowdhury, 2021.

[218] S. Meiboom and D. Gill, "Modified spin-echo method for measuring nuclear relaxation times", Review of Scientific Instruments **29**, 688–691 (1958).

[219] H. Bluhm, S. Foletti, I. Neder, M. Rudner, D. Mahalu, V. Umansky, and A. Yacoby, "Dephasing time of GaAs electron-spin qubits coupled to a nuclear bath exceeding 200 us", Nature Physics **7**, 109–113 (2010).

[220] J. Chan, T. P. M. Alegre, A. H. Safavi-Naeini, J. T. Hill, A. Krause, S. Gröblacher, M. Aspelmeyer, and O. Painter, "Laser cooling of a nanomechanical oscillator into its quantum ground state", Nature **478**, 89–92 (2011).

[221] Y. Seis, T. Capelle, E. Langman, S. Saarinen, E. Planz, and A. Schliesser, "Ground state cooling of an ultracoherent electromechanical system", Nature Communications **13**, 10.1038/s41467-022-29115-9 (2022).

[222] S. M. Meenehan, J. D. Cohen, S. Gröblacher, J. T. Hill, A. H. Safavi-Naeini, M. Aspelmeyer, and O. Painter, "Silicon optomechanical crystal resonator at millikelvin temperatures", Phys. Rev. A **90**, 011803 (2014).

[223] S. M. Meenehan, J. D. Cohen, G. S. MacCabe, F. Marsili, M. D. Shaw, and O. Painter, "Pulsed excitation dynamics of an optomechanical crystal resonator near its quantum ground state of motion", Phys. Rev. X **5**, 041002 (2015).

[224] J. D. Thompson, B. M. Zwickl, A. M. Jayich, F. Marquardt, S. M. Girvin, and J. G. E. Harris, "Erratum: strong dispersive coupling of a high-finesse cavity to a micromechanical membrane", Nature **452**, 900–900 (2008).

[225] L. Qiu, I. Shomroni, P. Seidler, and T. J. Kippenberg, "Laser cooling of a nanomechanical oscillator to its zero-point energy", Phys. Rev. Lett. **124**, 173601 (2020).

[226] A. H. Safavi-Naeini, J. Chan, J. T. Hill, T. P. M. Alegre, A. Krause, and O. Painter, "Observation of quantum motion of a nanomechanical resonator", Phys. Rev. Lett. **108**, 033602 (2012).

[227] A Chowdhury, P Vezio, M Bonaldi, A Borrielli, F Marino, B Morana, G Pandraud, A Pontin, G. A. Prodi, P. M. Sarro, E Serra, and F Marin, "Calibrated quantum thermometry in cavity optomechanics", Quantum Science and Technology **4**, 024007 (2019).

[228] P. Vezio, A. Chowdhury, M. Bonaldi, A. Borrielli, F. Marino, B. Morana, G. A. Prodi, P. M. Sarro, E. Serra, and F. Marin, "Quantum motion of a squeezed mechanical oscillator attained via an optomechanical experiment", Physical Review A **102**, 053505 (2020).

[229] A. Chowdhury, P. Vezio, M. Bonaldi, A. Borrielli, F. Marino, B. Morana, G. A. Prodi, P. M. Sarro, E. Serra, and F. Marin, "Quantum signature of a squeezed mechanical oscillator", Physical Review Letters **124**, 023601 (2020).

[230] C. M. Caves, "Quantum-mechanical noise in an interferometer", Phys. Rev. D **23**, 1693–1708 (1981).

[231] T. P. Purdy, R. W. Peterson, and C. A. Regal, "Observation of radiation pressure shot noise on a macroscopic object", Science **339**, 801–804 (2013).

[232] O. Hosten, N. J. Engelsen, R. Krishnakumar, and M. A. Kasevich, "Measurement noise 100 times lower than the quantum-projection limit using entangled atoms", Nature **529**, 505–508 (2016).